UNIVERSITÀ DEGLI STUDI DI PADOVA

Sede Amministrativa: Università degli Studi di Padova

Dipartimento: **Centre of Studies and Activities for Space CISAS - "G.Colombo" research department of the University of Padova**

SCUOLA DI DOTTORATO DI RICERCA IN : Scuola di Dottorato di Ricerca in Scienze Tecnologie e Misure Spaziali (STMS)
INDIRIZZO: Misure Meccaniche per l'Ingegneria (MMI)
CICLO: XXIV

Measurement techniques for assessing and reducing the risk posed by Micrometeoroid and Orbital Debris to Space vehicles

Direttore della Scuola: Ch.mo Prof. Giampiero Naletto

Coordinatore d'indirizzo: Ch.mo Prof. Stefano Debei

Supervisore: Ch.mo Prof. Alessandro Francesconi

Dottorando : Leonardo Barilaro

Contents

Riassunto

Negli ultimi anni un nuovo rischio ha iniziato ad emergere per i veicoli spaziali orbitanti attorno alla Terra: i detriti spaziali.
Questo termine descrive oggetti di origine umana in orbita attorno alla Terra che non hanno più uno scopo utile.
Il presente lavoro descrive tecniche di misura per stimare e ridurre il rischio creato da micrometeoriti e detriti spaziali (MMOD) ai veicoli spaziali.

Le principali aree di ricerca sono:

- Fenomenologia dell'impatto, metodologia per la stima del rischio, metodi di progettazione;
- Metodi sperimentali (ossia tecniche di accelerazione e strumentazione per la diagnostica);
- Modelli ingegneristici (ossia misure degli effetti dei MMOD e derivazione delle equazioni di danno).

Gli obiettivi e i contributi personali legati a queste aree di ricerca sono presentati relativamente a:

- Sviluppo della strumentazione del laboratorio per la simulazione di impatti iperveloci presso il CISAS (Centro Interdipartimentale Studi ed Attività Spaziali) "G. Colombo", ossia evoluzione del cannone bistadio a gas leggero e progettazione relativa a componenti di due cannoni monostadio a gas leggero, uno per il CISAS e uno per la Cranfield University, UK;
- Attività sperimentale relativa allo studio degli impatti, dove sono stati sviluppati strumenti per la caratterizzazione di ejecta e per il rilevamento di impatti primari;
- Derivazione delle equazioni di danno, questo ha portato allo sviluppo di nuove Equazioni di Limite Balistico, aventi base statistica e che forniscono un nuovo scenario riguardo il futuro della progettazione di scudi per i MMOD. Queste equazioni sono sviluppate per definire le condizioni di impatto (ossia diametro e densità del detrito, velocità e angolo di impatto) che risultano per il valore di soglia relativo al fallimento di uno specifico componente o sottosistema di un

veicolo spaziale.

I principali obiettivi di questa ricerca sono stati raggiunti e hanno portato a:

- Studio gasdinamico e progettazione del sistema ferma sabot per un nuovo cannone monostadio a gas leggero per il laboratorio per impatti iperveloci presso il CISAS;
- Progettazione della camera per gli impatti e del sistema ferma sabot per il cannone monostadio a gas leggero presso la Cranfield University, UK;
- Progettazione della sezione ad alta pressione e della struttura di supporto per il nuovo cannone bistadio a gas leggero presso il CISAS;

- Progettazione ed evoluzione di uno strumento per la caratterizzazione di ejecta;
- Progettazione di uno strumento per misure relative a impatti primari;

- Sviluppo di una metodologia per derivare equazioni di danno su base statistica per i satelliti Cosmo-Skymed;
- Sviluppo di una metodologia per derivare equazioni di limite balistico su base statistica per strutture inflatable.

Abstract

In recent years a new risk for Earth-orbiting spacecraft started to emerge: space debris. This term describes any man-made object in orbit around Earth that no longer has a useful purpose.
The present work describes measurement techniques for assessing and reducing the risk posed by Micrometeoroid and Orbital Debris (MMOD) to space vehicles.

The main research areas are:

- Impacts phenomenology, risk assessment methodology, and design methods;
- Experimental methods (*i.e.* acceleration techniques and diagnostic instrumentation);
- Engineering models (*i.e.* measurements of the effects of the MMOD and derivation of damage equations).

Related to these areas, the objectives and personal contributions are presented regarding:

- Hypervelocity facility developments, *i.e.* improvements of the CISAS (Center of Studies and Activities for Space) 'G. Colombo' two stage light gas gun (LGG) and a design study about 2 single stage LGGs, for the CISAS HVI (hypervelocity impacts) facility and for the Cranfield University, UK;
- Experimental activity for impacts' study, where instruments for the ejecta characterization and the primary impact detection were developed;
- Derivation of damage equations, this led to the definition of new Ballistic Limit Equations statistically based that give a new scenario for MMOD shields' design in the future. These equations are developed to define impact conditions (*i.e.* particle size, particle density, impact velocity, and impact angle) that result in threshold failure of specific spacecraft components or subsystems.

The main objectives of the research were met and they led to the:

- Gasdynamical study and sabot stopping system design for a new CISAS single stage Light Gas Gun;
- Impact chamber and sabot stopping system design for the Cranfield University (UK) single stage LGG;
- High pressure section and supporting structure design for a new CISAS two stage LGG;

- Design and evolution of an instrument for ejecta characterization;
- Design of an instrument for primary impact measurements;

- Development of a methodology to derive damage predictor equations statistically based for Cosmo-Skymed satellites ;
- Development of a methodology to derive ballistic limit equations statistically based for inflatable structures.

1 Introduzione

Dal lancio del satellite Sputnik il 4 ottobre 1957 sono stati effettuati oltre 5000 lanci fino ad oggi, i quali hanno posto in orbita circa 6000 satelliti, dei quali solo una piccola parte, circa 800, è operativa attualmente. ([1])
Con l'aumentare delle attività spaziali un nuovo rischio ha iniziato ad emergere: i detriti spaziali.
I detriti spaziali sono costituiti da milioni di pezzi di oggetti di origine umana posti in orbita attorno alla Terra, i quali non hanno più uno scopo funzionale.
Molti detriti sono troppo piccoli perché possano essere monitorati, ma anche troppo veloci e pesanti per avere adeguate protezioni sui satelliti. A causa dell'alta velocità di questi oggetti in orbita (circa 7 km/s in LEO usualmente), anche piccoli detriti (con una dimensione <1 cm) possono essere davvero pericolosi in una collisione.

Per questo genere di impatti si usa la terminologia di impatti iperveloci, che descrive l'impatto di un oggetto contro un target a velocità che superano ampiamente la velocità del suono del corpo impattato. Il termine ipervelocità tende a riferirsi a velocità nel range tra pochi km al secondo fino ad alcune decine di km al secondo.
In questo range di velocità anche i metalli si comportano come fluidi, con la presenza di fenomeni secondari, quali la creazione di plasma. Per metalli strutturali, in genere si parla di ipervelocità per valori al di sopra dei 2.5 km/s.

Questo causa una minaccia crescente per i veicoli spaziali e può impedire l'accesso a importanti orbite in futuro.

Ci sono differenti tipi di detriti:

- Satelliti non più operativi, usualmente i satelliti commerciali hanno un ciclo di vita attorno ai 15 anni, ciò è anche dovuto alle estreme condizioni presenti nell'ambiente spaziale;
- Ultimi stadi di razzi usati per lanciare i satelliti in orbita;
- Oggetti rilasciati durante le missioni;
- Frammenti generati da collisioni, esplosioni o degradazione di componenti di satelliti attivi.

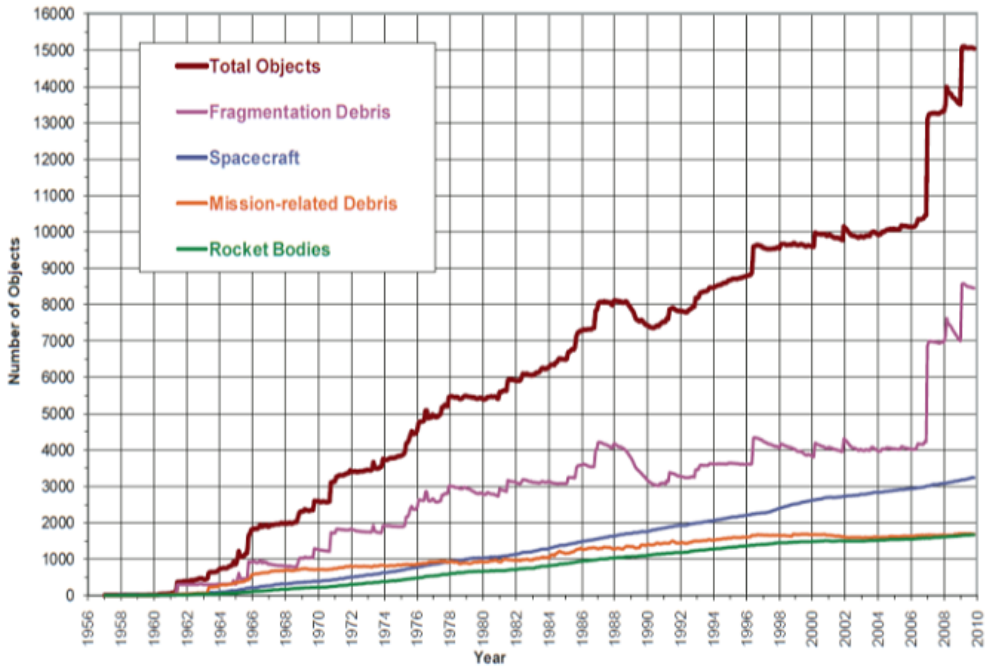

Fig. 1.1 – Numero dei detriti spaziali

Attualmente le collisioni rappresentano la fonte minore di frammenti.

Tuttavia, con l'aumentare dei detriti spaziali, le collisioni diventano più probabili e questo porterà a una sorta di effetto domino chiamato 'Kessler syndrome'.

Se l'andamento di questo processo non cambierà, sarà impossibile operare in sicurezza nello spazio in futuro.

Fig. 1.1 mostra il numero e il tipo di detriti spaziali catalogati nel tempo. L'aumento dei detriti causati da frammentazione nel 2007 è dovuto alla distruzione del satellite Fengyung-1C (800 kg), nel primo test cinese anti-satellite.

Nel febbraio 2009 vi è stata una collisione tra il satellite Iridium 33 (560 kg) e il satellite russo Cosmos 2251 (900 kg), ciò ha creato all'incirca 1400 nuovi oggetti catalogati.

Tab. 2-1 mostra tre categorie di detriti spaziali classificati per dimensione, numero e massa.

Dimension	Number	%Mass
>10 cm	**>9.000**	**99,93**
1-10 cm	**>100.000**	**0,035**
<1 cm	**>35.000.000**	**0,035**
Total	**>35.000.000**	**~5.000 ton.**

Tab. 1-1 – Dimensione e numero dei detriti spaziali

I detriti della prima categoria (dimensione >10 cm) in orbita LEO possono essere monitorati da Terra, in GEO la dimensione minima per rilevarli è attorno ad 1 m. In questo caso è possibile prendere misure per evitare collisioni.

La seconda categoria è molto pericolosa, perché la dimensione è sufficiente per distruggere un satellite, ma troppo piccola per essere monitorata.

Anche a causa del grande numero di oggetti presenti, gli studi riguardanti gli scudi protettivi per i veicoli spaziali si concentrano sulla terza categoria.

Circa il 45% dei detriti spaziali si trova sia in LEO che in GEO.

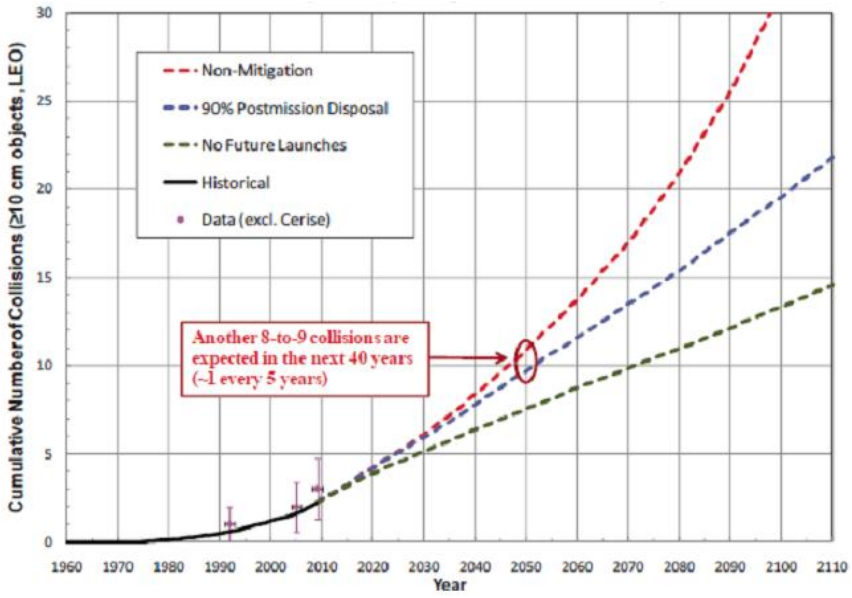

Fig. 1.2 – Probabilità di collisione

Il grafico in Fig. 1.2 mostra il numero di collisioni previste per il prossimo secolo, per gli oggetti della prima categoria. Anche in uno scenario privo di ulteriori lanci il numero di collisioni aumenterà. ([2])

La situazione appena descritta mostra che l'implementazione di appropriate tecniche di mitigazione per i detriti spaziali è di interesse comune per il genere umano, soprattutto considerando le attività spaziali per gli anni futuri.
Le tecniche di mitigazione dei detriti spaziali possono essere divise in due categorie principali:

- Protezione dei satelliti dai detriti

    - Scudi: Il problema principale collegato con gli scudi di protezione dei satelliti è l'effetto sulla massa totale del satellite. Al momento è il modo più studiato ed efficiente per preservare le missioni dal fallimento a causa di detriti.

    - Evitare le collisioni: E' difficile prevedere le collisioni in modo accurato con gli strumenti di misura disponibili attualmente e questo metodo è utile solo per grandi frammenti (>10 cm in LEO). Inoltre le manovre richiedono carburante e questo riduce la vita operativa dei satelliti, aumentando i costi.

- Riduzione del numero di detriti

    - Riduzione della creazione di detriti: Soluzioni a lungo termine prevedono la riduzione del numero di detriti generati (ad esempio evitando esplosioni e muovendo satelliti in orbite 'cimitero' fuori dalle regioni usate da satelliti attivi).

    - Rimozione dei detriti esistenti: L'affrontare la 'Kessler syndrome' richiederà di rimuovere oggetti dalla loro orbita, questo ridurrà l'ammontare di detriti generati (ad esempio l'uso di un sistema di propulsione su un detrito per spingerlo fuori dalla sua orbita). La rimozione attiva dei detriti è una sfida tecnologica difficile e può essere molto costosa.

Questa situazione dell'ambiente spaziale attorno alla Terra ha portato alla creazione di accordi internazionali non vincolanti e alla definizione di linee guida su come affrontare il problema.

L'associazione più importante è la Inter-Agency space Debris Coordination committee, ossia IADC. E' stata fondata nel 1993, comprende 11 agenzie spaziali nazionali tra cui NASA, ESA e ASI. Nel 2002 lo IADC ha adottato una serie di guide linea per la mitigazione del problema dei detriti, che hanno ottenuto un ampio consenso internazionale. ([6])

Lo scopo primario di tale organizzazione è quello di scambiare informazioni tra i membri delle agenzie spaziali sulle attività di ricerca inerenti i detriti, per facilitare le opportunità di cooperazione in questo tipo di ricerca, per osservare i progressi delle attività in corso e per identificare le possibilità per la mitigazione dei detriti.

La struttura principale delle attività dello IADC è composta dai seguenti punti:

1. Misure (osservazione e monitoraggio)
2. Database e modelli
3. Protezione e diagnostica
4. Mitigazione della proliferazione di space debris

Un veicolo spaziale è esposto al rischio di collisione con MMOD durante tutta la sua vita in orbita. Come descritto prima, a causa delle alte velocità di collisione (da 6-7 km/s fino a 35-40 km/s), gli impatti iperveloci possono causare danni significativi. Inoltre, durante un impatto iperveloce è generata una grande quantità di piccoli detriti e ciò è considerata come una delle fonti di nuovi detriti spaziali.
Per valutare il rischio conseguente all'ambiente particellare è necessaria la conoscenza della distribuzione di questi oggetti nello spazio e della direzione del loro moto. A quest'attività sono legati il punto 1 ed il punto 2.

Fino ad oggi sono state sviluppate e impiegate delle metodologie di protezione e diagnostica (punto 3), per tenere conto dell'ambiente particellare, poco raffinate e inadatte a fornire il necessario grado di confidenza ad un'attività di design di un sistema spaziale, in cui margini di progettazione sono spesso stretti e l'ambiente gravoso, comportando inefficienze progettuali non trascurabili.
Per esempio le protezioni dei sistemi spaziali non tengono in conto che differenti lati del veicolo richiedono differenti livelli di protezione, in base alla direzione di volo. ([7])
Le equazioni di limite balistico che definiscono la capacità di protezione dello scudo e che saranno descritte nei successivi paragrafi sono basate solo su un criterio fallimento-non fallimento, senza tenere in considerazione l'incertezza collegata con il rilevamento della soglia di fallimento per un dato materiale.

Questo porta ad avere scudi più pesanti del necessario.
Inoltre sensori per rilevare gli impatti e il relativo livello di pericolo sono attualmente ancora non utilizzati nell'usuale attività spaziale per scopi commerciali.

In forte crescita è anche l'attenzione e le risorse dedicate alla limitazione dell'aumento di space debris nell'ambiente dell'orbita terrestre (punto 4).
La IADC propone le seguenti linee guida da seguire nella mitigazione:

- Minimizzazione del rischio di rilascio durante le normali fasi operative;
- Previsione di una fase di dismissione del satellite, per non occupare inutilmente spazio in orbite di ampio utilizzo.

Si tende pertanto a progettare le missioni odierne per tener conto di queste problematiche, prevedendo sin dalla fase di concetto della missione una fase terminale di de-orbiting (modifica dell'orbita in modo tale da introdurre il veicolo su una traiettoria destinata a decadere naturalmente, per effetto del drag atmosferico, in un'orbita di rientro), di re-orbiting (riposizionamento dell'orbita per immettere il veicolo in un'orbita di parcheggio). Sono attualmente allo studio anche specifiche missioni allo scopo di ripulire lo spazio, in particolare in ambienti come quello geostazionario in cui le missioni richiedono investimenti notevoli e in cui altre strategie di pulizia come il rientro in atmosfera sono difficilmente applicabili.

Lo scenario appena descritto afferma la necessità di sviluppare nuove tecniche di misura per stimare il rischio causato dai detriti spaziali, definendo una nuova metodologia.
La metodologia classica relativa alla stima di rischio per sistemi spaziali si sviluppa secondo il seguente schema (Fig. 1.3):

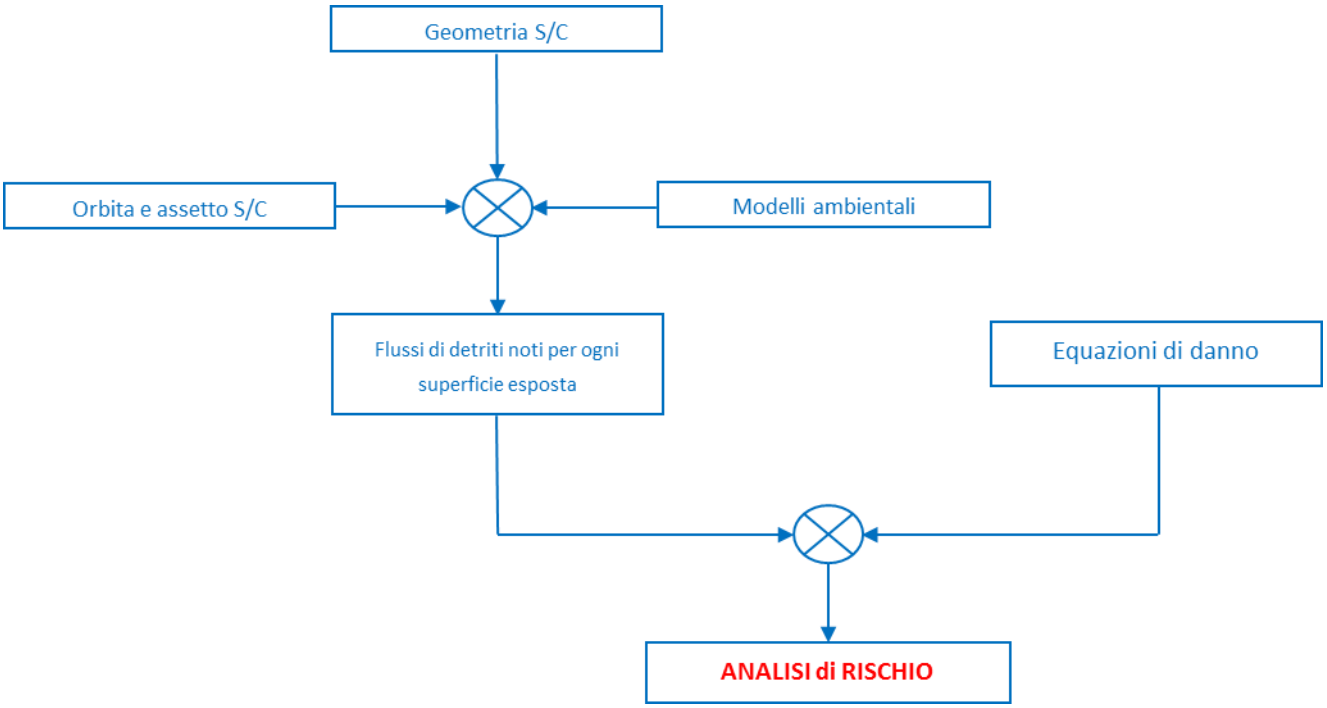

Fig. 1.3 – Obiettivi dell'attività di ricerca

Come punto di partenza è necessario conoscere la geometria del sistema in esame, con i relativi materiali impiegati e la disposizione dei sottosistemi critici, l'assetto e i parametri orbitali. Per mezzo di modelli ambientali è quindi possibile stimare il flusso di detriti che investe ogni superficie esposta.
Il flusso di detriti spaziali è definito come il numero di impatti per m^2 all'anno, attesi su una superficie planare orientata casualmente di una struttura spaziale in orbita. ([30])
Una volta noti i flussi previsti è possibile effettuare un'analisi di rischio per mezzo delle equazioni di danno.
Come introdotto in precedenza, tali equazioni sino a oggi sono state ricavate per via sperimentale e definiscono un valore di soglia oltre il quale avviene perforazione in seguito all'impatto iperveloce, i limiti di tale approccio consistono nell'avere un criterio "passa-non passa" senza potervi associare una banda di incertezza sperimentale e senza poter valutare l'entità del danno per impatti non perforanti ed altri effetti secondari, quali

la quantità di moto trasferita al sistema e l'influenza dei detriti secondari.
Questi limiti saranno descritti più approfonditamente nel par. 3.2.2 e par. 3.2.3.

Una maggior confidenza nella progettazione dei sistemi spaziali risulta quindi una necessità nella prospettiva odierna, per ridurre i costi ed aumentare la sicurezza non solo dei sistemi spaziali non abitati (satelliti) ma anche abitati (quale ad esempio la stazione spaziale internazionale ISS) che sembrano trovare nel prossimo futuro una nuova fase di sviluppo e crescita, con la rinnovata prospettiva di installare moduli abitati sulla Luna e su Marte.
Per studiare i fenomeni connessi all'ambiente particellare e sviluppare nuove metodologie è necessario creare dei sistemi in grado di replicare a terra le condizioni operative che si verificano nello spazio, con costi ragionevoli.
Tali sistemi presentano, nella loro realizzazione concreta, delle sfide tecnologiche importanti.

I cannoni bi-stadio a gas leggero (LGG) sono la tecnologia predominante, ciò è dovuto alla loro superiore affidabilità e ripetibilità se confrontati con altre tecnologie studiate al momento.
Un cannone a gas leggero (Fig. 1.4) è uno strumento che permette di simulare impatti iperveloci in laboratorio, usando gas, quali elio o idrogeno, per accelerare un proiettile che rappresenta il detrito spaziale.
Relativamente al cannone utilizzato presso il laboratorio per impatti iperveloci del CISAS, è presente un primo stadio riempito con gas, il quale da la spinta propulsiva ad un pistone, che a sua volta comprime il gas nel secondo stadio. Questo gas accelera un proiettile, usualmente una sfera composta di alluminio, protetto dalle alte temperature e pressioni con una struttura esterna chiamata sabot. Il proiettile impatta contro un target montato nella camera a vuoto.

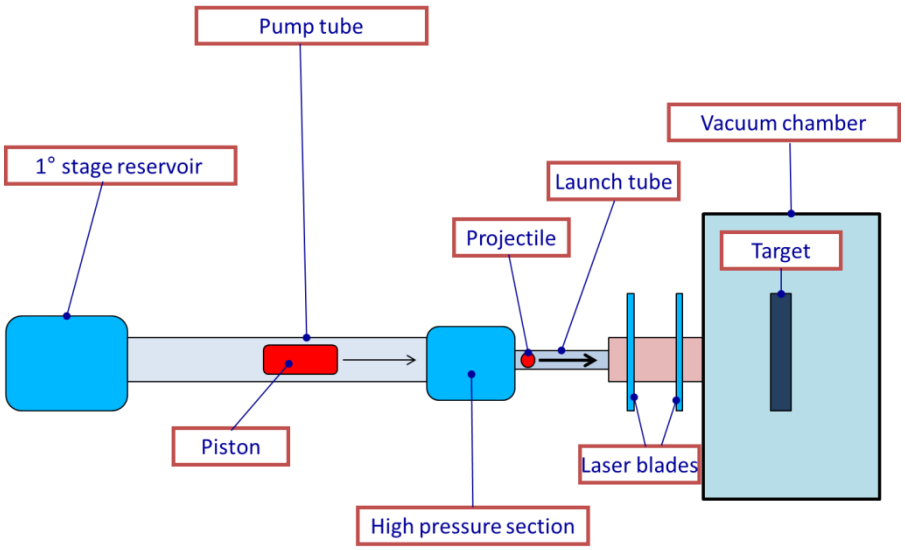

Fig. 1.4– Schema del cannone bi-stadio a gas leggero presso il CISAS

A seguito di questi studi è quindi possibile, grazie all'accresciuta conoscenza del fenomeno, definire criteri di progettazione, migliorare la caratterizzazione dei materiali e sviluppare schermi di protezione e strumentazioni diagnostiche più efficaci.

Gli obiettivi dell'attività svolta sono stati quelli di contribuire alla ricerca nel settore della valutazione del rischio e della protezione relativa agli space debris, secondo la logica descritta in Fig. 1.5:

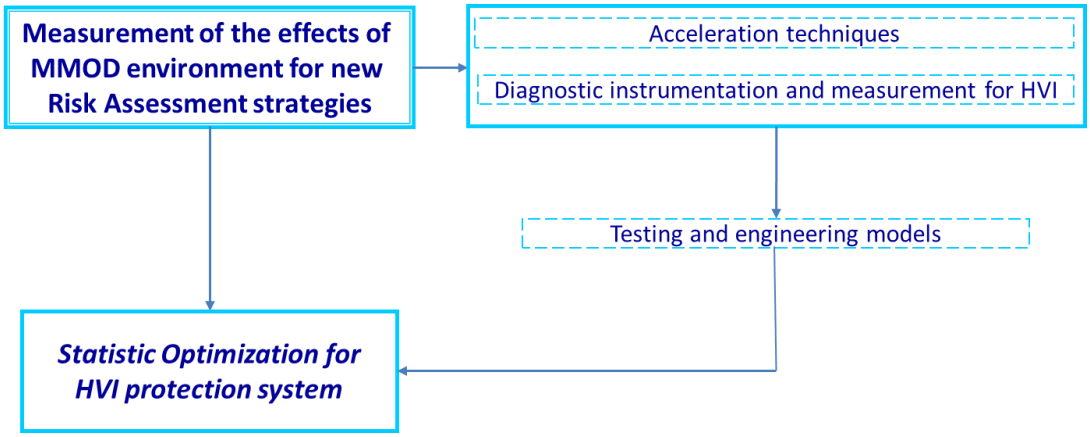

Fig. 1.5 – Organizzazione dell'attività di ricerca

Si descriveranno ora i vari obiettivi anticipati nello schema precedente.

1. Misure degli effetti dell'ambiente MMOD per nuove strategie di Risk Assessment

Lo sviluppo di equazioni di danno con approccio statistico consente di fornire risultati per i calcoli di Risk Assessment, assieme ai margini di incertezza ad essi associati.

Relativamente alle BLE classiche, si effettuano i test e i risultati sono riportati su un grafico con velocità e diametro del proiettile sugli assi, la curva di limite balistico è una semplice linea di demarcazione tra zone. Vi è la necessità di avere BLE su base statistica, per tenere in considerazione i fenomeni secondari collegati con l'impatto per avere bande di incertezza.
L'ottenere queste nuove equazioni richiede la definizione di un appropriato 'parametro di danno', collegato con il meccanismo di fallimento analizzato con i dati sperimentali.

Lo sviluppo è queste equazioni è fondamentale per ottimizzare la progettazione di ogni sistema di protezione spaziale.
Per ottenere questo obiettivo, che sarà discusso nel punto 2, è necessario sviluppare nuove strategie di Risk Assessment, le quali hanno come base necessaria l'effettuazione di misure atte a valutare l'influenza dei detriti spaziali su S/C.
Tali misure saranno possibili grazie ai punti illustrati qui di seguito:

1a. Tecniche sperimentali di accelerazione ad ipervelocità

Il punto di partenza per lo sviluppo di modelli e metodologie impiegabili nella valutazione del rischio e nella descrizione dei fenomeni fisici di impatto è la disponibilità di dati sperimentali completi sui fenomeni di impatto stessi. Tale attività sperimentale, dovendo riguardare fenomeni di impatto iperveloce in condizioni rappresentative a quelle che realmente si verificano nello spazio, richiede l'utilizzo di particolare strumentazione adeguata allo scopo. Attualmente il CISAS dispone di una facility per l'accelerazione iperveloce con velocità massime di 5-6km/s e proiettili di 3.2 mm di diametro.
Tale strumentazione permette di effettuare esperimenti nel range di dimensioni e velocità di interesse per lo studio di molti fenomeni di impatto da detriti spaziali su satelliti.

1b. Strumentazione diagnostica e misure per l'impatto iperveloce

Nel presente documento è descritta l'attività di ricerca riguardo strumentazione diagnostica di impatto per misure in situ, inizialmente pensata come strumentazione da laboratorio, ma concettualmente orientata sin dall'inizio alla prospettiva di sviluppare in futuro uno strumento diagnostico e di monitoraggio per applicazioni spaziali, ossia generalizzare lo strumento alle condizioni in orbita. Tale strumentazione è necessaria per comprendere meglio la fisica d'impatto, per effettuare misure di parametri, quali la quantità di moto trasferita e la caratterizzazione degli ejecta e per la costruzione di modelli ingegneristici

1c. Testing e sviluppo di modelli ingegneristici di danno

Una volta ottenuti i dati sperimentali di interesse si cercano dei modelli, siano essi empirici o fisici, che descrivano i fenomeni osservati.
L'attività di modellazione è supporto e mezzo per la determinazione delle equazioni di danno intese come veri strumenti di supporto alla progettazione e nuovo approccio alla trattazione del problema della valutazione del rischio d'impatto. Con le equazioni di danno è possibile correlare il danno ai parametri che lo influenzano, con le loro incertezze. Risulta quindi possibile anche attribuire un significato statistico ed un'incertezza al danno stesso, cosa non possibile nella metodologia classica. Nell'approccio delle equazioni di danno si sviluppa una relazione funzionale fra una grandezza fisica misurata (o una combinazione di grandezze significative dal punto di vista del danneggiamento) in grado di fungere da indice del danno subito dal sistema (a seconda della tipologia del fenomeno studiato), definito in letteratura come Damage Parameter (DP) ed i parametri fisici di influenza della tipologia di danneggiamento in gioco.
Con questo approccio risulta possibile definire anche in modo statistico, e quindi utilizzare la propagazione dell'incertezza dei parametri sul DP, il grado di confidenza sulla probabilità di danno stessa. Questo approccio ha il pregio di seguire il fenomeno dell'impatto e le sue conseguenze sul sistema nella sua evoluzione da impatto non critico a danno effettivo, permettendo di definire criteri di danneggiamento più raffinati rispetto agli attuali. D'altra parte questo rende necessaria una modellazione (empirica o fisica) del fenomeno d'impatto e quindi lo sviluppo di modelli per i vari aspetti fisici dell'impatto partendo dai dati sperimentali, quali ad esempio quelli risultanti dal punto precedente.

2. Ottimizzazione su base statistica di sistemi di protezione per HVI

In base ai punti descritti sarà possibile sviluppare nuove tecniche di progettazione ottimizzata per impianti e strutture aerospaziali, grazie alla metodologia messa a punto per misure relative ai detriti spaziali e per mezzo degli strumenti di diagnostica realizzati.
Tale aspetto è collegato con l'ottimizzazione della massa del MDPS, ossia il Meteoroid/Space Debris Protection System.
La progettazione delle protezioni degli S/C è effettuata di norma in base ai requisiti di sicurezza previsti utilizzando i modelli di ambiente disponibili per ottenere la stima di rischio, tuttavia spesso ciò non è effettuato facendo analisi per una efficiente distribuzione delle masse dei sistemi di protezione.
In anni recenti strutture inflatable per moduli abitati, quali ad esempio quelli per la stazione spaziale internazionale (ISS), hanno guadagnato un'importanza crescente.
Lo sviluppo di equazioni di danno collegate con questo genere di scudi porterà ad un miglioramento nella progettazione, in termini di massa, efficienza e costi.

1.1 Contenuti

In questo paragrafo è brevemente descritto il contenuto dei principali capitoli.

- Capitolo 1: Introduzione in lingua italiana.

- Capitolo 2: Questo capitolo introduce il tema principale della presente tesi di dottorato e fornisce una panoramica dell'attuale scenario relativo ai detriti spaziali e descrive la logica di studio legata all'analisi della stima del rischio di impatto.

- Capitolo 3: In questo capitolo viene descritto il background scientifico e tecnologico relativo al problema dei detriti spaziali. Grande importanza ha l'analisi critica delle metodologie per la stima di rischio, le quali conducono a nuovi metodi di progettazione per veicoli spaziali. Vengono inoltre introdotti due casi di studio.

- Capitolo 4: Sono qui presentati metodi sperimentali per misure degli effetti su componenti spaziali, relative ai detriti spaziali. Sono presentati gli obiettivi dello studio e successivamente è descritto lo sviluppo della strumentazione relativa al laboratorio per impatti iperveloci. Nell'ultima parte è descritto lo sviluppo della strumentazione per lo studio degli ejecta.

- Capitolo 5: Viene qui introdotta una nuova metodologia per derivare le equazioni di limite balistico (BLE). Partendo dalla descrizione della progettazione degli esperimenti e della test matrix, viene poi illustrata la fase di test e quella di misurazione degli effetti dei MMOD. Infine viene presentato il metodo per derivare le equazioni di danno.

1.2 Contributi personali

In questa tesi sono descritti i contributi personali dell'autore in tutte le principali aree di questa ricerca, ossia:

- Lo sviluppo dei sistemi d'accelerazione a gas leggero per impatti iperveloci;
- Attività sperimentale riguardo gli impatti;
- Derivazione delle equazioni di danno.

Gli argomenti che ora verranno descritti sono tutti strettamente connessi con le tecniche di misura per ridurre il rischio causato da micrometeoriti e detriti ai veicoli spaziali.

a. Sviluppo dei sistemi d'accelerazione a gas leggero per impatti iperveloci

   - CISAS cannone monostadio a gas leggero

     Un nuovo tipo di sistema ferma sabot è stato progettato per il cannone monostadio a gas leggero presso il CISAS, permetterà di lanciare masse fino a 0.12 kg a 1000 m/s.
     Con il termine sabot si intende la struttura esterna che circonda il proiettile e lo protegge dal gas durante la fase di sparo.
     Punto critico è la separazione del sabot dal proiettile.
     Il sistema ferma sabot che sarà descritto nel par. 4.2.1 permette di evitare interazioni tra il sabot e il tubo di lancio, proteggendolo da possibili danni.

   - Cranfield University cannone monostadio a gas leggero

     La parte di documento presente nel par. 4.2.2 descrive lo studio degli aspetti gasdinamici e meccanici del sistema ad alta pressione del cannone monostadio a gas leggero presente a Cranfield (UK).
     Introduce inoltre un nuovo approccio riguardo il design del sistema ferma sabot e della camera per gli impatti.

- CISAS cannone bistadio a gas leggero

  Il cannone bistadio a gas leggero presente presso il laboratorio CISAS per gli impatti iperveloci sta gradualmente venendo sostituito da una versione con un maggior range operativo dello stesso.
  Una versione più grande della sezione d'alta pressione è stata progettata e realizzata, con alcune nuove soluzioni riguardanti l'assorbimento dell'impatto dell'otturatore da parte della parte di coda di questo sistema, che sarà descritto nel par. 4.2.3.

b. Attività sperimentale riguardante lo studio di impatti

- Strumento per la caratterizzazione degli ejecta

  Partendo da un prototipo è stato sviluppato in diverse versioni un nuovo strumento per lo studio del fenomeno degli ejecta. La sua evoluzione è descritta nel par. 4.3.1 e nel par. 4.3.2.

- Strumento per lo studio degli impatti primari

  Oltre all'attività principale riguardante gli ejecta è stato realizzato anche uno strumento per lo studio degli impatti primari.
  Utilizza 3 differenti tipi di sensori contemporaneamente e sarà descritto nel par. 4.3.3.

c. Derivazione delle equazioni di danno

- Equazioni di danno per scudi dei satelliti Cosmo-Skymed

  I risultati di una campagna di test condotta dal CISAS per sviluppare equazioni di danno per strutture di uno dei satelliti Cosmo-Skymed sono presentati nel par. 5.3.2. Tali test sono stati condotti all'interno del progetto ASI relativo alla ricerca sui detriti spaziali.
  E' utilizzato un nuovo approccio di tipo statistico nel ricavare Equazioni di Limite Balistico per scudi Whipple Shield ed equazioni di danno per strutture in honeycomb e honeycomb ricoperto da MLI.

- Equazioni di danno per sistemi di protezione inflatable

  I risultati di una campagna di test condotta dal CISAS per sviluppare Equazioni di Limite Balistico per sistemi inflatable sono presentati nel par. 5.3.3.

  Tali sistemi di protezione sono composti da uno scudo multi-layer con 3 principali parti: il sistema di protezione termica, lo scudo contro i MMOD e il sistema di contenimento per la pressione/aria.

  In particolare lo scudo contro i MMOD è composto da diversi strati di materiale flessibile, come Kevlar e Nextel, posti ad adeguata distanza tra loro.

  La parte più originale di questo studio riguarda l'applicazione di un innovativo approccio per la derivazione delle Equazioni di danno, basato sulla stima del danno prodotto dall'impatto su diversi strati dello scudo con differenti condizioni di impatto.

  A differenza dei metodi tradizionali, è proposta una possibile procedura per derivare statisticamente le Equazioni di danno, partendo da esperimenti dove l'evoluzione del parametro di danno è legata la meccanismo di fallimento della struttura.

  Le Equazioni di danno sono presentate assieme alle bande di incertezza derivate statisticamente.

2 Introduction

Since the launch of Sputnik on the 4th of October 1957 about 5000 launches have placed around 6000 satellites into orbit, of which only a minor fraction, about 800, are still operational today. ([1])
With increasing space activities a new risk started to emerge: space debris.
Space debris consists of millions of pieces of man-made objects in orbit around the Earth that are not operational.
Many debris are too small to be monitored but too fast and heavy to shield satellites properly. Due to the high speed of objects in orbit (~ 7km/s is typical in LEO, low earth orbit), also small (size <1 cm) debris can be very damaging in a collision.

For these kind of collisions the terminology of hypervelocity impacts is used; this describes the impact of an object into a target at a speed that greatly exceeds the speed of sound in the struck body. Hypervelocity tends to refer to velocities in the range of a few kilometres per second to some tens of kilometres per second.
In this range of velocities even metals behave like fluids under hypervelocity impact, with the presence of secondary phenomena like the creation of plasma. For structural metals, hypervelocity is generally considered to be over 2.5 km/s.

This poses a growing threat to spacecraft and could prevent the access to important orbits in the future.

There are different types of debris:

- Not operational satellites, usually commercial satellites have a life cycle of around 15 years, this is also due to the harsh environment in space;
- Last stages of rockets used to launch satellites into orbit;
- Objects released during missions;
- Fragments caused by collisions, explosions or degradation of active satellites' components.

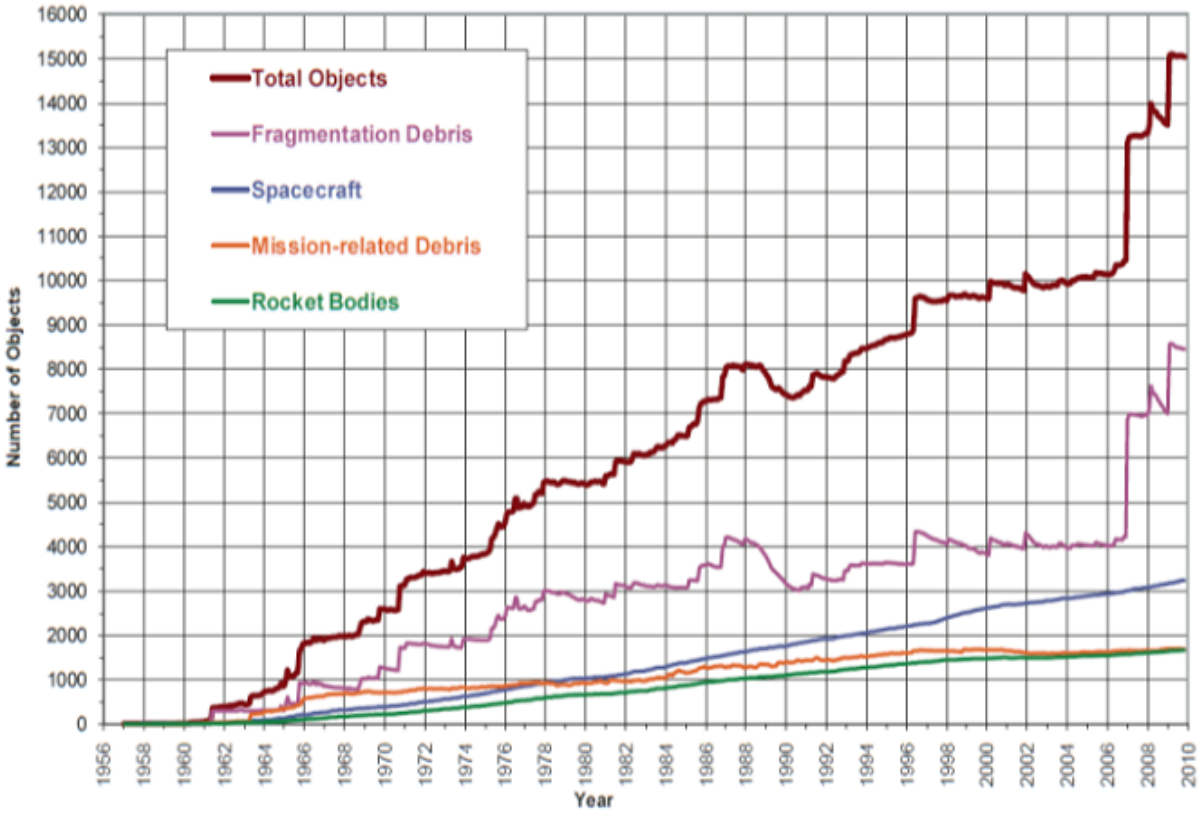

Fig. 2.1 – Number of Debris Objects. ([2])

At present collisions are the smallest part of fragments. However, with the increasing of debris objects, collisions become more likely and this will create a sort of domino effect called 'Kessler syndrome'.

If the trend of this process will not change it will be impossible to operate in space safely in the future.

Fig. 2.1 shows the number and type of catalogued debris objects over time. The increase of fragmentation debris in 2007 was due to the destruction of the satellite Fengyung-1C (800 kg), in the first Chinese anti-satellite test.

In February 2009 there was the collision between the Iridium 33 satellite (560 kg) and the Russian Cosmos 2251 satellite (900 kg), this created around 1400 catalogued debris objects.

Tab. 2-1 shows three categories of space debris according to size, number and mass.

Dimension	Number	%Mass
>10 cm	**>9.000**	**99,93**
1-10 cm	**>100.000**	**0,035**
<1 cm	**>35.000.000**	**0,035**
Total	**>35.000.000**	**~5.000 ton.**

Tab. 2-1 – Size and number of debris objects. ([2])

Debris of the first category (size >10 cm) in LEO can be tracked from Earth, in GEO the lower size limit for tracking is around 1 m. In this case it may be possible to take measures to avoid collisions.

The second category is very dangerous because the size is enough to destroy a satellite but too small to be tracked.

Due also to the great number of objects the studies about spacecraft's shielding are focusing in the range of the third category, to protect systems from failure.

Roughly 45% of these space debris are both in LEO and GEO.

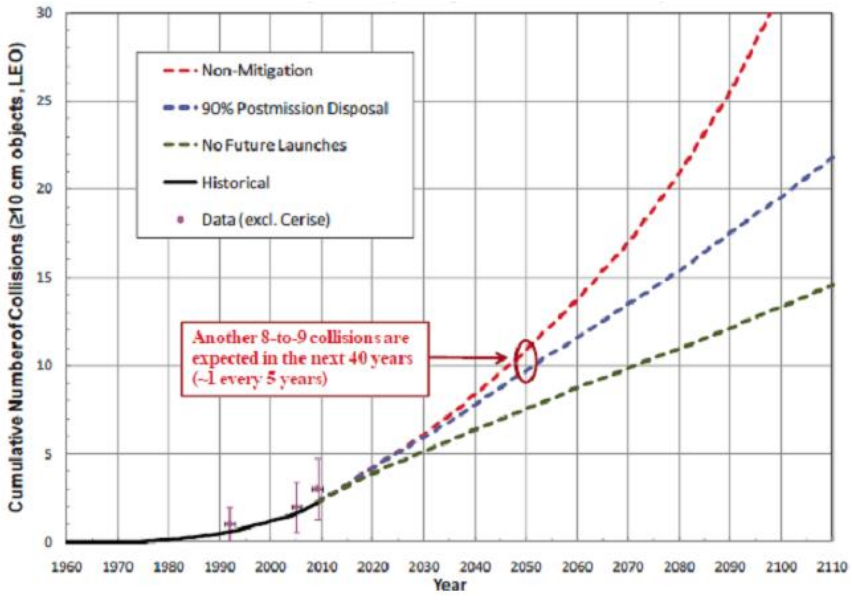

Fig. 2.2 – Probability of collisions. ([2])

The graph in Fig. 2.2 shows the number of collisions for objects of the first size category expected over the next century. Even in a scenario with no more launches the number of collisions will increase. ([2])

The situation described above states that the implementation of appropriate space debris mitigation measures is in humanity's common interest, above all considering the space activities in the next years.
Mitigation of space debris can be divided into two main categories:

- Protecting satellites from debris

    - Shielding: The main problem linked with shielding is the effect on the overall mass of the satellite. Nowadays this is the most studied and efficient way to prevent missions from failures due to debris.

    - Collision avoidance: It is difficult to predict collisions accurately with measurements instruments available nowadays and this method is useful only for big fragments (>10 cm in LEO). Moreover manoeuvres require fuel and this reduce the active life of satellites, increasing the costs.

- Reducing the amount of new debris

    - Reducing creation of debris: Long-term solutions to the problem involve the reduction of the debris created (like avoiding explosions and moving satellites into 'graveyards' orbit outside the regions used by active satellites).

    - Removing existing debris: To deal with the 'Kessler syndrome' will require to remove existing objects from orbit, this will reduce the amount of debris generated (like attaching a propulsion device to a debris objects to push it out of orbit or using a momentum exchange tether). Active debris removal would be expensive and a technically difficult challenge.

This condition of the space environment around the Earth led to the creation of non-binding international agreements and guidelines.
The most important association is the Inter-Agency space Debris Coordination committee, *i.e.* IADC. It was founded in 1993, comprising 11 national space agencies including NASA,

ESA and ASI. In 2002 the IADC adopted a set of recommendations for debris mitigation, that has achieved wide international recognition. ([6])

The primary purposes of the IADC are to exchange information on space debris research activities between member space agencies, to facilitate opportunities for cooperation in space debris research, to review the progress of on going cooperative activities and to identify debris mitigation options.

The main structure of its activities has the following outline:

1. Measurement (*i.e.* monitoring);
2. Environment models and database ;
3. Protection and diagnostic;
4. Space Debris mitigation.

A spacecraft is exposed to the risk of collision with Micrometeoroids and Orbital Debris (MMOD) throughout its orbit lifetime. As described before, because of the large collisions velocities (from 6-7 km/s up to 35-40 km/s), Hypervelocity Impacts (HVI) with MMOD may cause significant damages. On the other hand, during HVI a large amount of small debris is produced and the potential generation of small fragments is considered as one of the sources of new orbital debris.
To assess the risk due to the MMOD environment there is the need to know the distribution of these objects and their direction in space, this activity is linked with point 1 and 2.
Nowadays the protection and diagnostic techniques (point 3) used are still too rough to fit with high efficiency the needs of a space system's design, which have very strict safety factors.
For examples spacecraft shields don't take in account that different sides of the system need of different level of protection, according to the flight direction [[7]].
Ballistic Limit Equations that define the protection capability of the shield and that will be further described in the following paragraphs are based only on fail – no fail criteria, without taking in account the uncertainty linked to the detection of the failure threshold for a given material.
This leads to shields that are heavier than necessary.

Moreover sensors to detect impacts and the related level of danger are still not used in

normal commercial space business.
There is also an increasing attention and employment of resources to minimize the proliferation of space debris around the Earth (point 4).
The guidelines that IADC suggests for mitigation are:

- To contain the debris' release during standard operations;
- To set up of a phased disposal of satellites in order to not keep heavily used orbits busy.

Therefore the direction is to design new missions taking into account of these problems, scheduling a phase of de-orbiting or re-orbiting. At the present time there are also studies about specific missions with the aim of cleaning the space.

The scenario described above states the need to develop new measurement techniques to assess the risk posed by space debris, defining a new methodology.
The classic methodology for space systems' risk assessment regarding the risk of impact follows this scheme (Fig. 2.3):

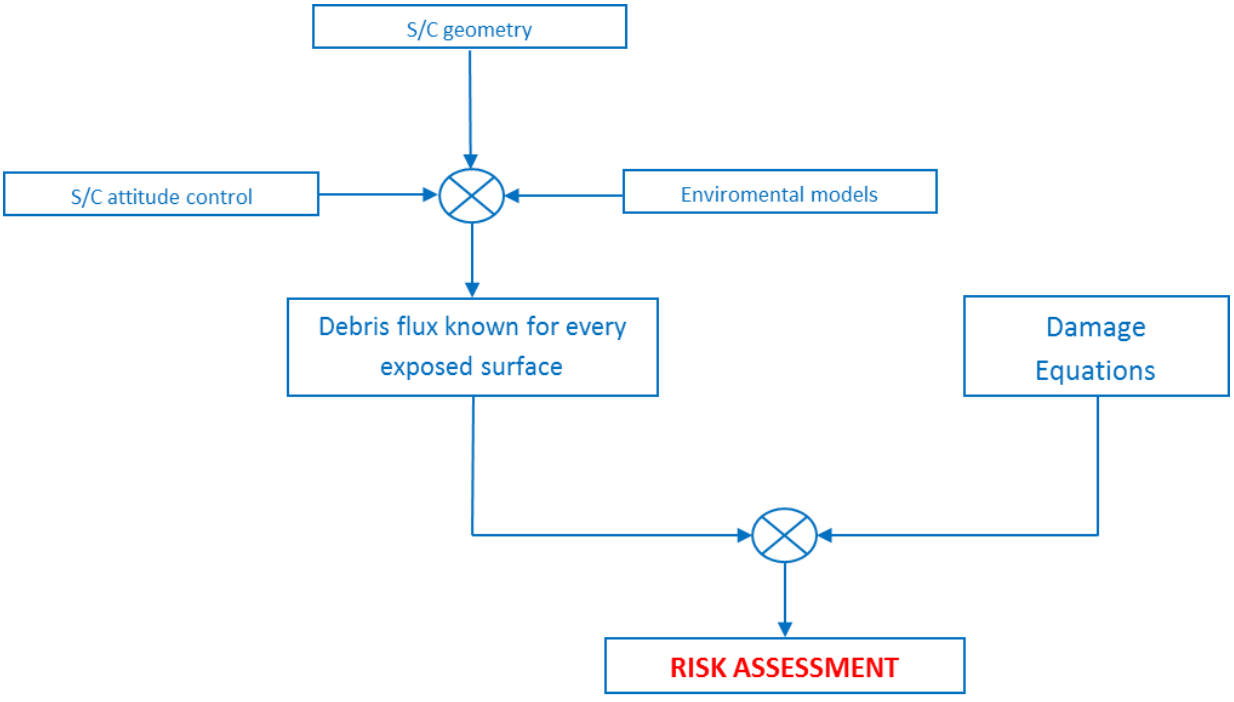

Fig. 2.3 – RA methodology

The starting point is the knowledge of the geometry, materials, critic subsystems' disposition, attitude control and orbital parameters of the spacecraft. With the environmental models it is possible to estimate the debris flux that collides with every exposed surface.
Space debris flux is defined as the number of impacts per square meter per year expected on a randomly oriented planar surface of an orbiting space structure. ([28])
In this way it is possible to do a risk assessment analysis through the use of damage equations, *i.e.* equations developed to predict the shielding performances .
These equations are obtained experimentally and define a threshold to discriminate the above value for penetration due to hypervelocity impact.
As stated before, their limits are that there is a 'pass-no pass' criterion without a value of experimental uncertainty and that there isn't the possibility to evaluate the level of the damage for not penetrating impacts and other secondary effects, like the transferred momentum and the effect of secondary debris.
These limits will be better described in par. 3.2.2 and par. 3.2.3.

A better development of these techniques is mandatory in the present situation, to reduce costs and to increase reliability both for manned (like the ISS) and unmanned (*i.e.* satellites) space systems. There seems to be new opportunities of development with the prospect of installing modules on the Moon and Mars.
To study the effect linked to MMOD environment and to develop new technologies it is necessary to create systems able to reply on ground the space operational conditions with reasonable costs, *i.e.* facilities for hypervelocity impacts and devices to study impacts' physics. They represent a great challenge and there is a lot of interest by the international community.

The two-stage light gas gun is the dominant technology, this is due to their superior reliability and repeatability by comparison with other technologies studied at the moment.
A light gas gun (Fig. 2.4) is a tool to simulate hypervelocity impacts in a laboratory, using a gas, like Helium or Hydrogen, to accelerate a projectile that represents the space debris.
Regarding the LGG used at CISAS HVI Facility, there is a first stage filled with the gas that propels a piston. This piston compresses the gas in the second stage that accelerates a projectile, a sphere usually made by Aluminium, protected by the high temperature and pressure from an external structure called sabot. The projectile impacts on a target mounted into the vacuum chamber.

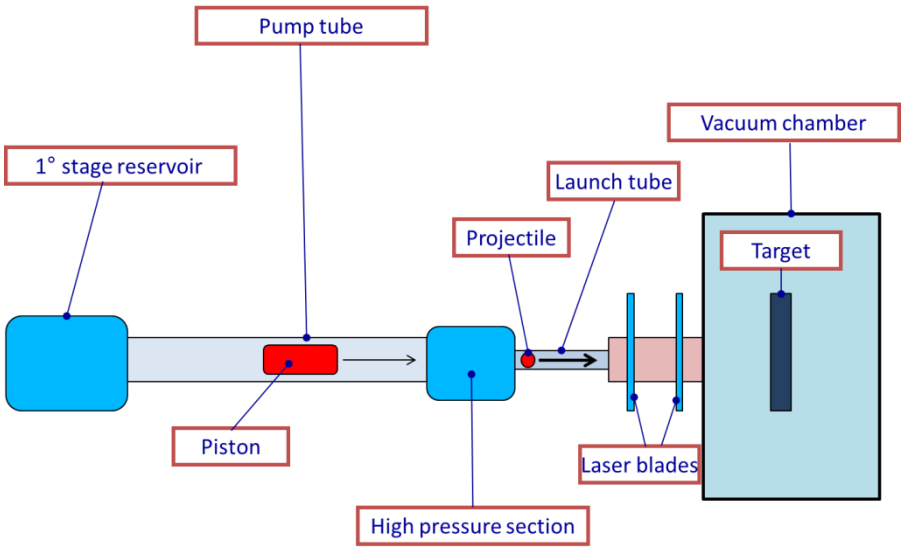

Fig. 2.4– CISAS two stage LGG schematic overview

With these studies it is possible to define design criteria to improve materials characterization and to develop more efficient shield systems and diagnostic instrumentation.

The objective of the activity described here is to contribute to the research in the field of risk assessment and protection related to space debris, following the study logic described in Fig. 2.5.

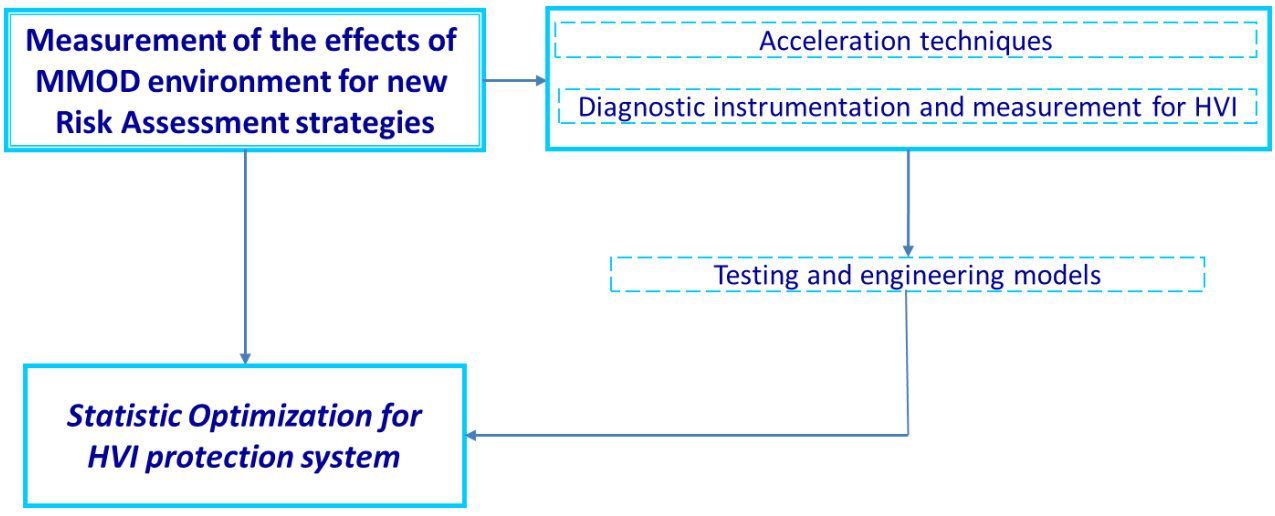

Fig. 2.5 – Objectives

It will follow now a description of the previous scheme.

1. Measurement of the effects of MMOD environment for new Risk Assessment strategies

The development of the statistical based Ballistic Limit Equations allows having results for Risk Assessment calculations with the values of uncertainty.

Regarding the Classic BLE, tests are done. The results are plotted in a projectile velocity-diameter graph; the ballistic limit curve is a simple line of demarcation between zones.
There is the necessity to have BLE statistically based, to take in account secondary phenomena linked to the impact and to have uncertainty boundaries.
The derivation of the new equations requires the definition of an appropriate 'damage parameter' Π, linked to the failure mechanism analysed with experimental data.

The development of these equations is mandatory to optimize the design of every protection system. To obtain this objective that will be described at point 2 there is the need to develop new RA strategies, they are based on measurements done to evaluate the space debris influence on S/C. These measurements are available thanks to:

1a. Acceleration techniques

The starting point to develop models and methodologies to assess risks and to describe impact's phenomena is the availability of experimental data. This activity needs of instrumentation that is able to simulate space hypervelocity impacts. CISAS facility has the possibility to explore this kind of impacts till 5-6 km/s of maximum velocity and 3.2 mm of projectile diameter. This allows doing tests in a range useful for the study of many impact phenomena. It will be also described the improvement of the facility that will allow to reach extended mass and velocity range.

1b. Diagnostic instrumentation and measurement for hypervelocity impacts

In this document it will be described the diagnostic instrumentation designed for in situ measurement, initially realized as laboratory instrumentation but oriented to develop a diagnostic and monitoring instrument for space applications. This is necessary to better understand the impact physic and to measure parameters like the transferred momentum and to characterize the ejecta, to set up new models.

1c. Testing and engineering models

With the experimental data it is possible to define models (empirical or physical) to describe the observed phenomena. The creation of new models is the way to determine Damage Equations, these equations support the design process and represent a new approach to assess the impact risk. Therefore, it is possible to give an uncertainty value linked to the damage.

In this kind of approach there is the development of a relation between the measured parameter (or a combination of significant parameters) that can describes the level of the system damage, defined as Damage Parameter (DP), and the physical parameters implied in the type of damage considered.

The link between the physical and measured parameters with the equations allows to define in a statistic way the confidence level on the damage probability and to use the uncertainty propagation of DP's parameters.

This approach allows obtaining more refined damage criteria.

2. Statistic Optimization for HVI protection systems

Thanks to the previous described points it will be possible to develop new optimized design techniques for space structures.

This aspect is linked with the optimization of the mass of Meteoroid/Space Debris Protection System (MDPS).

Usually the S/C protection system is designed following the safety requirement described by the environmental models to assess the risk, but this is not done with an analysis for an efficient mass distribution of the protection system.

In recent years inflatable structures for manned modules, like for the ISS, gained an increasing importance. The development of damage equations linked with this type of shields will lead to an improvement in their design, in terms of mass, efficiency and costs.

2.1 Thesis contents

In this paragraph the content of the main chapters will be shortly described.

- Chapter 1: Introduction in the Italian language.

- Chapter 2: This chapter introduces the overall research theme of the thesis by giving an overview on the actual space debris scenario and describing the study logic linked with the impact risk assessment analysis.

- Chapter 3: In this chapter the scientific and technological background about the space debris problem is described. The critical analysis of Risk Assessment methodologies has great importance as they lead to new design methods for space vehicles. Moreover, two selected case studies are introduced.

- Chapter 4: Experimental methods for space debris effects on space components measurements are here presented. The selected study's objectives are introduced, and then the impacts facility's requirements and its improvements are described. In the last part is shown the development of the instrumentation for the ejecta's study.

- Chapter 5: A new methodology to derive Ballistic Limit Equations (BLE) is here introduced. Starting from the description of the design of the experiments and test matrix, presenting the testing phase and then showing the measurements of the effects of the MMOD and the derivation of damage equations.

2.2 Personal contributions

In this paragraph are described personal contributions of the author in all the main areas of this research, *i.e.*:

- Hypervelocity facility developments
- Experimental activity for impacts' study
- Derivation of damage equations

The topics that now will be introduced are all strictly related to measurement techniques to reduce the risk posed by MMOD to space vehicles.

a. Hypervelocity facility developments

   - CISAS single stage Light Gas Gun

     Gasdynamical studies have been done and a new type of sabot stopping system has been designed for the CISAS single stage LGG, that will allow shooting launch packages up to 0.12 kg at 1000 m/s.
     The sabot is an external structure that surrounds the projectile and protects it from the gas during the firing phase.
     A critical point is the separation of the sabot from the projectile.
     The sabot stopping system that will be described in par. 4.2.1, it avoids the interaction between the sabot and the launch tube, protecting them from possible damages.

   - Cranfield single stage Light Gas Gun

     The part of the document in par. 4.2.2 describes the study of the gasdynamic and mechanical aspects for the high pressure system of the Cranfield University (UK) single stage light gas gun.
     It also introduces a novel study on the sabot stopping system and on the

impact chamber.

- CISAS two stage Light Gas Gun

  A bigger two stages LGG is replacing the one already operating since 10 years at the CISAS Hypervelocity Impacts facility.
  An upscaled version of the high-pressure section has been designed with some new solutions regarding the absorption of the shutter's impact with the back of this section. This system will be described in par 4.2.3.

b. Experimental activity for impacts' study

- Ejecta instrument

  A new instrument to study the ejecta phenomenon has been developed in different versions, starting from a prototype. Its evolution will be described in par. 4.3.1 and 4.3.2.

- Primary impact instrument

  Beside the main activity research about the ejecta also an instrument for primary impacts' study has been designed.
  It uses 3 different types of sensors at the same time.
  It will be described in par. 4.3.3.

c. Derivation of damage equations

- Cosmo-Skymed damage equations

  Results of an impact campaign carried out at the CISAS Impact Facility to develop damage predictor equations for structures of Cosmo-Skymed satellites are presented in par. 5.3.2.
  These tests are done in the ASI's framework about space debris research.
  A new statistically based approach for these equations is used for Whipple Shield, honeycomb and honeycomb covered by MLI.

- Manned modules protecting shields damage equations

  A procedure to derive Ballistic Limit Equations for inflatable shields is presented in par. 5.3.3.
  Such shields are composed by a multi-layer shell with three main functional parts: a thermal protection layer, a MMOD shield and a pressure/air containment layer. In particular, the MMOD protection system is composed by several layers of flexible materials such as Kevlar and Nextel placed at adequate spacing from each other.
  The most original part of the study is the application of a novel approach for BLE derivation, based upon the assessment of the impact damage produced on subsequent shield layers in different impact conditions. In contrast to common methods, it is proposed a possible procedure to statistically derive BLEs, starting from experiments in which the evolution of a damage parameter related to the failure is investigated. The procedure to derive BLE has statistically-based uncertainty bounds.

3 Scientific and technical background

The content of this chapter is summarized in the following flow chart (Fig. 3.1).

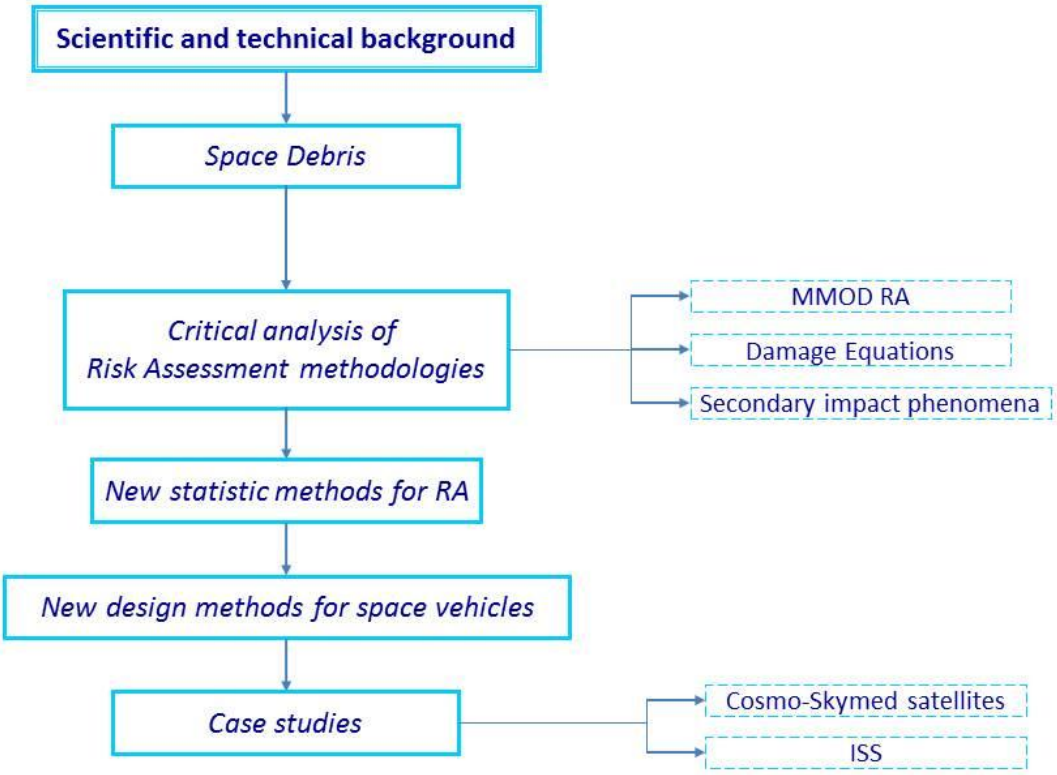

Fig. 3.1 – Chap. 3 overview

The scientific and technical background of the present work will be described starting from an introduction about the space debris problem.

Then there will be an overview about the Risk Assessment (RA) methodologies, an analysis about new statistic methods and new design methods.

In the end there will be introduced two case studies, *i.e.* the Cosmo-Skymed satellites and the International Space Station (ISS).

3.1 Space Debris: an increasing problem

Since the launch of Sputnik on the 4th October 1957 more than half a century of space flight activities has generated a significant man-made particle environment that is characterized by the name of 'space debris'. ([1])
According to the definition by IADC "space debris are all man-made objects including fragments and elements in Earth orbit or re-entering the atmosphere that are non-functional. This population of space objects must be taken in account in the design of a space mission, to ensure successful space operations, with an acceptable low risk".

The knowledge of the space debris environment is available doing ground-based radar and optical measurements:

- In LEO usually radars detect space debris size regimes above 5 to 10 cm;
- In GEO telescopes track objects from a size of 30 cm to 1 m during routine space surveillance;
- Regarding small debris sizes, in-situ impact detectors and retrieved surface material give important information.

By the year 2005 most of the on-orbit mass of about 5000 tons was concentrated in Launch and Mission Related Objects (LMROs).

Classification by object categories:

- Payloads – 31.8%
- Spent rocket upper stages and boost motors – 17.6%
- Mission related objects – 10.5%
- Debris, mainly from fragmentation events – 40.1%

Classification by orbit regimes:

- LEO – 69.2%
- MEO – 3.9%
- GEO – 9,3%
- HEO – 9.7%
- Outside the GEO region – 7.8%

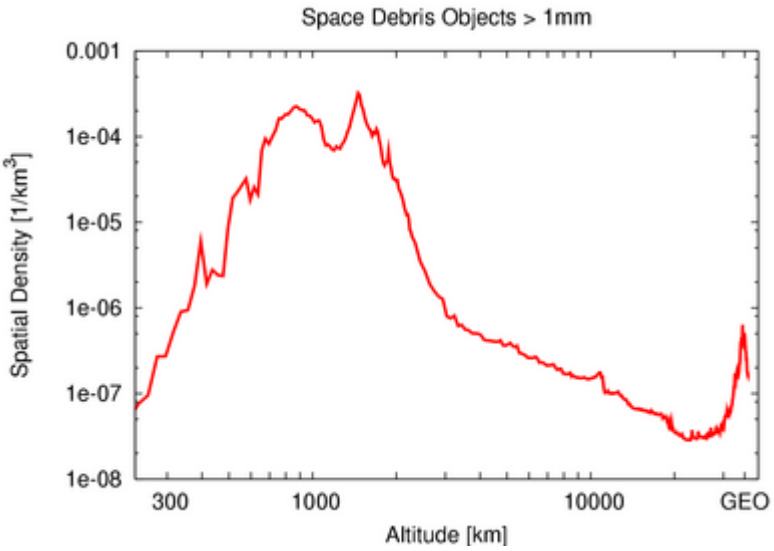

Fig. 3.2- Spatial density of space debris by altitude according to ESA MASTER-2001. This graphic does not include the large amounts of debris from the Chinese ASAT and 2009 collision events. ([2])

On 11 January 2007, the 880 kg weather spacecraft Fengyung-1C, launched on 10 May 1999 into a sun-synchronous orbit with a CZ-4B booster from the Taiyuan Satellite Launch Centre, was destroyed over central China as a result of the first successful Chinese anti-satellite weapon test. It was carried out with a direct ascent interception with a kinetic energy kill vehicle launched by an SC-19 missile, fired from a mobile ground platform close to the Xichang Satellite Launch Centre.

While the technical details of the test, probably the third attempt, and the characteristics of the weapon used remain shrouded in secrecy, the intentional breakup in polar orbit of the aging weather spacecraft, which was fully functional until 2005, produced a huge amount of debris in one of the orbital regimes already most affected by fragmentation events. At present, the US Space Surveillance Network has catalogued about 2000 objects larger than 5 cm, but the final tally might exceed 2200, even disregarding centimetre sized objects, many thousands of which have been probably generated as well.

After 2 decades of substantial international progress in the field of orbital debris mitigation, in order to preserve the low earth and geosynchronous environments for future space missions, the Chinese anti-satellite test and other unfortunate accidental breakups, like that over Australia, on 19 February 2007, of the derelict Briz-M rocket stage used for the failed launch of the satellite Arabsat-4A, represented a serious turnabout.

In fact, in less than six weeks at the beginning of 2007, the two worst documented fragmentations in 50 years of space operations, both tallying more than 1000 pieces larger than 10 cm, considerably boosted the number of catalogued debris in orbit. To give a rough idea of the impact of such events on the circumterrestrial environment, it is sufficient to realize that the Chinese anti-satellite test alone, in numerical terms, increased the number of catalogued orbital debris by an amount comparable the previous 14 years of space activity.

10th February 2009 another very important event was the collision between the Iridium 33 satellite (560 kg) and the Russian Cosmos 2251 satellite (900 kg), reported to be non-operational. This is the first case in history of two satellites colliding. The orbital altitude where the collision took place is among the most crowded in low Earth orbit, but statistically speaking, the enormous scale of space makes the chance that this kind of direct collision would occur completely by accident infinitesimal. ([2])

The data obtained during the observation campaigns are used to validate models of the debris environment like ESA-MASTER or the NASA-ORDEM. Such models are the only means of assessing the impact risk caused by space debris, as only larger objects can be regularly tracked:

- MASTER (Meteoroid and Space Debris Terrestrial Environment Reference) by ESA is a software package that can be used to analyse space debris flux and spatial densities. The following sources of debris are considered: launch and mission-related objects, explosion and collision fragments, solid rocket motor slag and dust, NaK droplets (these massive metal fragments consist of eutectic sodium–potassium alloy and have been released during RORSAT reactor core ejections mostly on orbits close to 950 km altitude), surface degradation products, ejecta, and meteoroids. MASTER can deliver flux and spatial density analysis for all epochs between 1957 and 2060. For all epochs, the lower size threshold is one micron. The analysis of the future debris environment is possible based on three different future scenarios (business as usual, intermediate mitigation, full mitigation). ([34])

- ORDEM 2000 is a semi-empirical, computer-based orbital-debris model which combines direct measurements of the environment with the output and theory of orbital-debris models. It approximates the environment with six different inclination bands. Each band has a unique distribution of semi-major axis, for near circular orbits, and a unique perigee distribution, for highly elliptical orbits. In addition, each inclination band has unique size distributions which depend on the source of debris. Collision probability equations are used to relate the distributions of orbital elements to flux on a spacecraft or through the field of view of a ground sensor. The distributions of semi-major axis, perigee, and inclination are consistent with the U.S. Space Command catalogue for sizes larger than about 10 cm, taking the limitations of the sensors into account. For smaller sizes, these distributions are adjusted to be consistent with the flux measured by ground telescopes, the Haystack radar, and the Goldstone radar as well as the flux measured by the LDEF satellite and the Space Shuttle. ([35])

Several space agencies are presently defining their concepts to conserve the space debris environment of the Earth at a level which allows continuing a safe execution of space programs in the next decades and beyond.

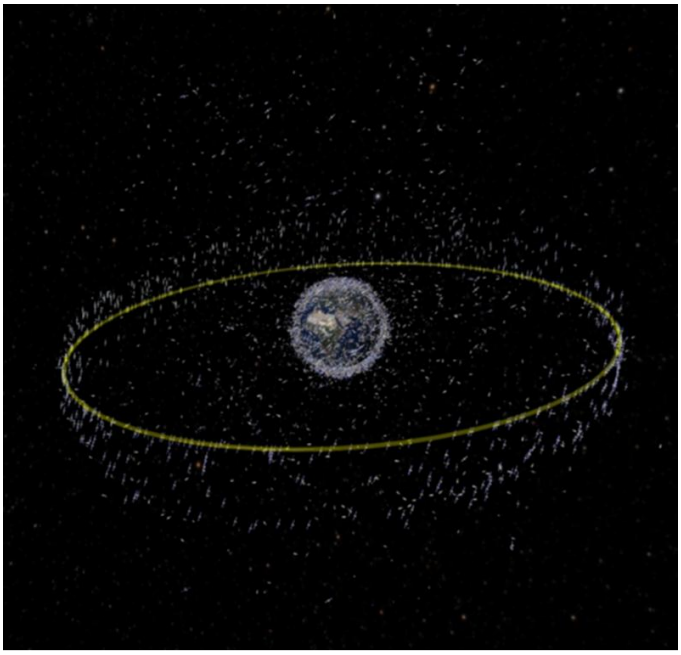

Fig. 3.3 – Artistic overview of the Space Debris scenario

The ESA Handbook describes the current debris environment and its corresponding collision and damage risk for typical earth orbits ([6]).

Space debris represents a textbook example of environmental economics: space is a public good (*i.e.*, despite the 1976 Bogota Declaration, in which eight equatorial countries claimed sovereignty over the portion of geosynchronous Earth orbit lying above their territory, there are no well-defined and enforceable property rights and no countries are excluded from launching satellites) and debris is a pollutant. More specifically, LEO is a renewable stock resource (much like air or water), in that debris eventually dissipates, albeit on an extremely slow time scale.

The two fundamental issues in environmental economics are to determine the target level of pollution and to decide how to achieve this target. ([21])

3.2 Critical analysis of Risk Assessment methodologies

3.2.1 Meteoroid/Orbital Debris Risk Assessment

The previous synthesis of the space debris environment states the need of mathematical models able to describe this phenomenon.
The behaviour of the space debris population is modelled in a statistical way starting from the use of the kinetic gas theory's laws. The implementation of statistical flux models is useful for debris which cannot be tracked and to predict the evolution for the future years.

The analysis codes, like Bumper (used by NASA and JAXA) and ESABASE (used by NASA), through the implementation of the model of space debris environment allow to provide safe and reliable operations for spacecraft. These codes quantify the probability of penetration of shielding and the damage to spacecraft equipment as a function of the size, shape, and orientation of the spacecraft; the parameters of its orbit; and the impact damage resistance of each spacecraft.
The BUMPER II software in particular is specifically designed for the ISS and contains several dozen ballistic limit equations that are based on results from thousands of hypervelocity impact tests conducted on ISS shielding, Space Shuttle, Mir, Extravehicular Mobility Units (*i.e.*, space suits), and other satellites and spacecraft. .
Significant effort has been expended to validate BUMPER and "benchmark" it to other MMOD risk assessment codes used by some ISS International Partners
The BLEs (Ballistic Limit Equations) and MMOD (MicroMeteoroids and Orbital Debris) environment models are embedded into the software. A FEM that describes the spacecraft geometry is created in and input into BUMPER. It calculates the number of predicted failures by determining the number of MMOD particles that exceed the ballistic limits for each element of the FEM, and calculates the total number of failures by summing the individual elements. BUMPER results are used to determine the "risk drivers," which areas on the spacecraft contribute most to the overall risk. Emphasis on risk reduction is placed on lowering the risk for the "drivers." ([28])

Meteoroid and debris are specified by their number density $n(t,\bar{r},\overline{V},\delta)$ in the phase space $(t,\bar{r},\overline{V},\delta)$, *i.e.* (time, space, velocity, size). The function $f = n|\overline{V}|$ is usually used, it represents a differential flux.
The time-averaged flux Fr against a single-sided randomly tumbling surface is calculated

by the formula

$$F_r = F_r(t, r, \delta_{\min}) = \frac{1}{4\pi} \iint_{4\pi} \left(\int_{\delta > \delta_{\min}} \left(\iiint n * (\bar{V} \bullet \bar{v}) dV \right) d\delta \right) d\bar{v} \quad , \qquad \text{[Eq. 3-1]}$$

where $\bar{v}$ is a surface normal unit vector and δmin is a ballistic limit size.
This formula applies for randomly tumbling plates, and not oriented surfaces as considered in the BUMPER code and other probability analysis codes. ([20])

The relevant area for Fr is the outer surface area of the spacecraft. It is possible also to define a "cross sectional area flux", Fc, for a randomly tumbling satellite, where the relevant area is the time averaged cross sectional area. For randomly tumbling objects with no concave surfaces (no self-shielding):

$$Fc = 4\ Fr \qquad \text{[Eq. 3-2]}$$

For spacecraft which fly with a fixed orientation, the debris fluxes have to be treated as vector quantities and the effects of directionality must be carefully evaluated. The great part of impacts is on the forward-surface, defined as the leading surface in the direction of motion of the spacecraft, *i.e.* the velocity direction or “ram” direction.

The number of impacts (N), from particles larger than a given diameter, increases linearly with exposed area (A), flux (F), and exposure time (T):

$$N = F\ A\ T \qquad \text{[Eq. 3-3]}$$

where F is the cumulative number of impacts per unit area and time.
The numbers of impacts from meteoroids and space debris can be summed to obtain the total number of impacts:

$$Ntot = Nmeteoroid + Ndebris \qquad \text{[Eq. 3-4]}$$

The probability for no impacts, P0 is thus given by:

$$P0 = e\text{-}N \qquad \text{[Eq. 3-5]}$$

The probability for no impacts P0 is:

$$P0 = e^{-N} \approx 1 - N \qquad \text{[Eq. 3-6]}$$

A widely used failure criterion is the complete penetration, *i.e.* "perforation", of the structural wall. Also other failure criteria are possible as well, like the creation of a hole larger than a given critical size, penetration depth that exceeds an allowable amount, *etc*.
If the failure criteria is 'no penetration' the probability for no penetration, P0, is also denoted PNP.
The most important issue for software packages that model the space environment is the determination of the particle flux F.

3.2.2 Damage Equations

3.2.2.1 Ballistic Limit Equations

Ballistic Limit Equations (BLEs) are developed to define impact conditions (*i.e.* particle size, particle density, impact velocity, and impact angle) that results in threshold failure of specific spacecraft components or subsystems. A combination of hypervelocity impact test results and analyses is used to determine the BLEs ([18]).

Structural materials used in spacecraft light-weight design are Aluminium alloys and fibre reinforced plastics. There can thermal insulation like MLI (multi-layer insulation), silica felt or ceramic tiles be to insulate the structure against heat. The structural parts may be connected by brackets and mechanisms are needed to allow required movements of structural parts.

The structure has to protect the payload against hypervelocity impacts which can be from micro-meteoroids or from orbital debris particles.

This problem represents a great technical challenge for manned missions and is becoming an important consideration in the design of unmanned spacecraft.

Catastrophic failure of loaded structures (pressure vessels, pressurised modules) has to be avoided as well as the generation of new orbital debris.

When a projectile impacts on a structure, high pressures and temperatures are generated, which may melt or even vaporise the material and produce a crater. ([20])

As an example of the behaviour under hypervelocity impacts, the BLEs for a typical double wall protection will now be described.

Whipple shields are named after Fred Whipple who invented a standoff bumper shield system for protecting spacecraft from meteoroid impacts in the 1940's [Whipple, 1947].

These shields (Fig. 3.4) consist of a single bumper, standoff, and the spacecraft structure that is to be protected.

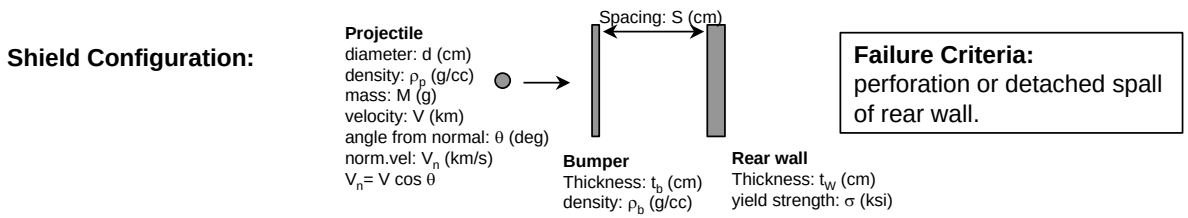

Fig. 3.4 - Whipple shield

The Ballistic Limit Equations derived by NASA are given below [Christiansen, 1993].

BL Equations (d_c is critical particle on ballistic limit threshold of shield)

for $V_n \geq 7$,

$$d_c = 3.919\, t_w^{2/3}\, S^{1/3}\, \rho_p^{-1/3}\, \rho_b^{-1/9}\, (\sigma/70)^{1/3}\, (V\cos\theta)^{-2/3} \quad (1)$$

for $3 < V_n < 7$,

$$d_c = 1.071\, t_w^{2/3}\, S^{1/3}\, \rho_p^{-1/3}\, \rho_b^{-1/9}\, (\sigma/70)^{1/3}\, (V\cos\theta/4 - 0.75) + ((t_w\, (\sigma/40)^{0.5} + t_b)/(1.248\, \rho_p^{0.5}\cos\theta))^{(18/19)}\, (1.75 - V\cos\theta/4) \quad (2)$$

for $V_n \leq 3$,

$$d_c = ((t_w\, (\sigma/40)^{0.5} + t_b)/(0.6\, (\cos\theta)^{5/3}\, \rho_p^{0.5}\, V^{2/3})^{(18/19)} \quad (3)$$

for $\theta \geq 65^o$, $d_c = d_c$ (at $\theta = 65^o$) (4)

Sizing Equations

$t_b = 0.25\, d\, \rho_p/\rho_b$ when $S/d < 30$; $t_b = 0.2\, d\, \rho_p/\rho_b$ when $S/d \geq 30$ (5)

for $V_n \geq 7$, $t_w = 0.16\, d^{0.5}\, M^{1/3}\, S^{-0.5}\, \rho_p^{1/6}\, \rho_b^{1/6}\, (70/\sigma)^{0.5}\, (V\cos\theta)$ (6)

Constraints/Discussion: Valid for aluminum bumpers and metallic rearwalls. Can be used for hi-strength non-metallic rearwalls with yield constrained to 100ksi. At 7km/s normal impact, when $t_b/d < 0.15$ and/or $S/d < 15$, the high-velocity equation tends to over-estimate critical diameter.

Ref. E.L. Christiansen, "Design and Performance Equations for Advanced Meteoroid and Debris Shields," *International Journal of Impact Engineering*, Vol.14, pp.145-156 (1993), Proceedings of the 1992 HVIS, November 1992.

Fig. 3.5 - Whipple shield equations (NASA)

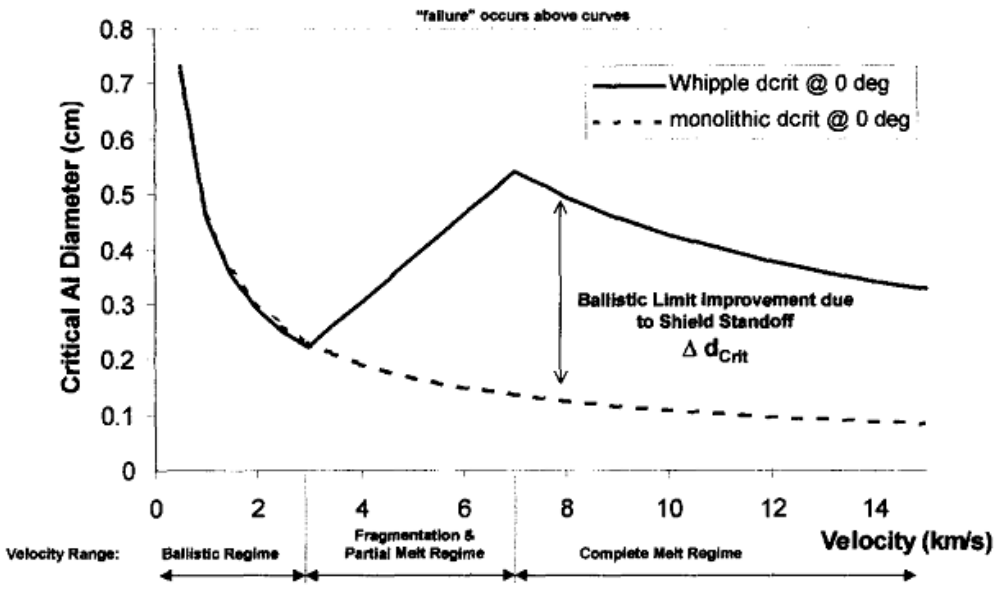

Fig. 3.6- Illustration of Ballistic Limits for Monolithic and Whipple Shield (equal mass)

It can be noticed that in the velocity range between 3 and 7 km/s there is an inversion of the trend of the critical debris diameter, this improvement is due to the effect of the fragmentation caused by the bumper, that is a sacrificial plate, and to the stand-off distance. Above the velocity of 7 km/s this effect decreases.

3.2.2.2 BLE's State of the Art limits

As showed before, this State of the Art in the approach to space debris protection is based on a fail/no fail criteria and it take in account only one type of damage, *i.e.* perforation.
The actual Ballistic Limit Equations are not statistically based and don't consider the other types of damage and the correlated uncertainty.

An example of the drawbacks of the actual procedure for BLE derivation has been evidenced in studies conducted with the NASA Bumper II code. ([19])
The BUMPER II code is a powerful tool, but it has limitations. Its results provide a point estimation of MMOD risk with no assessment of its associated uncertainty.
Considering how the existing BL equations are actually derived, it is impossible to state that any existing BL equation is accurate to within +/-X% with a confidence of Y%.
Schonberg et al. show as it may be possible to develop a quantitative measure that would indicate, at least at some level, the accuracy of a BL in separating the region of perforating projectile diameter-impact velocity combinations from non-perforating combinations.
Innovative approaches must be developed to obtain the required uncertainty information from existing BL equations and the data on which they are based, or re-derive the BL equations using a statistics-based approach so that uncertainty information is forthcoming out of the analyses along with the equations themselves.

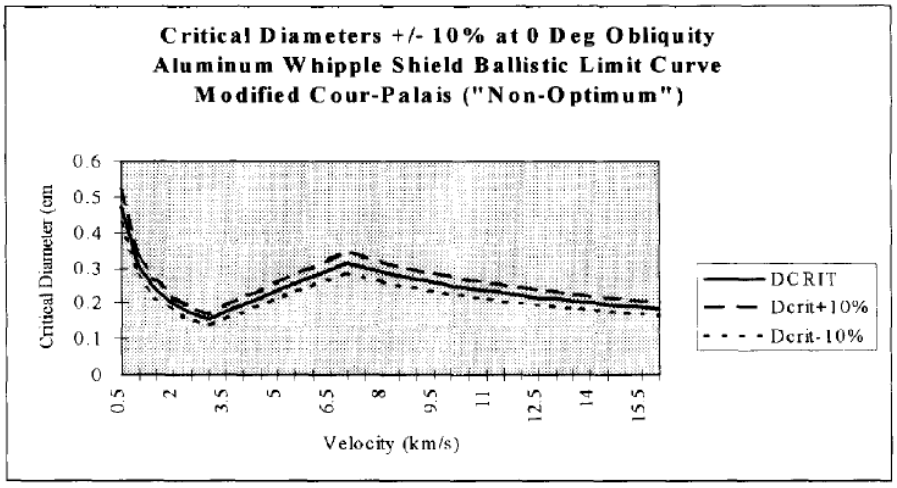

Fig. 3.7 – Critical diameters +/- 10% for a typical spacecraft shield

Fig. 3.7 shows an example of the limits of the ballistic limit curves used by BUMPER to predict whether or not a particle penetrates: the critical diameter causing penetration at a particular velocity and obliquity (*i.e.* Dcrit) from a ballistic limit relation is uniformly distributed about the mean with a 2 sigma value of 10% of the predicted Dcrit, to check

the effect on the variance of the Ppen/imp, *i.e.* the probability of penetration given that an impact has occurred (it is primarily a function of shield ballistic limit).
The dashed lines on the figure show the effect of a 10% variation on ballistic range that was used in the +/- 10% runs.
Clearly, the level of uncertainty in the ballistic limit equations is a crucial factor in the overall level of uncertainty in calculating Ploss (probability of loss, *i.e.* vulnerability). ([19])

In the usual practice, BLE are obtained from a series of HVI experiments which provide only a penetration-no-penetration information for the structure under test, with no statistic approach. In other words, BLE are derived by simply drawing lines of demarcation between fail and no-fail operating regions, without any possibility of following the damage evolution between different working conditions. As a consequence, it is not possible to specify the uncertainty bounds associated to the BLEs and no confidence intervals can be provided together with the risk predictions, whose reliability could be dramatically affected by the inaccuracy of the equations.

3.2.3 Secondary impact phenomena

3.2.3.1 Impact effects

MMOD impacts on spacecraft, according to the debris' dimensions, can generate:

- Small surface pits due to micrometre-size impactors (this lead to degradation of sensors and of surface properties);
- Clear hole penetrations for millimetre-size objects;
- Mission-critical damage for projectiles larger than 1 cm;
- Any impact of a 10-cm catalogue object on a spacecraft or orbital stage will most likely imply a catastrophic disintegration of the target. This destructive energy is a consequence of high impact velocities.

The effects of hypervelocity impacts are a function of projectile and target material, impact velocity, incident angle and the mass and shape of the projectile.

At low velocities, plastic deformation normally prevails. With increasing velocities the impactor will leave a crater on the target. Beyond 4 km/s, depending on the materials, an impact will lead to a complete break-up and melting of the projectile, and an ejection of crater material to a depth of typically two to five times the diameter of the projectile.

In hypervelocity impacts, the projectile velocity exceeds the speed of sound within the target material. The resulting shock wave that propagates across the material is reflected by the surfaces of the target, and reverses its direction of travel. The superimposition of progressing and reflected waves can lead to local stress levels that exceed the material's strength, thus causing cracks and/or the separation of spalls at significant velocities.

With decreasing target thickness, the effects range from cratering, via internal cracks, to spall detachment, and finally to clear hole perforations.

Usually when the impact risk from meteoroids and orbital debris is assessed the main concern is usually structural damage, but there are also many secondary phenomena that can affect the efficiency of a space mission.

The following list gives an overview of potential effects from hypervelocity impacts ([9]):

Cratering and ejecta

- Surface erosion and degradation leading to a change in thermal, optical or electrical properties;
- Degradation of sensors and mirrors, including impacts on internal instruments by secondary ejecta;
- Degradation of windows (even relatively small craters require the exchange of Space Shuttle windows);
- Sealing problems if *e.g.* exposed hatches have to be closed.

Structural damage

- Penetration of spacecraft walls, leading to structural damage of inner subsystems;
- Penetration of pressurised vessels (tanks, manned modules, coolant loops);
- Cutting of cables or tethers;
- Short circuits;
- Damage to exposed focal plane arrays like CCDs;
- Complete destruction of impacted spacecraft or spacecraft subsystem by larger object.

Plasma effects

- Electrical interference;
- Current flow;
- Triggering of electrostatic discharges;
- Light flashes.

Momentum transfer

- Change of attitude;
- Loss of target lock;
- Loss of formation flying.

While these effects are usually detrimental to spacecraft several have been exploited as detection methods for in-situ impact detectors. Past detectors have *e.g.* been based on impact ionisation, momentum transfer, capacitor breakdown triggered by impact, penetration of pressurised cans, etc.

Any hypervelocity impact on a spacecraft creates new space debris particles in the process.

3.2.3.2 Ejecta

The particles thrown from a crater during its formations after a hypervelocity impact are called ejecta.

The main impact process has a duration of an order of only few microseconds.
Hypervelocity impacts create a shock wave in the target material and lead to very high pressures (>100 GPa) and temperatures (>10000 K). The maximum pressures and temperatures are a strong function of the impact velocity. ([9])

The impacting object and the target material are fragmented, molten or vaporised. The ratio depends on the impact velocity and materials:

- Up to about 5 km/s most of the ejected material are solid fragments.
- Ejecta from impacts in the velocity range 5 - 20 km/s are a mixture of solid fragments, molten droplets and vapour.
- Above 20–25 km/s the ejecta is completely vaporised.
- A small fraction of the ejected material is ionised. This fraction is a strong function of the impact velocity but does not exceed about 1% for even the fastest debris.

The ejected mass can be much larger (up to 10 - 1000 times) than the mass of the original impactor. Typically, a large fraction of the impact energy ends up in the ejecta. Ejecta can be very numerous. For solid ejecta, the largest particles are comparable to the size of the impactor and the maximum ejection velocity is similar to the impact velocity. A small portion can even be ejected at higher velocities, this is called jetting effect. For brittle materials (*e.g.* glass) larger spall fragments can be ejected at lower velocities around the main crater.

A schematic view, according to the work of Siguier and Mandeville, of the main cratering and ejection features resulting from a hypervelocity impact is presented in Fig. 3.8.

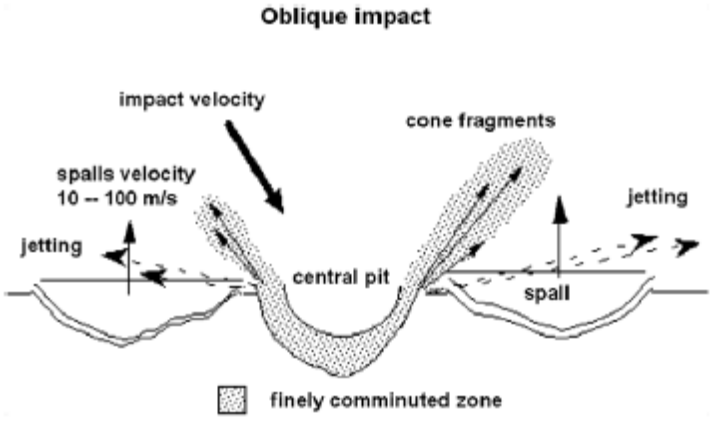

Fig. 3.8 - Sketch of main impact crater features resulting from an oblique impact

In this image three types of ejecta can be distinguished:

- Spall fragments: they are originate from outer and shallower parts of the crater and they are the largest fragments and ejected with relative low velocities of only 10–100 m/s.
- Cone fragments: they contain most fragments of the central crater pit. They have a wide range of velocities with a maximum near the impact velocity (typically 10–20 km/s).
- Jet particles: Jetting is mainly found for highly oblique impacts. The jetted mass is small and made of small fragments but their velocity can exceed the velocity of the impactor.

3.2.3.3 Effects of secondary debris

Now the attention will be focused on the following secondary effects due to the ejecta:

a- Mechanical effects:

- Ricochet debris cloud
- Solar Cells
- CCD
- Momentum transferred
- Induced vibrations

b- Electromagnetic effects

c- Effects on astronomy observations

Hereinafter the description.

a- Mechanical effects

- Ricochet debris cloud ([7])

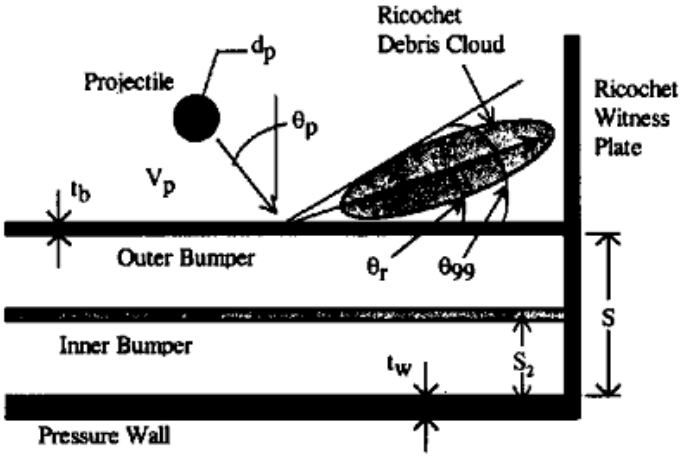

Fig. 3.9 – Schematic representation of the ricochet debris cloud for a multi-wall shield. ([8])

In an oblique HVI usually there is the generation of 3 types of debris clouds [Fig. 3.9]. Considering the set-up for a shield shown in the previous figure two of these debris clouds (projectile and outer bumper) travel inward towards and eventually strike the pressure wall.

The third debris cloud, often referred to as the "ricochet" debris cloud, travels backwards, away from the multi-wall system.

In addition to threatening the operation of the spacecraft itself, on-orbit impacts also generate a significant amount of damaging ricochet ejecta particles. These high-speed particles can destroy critical external spacecraft subsystems, which also poses a threat to the spacecraft and its inhabitants. Since the majority of on-orbit debris impacts are expected to occur at oblique angles, the characterization of ricochet debris created in an orbital debris particle impact is an issue that must be addressed. ([8])

Ricochet debris particles also increase the contamination of the orbital environment and, as a result, constitute an increased threat to other missions. As a result, in a hazard analysis, spacecraft design engineers will need to increase the total primary flux by 10% or more to compensate for secondary debris impact effects.
A comparison of the results from 45 ° and 60 ° MMOD impacts revealed that penetration ejecta had greater damage potential at 45 ° and ricochet ejecta had greater damage potential at 60 °.

The significant ricochet damage was concentrated within an angle of 15 ° with respect to the primary target. ([6])

- Solar cells

Solar cells with their brittle cover glass are a very good source of information for the study of impact craters. Two complete HST solar array wings were retrieved in March 2002 by the Shuttle Columbia. These HST solar arrays had been deployed during the first servicing mission in December 1993. The total exposure duration from deployment until retrieval was 3011 days (8.24 years). The HST orbit was nearly circular around 600 km altitude at an inclination of 28.5°. With a total exposed area of 120 m^2, of which about 40 m^2 are covered by solar cells, the arrays provide the largest survey area of a single substrate ever retrieved and present a unique opportunity to gain information on the meteoroid and space debris population in space. ([8])

A typical example of impact features on the HST sola array is shown in Fig. 3.10.

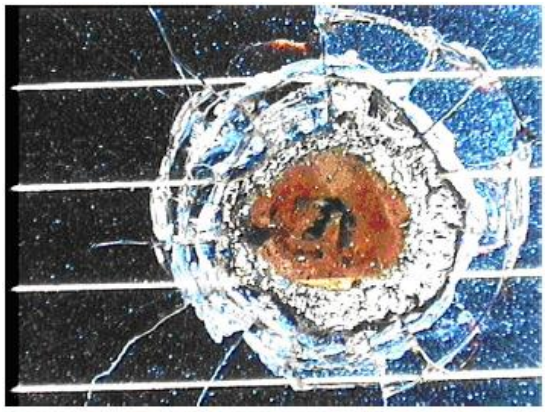

Fig. 3.10 - The material ejected during the impact process can lead to numerous small secondary craters in the vicinity of a primary impact. ([8])

- CCD

Impact ejecta could have detrimental effects on sensitive instruments like mirrors, sensors and CCD detectors.
Ejecta from impacts on side walls or baffles near sensitive equipment could be more damaging then a direct hit by the primary projectile would have been.
Micron size particles can damage exposed CCDs or other types of sensitive focal plane detectors.

One example is represented by the experiment XMM-Newton, the X-ray astronomy observatory, where a debris scattered under a small angle off the telescope mirror surface, reaching the focal plane detector and producing the damage.

- Transferred Momentum

Every impact implies a transfer of momentum. This can lead to a change of attitude of the spacecraft.
As a consequence of secondary ejecta the transferred momentum can be larger than the momentum of the impactor. Quantitative information is sparse but enhancement factors of 2–20 for impacts on solid targets appear realistic. For high velocity impacts on the Giotto spacecraft enhancement factors in excess of 20 were expected.
A change of attitude by impacting particles is of concern for future science missions which have very high requirements for stability in attitude.
Most demanding are interferometer missions where required accuracy is in the range of nm and/or arcsec. Momentum transfer from small particles can lead to loss of formation and interruption of the measurements.
Examples are formation flying missions like LISA for the detection of gravity waves or missions like DARWIN which look for extra solar planets by nulling interferometry. ([16])

- Induced vibrations

Some experiments recognized that the vibration environment induced by HVI could be close to that generated by pyroshock devices, being therefore a real threat for components and instrumentation. ([14]).
It was recognized the need of getting a collection of impact test data regarding the shock spectrum response inside spacecraft resulting from space debris impacts on the external walls of the body, with the final goal of defining a general approach for characterizing and predicting the vibration environment around selected components, with its dependence from impact conditions (*i.e.* micrometeoroid or orbital debris mass, impact speed, impact angle).

The next generation of European satellites will employ ultrahigh sensitivity equipment which requires platform stability orders of magnitude higher than those of previous missions, *e.g.* ESA's Global Astrometric Interferometer for Astrophysics (GAIA).
GAIA will operate in a Lissajous orbit about the Earth-Sun L2point, at which the primary debris environment consists of natural, micro-sized particles traveling at velocities over 20 km/s. ([16])

b - Electromagnetic effects

Plasma, vapour and debris associated with an impact or explosive event have been demonstrated in the laboratory to produce radiofrequency and optical electromagnetic emissions that can be diagnostic of the event. ([12])
Such effects could potentially interfere with communications or remote sensing equipment if an impact occurred on a satellite.
Impact generated plasma could also end the life of a satellite by mechanisms that nowadays are still not well understood and not normally taken into account in satellite design.
For example, arc/discharge phenomena resulting from highly conductive plasma acting as a current path across normally shielded circuits may have contributed to the loss of the Olympus experimental communications satellite on August 11, 1993.

The impact plasma can also trigger a discharge of electrostatically charged dielectric surfaces or bulk material, this discharge current can reach Ampere levels.
Each hypervelocity impact also produces a flash of light.

c - Effects on astronomy observations

Debris trailing is a phenomenon which affects optical astronomy in particular. If a piece of space debris crosses the field of view of an optical telescope, the trail produced by the piece of debris, by reflecting sunlight into the telescope, will be recorded.
Optical observations for astronomy are of three main types: direct imaging, photometry and spectroscopy.
From the point of view of spectroscopy, debris trailing is not yet a significant problem. For direct imaging and photometry, the effects of debris trails are now significant and are an annually increasing hazard. ([10])

Debris trails also affect astronomical photometry.
Photometry, using both broad and narrow band filters, is an important and sensitive astronomical technique, it is a sort of low resolution spectroscopy.
Astronomy faces a very serious problem from space debris, as the amount of space debris grows, the astronomical hazard will continue to increase.

3.3 New statistic methods for RA

3.3.1 New methods requirements

The limits described before point out the need to develop new statistic methods for the space debris risk assessment (see 3.2.2.2).

The aim is to take in account:

1- Different types of damage

- Effects of the secondary debris cloud on the subsystems and their measurement

2- A new scientific approach for the measurements

- Uncertainty bounds

This new kind of approach in the measurement of impacts' effect is innovative and it represents the core of this work.
Its preliminary results will help to create the base for a revolutionary way of thinking about the space missions' design.
This will lead to safer and more cost-effective spacecraft.

3.3.2 Possible developments

The derivation of the new equations requires the definition of an appropriate 'damage parameter' Π, linked to the failure mechanism analysed with experimental data.
For every protection system the value of the damage parameter is measured and related to the impact conditions (*i.e. dp, vp,* α, etc.), to obtain an empirical correlation *f* (Damage Predictor Equation) that describe the variation of Π within the analysed bounds:

$$\Pi = f\,(dp, vp, \alpha, \ldots)$$

The Damage Predictor Equations allow to follow the evolution of the damage parameter, in this way it is possible to assess the experimental conditions the lead to failure the tested material.
The 'critic' threshold is detected from the tests as an uncertainty bandwidth $\Pi crit \pm U$ that represent the absolute values of Π when the failure occurs. ([17])

It is very important to notice that $\Pi crit$ can be specified combined with his uncertainty bandwidth, because the critic value is estimated from the measures of Π.

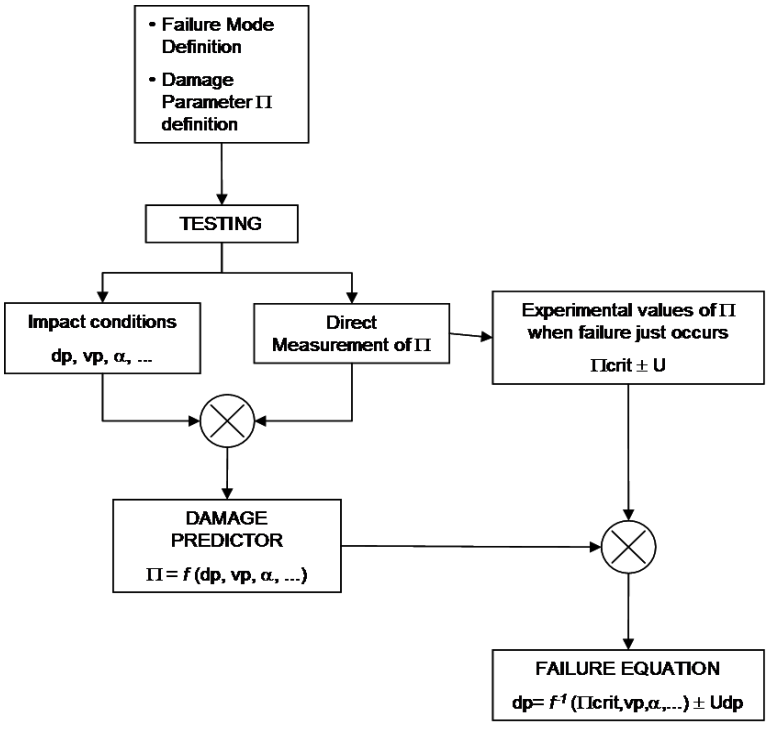

Fig. 3.11 – Failure equations and damage parameter

At this stage the $\Pi crit$ value has to be introduced in the Damage Predictor Equation, obtaining a set of experimental points (*dp, vp,* α, etc.) that lead to the test failure.
This is the desired damage equation.
With this approach the equation, that substitutes classic ballistic limit equations, has uncertainty bounds, spreading the uncertainties on experimental parameters and on the used model (Damage Predictor), in agreement with the applicable statistic methods.

3.4 New design methods for space vehicles

3.4.1 Meteoroid/Space Debris Protection System

The derivation of the new equations defining a 'damage parameter', is linked with the optimization of the mass of Meteoroid/Space Debris Protection System (MDPS).

In particular in recent years, the development of flexible, inflatable structures for human space flight has drawn increased attention from space industries, *e.g.* the new modules for ISS.

The development of BLE presented together with statistically-based uncertainty bounds for these kind of shields can lead to preliminary studies about spacecraft using a novel approach for future landing missions with manned vehicles on the surface of Earth-like planets for example. ([36])

This kind of research will allow improvements in the reduction of transport costs, therefore the possibility to implement this methodology in the pre-design process of a S/C will give a faster and reliable design of MDPS.

3.5 Case studies

In the above scenario there is the need to define case studies to analyse and develop the application of the techniques for the new RA statistic methods.
In the following paragraphs 2 cases will be described, one for unmanned and one for manned space vehicles.

3.5.1 Unmanned space vehicle: Cosmo-Skymed satellite

COSMO-SkyMed (COnstellation of small Satellites for Mediterranean basin Observation) is at the moment the largest Italian investment in Space Systems for Earth Observation, commissioned and funded by Italian Space Agency (ASI) and Italian Ministry of Defence (MoD), and it is "natively" conceived as a Dual-Use (Civilian and Defence) end-to-end Earth Observation System aimed to establish a global service supplying provision of data, products and services compliant with well-established international standards and relevant to a wide range of applications, such as Risk Management, Scientific and Commercial Applications and Defence/Intelligence Applications.
The system consists of a constellation of four Low Earth Orbit mid-sized satellites, each equipped with a multi-mode high-resolution Synthetic Aperture Radar (SAR) operating at X-band and fitted with particularly flexible and innovative data acquisition and transmission equipment.
The system is completed by dedicated full featured Ground infrastructures for managing the constellation and granting ad-hoc services for collection, archiving and distribution of acquired remote sensing data.
The system is conceived to pursue a multi-mission approach thanks to its intrinsic inter-operability with other earth orbit missions and expandability towards other possible partners with different sensors typologies to implement an integrated space-based system providing Earth Observation integrated services to large User Communities and Partner Countries (IEM capability).
These features designate COSMO-SkyMed as a system capable to provide "Institutional Awareness" in order to make proper decisions in preventing and managing world-wide crisis.
In a Dual-Use environment, particular emphasis has to be put on Dual-Use Mission Planning functionality in order to optimize system utilization and fulfilling at the same time different user classes needs: an insight into the peculiar characteristics of the COSMO-SkyMed Dual-Use Mission Planning and the technical methodology approach to the sharing of System

Resources in a Multi-User setting is provided ([23]).

3.5.1.1 Critical problems

From the described scenario the main potential problems are:

- Mechanical damage
    - Generation of ejecta
- Momentum transferred
    - Change of attitude
    - Loss of target lock
- Plasma effects
    - Electrical interference
    - Current flow
    - Triggering of electrostatic discharges
    - Light flashes

These problems can affect the main payload, *i.e.* the Synthetic Aperture Radar (SAR) instrument and the Payload Data Handing and Transmission (PDHT).

The SAR system is made by an array of 1200 micro-antennas (SAR antenna characteristics: 5.6m × 1.4m, 1.1° 3dB elevation aperture, 0.28° 3dB azimuth aperture), that with a process similar to the concept of interferometry increase the radar resolution.
The size of these antennas is of the centimetric order, in case of impact dedicated algorithms allow to re-configure the system, but there is anyway a loss of resolution. This lead to the degradation of the image, like in a CCD sensor with damaged pixels.

The plasma generation can also create reflections (if it is near to the critic frequency) of the SAR signal, this increase the bit error rate in the communications with the ground segments.

Moreover the change of the attitude due to the transferred momentum implies problems for the pointing requirements of the SAR antenna and for the formation flight, so for the overall system efficiency.([23])

In the worst case these aspects can lead to the failure of the mission.

3.5.1.2 RA methodology

The study of these secondary, but very important phenomena needs an appropriate RA analysis.

Regarding the mechanical damage linked with ejecta's generation the procedure may have the following scheme:

- Ejecta generation's study
    - Definition of a damage parameter(s)
    - Test campaign in the available experimental velocity range in different impact conditions
    - Analysis of the samples
    - Statistical analysis of the acquired data
    - Derivation of the damage predictor equations with their uncertainty bandwidth

3.5.2 Manned space vehicle: International Space Station

The International Space Station (ISS) is an internationally developed research facility that is being assembled in LEO, it represents the best example of a manned space vehicle. The construction of the station began in 1998, it is expected to remain in operation until at least 2015 and likely 2020. It is by far the largest artificial satellite that has ever orbited Earth. The ISS serves as a research laboratory that has a microgravity environment in which crews conduct experiments in biology, chemistry, human biology, physics, astronomy and meteorology.

The station has a unique environment for the testing of the spacecraft systems that will be required for missions to the Moon and Mars. The ISS is operated by Expedition crews, with the station programme maintaining an uninterrupted human presence in space since the launch of Expedition 1 on 31 October 2000 ([30]).

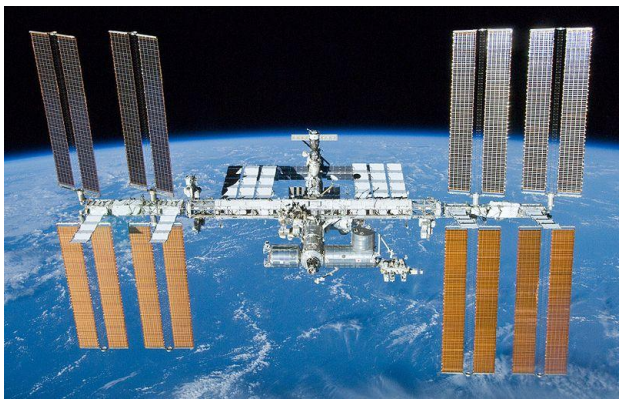

Fig. 3.12 – ISS

At the low altitudes at which the ISS orbits there is a variety of space debris, consisting from entire spent rocket stages and defunct satellites, to explosion fragments, paint flakes, slag from solid rocket motors, coolant released by RORSAT nuclear powered satellites, small needles, and many other objects. These objects, in addition to natural micrometeoroids, pose a threat to the station as they have the ability to puncture the pressurised modules and cause damage to other parts of the station. Micrometeoroids also pose a risk to spacewalking astronauts for EVAs, as such objects could puncture their spacesuits, causing them to depressurize ([31]).

Debris Avoidance Manoeuvre (DAM) are not uncommon, taking place if computational models show the debris will approach within a certain threat distance. Eight DAMs had been performed prior to March 2009, the first seven between October 1999 and May 2003. If a threat from orbital debris is identified too late for a DAM to be safely conducted, the station crew close all the hatches aboard the station and retreat into their Soyuz spacecraft, so that they would be able to evacuate in the event it was damaged by the debris. This partial station evacuation has occurred twice, on 6 April 2003 and 13 March 2009 ([32]).

3.5.2.1 Critical problems

The ISS is a mission with human presence, so the main problem is related to the crew survival. The actual BLE use only a passed/not passed criterion as discussed before. These equations are again simply lines of demarcation between regions of penetration and non-penetration and are not statistically based.
Alternative, innovative approaches must be developed to obtain the required uncertainty information from existing BLEs and the data on which they are based, or to rederive the BL equations using a statistics-based approach so that uncertainty information is forthcoming out of the analyses along with the equations themselves.

Moreover actually all the shields are designed with the same procedure, this means inefficiency in the shields' distribution and in the mass distribution.

For example a differentiation is needed for:

- Pressurized / Not pressurized modules
- Modules directly exposed to the flight direction
- Zones directly involved in the crew survival

3.5.2.2 RA methodology

The procedure for a new RA methodology may have the following scheme:

- Selection of a manned module;
- Identification of the type of shield to analyse;
- Definition of a damage parameter(s);
- Test campaign in the available experimental velocity range in different impact conditions (*i.e.* projectile diameter, inclination, material);
- Analysis of the samples ;
- Statistical analysis of the acquired data;
- Derivation of the damage equations with their uncertainty bandwidth;
- Derivation of new Ballistic Limit Equations.

4 Experimental methods for space debris measurement

The content of this chapter is summarized in the following work breakdown structure (Fig. 4.1).

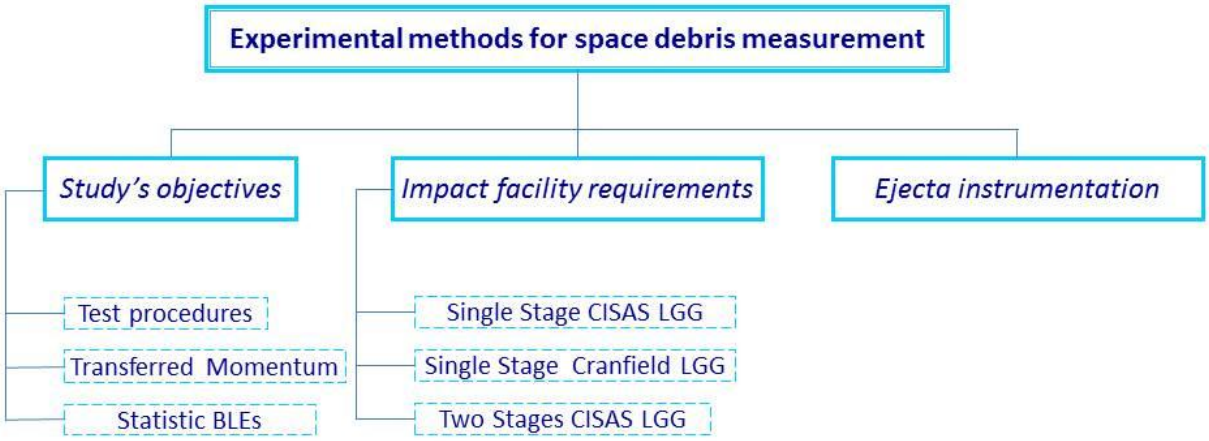

Fig. 4.1 - Chap. 4 overview

The experimental methods for space debris measurement will be described, focusing of the selected study's objectives and the impact facility requirements.
A great importance will have the presentation of different ejecta instruments development.

4.1 Selected study's objectives

In this paragraph will be described the study's objectives, selected among the scenario described above, *i.e.*:

1- Test procedures for the characterization of the ejecta phenomena

2- Secondary phenomena: Transferred Momentum

3- Statistic Ballistic Limit Equations

4.1.1 Test procedures to evaluate spacecraft material ejecta upon hypervelocity impact

In the development of the instrumentation the ISO proposal to standardize the ejecta characterization experiments is considered. ([33])

The main features of this proposal are:

- The counting of the craters on copper witness plate, with a stand-off of 50 mm from the surface from which the fragments are ejected. This craters are measured and divided in 4 classes according to the dimension of their equivalent diameter (0.025–0.05 mm; 0.05-0.1 mm, 0.1-1 mm, >1 mm).

- (Optional) The derivation of information about the fragments' mass and velocity distribution, starting from the measure of the craters, with the use of semi-empirical relations that describe the craters' dimensions as a function of the impact conditions. These relations, experimentally derived, are of the following type:

$$\begin{cases} p = k_1 \rho_p^{k_2} m^{k_3} v_n^{\ k_4} \\ \dfrac{p}{d_C} = k_5 v_n^{k_6} \end{cases} \qquad \text{[Eq. 4-1]}$$

p and d_c are the depth and the diameter of the crater; ρ_p, m and v_n are the density, mass and velocity of the fragments; k_1-k_6 are constants obtained with the regression of the data.

Both the 2 previous points need appropriate instrumentation to measure and count the crater and to obtain an additional info to solve the ambiguity in [Eq. 4-1 between debris mass and velocity.

In detail the requirements are described hereinafter.

4.1.1.1 Impact parameters

The ISO proposal states also that the projectile shall satisfy the following parameters:

- Material : aluminium alloy (Al 2017T4 or Al 2024 is recommended);
- Size and shape : 1 mm +/- 0.1 mm diameter sphere;
- Impact velocity : 5000 m/s (or higher) are recommended;
- Impact angle of incidence relative to target normal: 0°.

The target shall satisfy the following parameters:

- Size: at least 50 mm x 50 mm, in order to avoid edge effects upon impact;
- Material : representative of the material to be flown on the spacecraft;
- Thickness: representative of the material to be flown. Note that the ejecta process depends on the ratio of target thickness to projectile diameter (t/d). In the case where there is a perforation of the sample under test, it is necessary to evaluate the amount of ejecta from the front side and from the rear side.
- Held in place by fixing on the edges only;
- Rear side left free to allow ejecta collection if perforation or if rear side spall occurs.

Witness plates shall be used to collect ejecta particles released from the front side and the rear side of the target during impact.

The witness plates shall satisfy the following parameters:

- size: 250 mm x 150 mm, a circular hole (diameter 30 mm) will be cut in the centre of the front witness plate in order to let the projectile go through.
- material: copper is recommended. The choice is based on international standards such as JIS H3100 C1100P-1/4H, ASTM B152 C11000;
- thickness: 2 mm;
- distance and position (angle) to the target: 50 – 100 mm in front and parallel to the target plane;
- similarly a witness plate will be placed behind the target;
- fixing: by threaded rods and bolts, fixed on the target holding plate.

4.1.2 Transferred Momentum

The starting point for the momentum transfer evaluation is the classic ballistic pendulum concept. According to such a solution, the target will be mounted on a flexible system and will be left free to oscillate following the supporting structure's dynamical behaviour.
In a theoretically-ideal situation, the pendulum oscillation occurs just along the projectile's flight path direction (*i.e.* the pendulum is a single-degree-of-freedom system). In this case, the conservation of energy can be easily applied between the initial state t_0 immediately after the impact (in which the target has just acquired the initial velocity v_{target}) and the final position x_{max} occurring at $t=t_{max}$ (the velocity is zero and all the initial kinetic energy is converted to elastic energy):

$$\frac{1}{2} \cdot m \cdot v_{t\arg et}^2 = \frac{1}{2} \cdot k \cdot x_{\max}^2 + E_d$$

In the previous equation, m is the overall pendulum mass, k is the equivalent single-degree-of-freedom stiffness of the suspending system and Ed is the energy dissipated between t0 and tmax (by atmospheric drag on the pendulum, elastic hysteresis of the suspending system and friction between fibres constituting target's fabrics). Neglecting Ed, it is clear that the momentum transferred to the structure can be derived from the measurement of the target displacement xmax.

Although the measuring approach just outlined appears to be simple and reliable, several issues must be addressed to implement it into a real system:

- The real arrangement will require a design as close as possible to that of a single degree of freedom system, allowing momentum gain only in the direction of interest: spurious translational or rotational modes could interfere with the measurement procedure;

- The technique to measure the target displacement will require high accuracy and simplicity. High-speed photographs will be considered together with point displacement sensors (*e.g.* low-cost laser Doppler transducers) to allow for cross-calibration and cross-check between different methods;

- Proper calibration procedures (*i.e.* by drop tests and/or impact hammer) will be mandatory to estimate the instrument sensitivity, even accounting for energy dissipation terms (which contribute to the overall uncertainty);

- Proper measuring procedures and operational sequences will be defined in order to limit at a minimum the effects of every disturbing input.

Finally, the measurement uncertainty will be assessed combining the contribution related to the calibration procedure with that of the momentum transferred by the propellant gas hitting the target. This latter part is probably the most important source of uncertainty and can be modelled as a systematic pulse which can be measured and subtracted from the momentum estimation. For this reason, a specific LGG test is foreseen to assess the gas interfering contribution: an empty sabot will be launched to allow only the gas to reach the target, thus providing the opportunity of measuring the momentum transferred by the propellant to the assembly.

Moreover, the transferred momentum evaluation will be assess using indirect methods, like correlating the inputs' analysis of impact sensors with the test condition, *i.e.*mass and velocity of the projectile.

4.1.3 Statistic BLEs

The following cases will be analysed:

- Statistic BLE for Whipple Shields
- Preliminary results for Damage (crater) Equations for the internal damage evaluation for Cosmo-Skymed satellite

For both the situations, the determination of the equation follows the procedure described in 3.3.2, that defines a 'damage parameter' Π linked to the failure mechanism.

Moreover it will be analysed a novel approach for BLE derivation for flexible MMOD shields, based upon the assessment of the impact damage produced on subsequent shield layers in different impact conditions.

4.2 Impact facility developments

The following topics will now be described:

- Study of a new single stage light gas gun for the CISAS impact facility;
- Improvements of a single stage light gas gun for Cranfield University's impact facility;
- Improvements of the new two stage light gas gun for the CISAS impact facility. This study includes the conceptual analysis, starting from the requirements definition, and the development of the final solution.

4.2.1 Single Stage CISAS LGG

This paragraph describes the study of the gasdynamic aspects for a new single stage light gas gun for the CISAS Hypervelocity Impacts Facility.
It also introduces a study on the sabot stopping system.

4.2.1.1 LGG's study

A first set of gasdynamic simulations done with a zero-dimensional model implemented in Simulink software will be now presented.
This model is the same developed for the CISAS two stage light gas gun (LGG) and then adapted for a single stage light gas gun (Fig. 4.2).

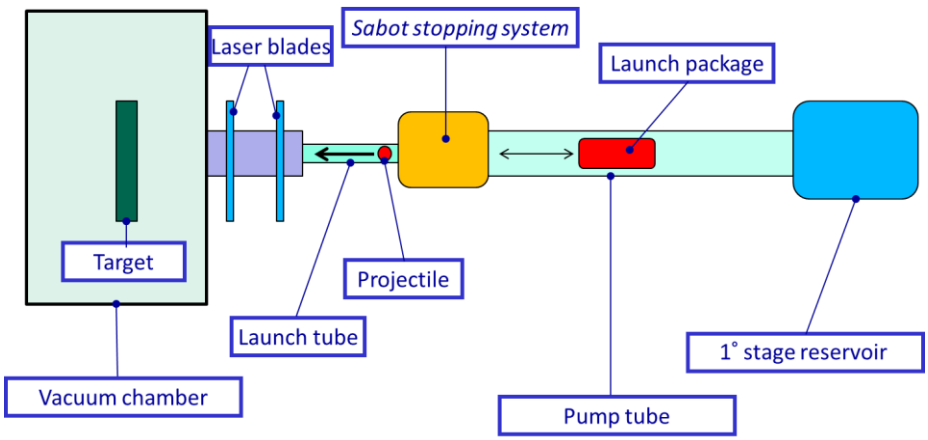

Fig. 4.2 – Single stage Light Gas Gun schematic overview

The aim of this gasdynamic model is simulate the functioning of the light gas gun, in order to design the dimensions of the first stage reservoir, the pump tube length and the dimensions of the sabot surrounding the projectile.
The model uses the traditional gasdynamic equations, integrated in a chosen time interval. Varying the parameters of this model, like the pressure in the reservoir, it is possible to assess the performances of the system.
The single stage LGG has the following main parts:

- First stage reservoir: a light gas, like Helium, is stored at high pressure in this reservoir;
- Pump tube: in this tube the launch package, made by the sabot and the projectile, is accelerated;
- Sabot stopping system: this component allow the separation of the projectile from the sabot, stopping it;
- Launch tube: the projectile continues his way towards the target and its velocity is measured by 2 laser blades;
- Vacuum chamber: the projectile hits the target in the impact chamber.

The starting point for the set-up of these simulations is represented by the requirements for this new LGG, *i.e.* :

- Max projectile velocity: 1000 m/s
- Max launch package mass: 120 g

The Simulink model has the following parameters (Tab. 4-1):

Max reservoir volume	9e-03 m3
Max equivalent reservoir diameter	0.186 m
Max equivalent reservoir length	0.33 m
Launch package length (sabot + projectile)	50 mm
Launch package diameter (sabot + projectile)	35mm
Max launch package mass (sabot + projectile)	120 g
Max pump tube length	4.5 m
Pump tube inner diameter	35 mm
Max reservoir initial pressure	150e5 Pa
Pump tube initial pressure	5e2 Pa

Tab. 4-1 – LGG parameters

The choice of these parameters for the reservoir and pump tube dimensions is due to mechanical constrains deriving from adapting the already existing two stage LGG configuration.

The results of simulations done varying different key parameters will be now described.

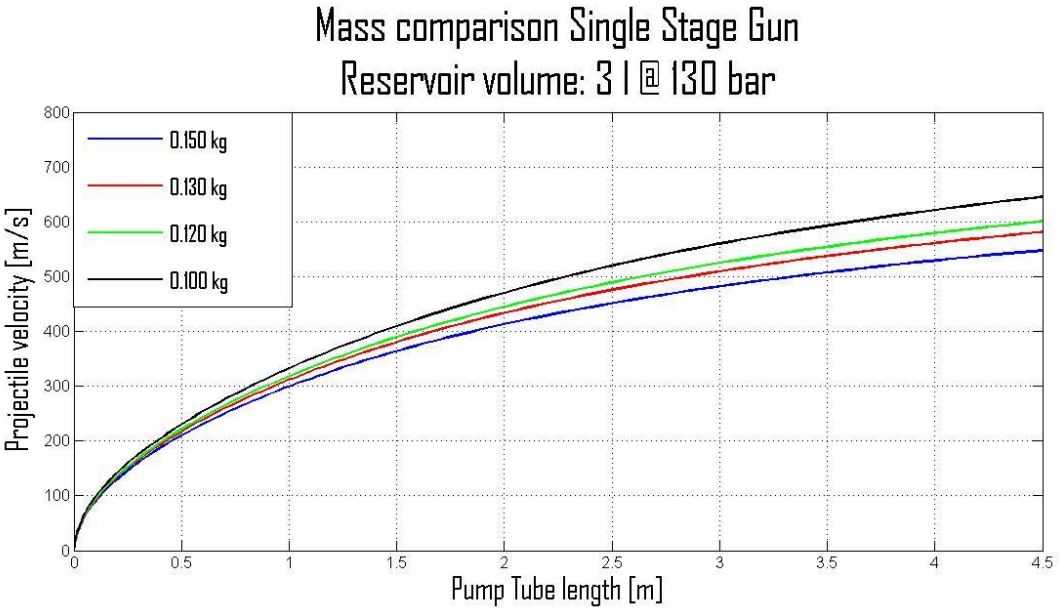

Fig. 4.3 – Launch package mass comparison CISAS single stage LGG

Fig. 4.3 shows a set of simulations using a 3 litres reservoir at 130 bar. A decreasing performance of around 15% with a variation of mass of 50 g can be discerned.

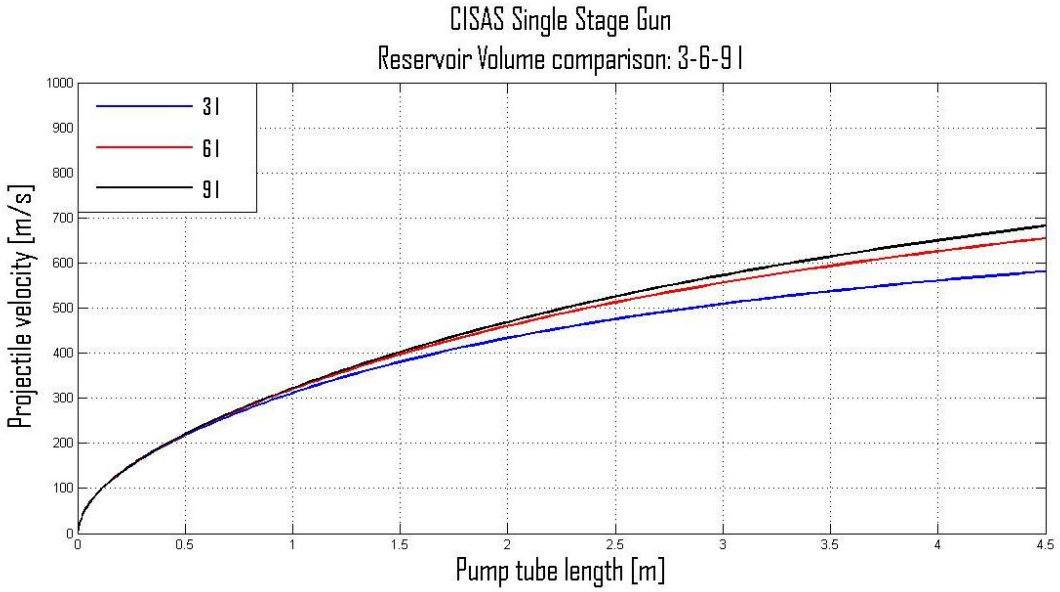

Fig. 4.4 – Reservoir volume comparison CISAS single stage LGG

Fig. 4.4 reports a set of simulations using different reservoir volumes.

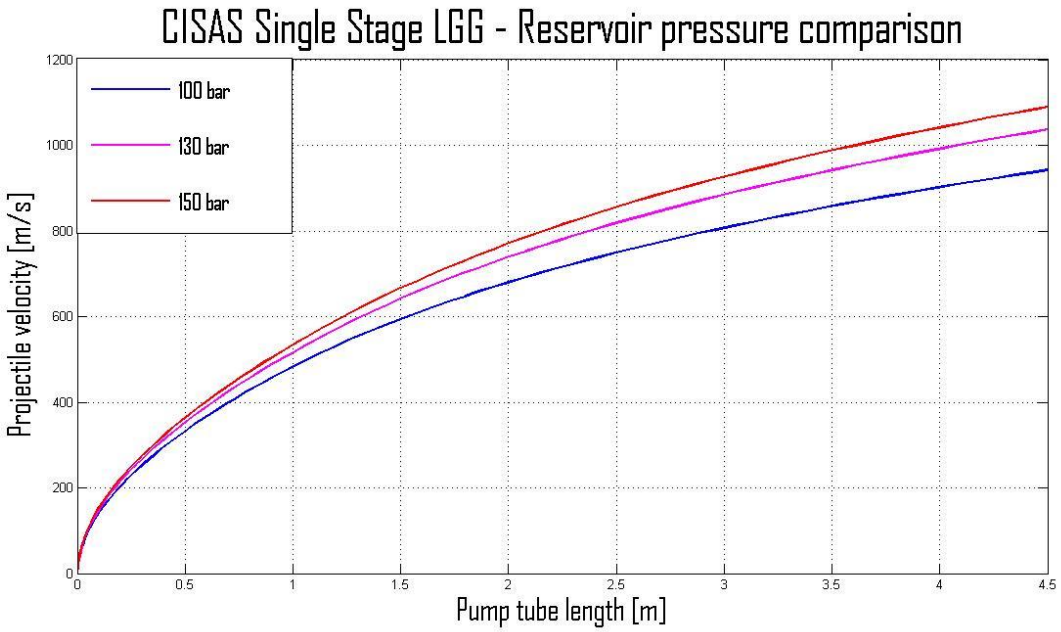

Fig. 4.5 – Reservoir pressure comparison CISAS single stage LGG (launch package mass: 50 g)

The behaviour of the single stage gun at different reservoir pressures is shown in Fig. 4.5.

The results using a launch package of 50 g, taking in account the expected usual test's conditions, are plotted in Fig. 4.6.

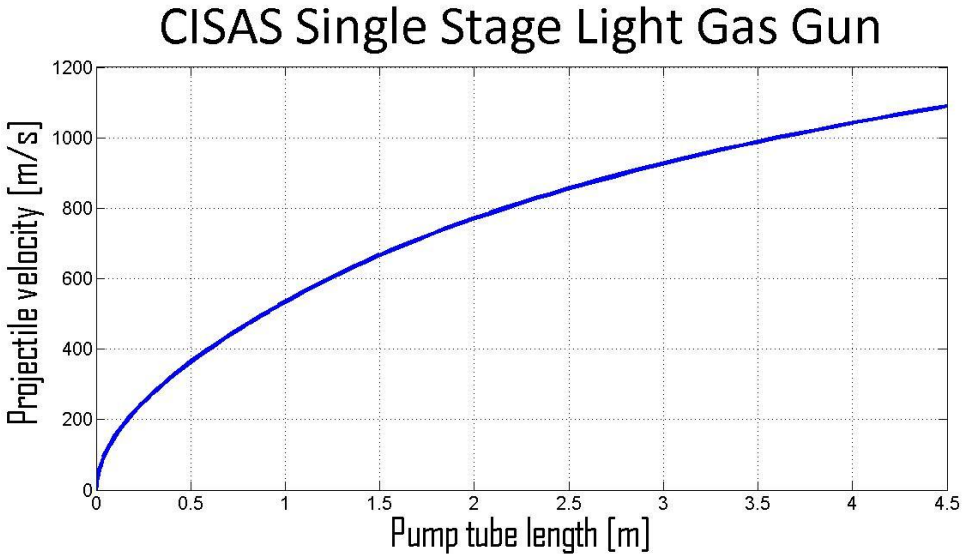

Fig. 4.6 – Standard configuration CISAS single stage LGG

4.2.1.2 Sabot stopping system

A design for the configuration of the LGG's sabot stopping system will now be introduced.

The system that will be described is mechanically decoupled in the interaction with the impact chamber and the pump tube.
This will avoid damages in case of failures, moreover it allows easier operations during the pre and post-test phases. Fig. 4.7 reports a sketch of the system.

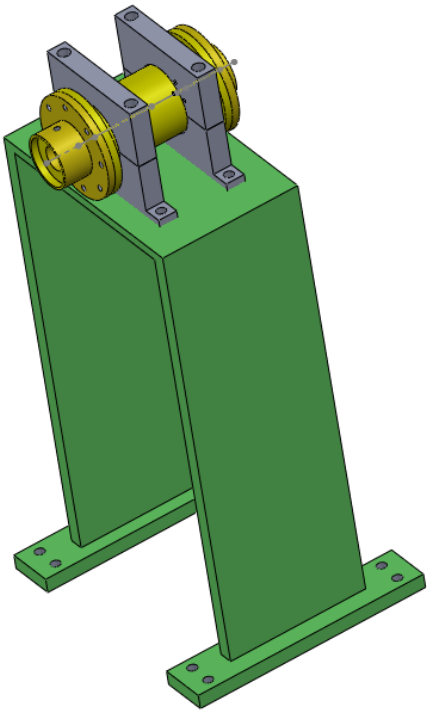

Fig. 4.7 – Overview of the sabot stopping system.

The sacrificial impact tube is the main component, in direct contact with the sabot after the shot.

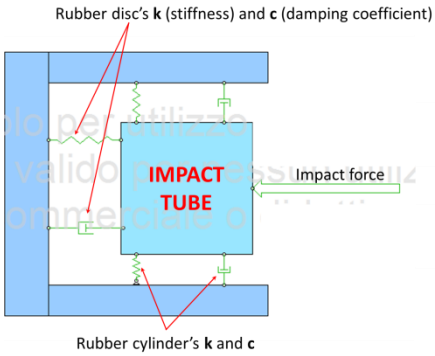

Fig. 4.8 – Sabot stopping system's working principle

A 2D section of the system's preliminary design is reported in Fig. 4.9, where the main components are:

- Impact tube (with threaded holes for easy extraction from the sabot stopping system in case of heavy deformation after the impact);
- Rubber disc;
- Rubber cylinder;
- Holder (that contains the first 3 elements);
- Supporting structure (with supporting flanges);
- Flange A;
- Flange B;

The working principle is (Fig. 4.8):

- The launch package hits the sabot stopping system and deliver a force to the impact tube that partially destroy the sabot that is separated from the projectile;
- The structure is protected by the transferred momentum by the properties of stiffness and damping of a rubber disc (for radial deformations) and cylinder (for axial deformations) that surround the tube, avoiding damages to the holder, that is sustained by the supporting structure and constrained by the 2 flanges.

  One pro of this configuration is the possibility to test different shapes of impact tubes, without increasing the complexity of the system.

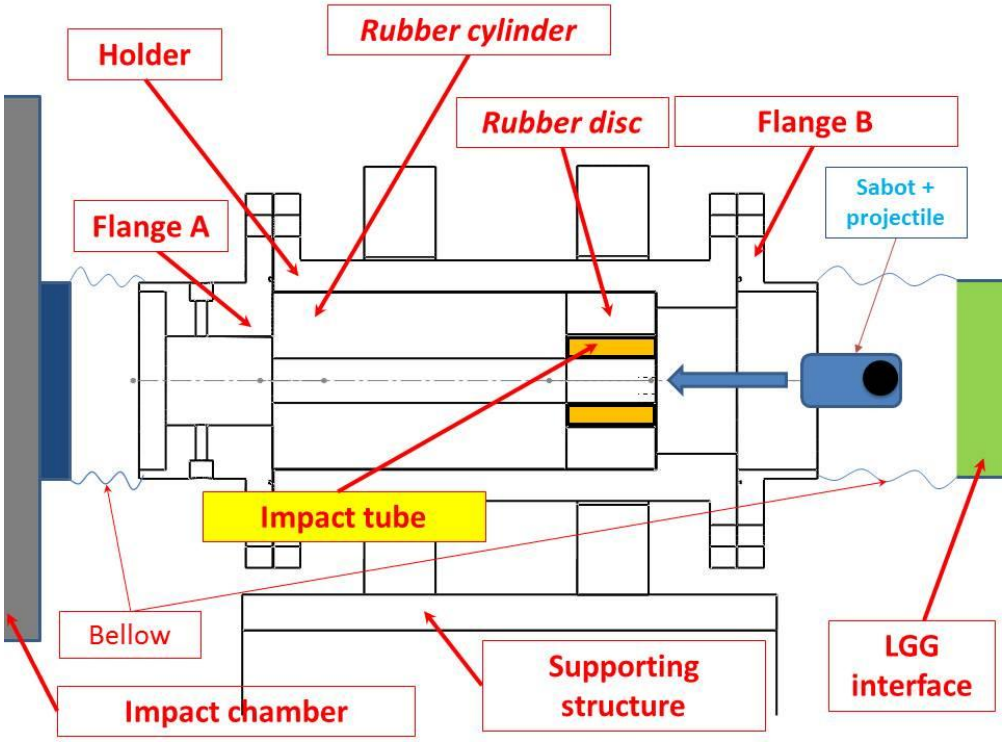

Fig. 4.9 – 2D section of the sabot stopping system

In Fig. 4.10 there is an exploded view of the sabot stopping system.

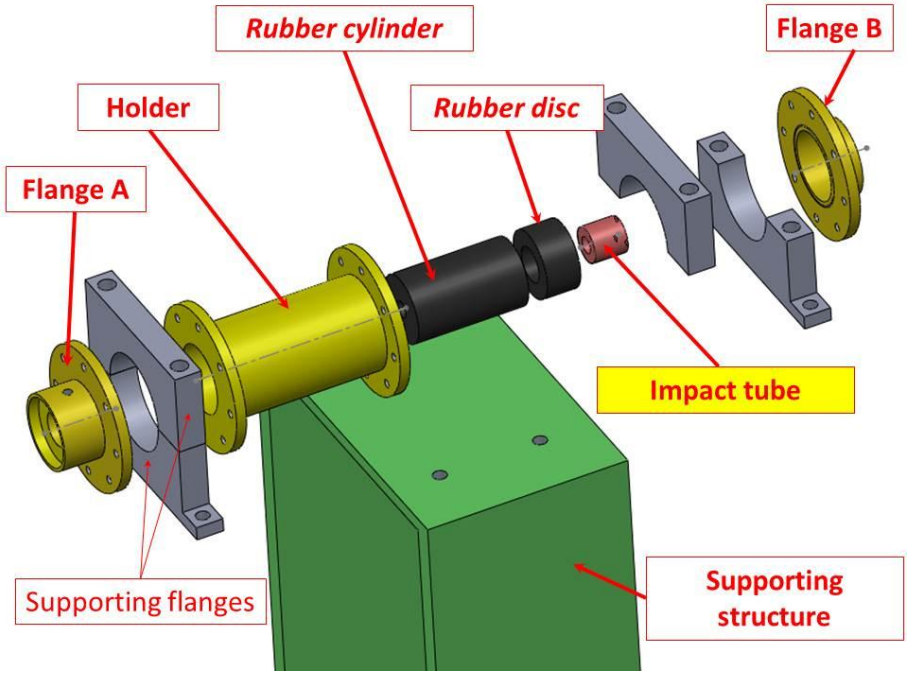

Fig. 4.10 – Sabot stopping system exploded view

The study of this system is divided in two phases, both have a very conservative approach:

a. Mass-spring-damper Simulink model to assess the reaction force of the system to the impact (Fig. 4.11):

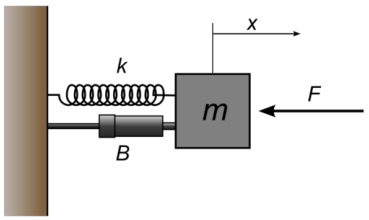

Fig. 4.11 – Mass-spring-damper system

To have a very conservative evaluation the worst load condition case is considered.

The Simulink model has the following set:

- He @ 150 bar,
- Launch package mass: m=120 g,
- All the launch package is supposed to impact the sabot stopper,
- Spring and damper coefficients have the same order of magnitude of steel, even though in the real application rubber cylinder and disk will be used. This allows a more conservative approach in the design of the system.

Knowing the velocity of the launch package allows to assess the transferred momentum and in this way the reaction force of the structure due to the impact, from the relation:

$$Q=mv=Fdt$$

The first evaluations, using different time interval dt, assess a range of this force between F = 1e5 N and F = 1e7 N.
It will be reported now the results only for the worst case.

b. FE analysis to assess the behaviour of the structure (Fig. 4.12):

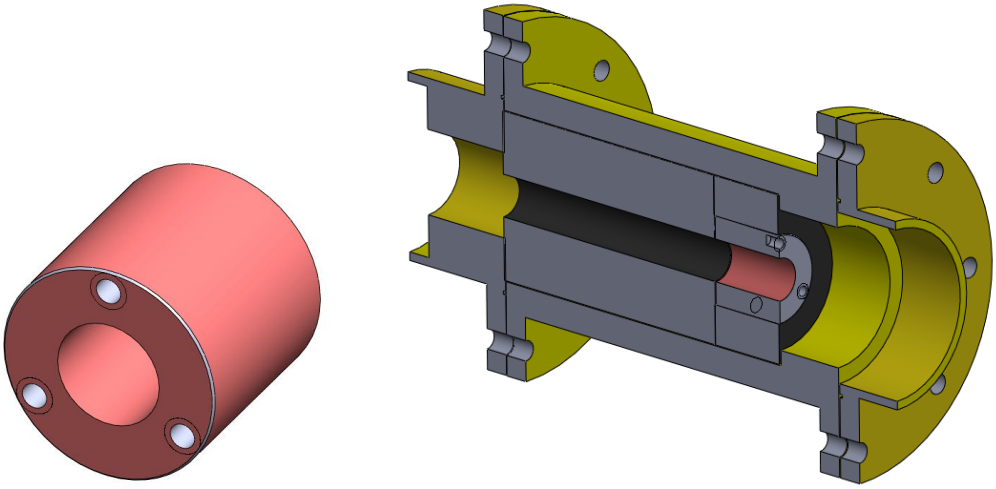

Fig. 4.12– Impact (sacrificial) tube (left) and sabot stopping system (right)

The results of phase A allow to set a FEM simulation of the sacrificial tube and of the sabot stopper (Fig. 4.13) .

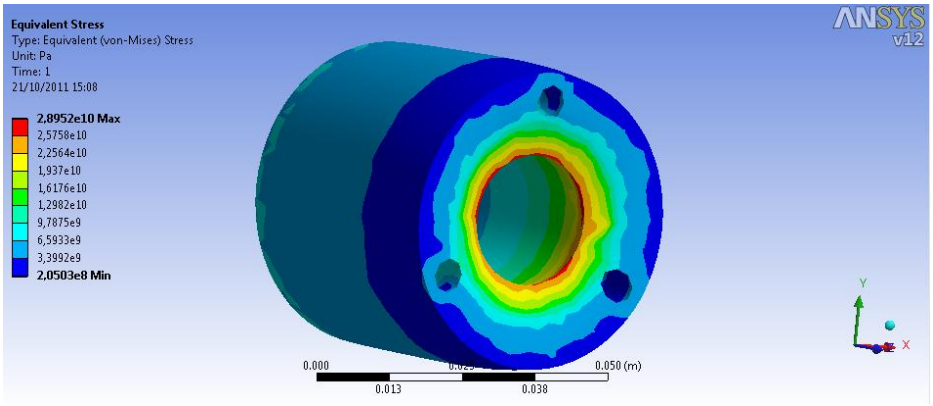

Fig. 4.13 – Impact tube's Equivalent Von Mises stress

Fig. 4.13 reports the results for Von Mises Equivalent stress of a first static structural simulation for the sacrificial impact tube (also this approach is conservative).

A force of 1e7 N is applied on the initial impact zone and a fixed constrain is applied on the other side of the component.
The results show mean values for the Von Mises stress around 500 MPa, in the zone with the highest stress the safety factor is minor of 1. Taking in account all the

surrounding structure we can consider this as a fail-safe approach.

A second static structural simulation for the support supporting structure of the sabot stopper is shown in Fig. 4.14.

This simulation has the following conservative assumptions:

- All the impact force is transmitted to the supporting structure,
- Fixed constrains are used, even though in the real situation the other components will help in the damping effect after the shot.

The results assess that also in the worst case the structure's deformation is within reasonable limits (around 8 mm).

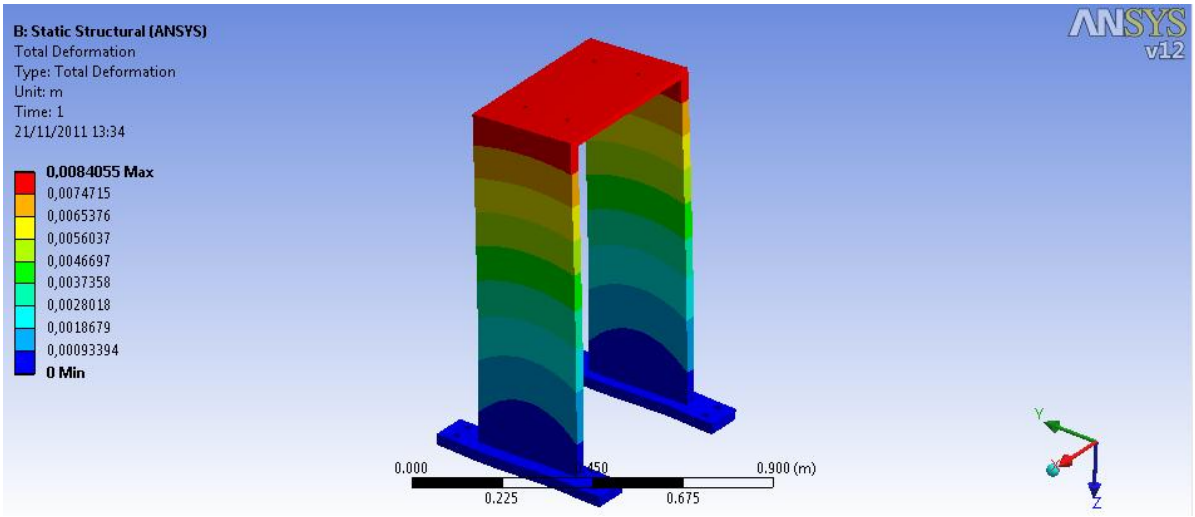

Fig. 4.14 – Sabot stopper's total deformation

4.2.2 Single Stage Cranfield LGG

This paragraph describes the study of the gasdynamic and mechanical aspects for the high pressure system of the Cranfield University (UK) single stage light gas gun (Fig. 4.15).
It also introduces a study on the sabot stopping system and on the impact chamber.

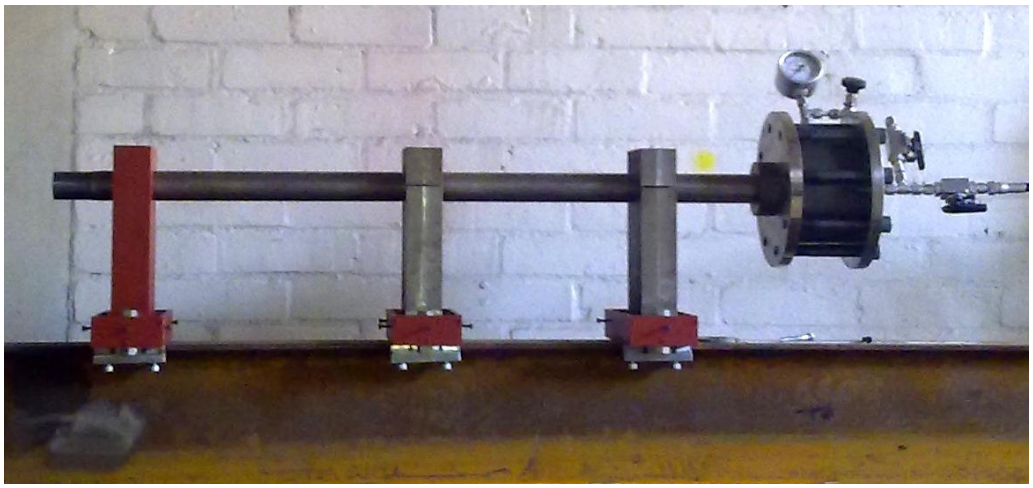

Fig. 4.15 – Single stage light gas gun overview

The content is summarized in the flow chart in Fig. 4.16:

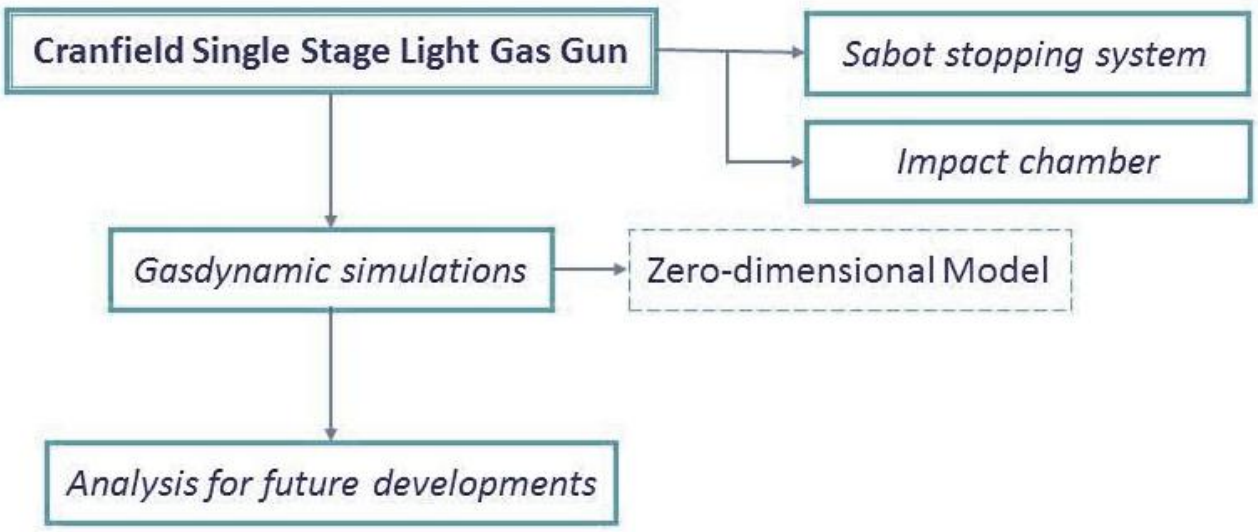

Fig. 4.16 – Single Stage Cranfield LGG analysis' overview

4.2.2.1 Gasdynamic simulations

A first set of gasdynamic simulations done with a zero-dimensional model implemented in Simulink software will be now presented.
This model is the same developed for the CISAS two stage light gas gun (LGG) and then adapted for a single stage light gas gun.

The starting point for the set-up of these simulations is represented by the 3D model of the LGG and by the experimental data retrieved, *i.e.*:

- Reservoir pressure: **N2 @ 40 bar**
- Max launch package mass: **40 g**
- Max launch package velocity: **218 m/s** (uncertainty in the measurement is unknown)

The Simulink model has the following parameters (Tab. 4-2):

Reservoir Volume	9.4e-04 m3
Equivalent reservoir diameter	0.1355 m
Equivalent reservoir length	0.06534 m
Launch package length (sabot + projectile)	40 mm
Launch package diameter (sabot + projectile)	31mm
Launch package mass (sabot + projectile)	40 g
Pump tube length	1 m
Pump tube inner diameter	31 mm
Reservoir initial pressure (gas: N2)	40 bar
Pump tube initial pressure	1 bar

Tab. 4-2 – Cranfield LGG parameters

The results are plotted in Fig. 4.17.

The simulations have some assumptions, *i.e.*:

- Valve opens 'instantly' (red curve) ;
- Inertia of the pneumatic valve is taken in account and the supposed opening time (one order of magnitude greater than an electronic valve) is 1e-2 s (black curve);
- The supposed radial clearance (Fig. 4.18) between the launch package and the pump tube is 0.1e-3 m (green curve).

These assumptions consider the loss of efficiency of the real LGG, which is around 23% in comparison with the ideal model.

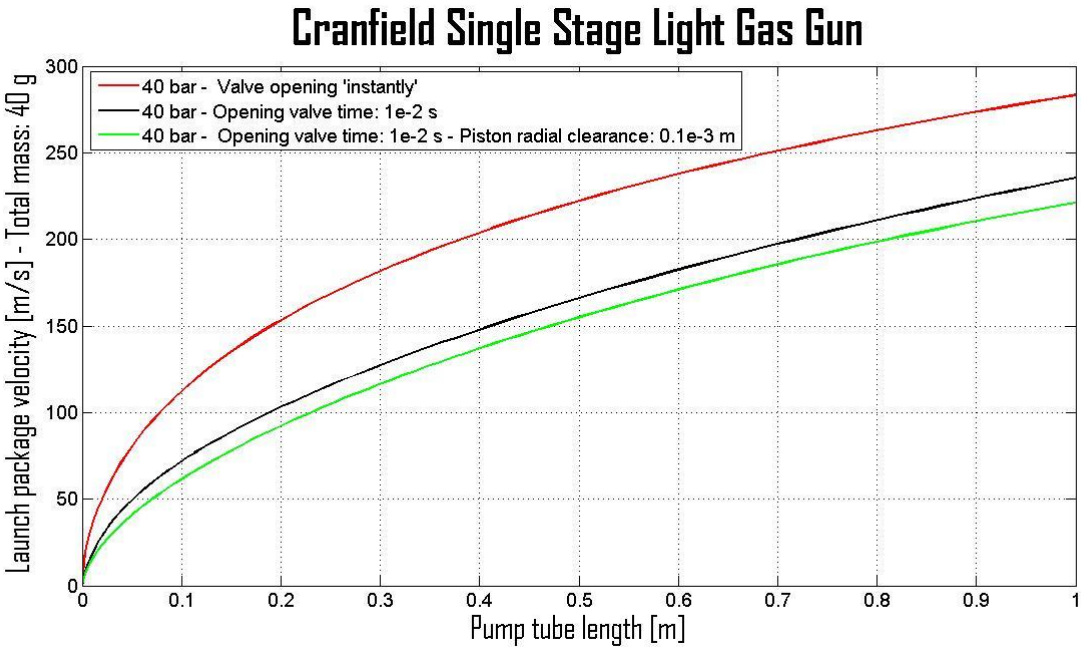

Fig. 4.17– Cranfield LGG simulations

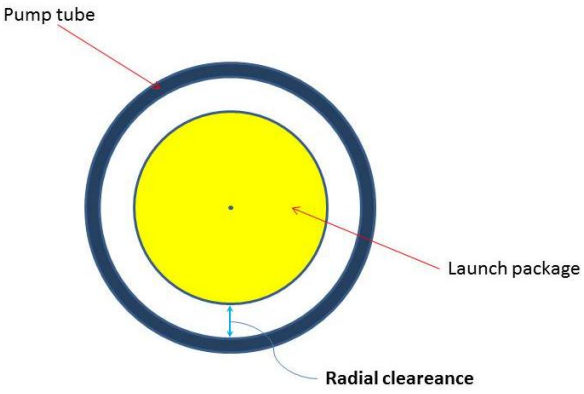

Fig. 4.18 – Radial clearance

The results show a good agreement with the experimental data. The velocity obtained for the third case (green curve) is around **221 m/s**.

A further check made with the LGG Lockheed Martin model is shown in Fig. 4.19.

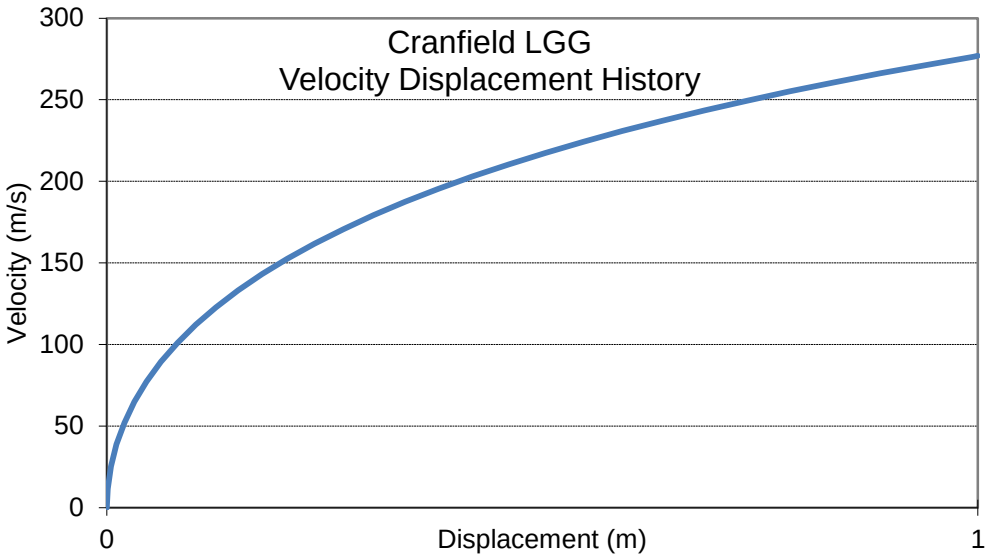

Fig. 4.19 – LGG Lockheed Martin model

There is a quite good agreement in the preliminary results:

- LGG Lockheed Martin model: Max velocity = 277 m/s ;

- LGG CISAS model: Max velocity = 284 m/s (Fig. 4.17, red curve).

There is the need to investigate deeper the sources of loss for the LGG and to do a model to understand the behaviour of the pneumatic valve.

Another set of simulations (Fig. 4.20) shows a preview of the LGG's performances, increasing the reservoir pressure. At 50 bar the launch package velocity is about 8% higher.

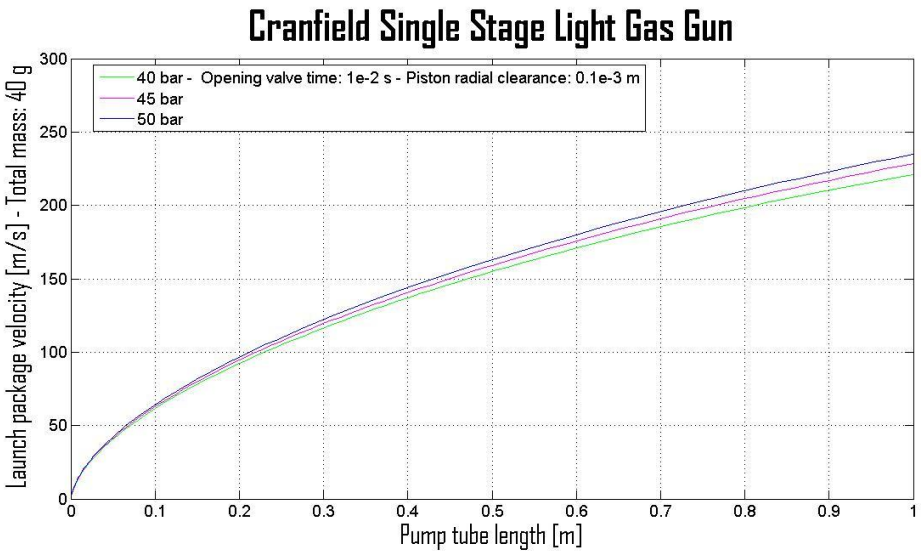

Fig. 4.20 –LGG's performance preview

Considering as reference configuration the green curve in Fig. 4.17 (N2 @ 40 bar, valve opening time: 1e-2 s, launch package radial clearance: 0.1e-3 m) the pressure along the pump tube is analysed (Fig. 4.21), both for the front (blue curve) of the launch package and for the back (red curve).

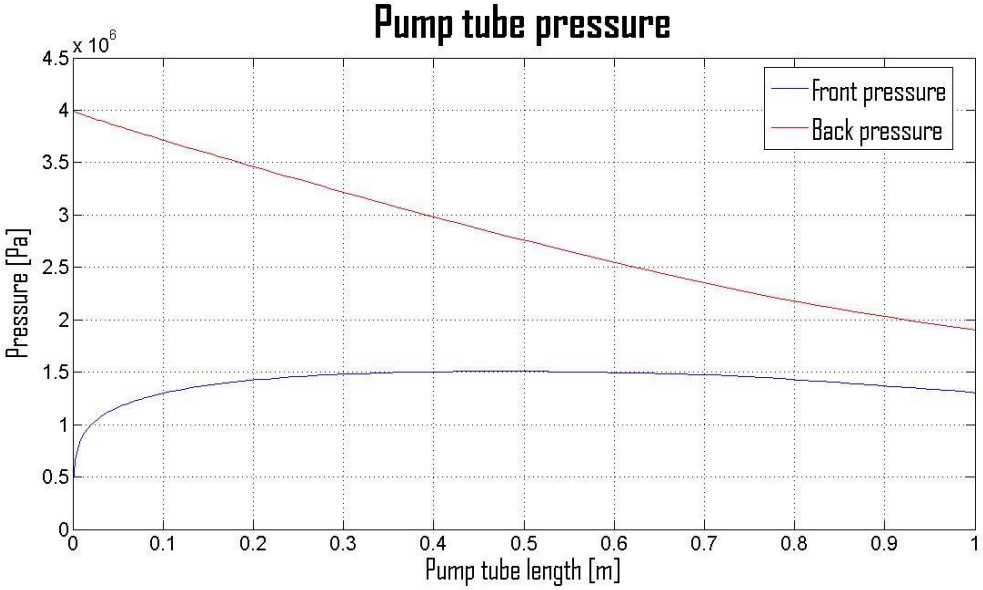

Fig. 4.21 – LGG's pump tube pressure plot

To check the values of the pressure along the pump tube a static fluid dynamic simulation, using ANSYS CFX, with a rough mesh and without the presence of the launch package was done.

Fig. 4.22 shows similar trend in the pressure's drop, regarding the results of the zero-dimensional model, with a difference in the outlet N2 pressure. The zero-dimensional model gives a value of 13 bar, the rough cfd model a value of 7 bar.

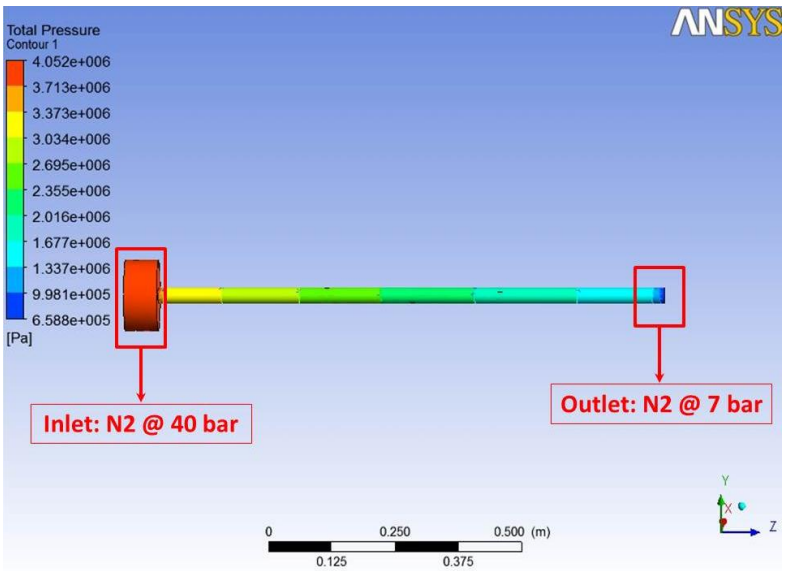

Fig. 4.22 – CFD simulation using ANSYS CFX

4.2.2.2 Sabot stopping system

A design for a configuration of the LGG's sabot stopping system will now be described.

The system considers the impact chamber mounted onto rails clamped on the steel table available in the laboratory.
This will allow easier operations during the pre and post-test phases. Fig. 4.23 reports a sketch of the impact chamber.

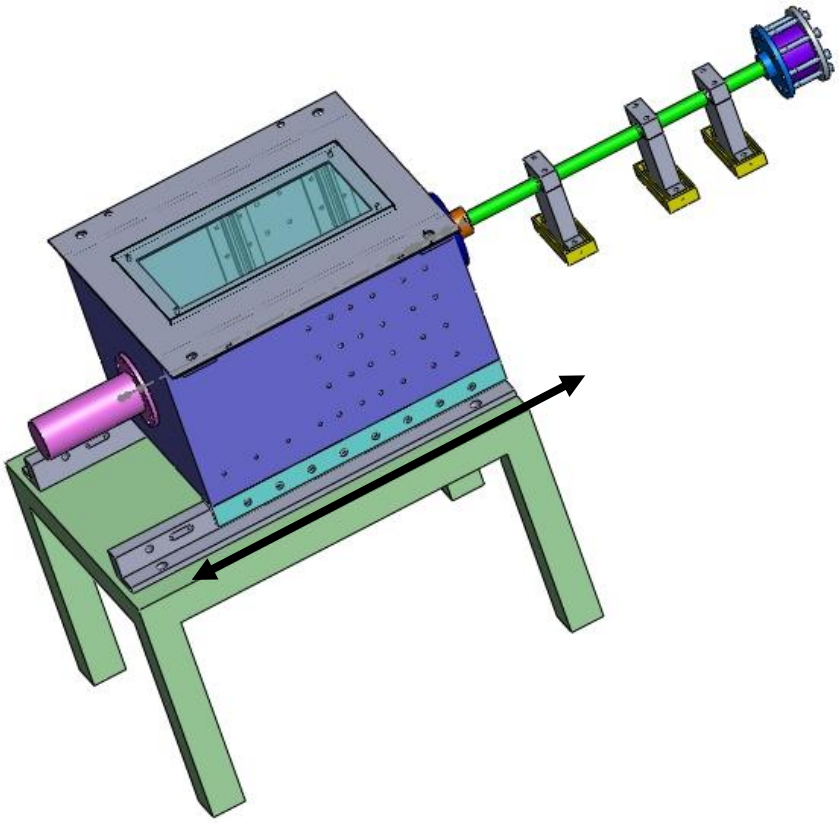

Fig. 4.23 – Overview of LGG, sabot stopping system and impact chamber

The sabot stopping system working principle is the same described for the CISAS single stage LGG and shown in Fig. 4.8.
Also in this configuration the sacrificial impact tube is the main component, in direct contact with the sabot after the shot.
Moreover the interaction between the LGG and the chamber is mechanically decoupled.

A 2D section of the system's design is reported in Fig. 4.24, where the main components are:

- Impact tube (with threaded holes for easy extraction from the sabot stopping system in case of heavy deformation after the impact);
- Tube screwed on the last part of the LGG pump tube as interface (after the test this component also allows easy post shot operations with the impact tube);
- Rubber disc;
- Rubber cylinder;
- Supporting structure that contains component n. 1, 2, 3;
- Flange A, inserted in the pump tube;
- Flange B, connected with the impact chamber;

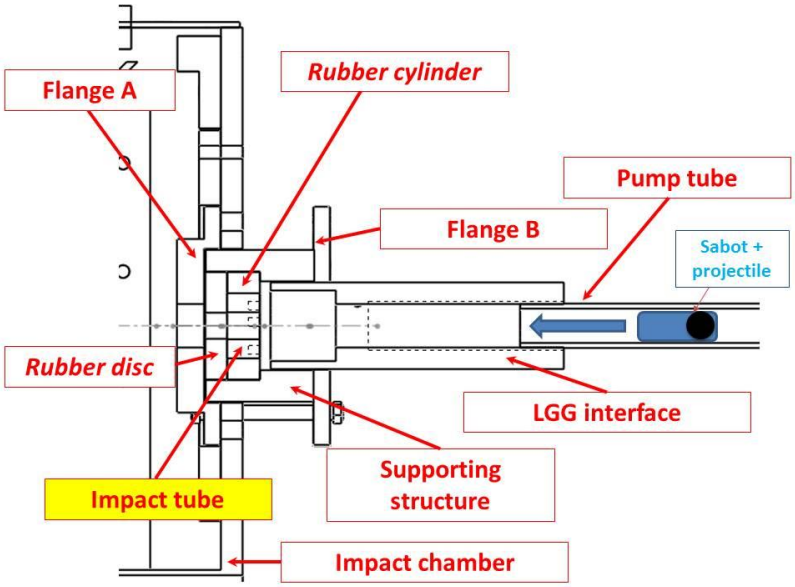

Fig. 4.24 – 2D section of the sabot stopping system

In Fig. 4.25 there is an exploded view of the sabot stopping system.

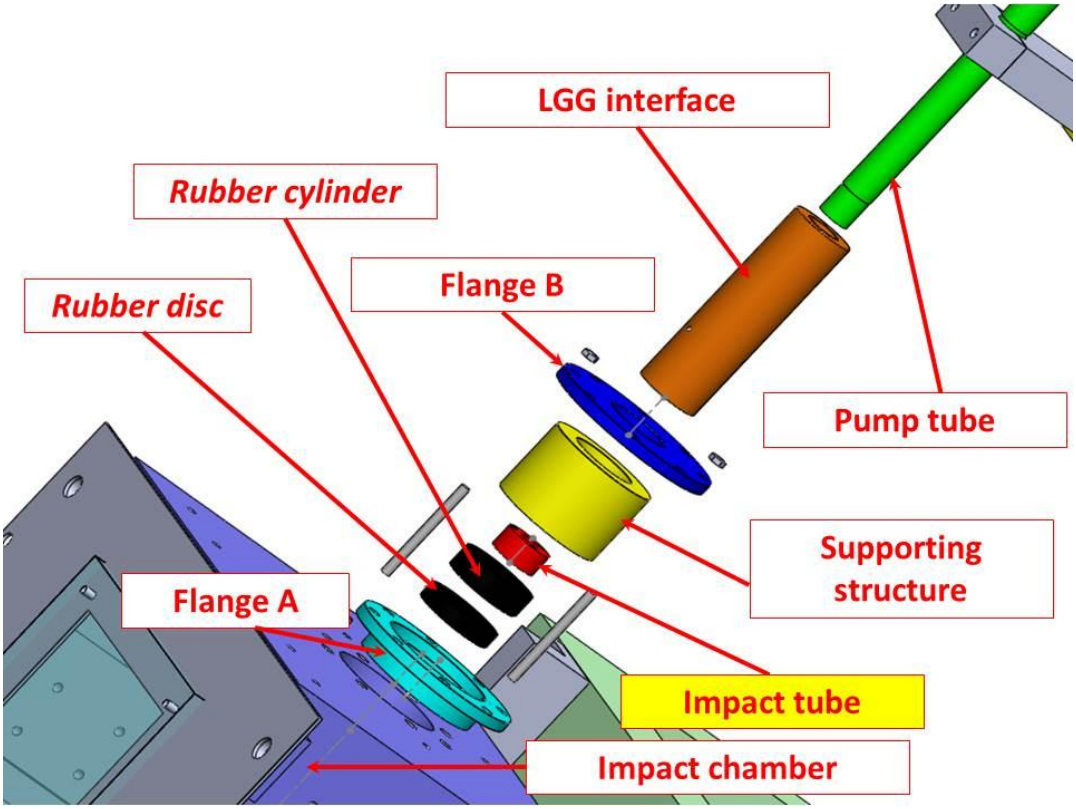

Fig. 4.25 – Sabot stopping system exploded view

The study of this system was conducted in the same way used for the CISAS single stage LGG. Like for the previous model it is divided in two phases:

a. Mass-spring-damper Simulink model to assess the reaction force of the system to the impact:

   To have a very conservative evaluation the worst load condition case is considered and presented here, with an impact force F = 1e6 N.

   The Simulink model has the following set, with the same assumptions made for the CISAS model:

   - N2 @ 100 bar,
   - Launch package mass: 40 g,

   In this way it is possible to assess the reaction force of the structure due to the impact.

b. FE analysis to assess the behaviour of the structure (Fig. 4.26):

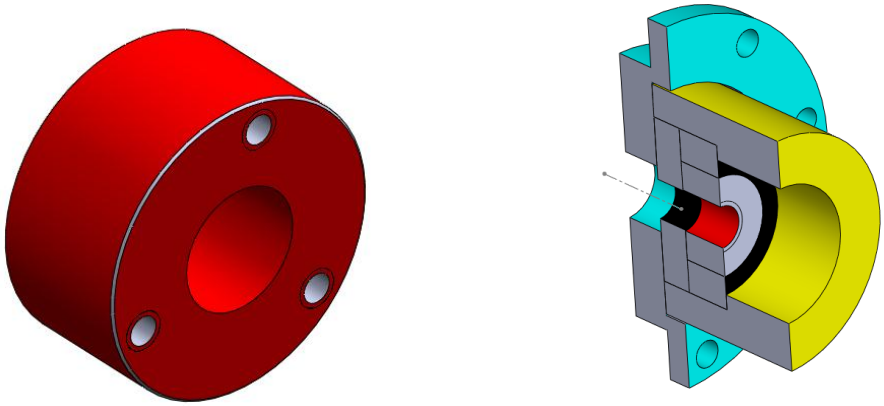

Fig. 4.26 – Impact (sacrificial) tube and sabot stopping system

The results of phase A allow to set a FEM simulation of the sacrificial tube and of the sabot stopper.

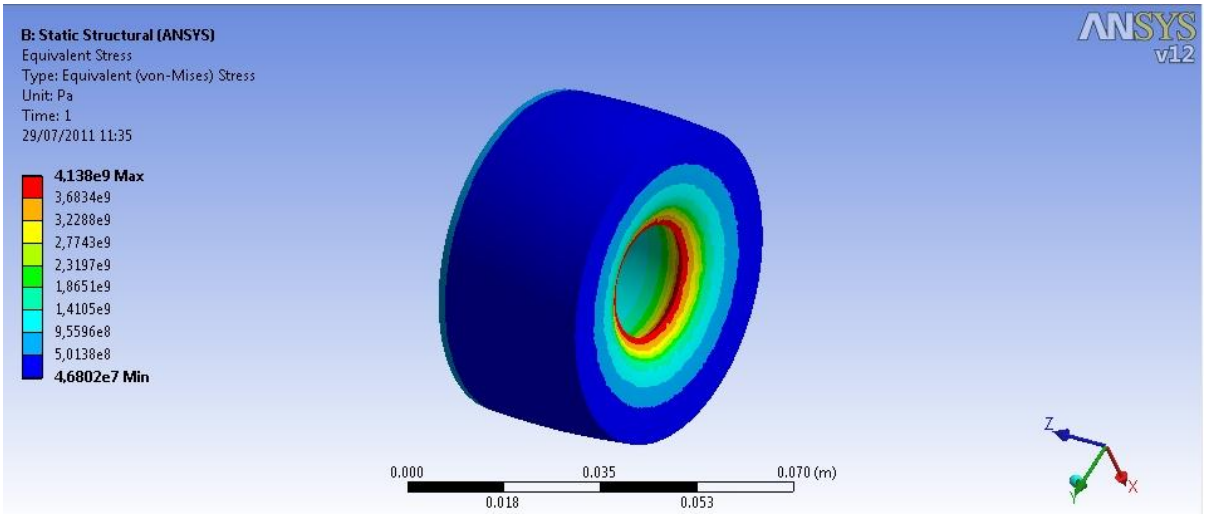

Fig. 4.27 – Impact tube's Equivalent Von Mises stress

Fig. 4.27 reports the results for Von Mises Equivalent stress of a first static structural simulation for the sacrificial impact tube (also this approach is conservative).

A force of 1e6 N is applied on the initial impact zone and a fixed constrain is applied on the other side of the component.
The results show mean values for the Von Mises stress around 500 MPa, in the zone with the highest stress the safety factor is minor of 1. Taking in account all the surrounding structure we can consider this as a fail-safe approach.

A second static structural simulation of the sabot stopper is shown in Fig. 4.28.

This simulation has the following conservative assumptions:

- For the cylinder and the disc surrounding the sacrificial tube the used material is steel and not rubber,
- Fixed constrains are used, even though in the real situation the impact chamber will help in the damping effect after the shot.

The results assess that also in the worst case the structure is able to withstand the highest level of stress.

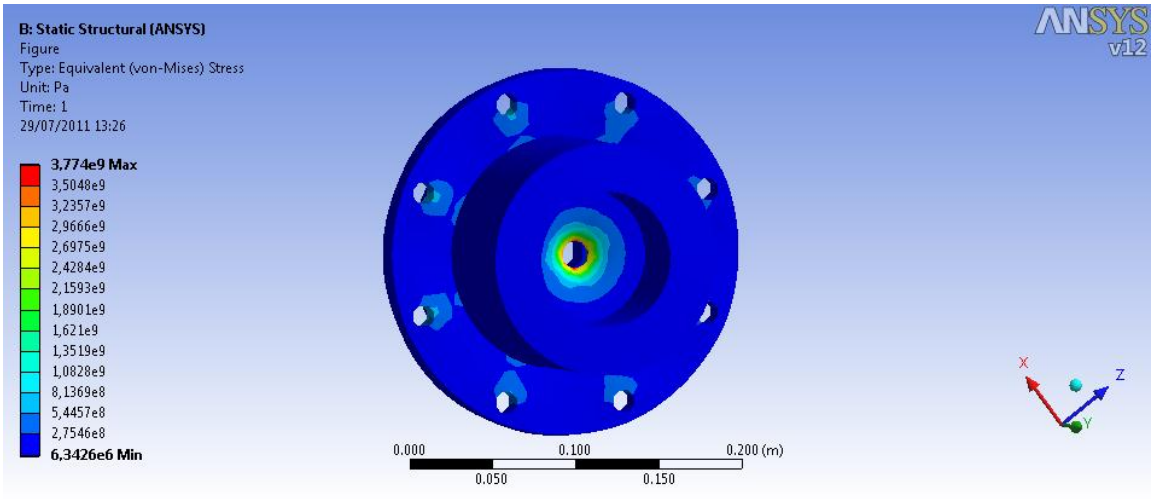

Fig. 4.28 – Sabot stopper's Equivalent Von Mises stress

- **Bolts' design**

Analytical formulas are used to design the bolts (Fig. 4.29) of the sabot stopping system for the maximum load condition.

The scheme used to assess the Equivalent Von Mises Sigma for the bolts is the following:

- Bolts and flange coefficients

$$k_V = \frac{EA}{l} \cong 280000 N/mm \quad ;$$

$$k_f = \frac{EA_{eq}}{l_{eq}} \cong 5e7 N/mm \quad ;$$

$$\frac{k_f}{k_v} \cong 180$$

- Clamping force

$$F_{serr} \cong 1.2 \cdot F_{es,\max} \quad ;$$

$$F_{es,\max} = F_{sabot+projectile} + F_{spring} \cong 1e6N;$$

$$F_{v(8)} \cong 150000N$$

- Check σ (Tensile Strength)

$$F_{TOT,vx} = F_{serr} + F_{es,v} = F_{serr} + \frac{1}{1+\frac{k_f}{n_v + k_v}} \cdot F_{es,\max} \cong 1.2e6N;$$

$$\sigma = \frac{F_{TOT,v}}{n_v A_v} \cong 750Mpa$$

From these results the bolts' characteristic can be derived:

- Bolts diameter: 16 mm
- Bolts length: 150 mm

- Material suggestion: 39NiCrMo3

  $\sigma_s \cong 785Mpa$; $\sigma_R \cong 1000Mpa$

Fig. 4.29 – Bolt's design

4.2.2.3 Impact chamber

An impact chamber design will now be described.

The starting point was a rough preliminary model previously designed at Cranfield University.

Fig. 4.30 reports the impact chamber layout.

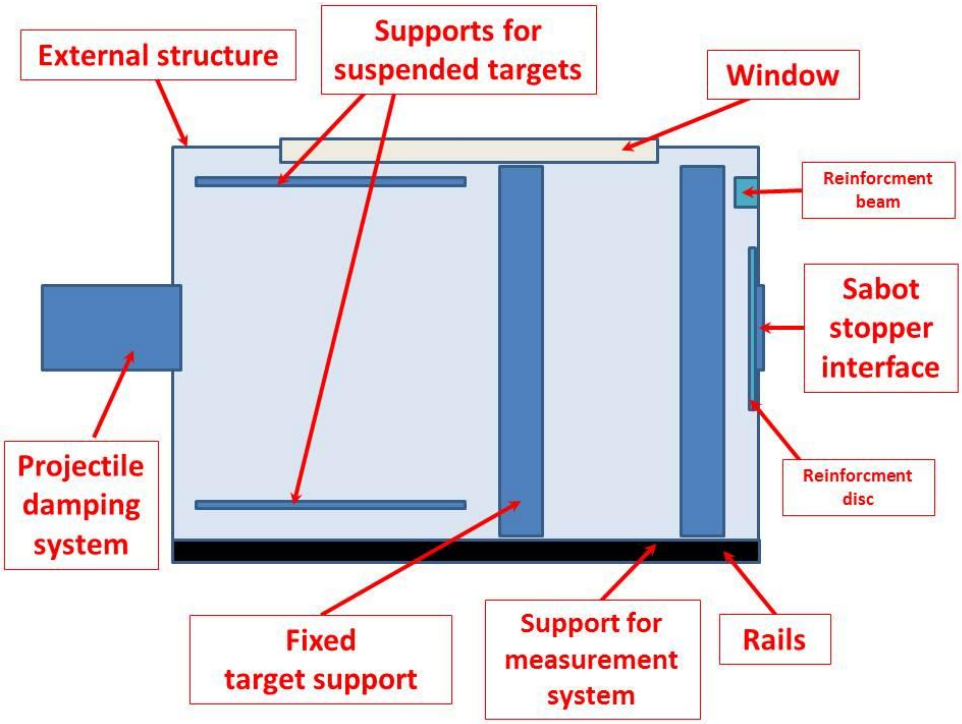

Fig. 4.30 – Impact chamber layout

The main parts are:

- External main structure,
- Sabot stopper interface,
- Rails to move the impact chamber for the pre and after test phases,
- Measurement system support,
- Fixed target support,
- Supports for suspended targets,
- Projectile damping system (that can be fulfilled with high damping coefficient material),
- "Window" to allow the use of instrumentation like high speed camera,
- Reinforcement disc for the front wall (with the sabot stopping system),
- Reinforcement beam.

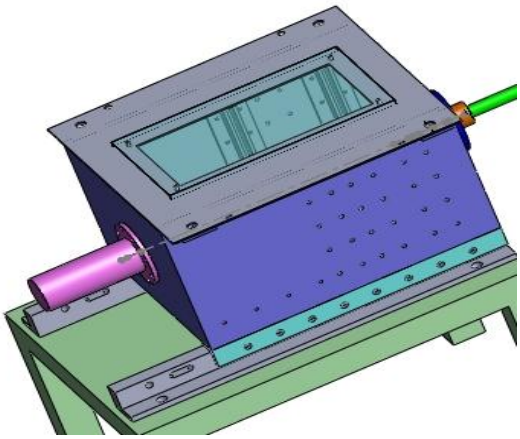

Fig. 4.31 – Impact chamber overview

In Fig. 4.31 there is a general overview of the impact chamber and in Fig. 4.32 there is a section view with the different components.

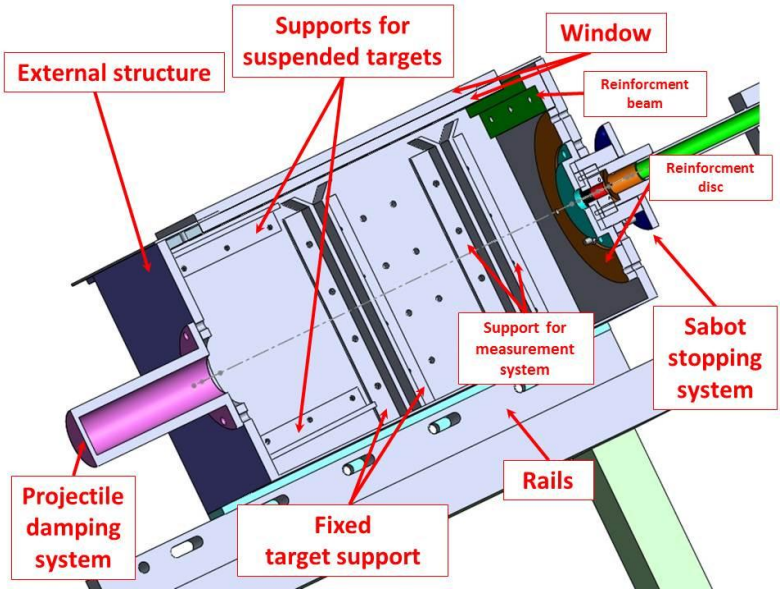

Fig. 4.32 – Impact chamber components

The projectile damping system is designed for the maximum load condition described before, *i.e.* an impact force F=1e6 N. Fig. 4.33 reports the results of a structural simulation. The highest level of Equivalent (von-Mises) Stress of 450 MPa is in the zone of conjunction between the main cylinder and the flange.

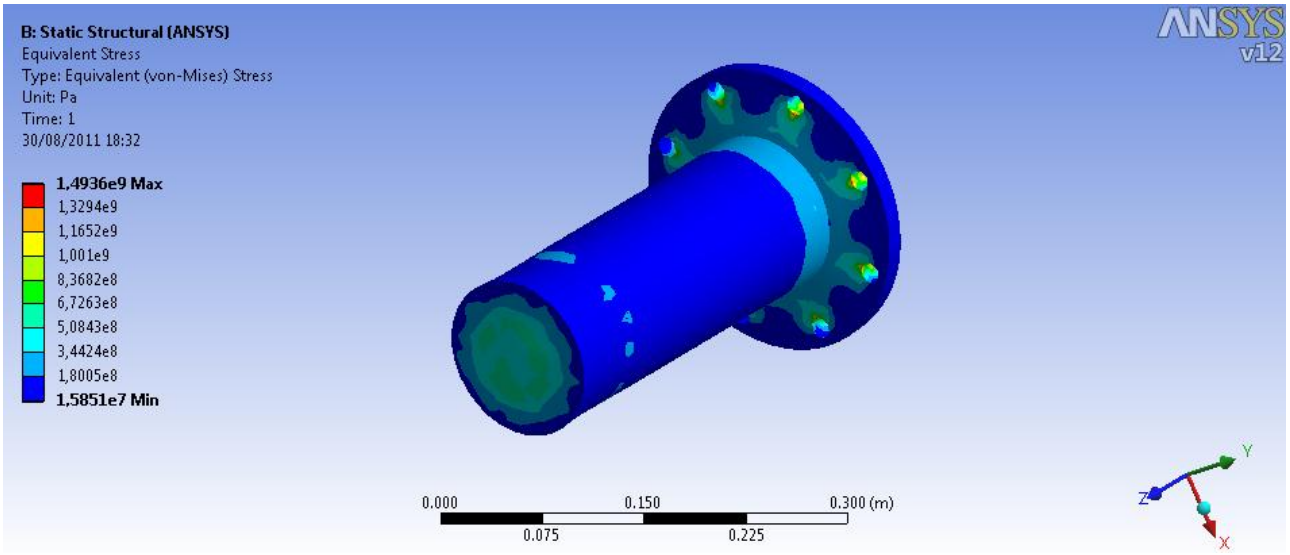

Fig. 4.33 – Projectile damping system Von Mises equivalent stress

Another option for the configuration of the chamber regarding the impact absorber system in case of failure is showed in Fig. 4.34.

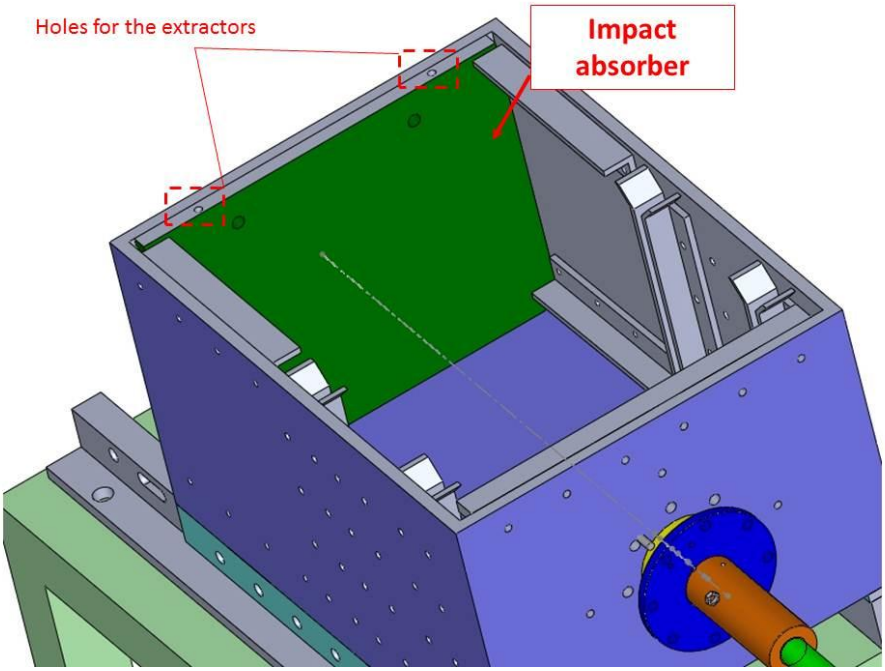

Fig. 4.34 – Overview with impact absorber plate

In this solution the projectile damping system is substituted by a steel plate inserted in the rear part of the impact chamber.

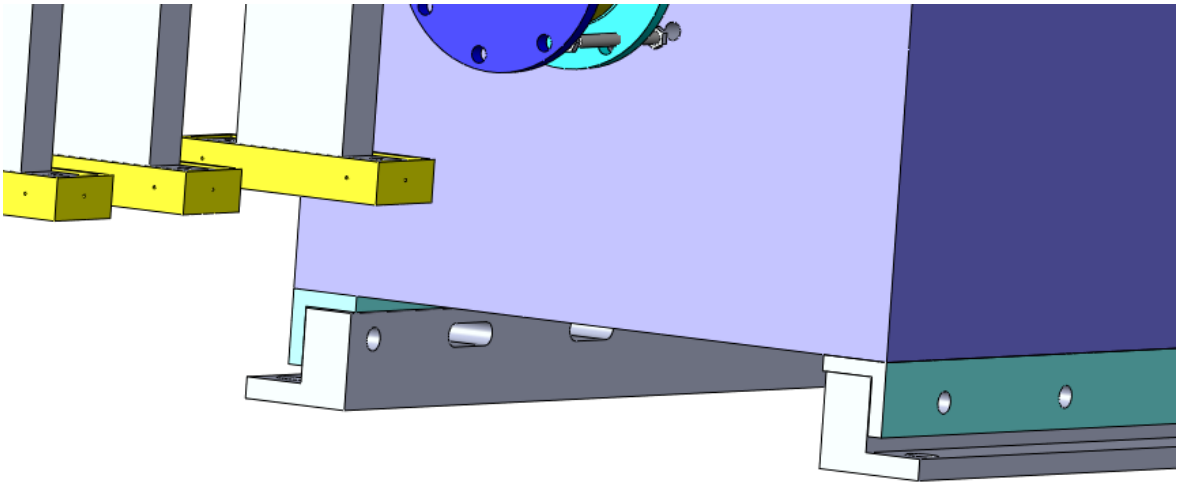

Fig. 4.35 – Impact chamber detail: rails

In Fig. 4.35 is visible a detail of the impact chamber, the rails (welded onto the main structure). The chosen design with the use of eyelets allows additional degrees of freedom in the handling of the impact chamber during all the test phases.
Another detail is showed in Fig. 4.36, the L-beams to support the fixed target and the measurement system have an inclined guidance to allow an easier insertion of the components inside the impact chamber.

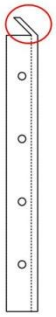

Fig. 4.36 – L-beam with guidance

A conservative approach FE simulation also for the impact chamber is reported in the following Fig. 4.37 and Fig. 4.38, where F=1e6 N is applied.

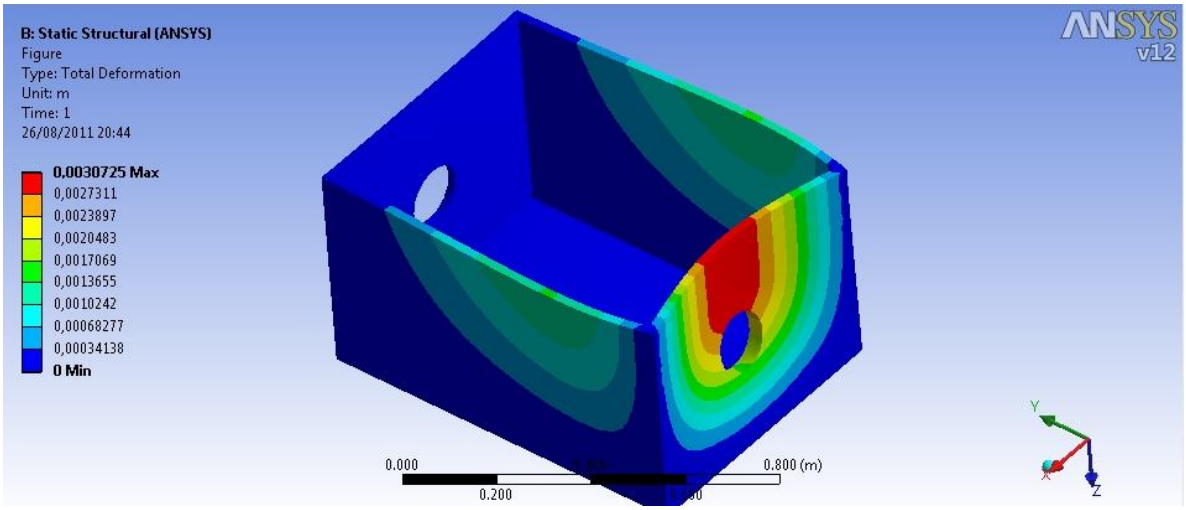

Fig. 4.37 – Impact chamber deformation

Fig. 4.37 shows that the directional deformation is around 3 mm in the highest stressed zone (front side, connected with the sabot stopping system).

As stated before this value is obtained for the most critical load condition (F=1e6 N), without taking in account any damping effect due to the overall structure.

To limit this value in the simulation a reinforcement disc and beam are used and they are suggested to be used in the real application.

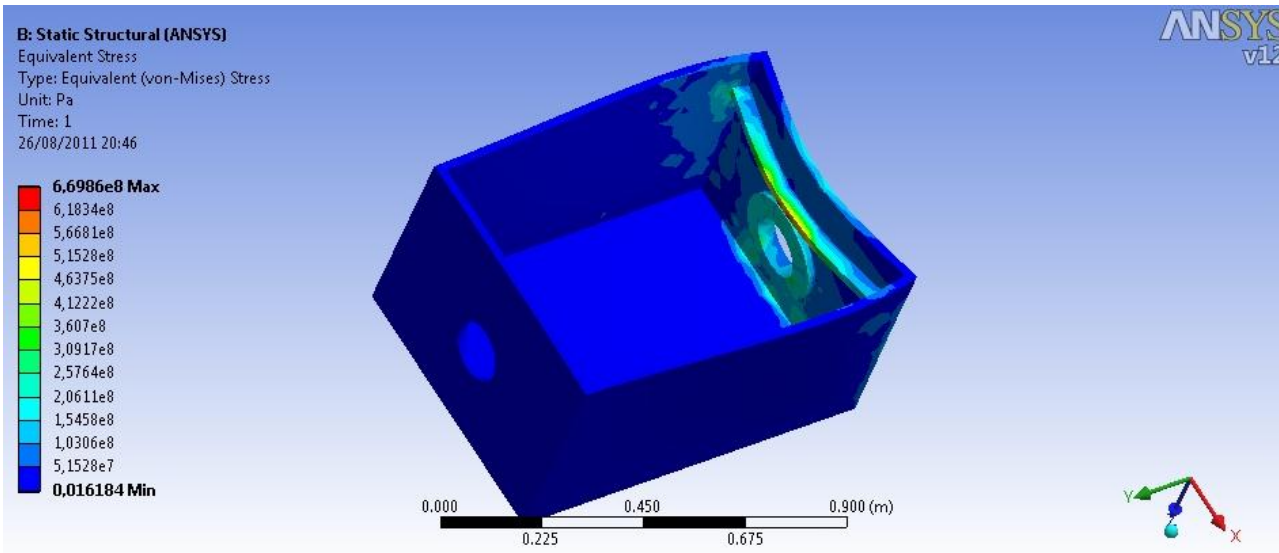

Fig. 4.38 – Impact chamber's Equivalent Von Mises stress

The mean value for the Equivalent Von Mises (Fig. 4.38) stress for the most critical zone is

around 250 MPa.

Also for this simulation the worst case is considered, *i.e.* all the launch package impacting on the structure with fixed constrains, using the relation Q=mv=Fdt.

This design of the impact chamber allows many different configurations for the tests.

Fig. 4.39 and Fig. 4.40 report 2 examples.

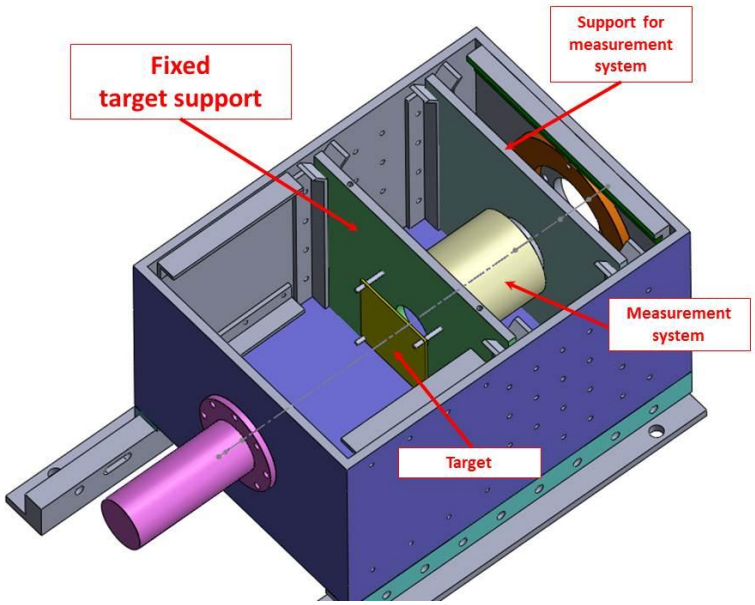

Fig. 4.39 – Configuration for fixed targets

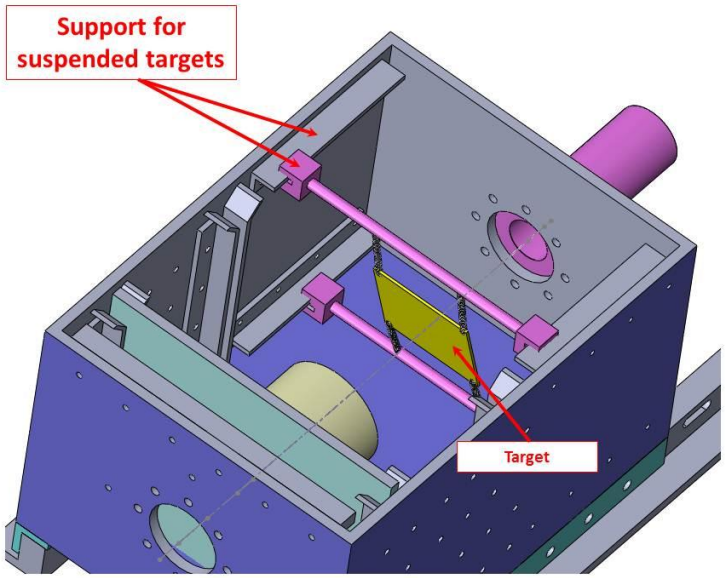

Fig. 4.40 – Configuration for suspended targets

To allow a greater flexibility in the set-up of the impact chamber a series of further holes is added (Fig. 4.41).

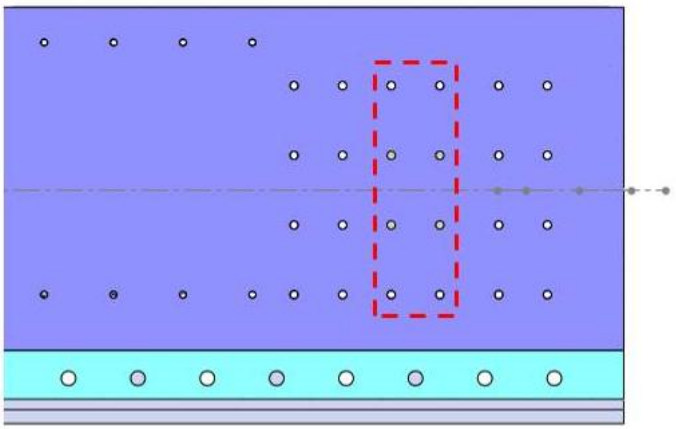

Fig. 4.41 – Series of additional holes

Before the manufacturing of the components a further check of the pump tube overall height from the laboratory's floor and of the pump tube type of threading is required.

4.2.2.4 Analysis for future developments

A first preliminary FEM analysis of the first stage reservoir is presented here (Fig. 4.42 and Fig. 4.43).

The aim is to study a possible increase of the pressure to improve Single Stage LGG's performances.

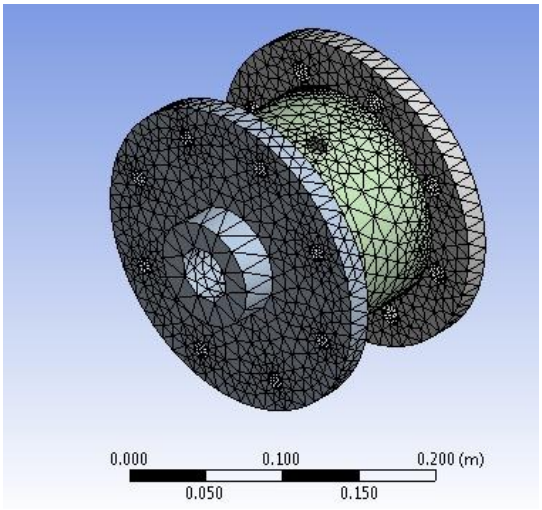

Fig. 4.42 – Reservoir FEM mesh

This first model has a rough mesh (solid elements) and uses a structural steel. Inside the reservoir a boundary condition of pressure at 200 bar is set.

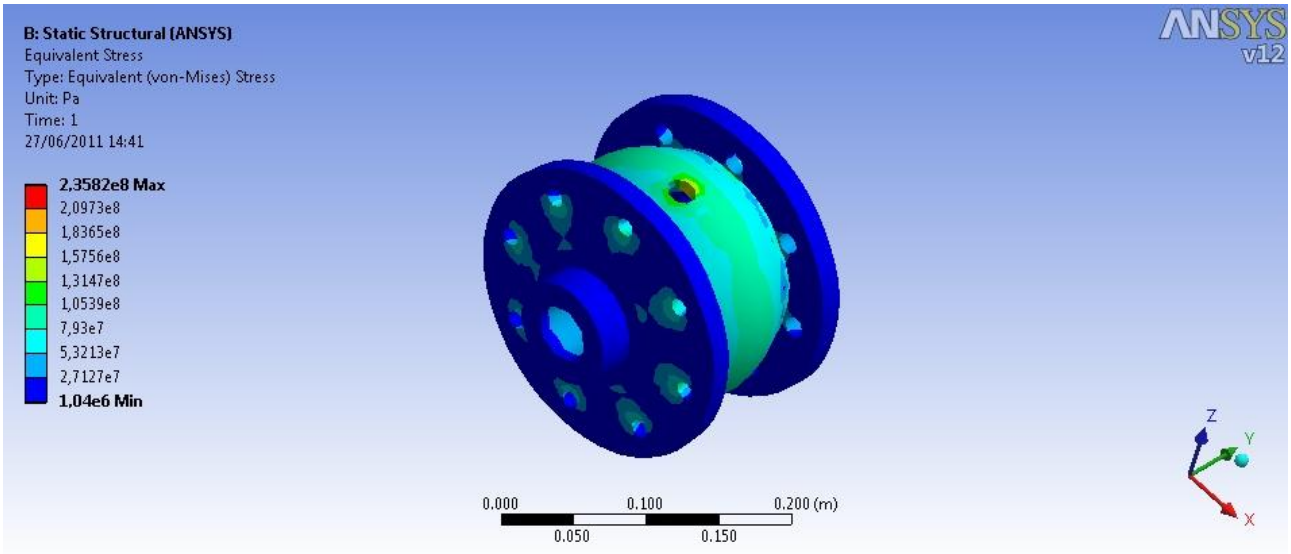

Fig. 4.43 – Reservoir Equivalent Von Mises stress

The first analysis shows that the structure has a Safety Factor around 3 using a structural steel, the highest Von Mises stress is around 120 MPa.

For the development of the LGG a set of new gas dynamic simulations, using the same Simulink model as described before, is now presented to improve the performances.

These simulations evaluate:

a. The effects of increasing the pressure in the reservoir,
b. Different pump tube lengths,
c. Different gases, like Helium,
d. Performance in vacuum.

a. Pressure increasing in the reservoir

In Fig. 4.44 are presented results for different pressure values in the reservoir with a fixed configuration (opening valve time: 1e-2 s and piston radial clearance: 0.1e-3 m).

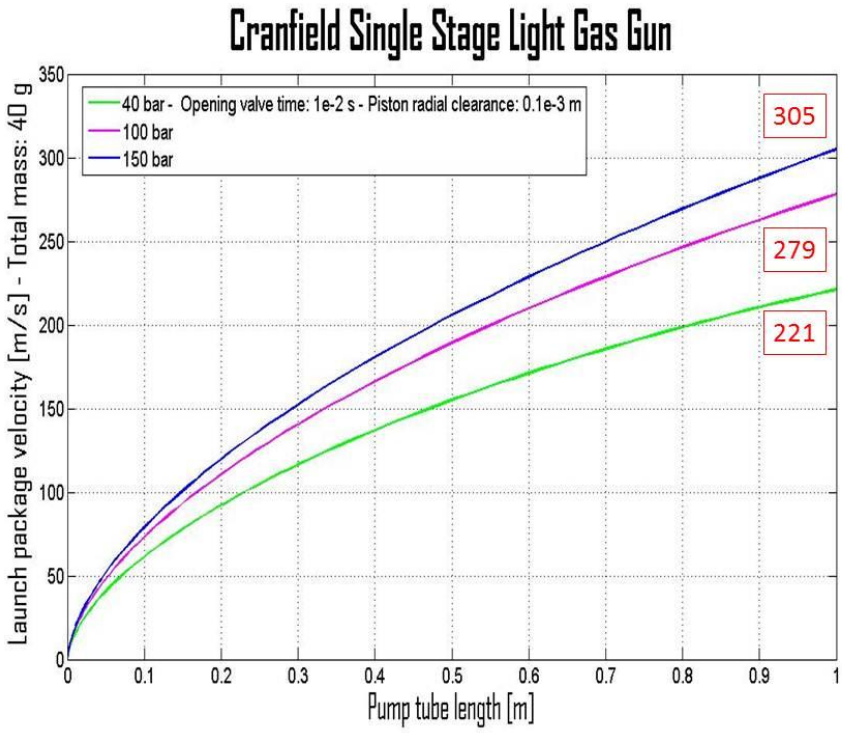

Fig. 4.44 – Pressure increasing in the reservoir

It can be observed that at 150 bar the launch package is 1.4 times faster than the present LGG's configuration.

b. Pump tube length

Fig. 4.45 shows the effect of the pump tube length's increasing.

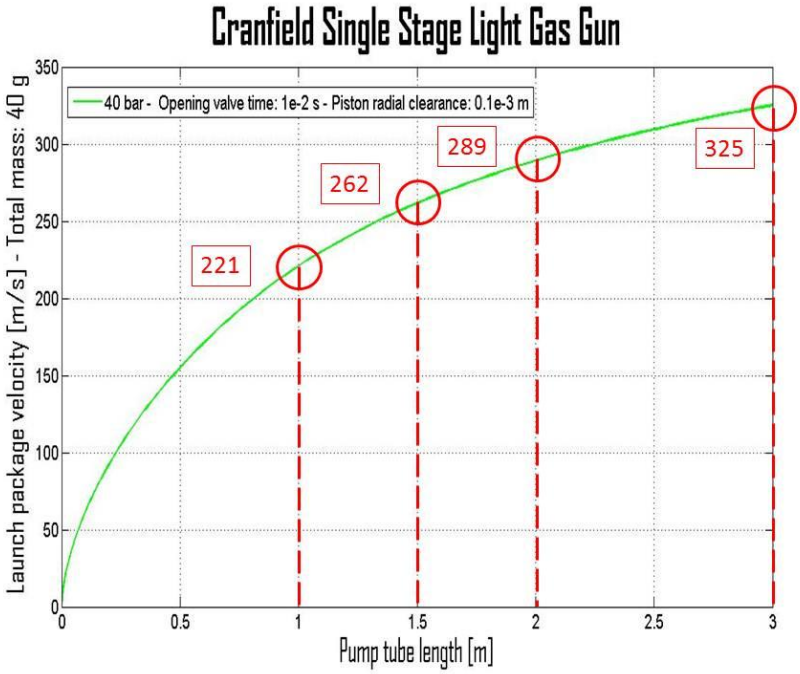

Fig. 4.45 – Different pump tube lengths

The launch package is 1.5 times faster with a pump tube 2 m longer.

c. Performances with Helium

In Fig. 4.46 is reported the comparison between the use of N_2 and He.

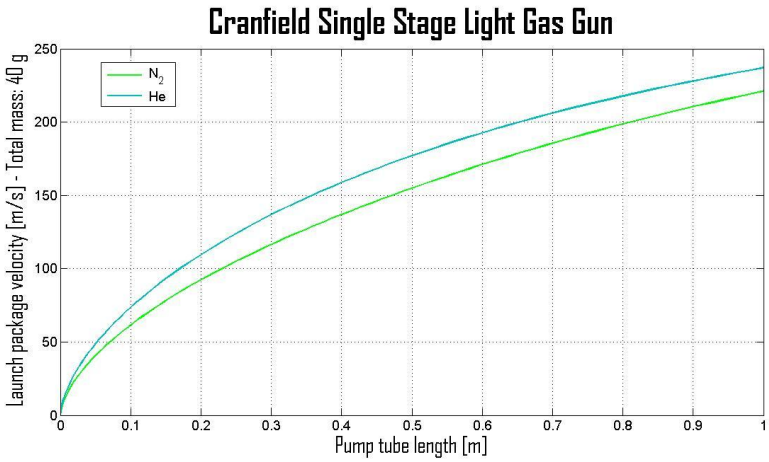

Fig. 4.46 – Performances with He

d. Performances at different pressures in the impact chamber

Simulations for different values of impact chamber pressure (1000 mbar, 500 mbar and 5 mbar) are showed in Fig. 4.47.

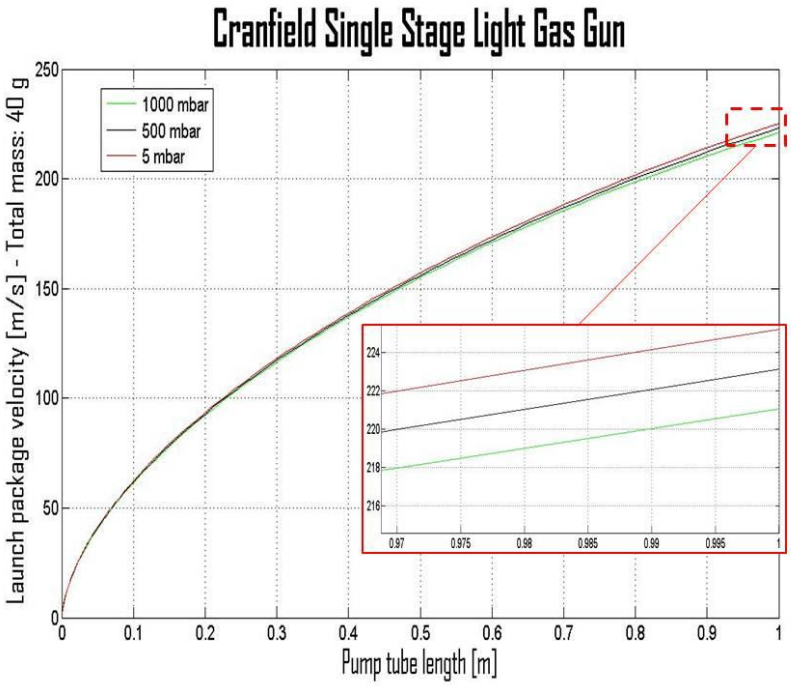

Fig. 4.47 – Performances at different pressures in the impact chamber

In these conditions the improvement in the performance is negligible, however to set the LGG to fire in vacuum conditions will allow tests also for space applications.

There is the need to investigate deeper the sources of loss for the LGG and to do a model to understand the behaviour of the pneumatic valve.
Further gasdynamic simulations done for future developments show how the actual LGG system could be improved.

4.2.3 Two stage CISAS Light Gas Gun

This paragraph describes the study of the fluidynamical and mechanical solutions for the high pressure system of a two stage light gas gun, of ½" calibre.
This study includes the conceptual analysis, starting from the requirements definition, and the development of the final solution.
It is also described a study about the new supporting structure for the two stage LGG.

The process for the fluidynamical and mechanical analysis is divided in the following steps:

- Axial-symmetric 2-D fluid dynamics analysis of the high pressure system, in steady regime, to optimize the critical zones;
- Optimization of the piston damping system;
- Dynamic analysis of the shutter motion and design of a system to absorb the end of stroke hit;
- Shutter's FEA;
- Realization of 3-D models of the high pressure section.

4.2.3.1 High pressure system fluid dynamic analysis

Fluid dynamic analysis of high pressure system is mandatory to maximize energy transfer between the compressed propellant in the pump tube and the launch set.
Fluid dynamics simulations were done using Ansys Cfx 11.0 software.

In particular 2 different solutions are analysed and compared: the first one is an up-scaling of the actual used solution, the second one is a totally new solution.

4.2.3.1.1 Fluid dynamic analysis of the up-scaled actual solution

The scheme used for the simulation is:

a. Fluid volume extraction
b. Rough mesh
c. First steady analysis to set up the parameters
d. Refined mesh
e. Steady analysis with different outlet conditions to monitor the fluid behaviour at different value of input/output pressure ratio (static pressure values of 400, 300, 200, 50 bar)

a- Fluid volume extraction.

Using Solid Works the solid volume is extracted (Fig. 4.48), the obtained Iges file is then used by the program that creates the mesh for Ansys Cfx 11.0.

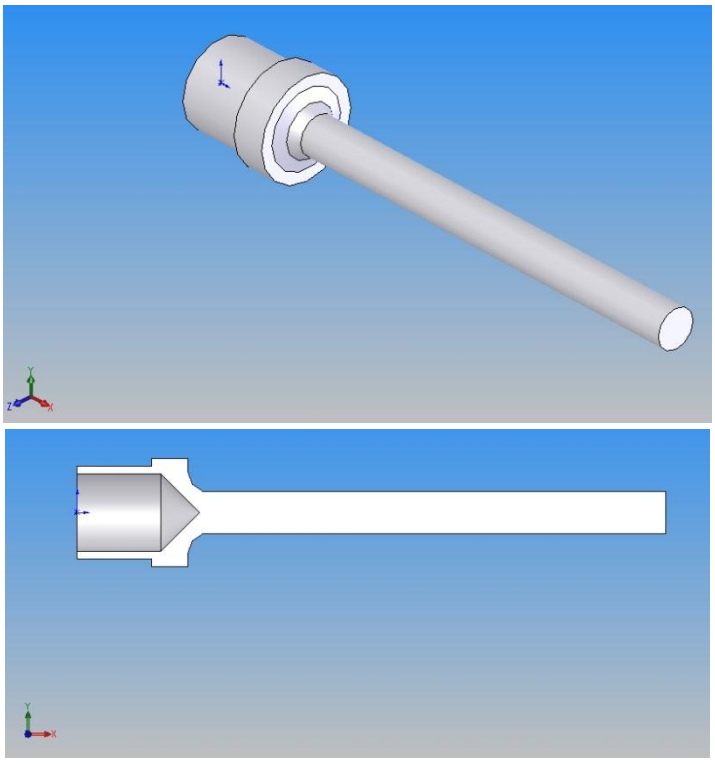

Fig. 4.48 - Fluid volume

b- Rough mesh. A rough mesh with the following characteristics is creates as first attempt (Fig. 4.49):

- Nodes total number: 5851
- Elements total number: 23368
- Minimum element length: $2,5*10^{-3}$ m

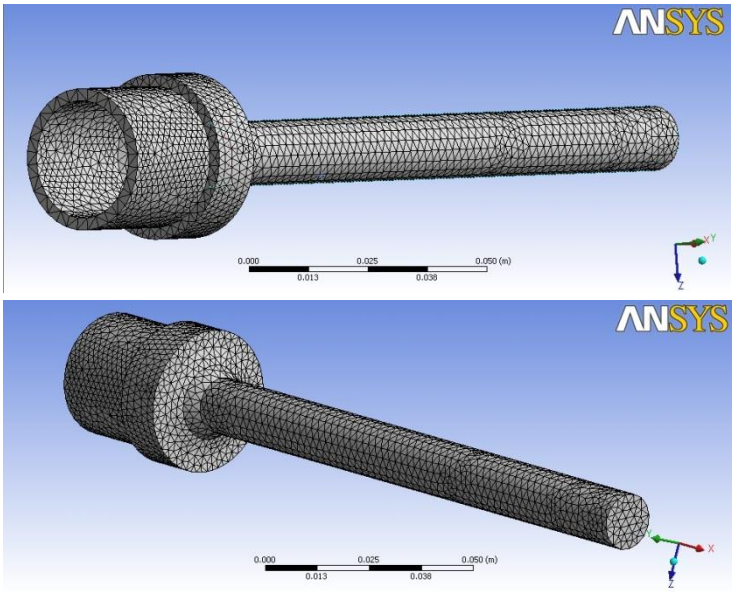

Fig. 4.49 - Rough mesh

c- First steady analysis

A first steady analysis is done to set up the parameters and to evaluate the software behaviour with the operating pressure ratio of the two stage light gas gun.
The simulation parameters and the boundary conditions are (Fig. 4.50):

- Inlet: Total pressure 6000 bar
- Outlet: Static pressure 1 bar
- Fluid: Hydrogen at 3000 K
- "Wall (no slip)" condition (*i.e.* the fluid will have zero velocity relative to the solid boundary) on external fluid volume surfaces
- Turbulence model: k-epsilon (usually it is the most robust model that gives good reliable preliminary results)
- Fluid Timescale Control: Automatic
- Resolution scheme: High Resolution
- Iterations max number: 150

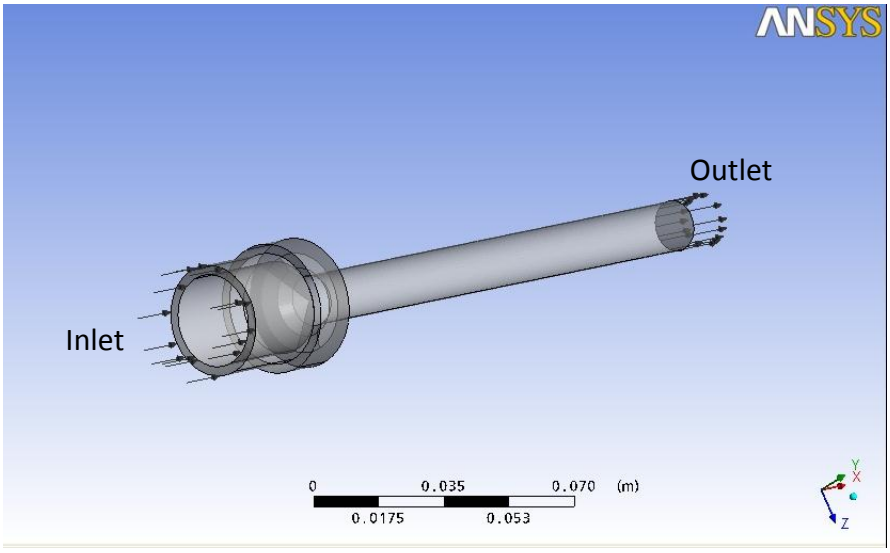

Fig. 4.50 - Boundary conditions

Main parameters values are plotted during post processing (Mach number, Fig. 4.51and total pressure, Fig. 4.52) along the mid-line of the analysed fluid volume to verify that results fit together with a fluid dynamic model previously developed for the first version of the LGG.

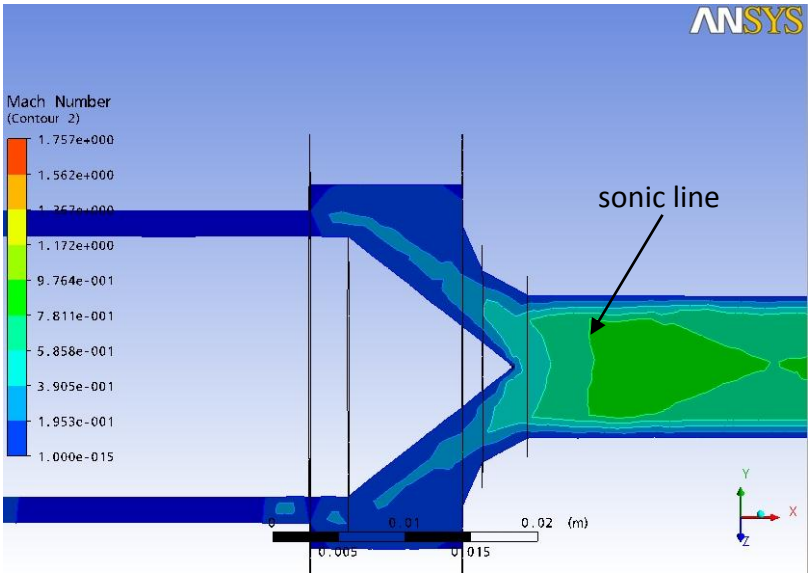

Fig. 4.51 - Mach number trend

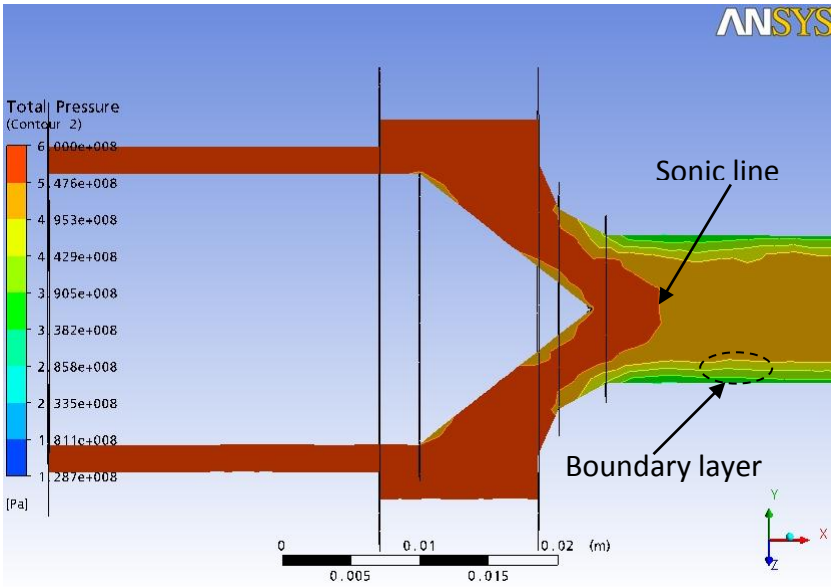

Fig. 4.52 - Total pressure of the accelerating fluid

From previous figures it is visible that near the sonic line there is a high total pressure value reduction. An additional reduction is due to the boundary layer.

d- Refined mesh.

The final mesh (Fig. 4.53 and Fig. 4.54) has the following characteristics:

- Nodes total number: 61776
- Elements total number: 318156
- Minimum element length: $1*10^{-3}$ m

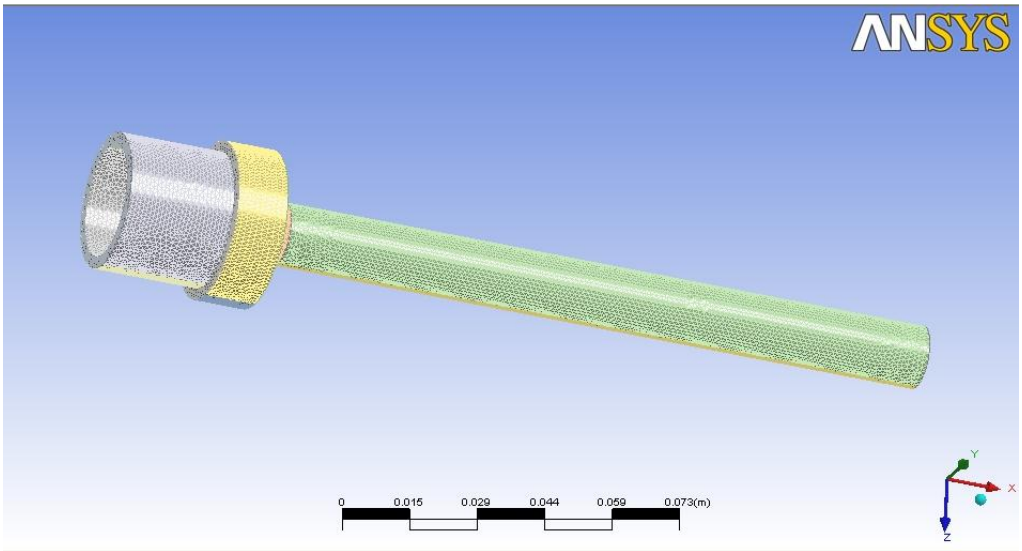

Fig. 4.53 - Refined mesh overview

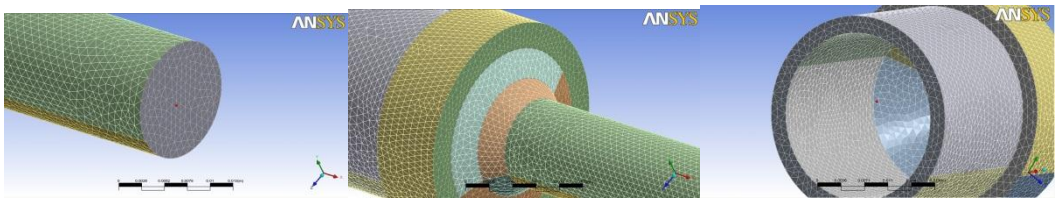

Fig. 4.54 - Refined mesh details

e- Steady analysis with different outlet conditions

An example of the simulations' results is shown (pressure: 400 bar). All the simulations have the same condition of the previous situation with the variation of the outlet conditions to monitor the fluid behaviour at different value of input/output pressure ratio (Fig. 4.55 and Fig. 4.56).

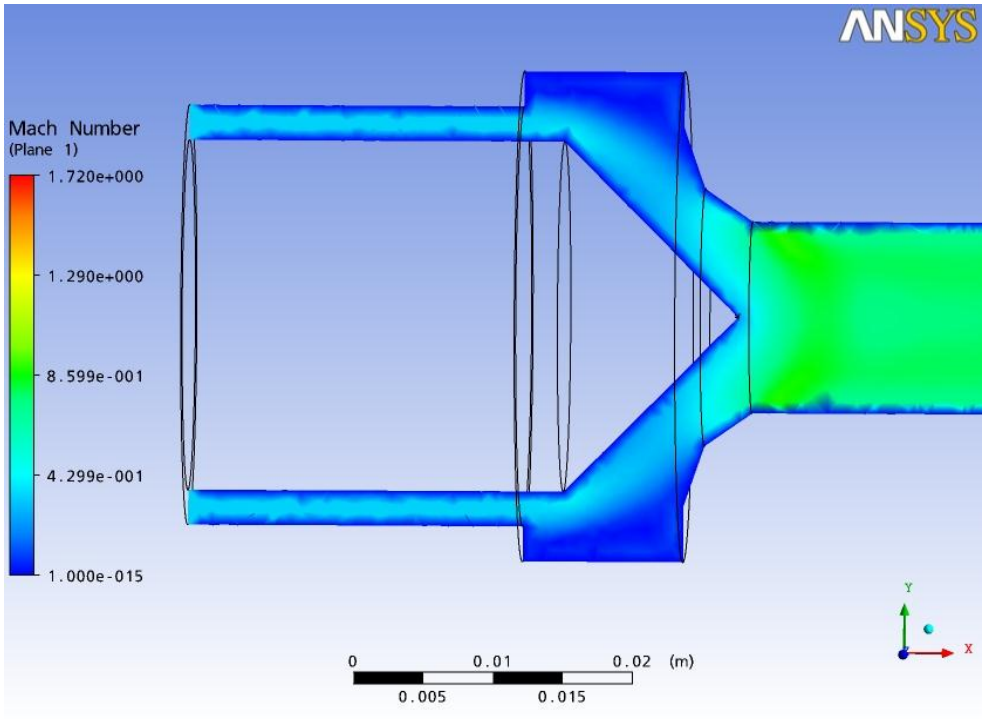

Fig. 4.55 - Mach number trend, outlet static pressure: 400 bar

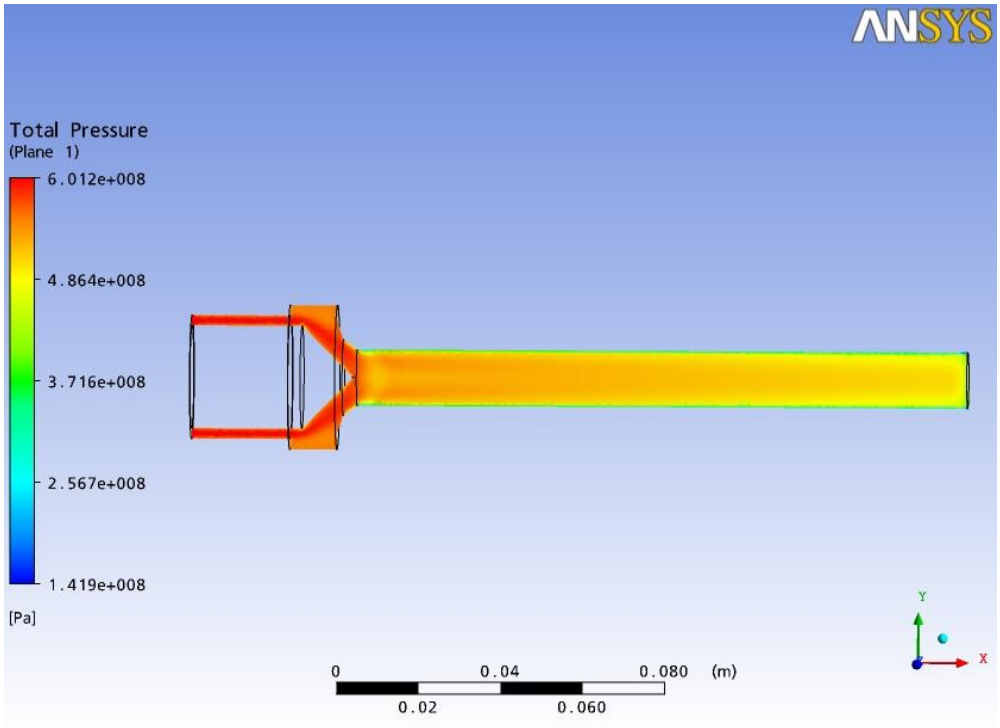

Fig. 4.56 - Total pressure trend, outlet static pressure: 400 bar

In the previous figures it is visible a good regularity of the flux, in particular in the zone near the cone, that is the most critical, because there are high section variations.

In every simulation is also visible a re-cycle stream zone of the high pressure and temperature flux: in Fig. 4.57 there is the plot of the velocity vectors of this zone of the last presented simulation.

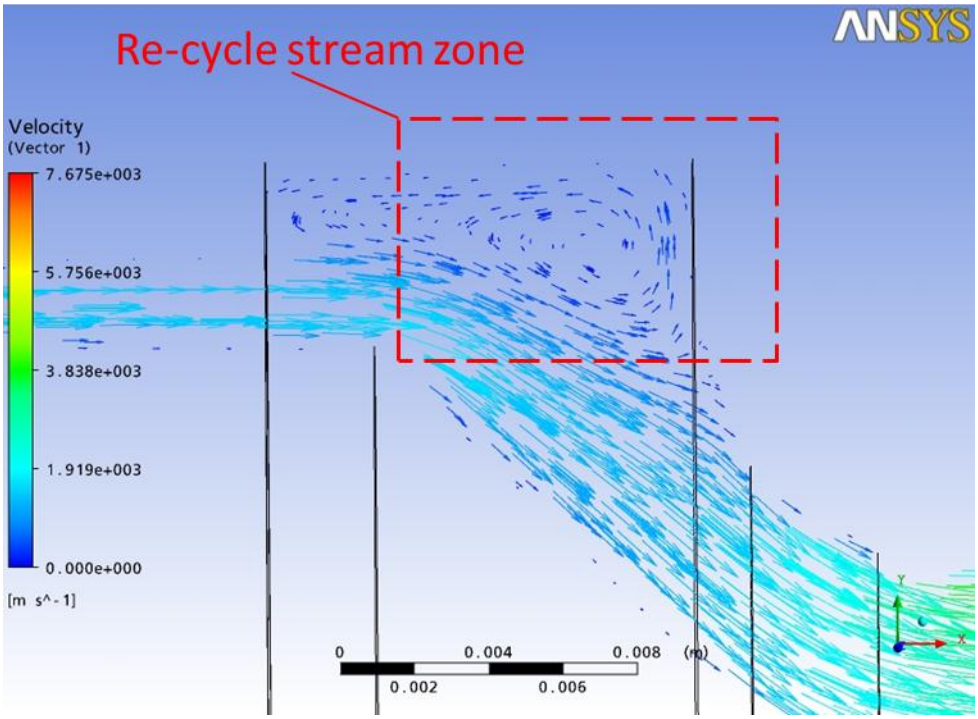

Fig. 4.57 - Re-cycle stream zone

In
Tab. 4-3 and Fig. 4.58 there is represented the fluid dynamic efficiency of this solution, it is defined as the ratio between total and static outlet pressure:

Ptot_out / Pstat_out

This coefficient is for a total inlet pressure of 6000 bar.

Pressure [bar]		**Efficiency**
Static - outlet	*Total - outlet*	Ptot_out/Pstat_out
400	4864	12,16
300	4855	16,18
200	4848	24,24
100	4840	48,40
50	4837	96,74

Tab. 4-3 - Overview of the simulation for the scaling of the actual solution

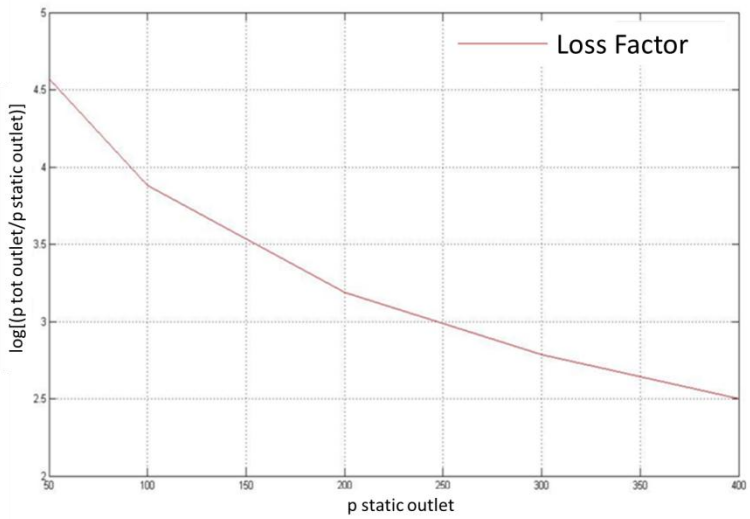

Fig. 4.58 - Fluid dynamic losses for the scaling of the actual solution

The use of this parameter, called Loss Factor, allows to assess the efficiency of the system at different static outlet pressures.

4.2.3.1.2 Fluid dynamic analysis of the new solution

The concept of the new solution is the following (Fig. 4.59):

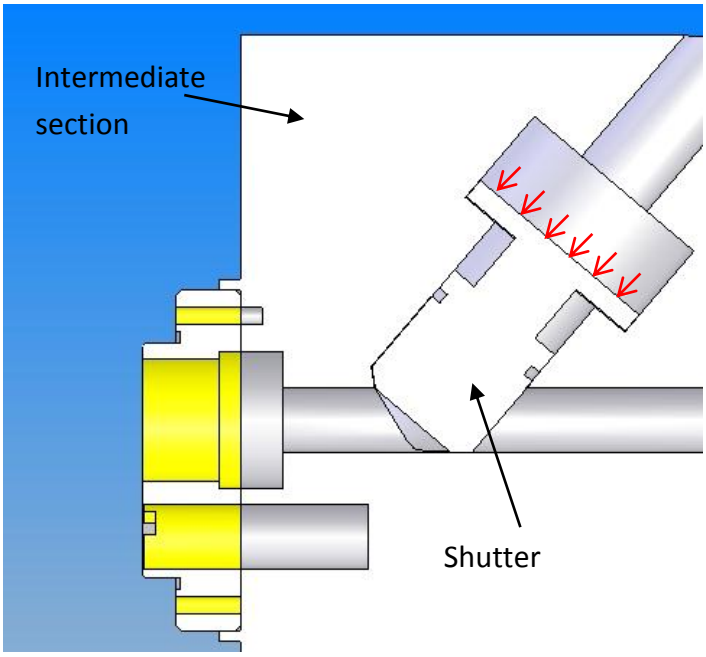

Fig. 4.59 - Closed valve (red arrows highlights the action of the pneumatic back pressure)

The pump tube (not visible in the figure) gives the gas from left to right and when there is the pressure peak the valve closes after that the force is bigger than the one of the back

pressure (Fig. 4.60).

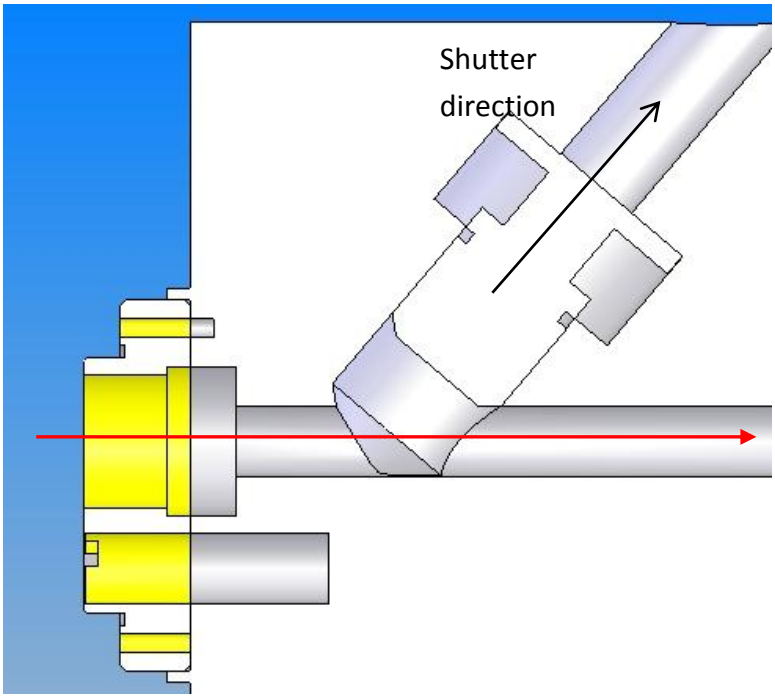

Fig. 4.60 - Open valve (the red arrow highlight the path followed by the high pressure gas)

Without previous experience about the fluid dynamic behaviour of this solution the simulations follow a different logic scheme if compared with the others.
After a preliminary set up of the model, 3 couples of values of total pressure a and temperature are chose, depending on data gives by another gasdynamic model of the light gas gun, in this way it is possible to simulate a representative trend of the physic phenomena.

In
Tab. 4-4 there are the 3 couples of values. Couple number 3 is plotted as example in Fig. 4.61.

Couple	T inlet [K]	P tot inlet [bar]
1	1560	1000
2	1860	1600
3	2500	5000

Tab. 4-4 - Total pressure and temperature value

With this gradual change of the outlet conditions (Tab. 4-5) the static pressure, velocity, temperature and density variations are monitored, with particular attention to the flux's geometry and to the search of re-cycle stream/stagnation zones.

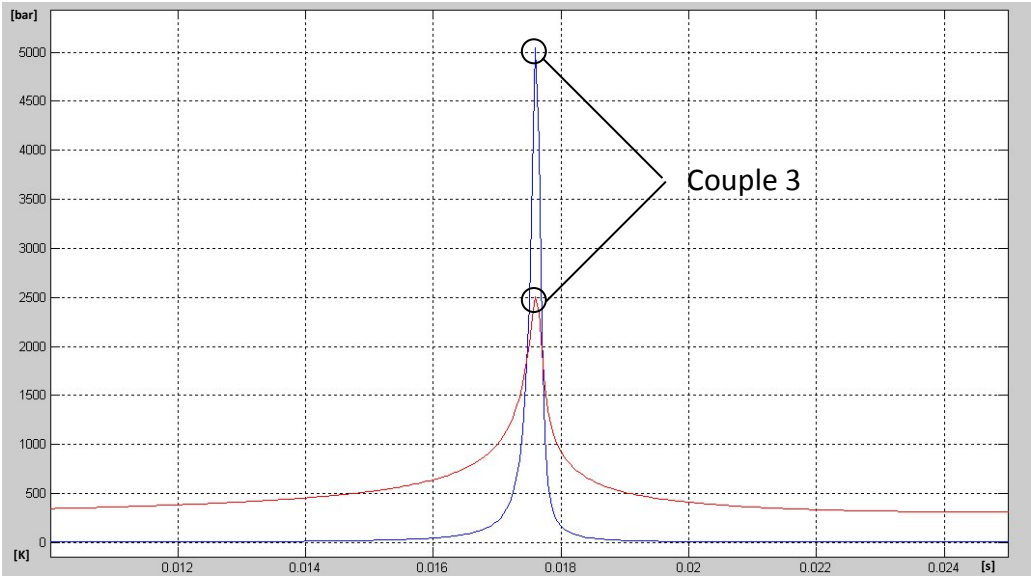

Fig. 4.61 - Pressure (blue) and temperature(red) curve, these values are obtained using the zero-dimensional model of the new LGG configuration

	P tot outlet [bar]	P tot inlet [bar]
Couple 1	500	1000 @ 1560K
	100	
	1	
Couple 2	800	1600 @ 1860K
	160	
	1	
Couple 3	2500	5000 @ 2500K
	500	
	1	

Tab. 4-5. Overview of the couples of values

The simulations have the following scheme:

a. Fluid volume extraction
b. Creation of the mesh
c. Steady analysis with different inlet, outlet and temperature conditions

a- Fluid volume extraction

Using Solid Works 2003 the solid volume is extracted (Fig. 4.62), the obtained Iges file is then used by the program that creates the mesh for Ansys Cfx 11.0.

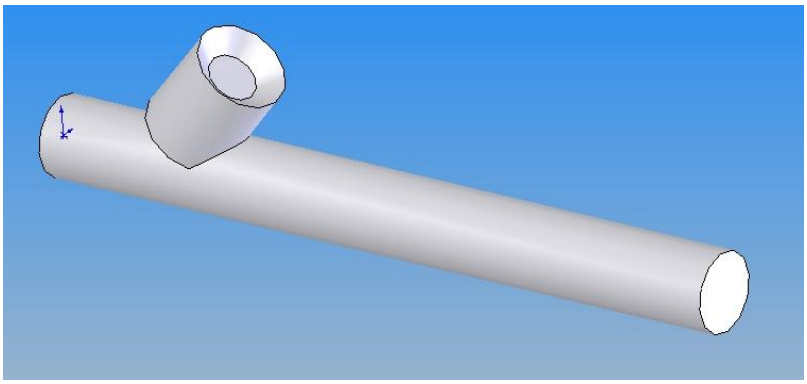

Fig. 4.62 - 3-D fluid volume model

b- Creation of the mesh.

The refined mesh (Fig. 4.63) has the following characteristics:

- Nodes total number 15440
- Elements total number (tetrahedron) 77421
- Minimum element lenght: $2*10^{-3}$ m

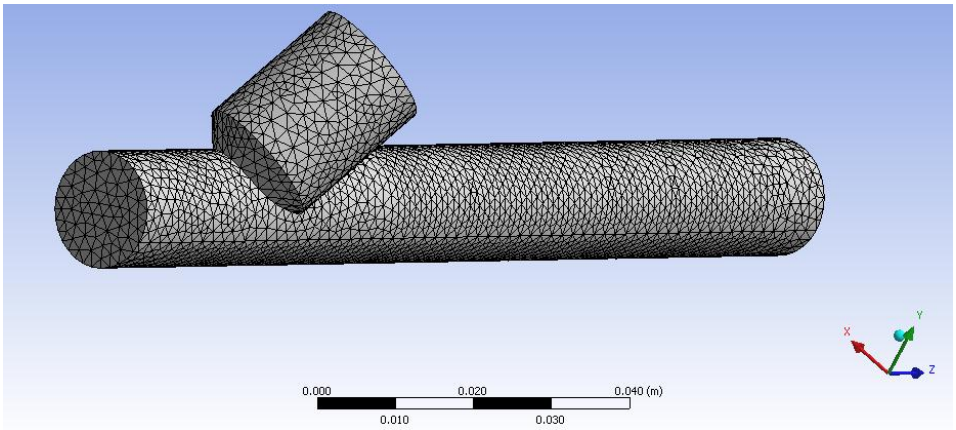

Fig. 4.63 - Meshed fluid volume

c- Steady simulation.

The simulation conditions are:

- Fluid: Hydrogen
- “Wall (no slip)” condition on the external surfaces of the fluid volume
- Turbulence model: Kw-SST
- Fluid Timescale Control: Automatic
- Resolution scheme: High Resolution
- Maximum number of iterations 100

To be brief here it is reported only the plot for the values regarding couple n.3, a table with an overview of all the simulations will be reported.

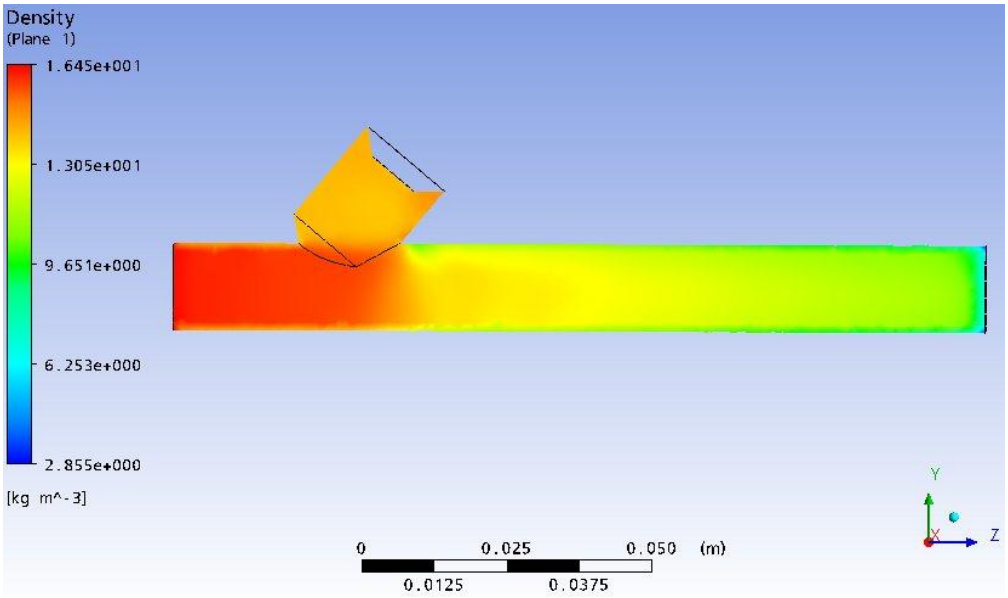

Fig. 4.64 - Density trend, couple 3

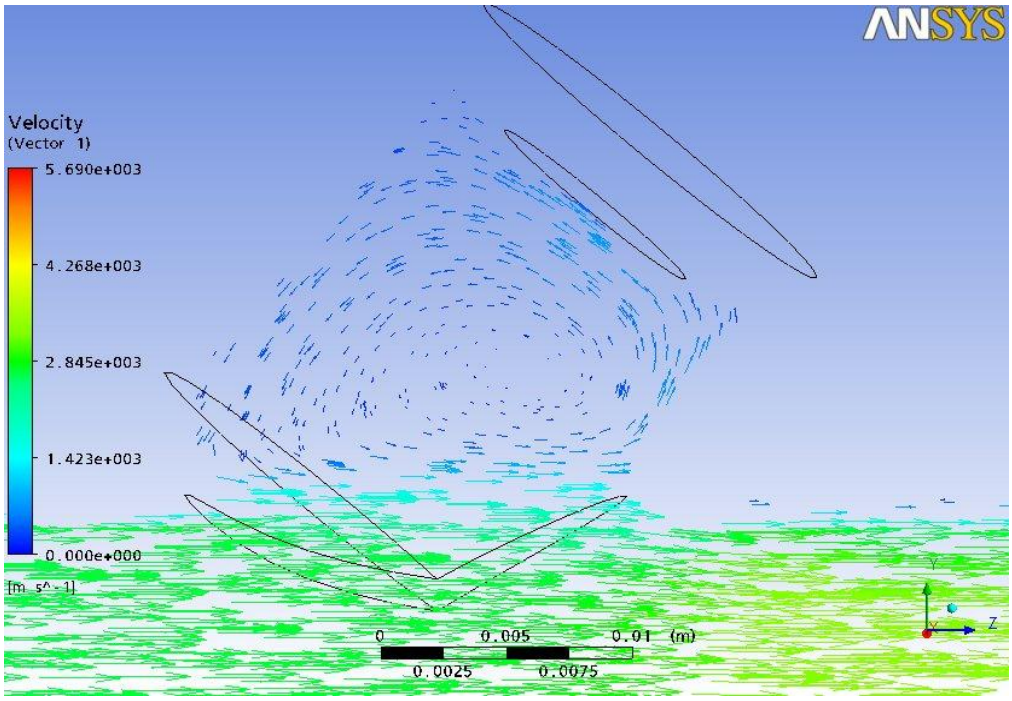

Fig. 4.65 - Velocity trend, couple 3

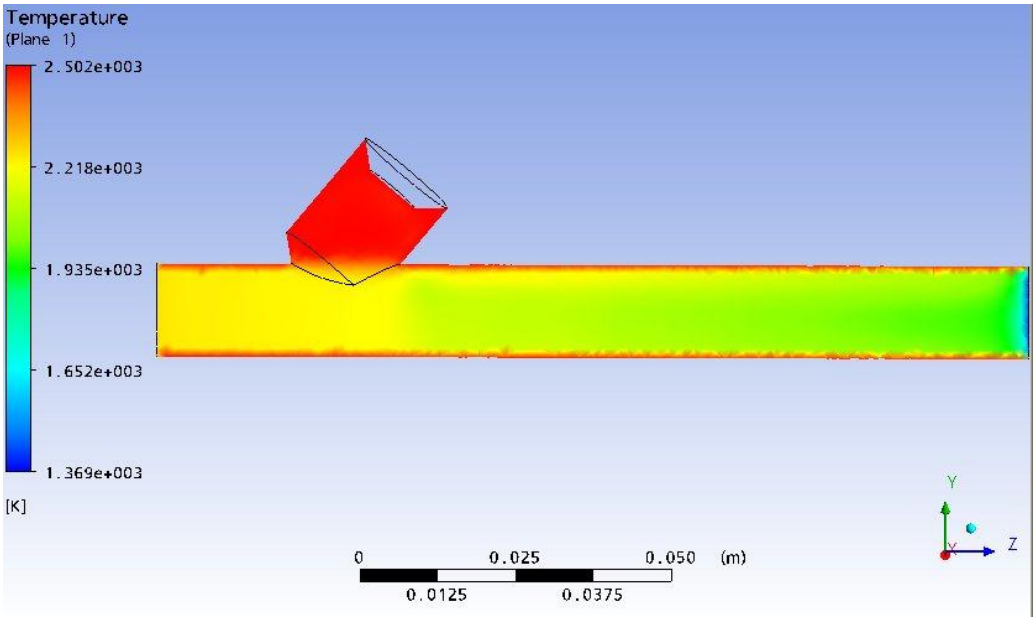

Fig. 4.66 - Temperature trend, couple 3

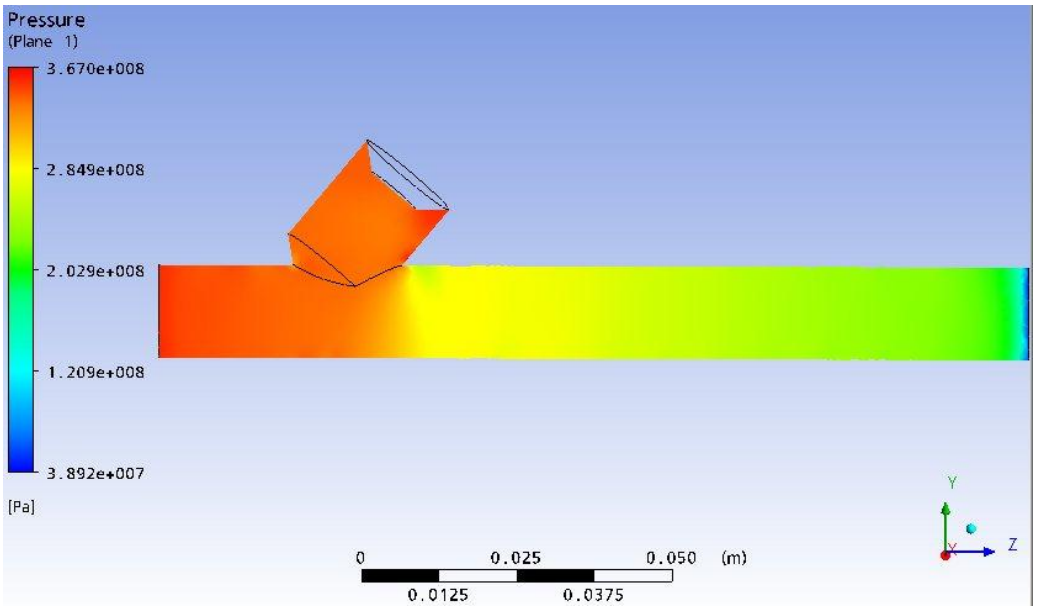

Fig. 4.67 - Pressure trend, couple 3

In these simulations there is a good trend of the main analysed parameters (*i.e.* density, velocity, temperature, pressure), this is visible both from the plots and from the output values (from Fig. 4.64 to Fig. 4.67).

Moreover the re-cycle stream zone in the shutter's guide is very little and its influence on the principal flux is negligible.

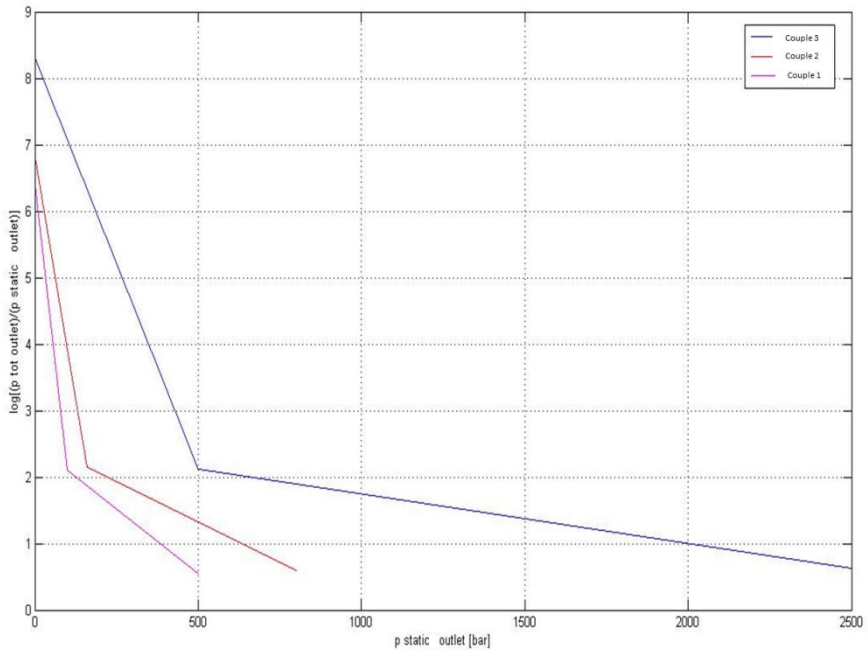

Fig. 4.68 - Fluid dynamic losses of the new solution, comparison between the 3 couples of values

In the previous graph (Fig. 4.68), in which the efficiency is represented in logarithmic scale, it is visible that the different simulations have a comparable trend.

Hereafter there is a summarizing table of the simulations and a graph with a comparison between the two analysed solutions.

Tab. 4-6 reports the observed velocity range, the minimum temperature and the maximum static pressure. These values are compared with the inlet conditions and the density range.

These values are evaluated for the 3 couples, modifying the outlet conditions (case a, b and c).

It is observable that the new solution improves fluid dynamic solutions if compared to the scaled actual solution (Fig. 4.69).

		Velocity [m/s]		Temperature min [K]	Max static pressure [bar]	Density [kg m^-3]		Outlet [bar]	T inlet [K]	Inlet [bar]
		min	*max*			*min*	*max*			
Couple 1	*a*	0	4903	720	730	2,12	12,26	1	1560	**1000**
	b	0	4490	855	734	2,86	12,3	100		
	c	0	2807	1284	755	7,66	12,5	500		
Couple 2	*a*	0	5355	858	1160	2,85	16,44	1	1860	**1600**
	b	0	4905	1019	1174	3,84	16,5	160		
	c	0	3067	1531	1208	10,278	16,84	800		
Couple 3	*a*	0	6209	1153	3649	6,63	38,19	1	2500	**5000**
	b	0	5688	1369,7	3637	8,97	37,55	500		
	c	0	3558	2058	3770	23,87	39,1	2500		

Tab. 4-6 - Simulations' overview for the new solution

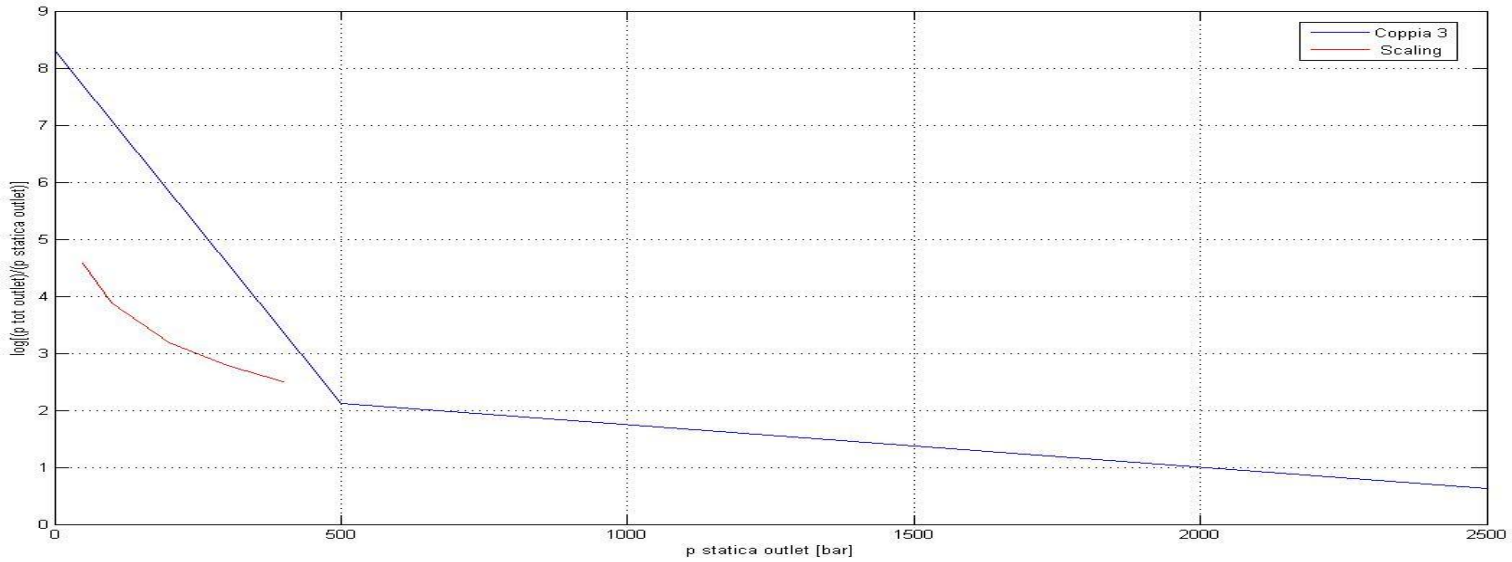

Fig. 4.69 - Fluid dynamic losses comparison between the 2 solutions

4.2.3.2 CISAS light gas gun development

4.2.3.2.1 Second stage design

This paragraph describes the design of the new light gas gun second stage, interface with the pump tube included.
After the fluid dynamic analysis described in the previous paragraph here there is a description of the dynamic (opening and closing transient states), mechanical and structural problems.

Two solutions are considered, the first one with a low risk factor, due to the knowledge gained in the past years, the second one is innovative instead.

The first solution (Fig. 4.70) analyse the existing solution already implemented for the LGG and realize an up-scaling.
The main advantage is that the system has a long operative history and is well knew, so it is easy to implement, this allow a considerable reduction of the production time.

On the other hand there are some disadvantages:

- Increasing the dimensions requires an increase of the involved inertias and forces, this creates structural problems and loss of efficiency in the energy transfer between the pump and launch tube problems, which in turn is linked to the greater duration of the transient opening state of the shutter.

- The increase of the structural stresses needs of the development of new conceptual solutions to damp the shutter's motion and for the structure of this system.
  The shutter is opened with the action of the pressure that accelerates it. Then it is stopped from the bottom section, hitting it.
  This involves structural problems due to the inertias. In the previous version of this valve, the damping was done by the structure itself, however in this new situation the bottom section is divided in two parts to put a custom damping system.

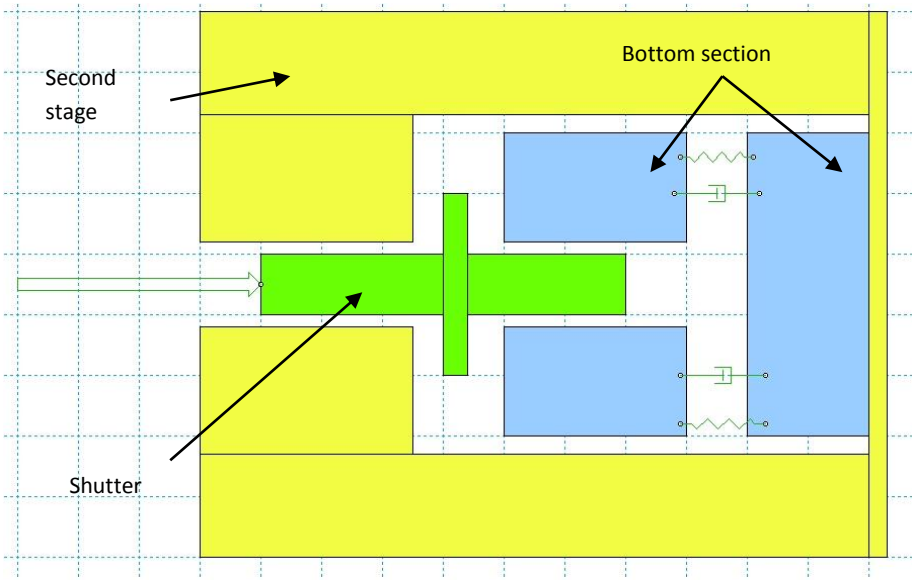

Fig. 4.70 - Scaled solution's scheme

The second solution (Fig. 4.71) is the new solution described in above, where the shutter is in an oblique position relative to the flux principal direction.

This system has 2 advantages:

- The concept of the system is simpler;
- There are less components;
- Higher fluid dynamic efficiency

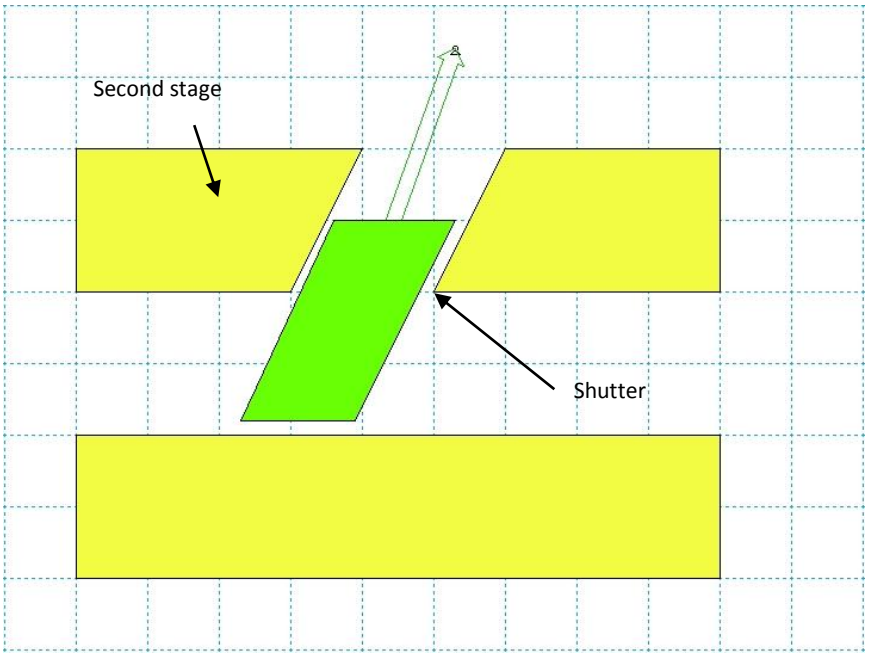

Fig. 4.71 - New solution scheme

The main negative aspect is the lack of experience for this solution, so it is impossible to foresee the complexity of the development phase and the reliability of the set up.
During the conceptual design a structural problem due to the geometric constraints was noticed (Fig. 4.72), this led to the abandon of the solution.

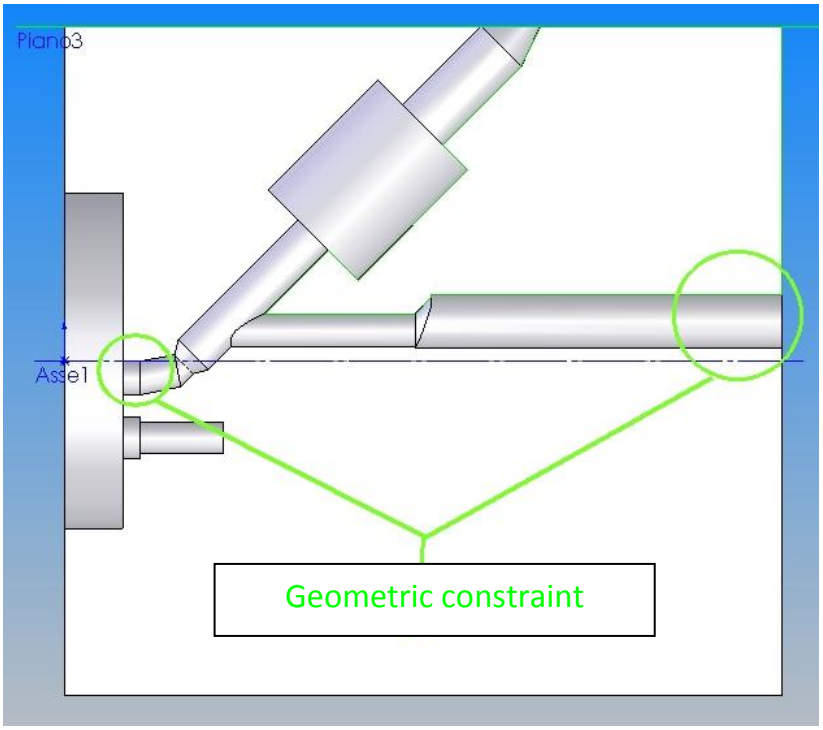

Fig. 4.72 - Second stage for the new solution

From Fig. 4.72 is visible that the different sections of the flux tube due to the geometric constrains will decrease the energy transfer efficiency from the pump tube to the launch tube. This solution will force to build the system in two parts, causing realization and safety problems, moreover the hosting of the damping system will be complicate.

For these reasons, the design is focused on the up-scaling of the actual solution.

The cad model is shown in Fig. 4.73, Fig. 4.74 and Fig. 4.75.
The pressure peak at 6000 bar (this is the maximum expected pressure) that the piston gives allow to open the shutter, this one is kept closed by the back pressure acting on the back area of the 'plate'.
It is 10 years that this solution is used, there is a long experience on it and is very reliable.

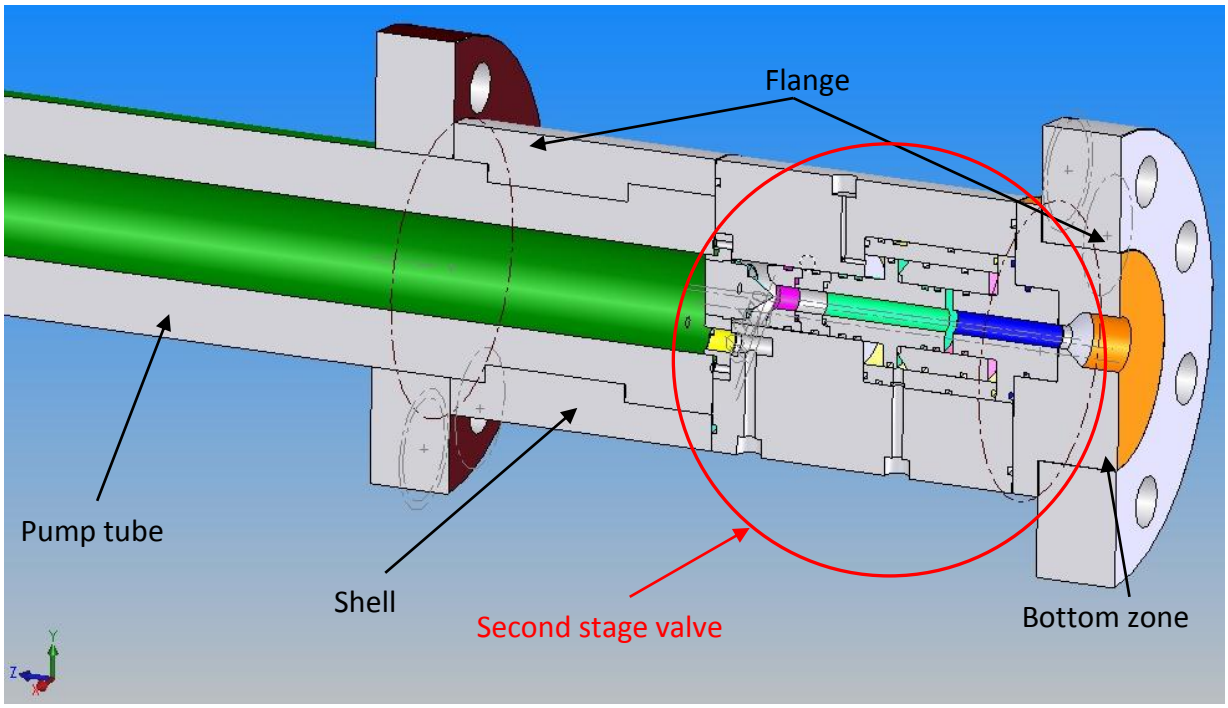

Fig. 4.73 - Overview of the scaled solution

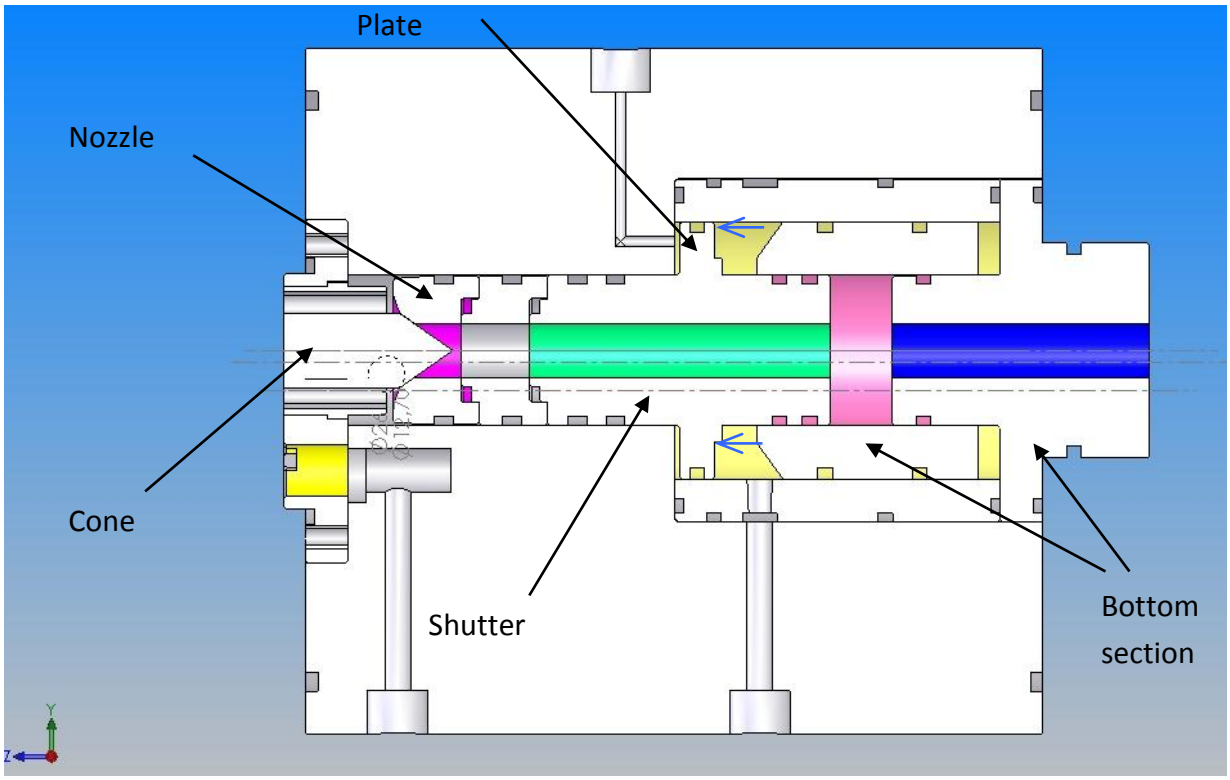

Fig. 4.74 - Closed valve (blue arrows show the action of the back pneumatic pressure)

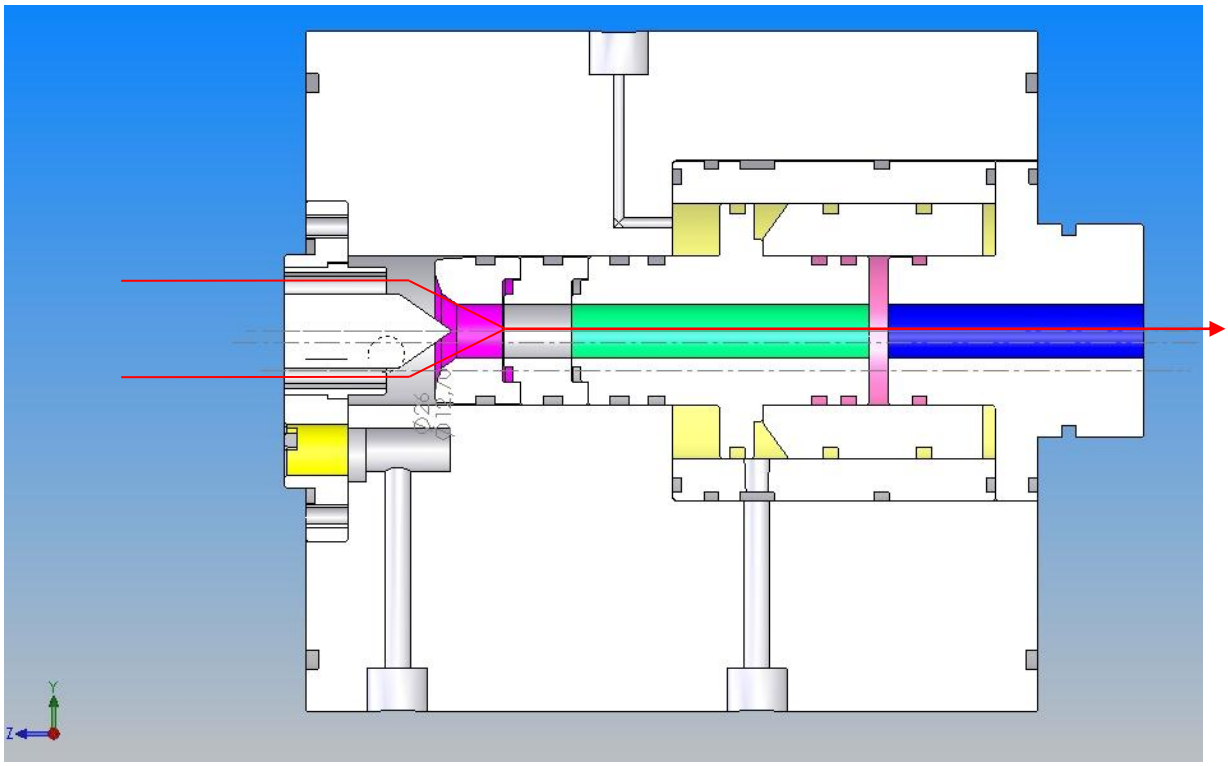

Fig. 4.75 - Open valve (red arrow show the path of the high pressure gas)

After the fluid dynamic simulation described before the design process followed this scheme:

1. Analysis of the damping system efficiency for the piston motion in the new light gas gun. This analysis is done with a zero-dimensional Simulink model. This analysis is mandatory to understand the overall behaviour of the system and allows to assess the risk of strike of the piston in the last part of the pump tube, which is in direct contact with the high pressure session.

2. Shutter mechanical analysis
   - Analytic model, for a preliminary evaluation of the structural strength;
   - Finite Element Analysis, for a detailed evaluation of the structural strength;
   - Dynamic Simulink model, to analyse the shutter motion inside the main valve and its interaction with the bottom zone;
   - 3-D model to do the mechanical drawings;

3. Realization of the 3-D models of the head group;
4. Screw and flange design;
5. FEM models of the terminal zone of the pump tube.

The 5 points are described hereinafter.

1. Analysis of the damping system efficiency.

   The overall layout of the two stages LGG is shown in Fig. 4.76.

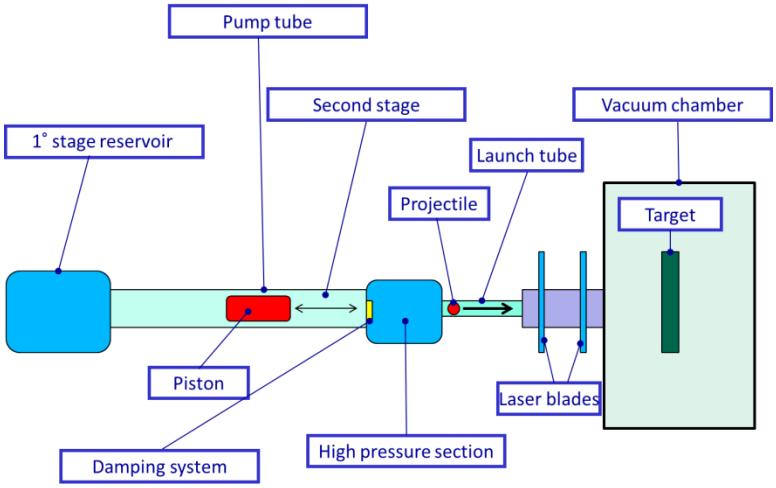

Fig. 4.76 – CISAS two stages LGG layout

The gas at high pressure in the first stage reservoir flows through a valve and the piston is accelerated. It compresses the gas in the second stage, that can be modelled as a second reservoir that changes its dimensions during the motion of the piston. The piston arrives close to the high pressure section, that delivers the thrust to the projectile, and to avoid strikes the damping system injects gas.
This system has to control the motion of the piston inside the pump tube and has to avoid the impact with the second stage during the second pressure peak.
The LGG Simulink model (Fig. 4.77) analyses the damping system efficiency and represents the whole pump tube and piston working principle (conceptual scheme is reported in Fig. 4.78), it evaluates pressure and temperature value up and down stream the piston's motion (zone 1 and 2).
This model gives also data about the damping system, it consists in the injection of pressurized gas to decrease the bounces of the piston inside the pump tube after the shutter's opening inside the valve, when the gas goes to the launch tube (Fig. 4.79).

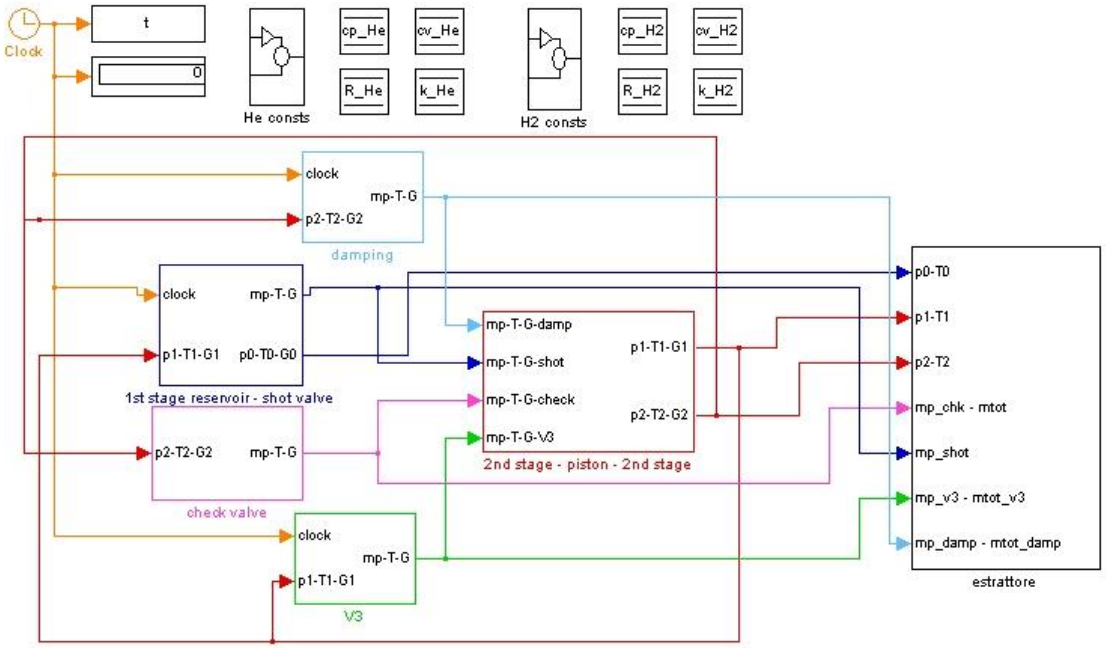

Fig. 4.77 - LGG Simulink model

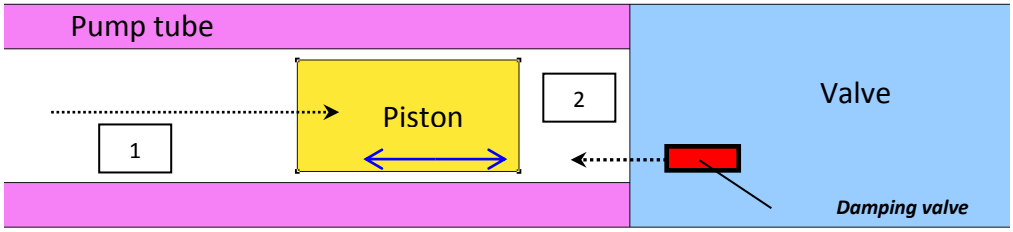

Fig. 4.78 - Piston-valve-damping valve system's scheme

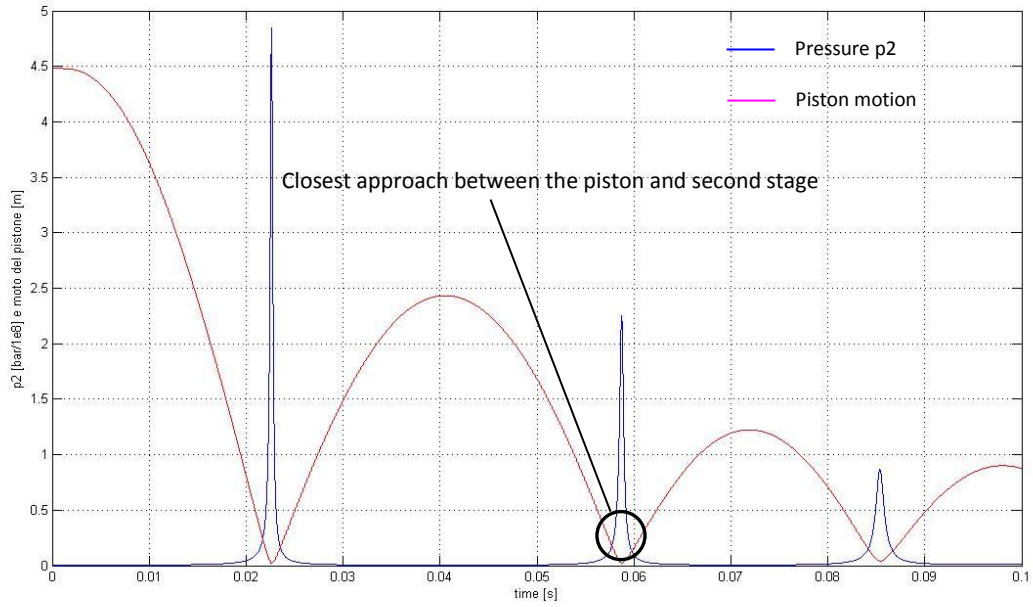

Fig. 4.79 - Pressure p2 in zone 2, compared with the piston's motion inside the pump tube

To evaluate the damping system efficiency the main parameters are modified step by step, from the actual configuration to the new one:

- Reservoir1 length: 0.35 m → 1.5785 m
- Stage reservoir, shot valve, electron valve, piston 2nd stage, reservoir1 diameter: deq= 35e-3 m → 60e-3 m
- Piston length: 50e-3 m → 60e-3 m
- Pressure in the first stage p_0= 120e5 Pa → 150e5 Pa
- Piston mass = 0.350 kg → 2.5 kg
- Reservoir 2 initial length = 2.980 m → 4.980 m
- Pressure H_2 = 2.9 bar → 4 bar
- Damping valves reservoir volume: 1.6 dm^3 → 3.2 $dm^{3,}$
- Shot valve clock (it is the time interval required to open the damping valve): 10e-3 s → 6e-3 s
- Check valve:
    - Diameter: Φ 10 mm
    - Diameter: Φ 15 mm

Testing different damping architectures (Tab. 4-7) allowed for the closest approach (clap) to be obtained, *i.e.* the minimum distance between the piston and the valve during the second pressure peak, this is a measure of the LGG limit.
The damping system efficiency is proportional to the quantity of injected gas, *i.e.* the mass flux. It is possible to increase this quantity acting both on the pressure used to inject the gas an on the diameter of the flux section. The solution with 3 valves has been chosen, it allows the best compromise between a safety damping for the structure and the geometric constrains due to the dimensions of the other components.

	Φ eq [mm]	Second peak min clap [m]
No damping	0	0.00782
1 valve	6	0.0132
2 valve	8.484	0.0191
3 valve	10.392	*0.0244*

Tab. 4-7. Simulated configuration for the damping system

Then the choking conditions are analysed, *i.e.* for which values of the injected mass the efficiency doesn't increase with the increasing of the injection pressure, because the channel is in sonic condition (

Tab. 4-8).

1 valve	**Φ eq=6mm**	**max mp_damp [kg/m^3]**	**p [bar]**
		0,028	50
		0,057	100
		0,078	140
		0,117	200
		0,175	300
		0,204	350
		0,233	400
		0,251	430
		0,263	450
		0,263	600
2 valve	**Φ eq=8,484mm**	0,110	100
3 valve	**Φ eq=10,392mm**	0,167	100

Tab. 4-8. Mass flow with different configurations

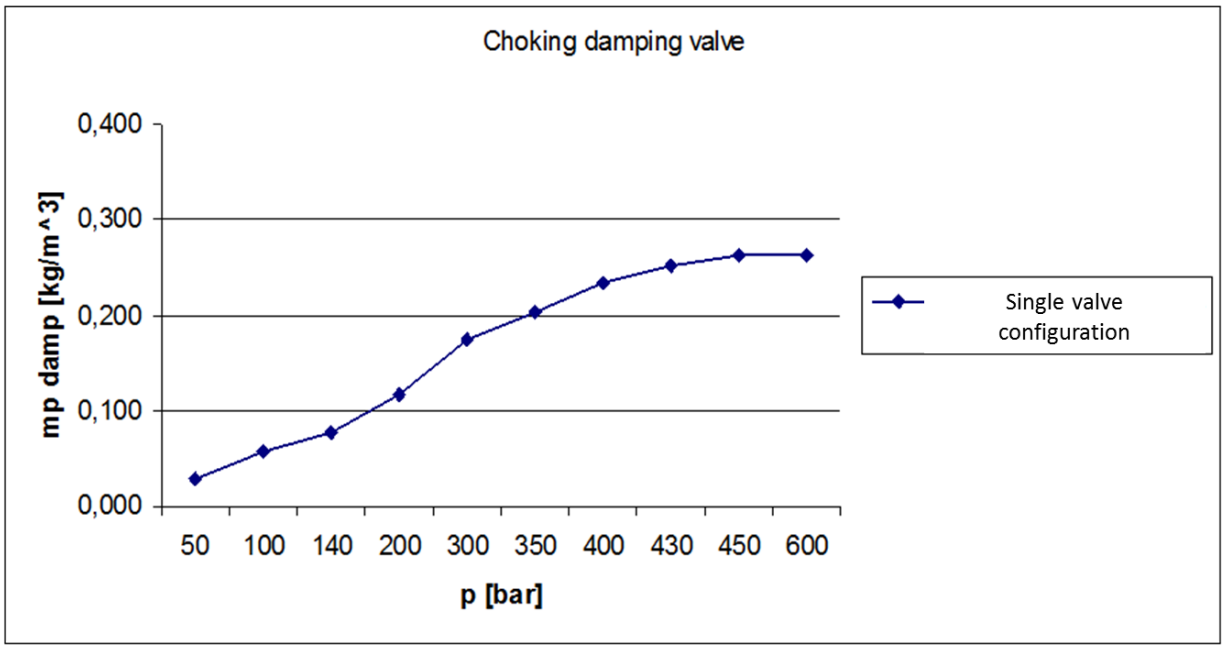

Fig. 4.80 - Mass flow – damping pressure trend

Results show that there is the choking for values higher than 450 bar (Fig. 4.80), these values are not possible with traditional tanks, limited to 150 bars.
So an operative pressure of 100 bar is chosen.

2. Shutter mechanical analysis

The shutter is the most critical component, due to the high strains it is subjected.
Structural models, analytical and FEM are built and the dynamic of the shutter

motion is studied to estimate the opening transient state and the dynamic load on the plate during the stopping phase, *i.e.*, a mechanic hit in the bottom section.

- Analytical model

Analytic model is used for a first design of the component, the limit is the use of equations for infinite length geometries and for unconstrained systems.

Three conceptual solutions are analysed, *i.e.*:

- Shutter made of maraging steel: as starting point the material with the best performances for this situation is chosen;

- Jacketed shutter: this is a solution that allow to reduce the component weight, it is made of two layer of titanium, combined with interference, in this way is possible to increase the mechanical properties, thanks to the pre-compression of the internal shell (Fig. 4.81).

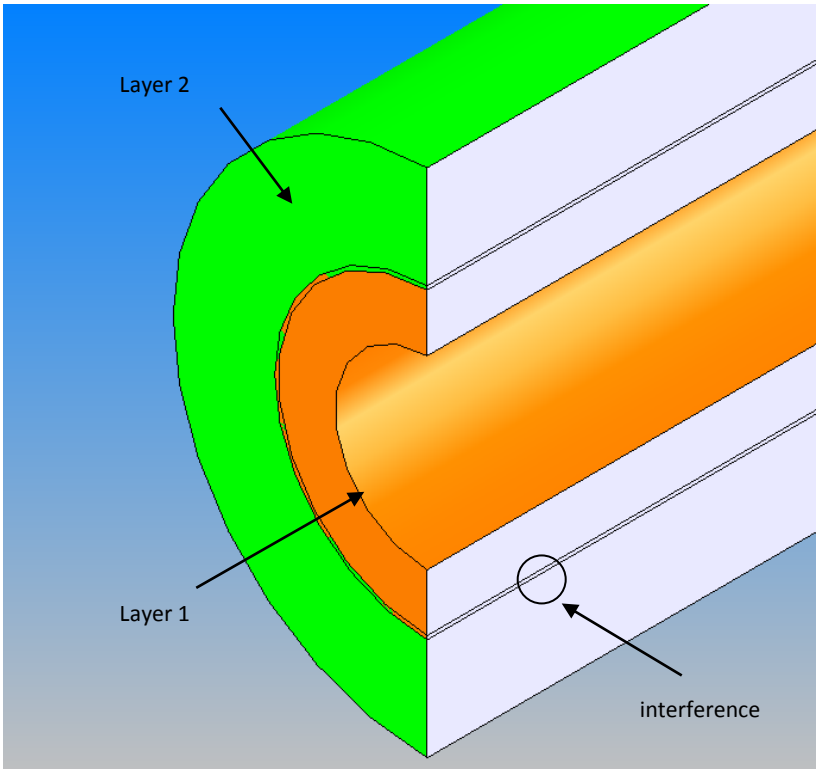

Fig. 4.81 - Section view of the jacketed shutter

- Titanium shutter: this solution is the better regarding the simplicity in the construction of the component.

The final shutter has the following characteristics:

- Internal diameter: 12.7 mm
- External diameter: 35 mm
- Material: Ti6Al4V
- Maximum operative pressure: 6000 bar

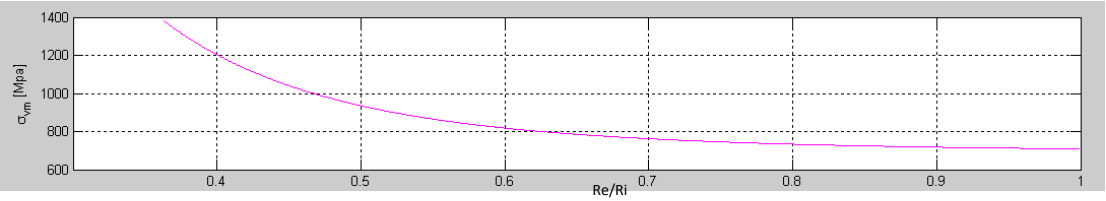

Fig. 4.82 - Von Mises sigma trend along the shutter radius

In Fig. 4.82 is visible that the shutter works at limit conditions for 40% of its thickness (safety factor less than 1), nevertheless this is tolerated because the maximum pressure foreseen for only a little percentage of the total shots, moreover to the structural properties cooperate also local plasticity phenomena that take part in the overcoming of the threshold value.

The shutter is also designed with a 'fail safe' logic: after a number of tests that depend on the shot condition, the component is replaced.

- Finite Element Model (Ansys 11.0)

The free type mesh (Fig. 4.83) uses brick elements (SOLID45), with the following characteristics: 97204 nodes and 501438 elements.

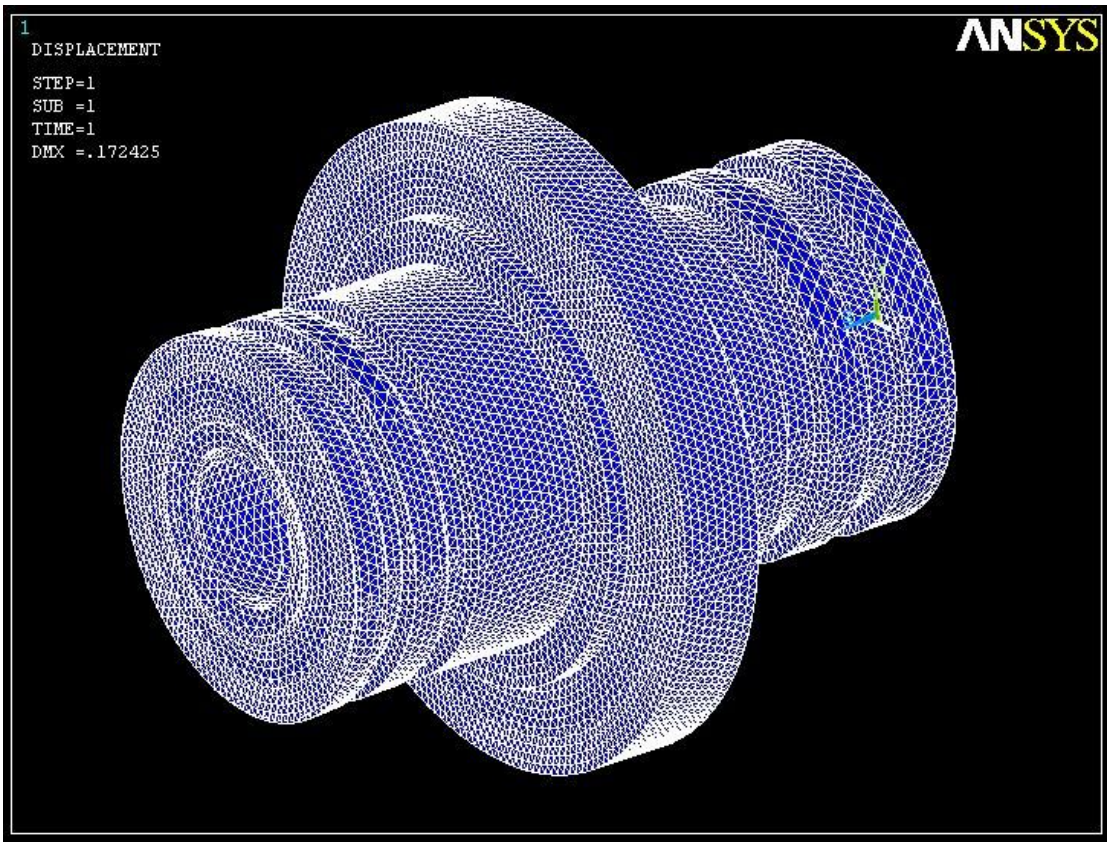

Fig. 4.83 - Shutter mesh

The motion along the longitudinal axis has a constraint on the back surface of the plate (Fig. 4.84), on all the internal surface of the tube there is a load condition of 6000 bar.

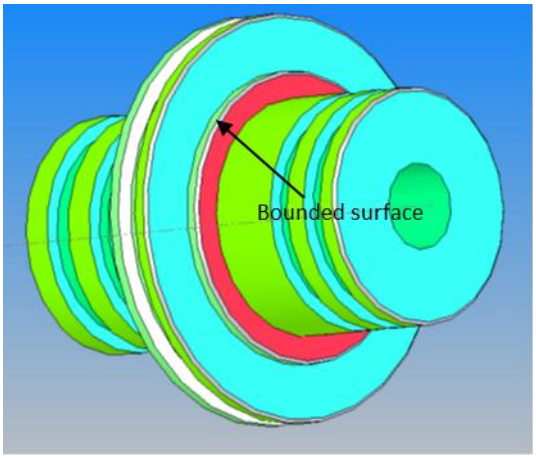

Fig. 4.84 - Constrains of the FEM model

The plot of the maximum Von Mises sigma gives values a little bit higher than the one of the analytical model (Fig. 4.85 and Fig. 4.86):

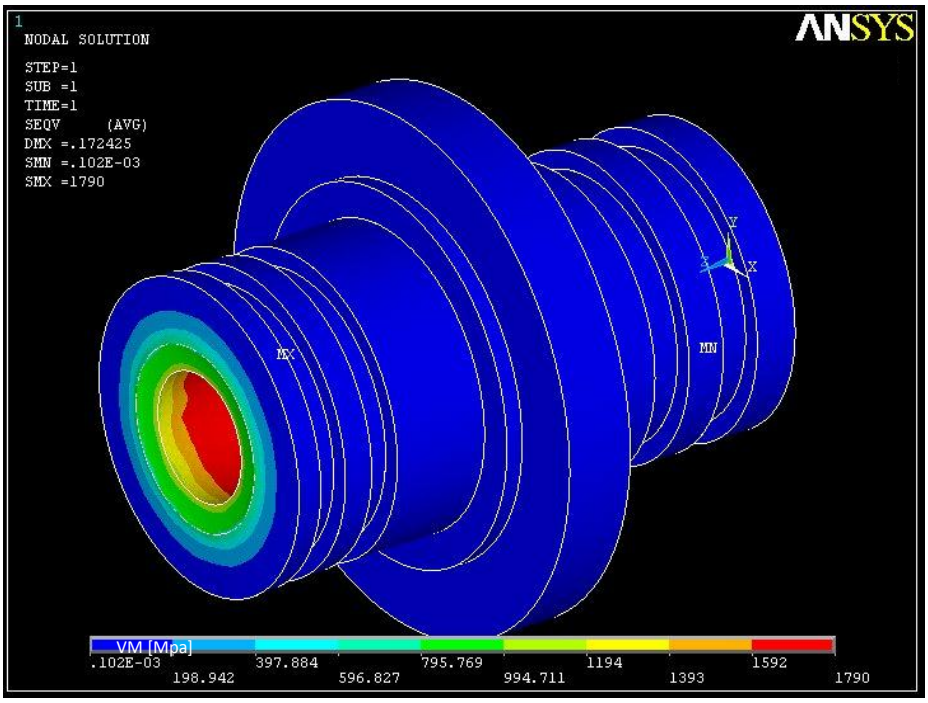

Fig. 4.85 - Von Mises sigma

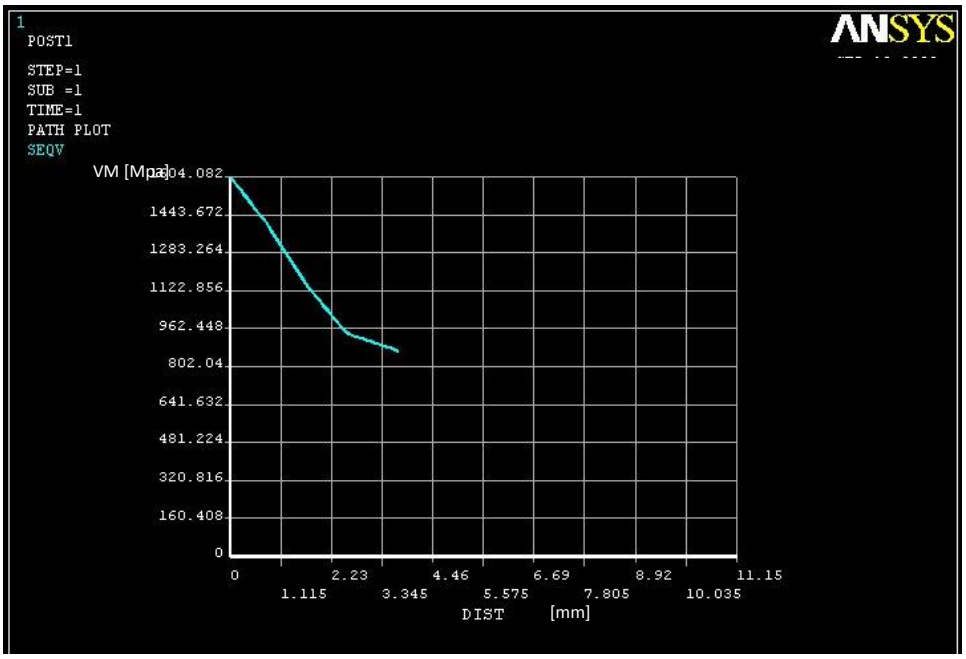

Fig. 4.86 - Von Mises sigma trend along the radius of the internal shell

- Dynamic model

To analyse the shutter motion dynamic inside the valve a Simulink model is used (Fig. 4.87), it allows to evaluate the shutter motion and the interaction with the mobile part of the back zone.

It is analysed also the effect of the inertia on the opening time of the system, the effect of the back pressure on the plate with its area, the mass of the mobile part of the back zone and of the interjected material between the mobile and the fixed part of the back zone, that can be assimilated to a mass-spring-damper system (Fig. 4.88).

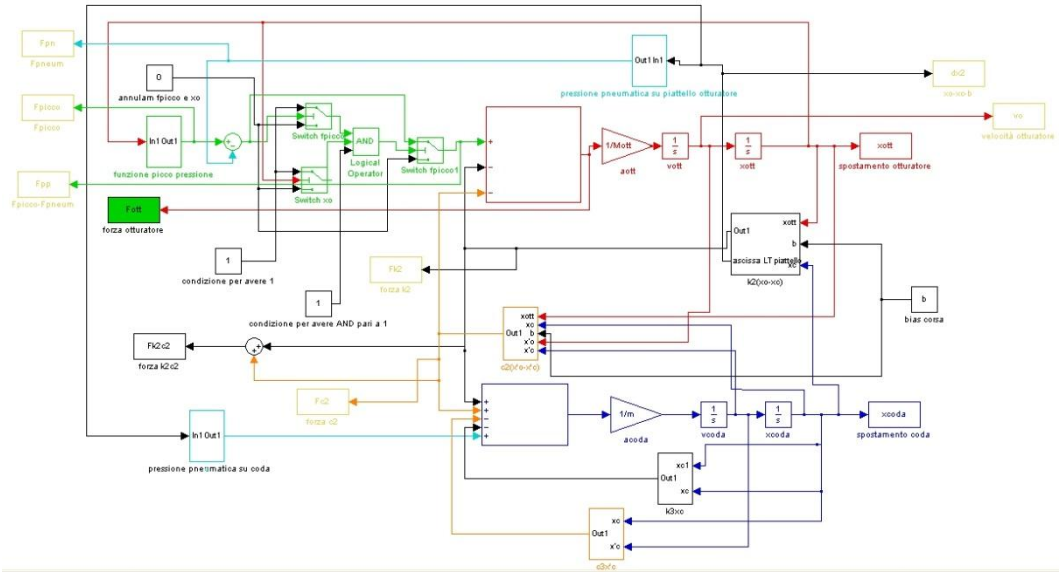

Fig. 4.87 - Simulink model of the shutter and back zone

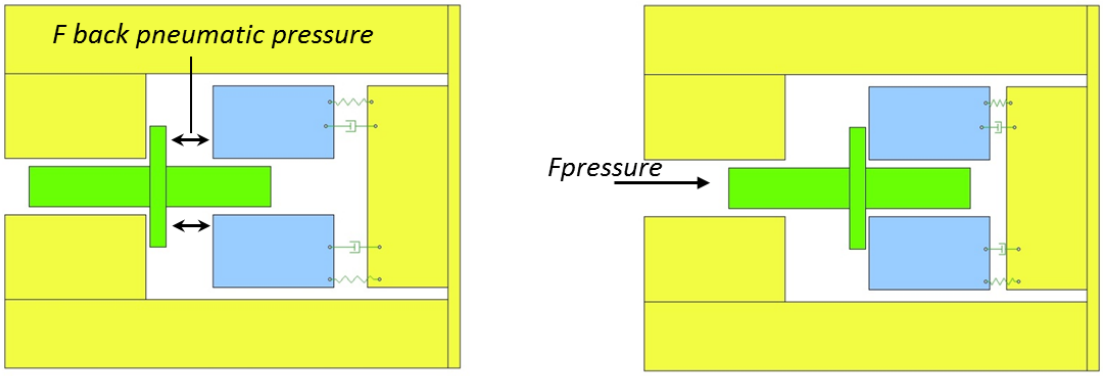

Fig. 4.88 - Shutter scheme in open and close configuration

The results of the calibrated model are plotted in Fig. 4.89, they take in account the damping effect due to the mobile part of the back zone (in the plot dx2 is the relative displacement between the shutter and the back zone).
It is visible that there is maximum displacement in correspondence of the pressure peak (Fig. 4.90).

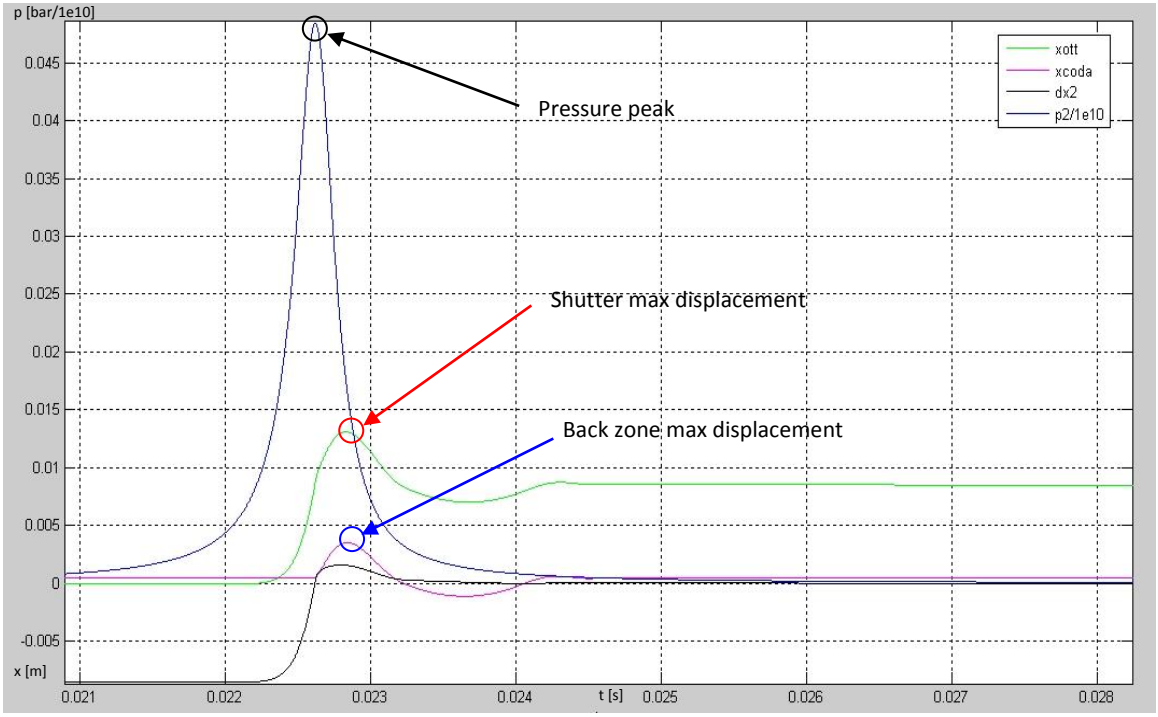

Fig. 4.89 - Shutter displacement (xott) , back zone displacement (x back zone), relative displacement (dx2) and pressure trend (p2/1e10)

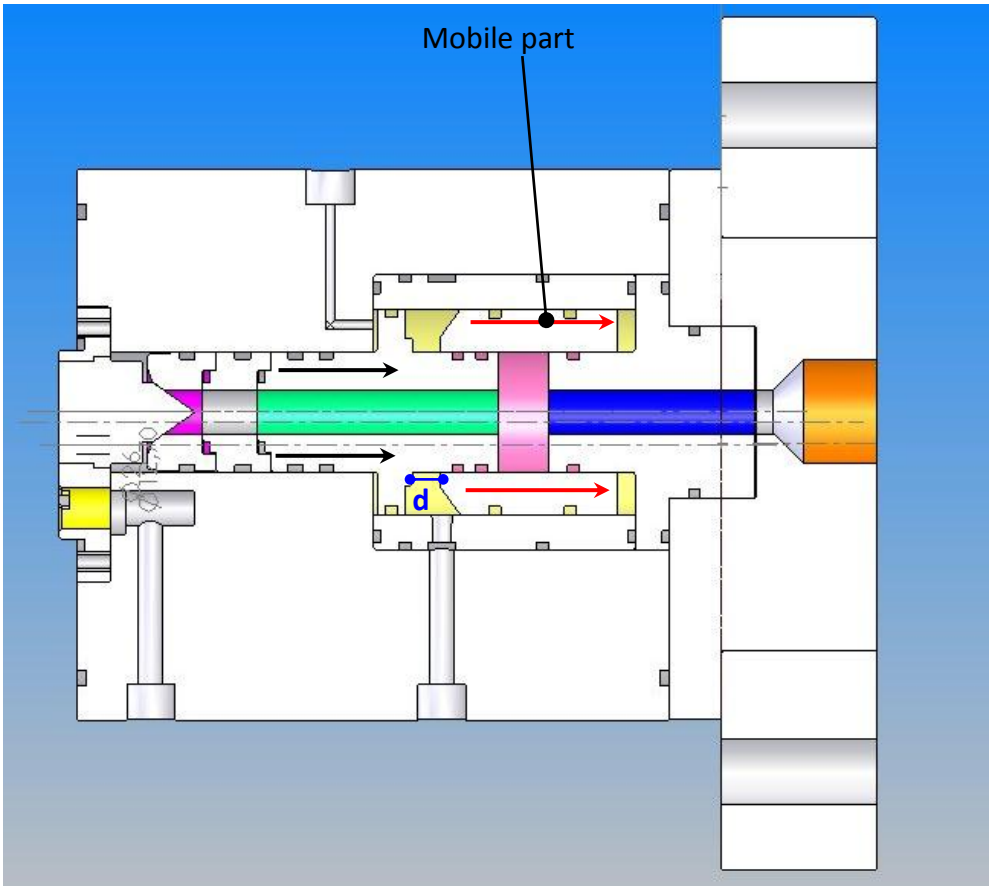

Fig. 4.90 - Section view

- 3-D solid model

The final 3-D model is created with the software SolidWorks (Fig. 4.91).

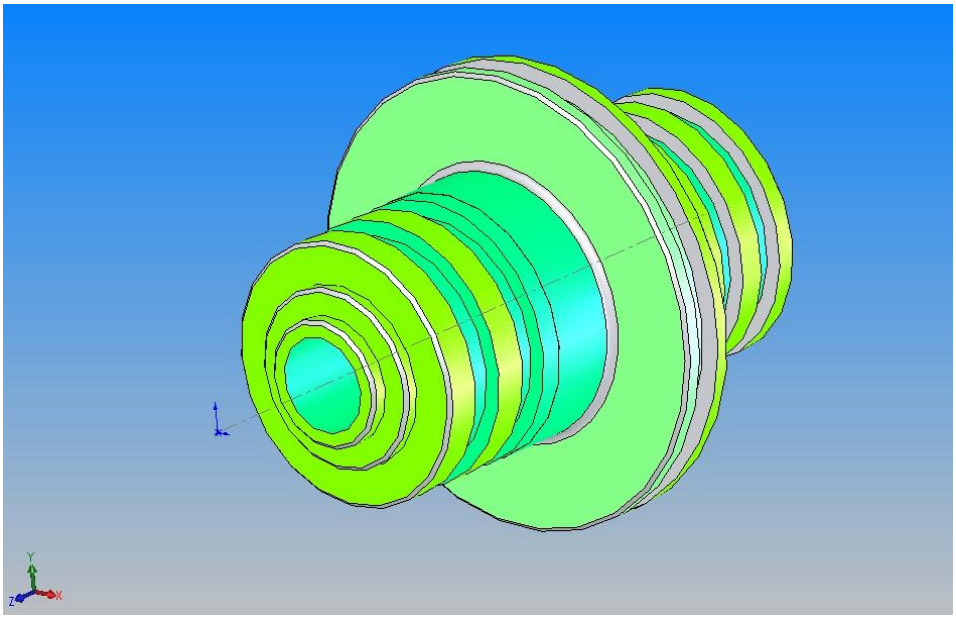

Fig. 4.91 - Shutter 3-D model

3. 3-D models of second stage components

The main second stage components 3-D models are shown in Fig. 4.92. All the parts are designed as a scaling of components with a long experience of use and taking in account the new problems caused by the increase of the dimensions.

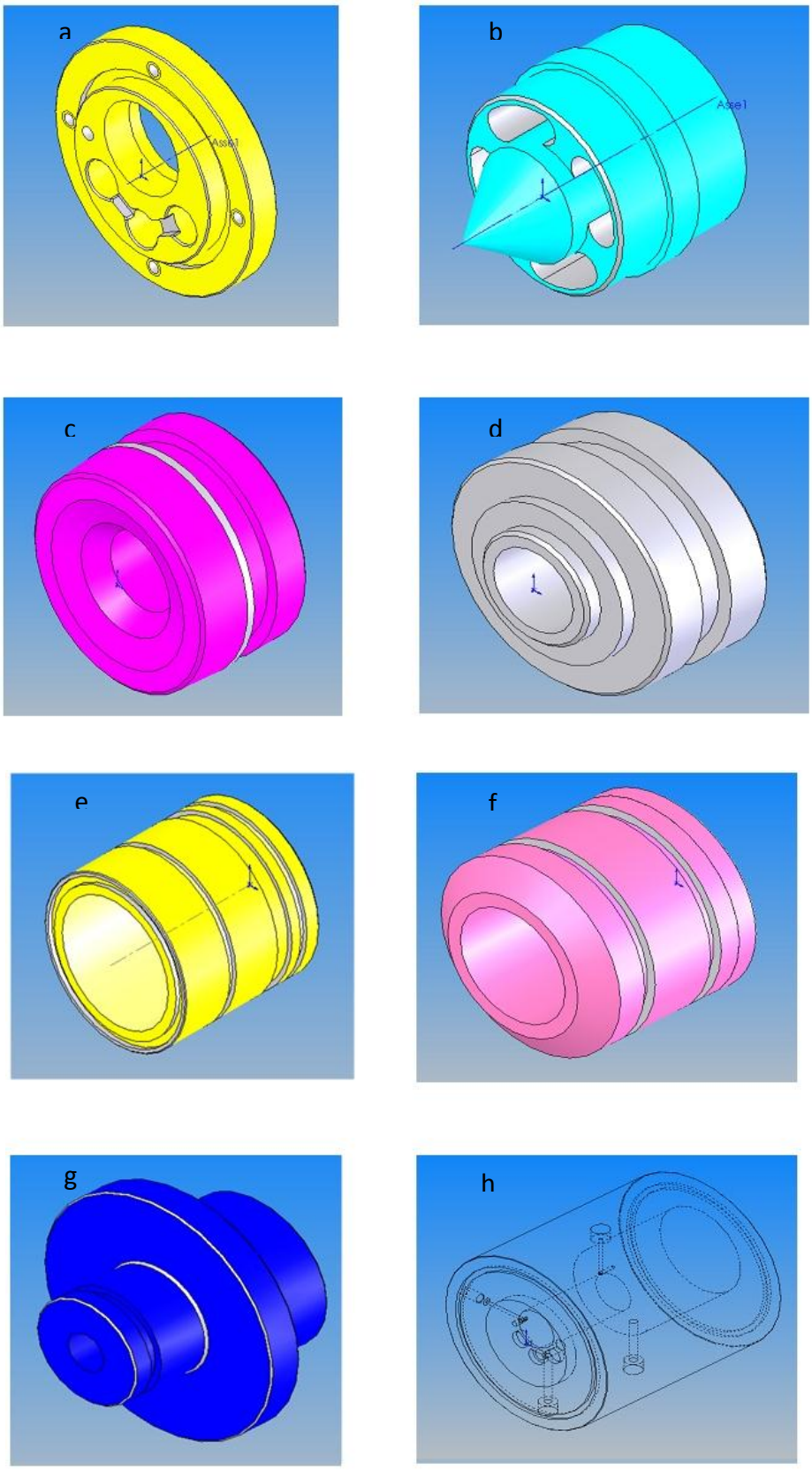

Fig. 4.92 – Second stage valve components: a- Pump tube interface ; b- Cone ; c- Nozzle ; d- Extension ; e- Case ; f- Back zone A ; g- Back zone B ; h- Second stage case

Fig. 4.93 shows an overview of the main components described before.

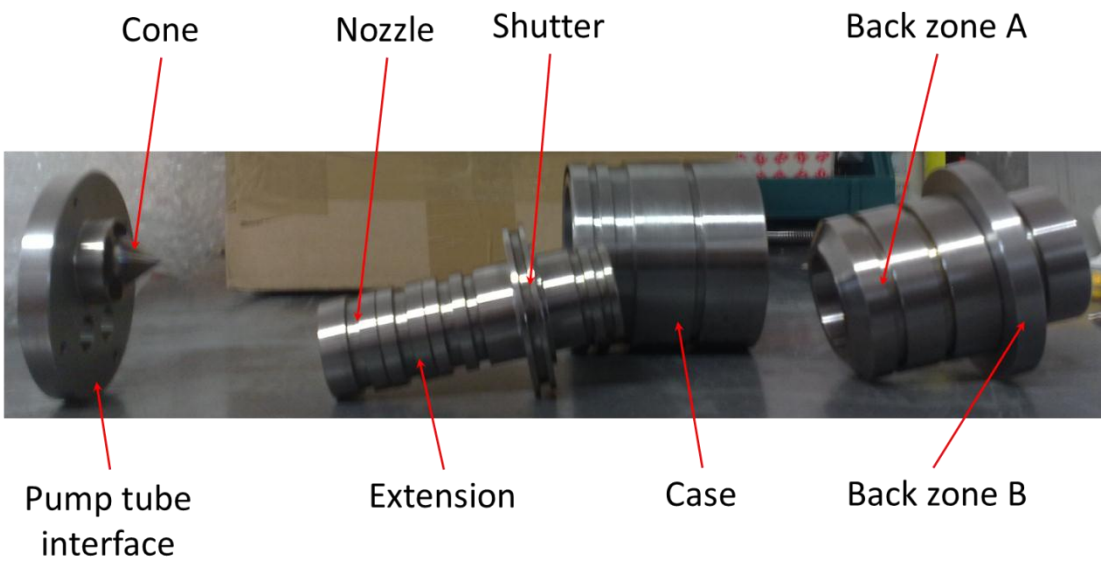

Fig. 4.93 – Overview of the high pressure section's components for the CISAS two stages LGG

4. Screw and flange design

The design of the system to connect the pump tube to the second stage is done with an analytic model implemented by Microsoft Excel.
An additional analysis of the flange is done with an Ansys FE model (Fig. 4.94 and Fig. 4.95) to have a better assessment of the risks, using a scheme nearer to the real situation.

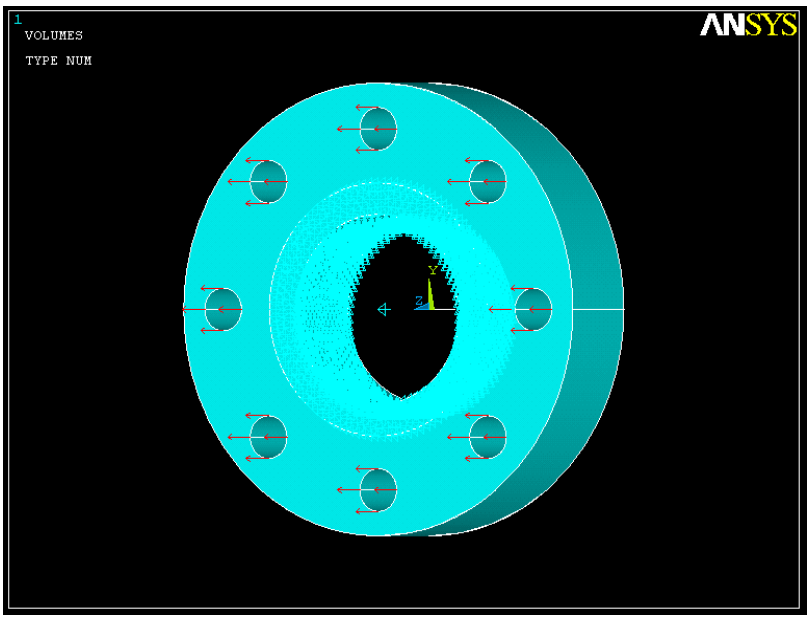

Fig. 4.94 - Flange's FEM with loads and constrains

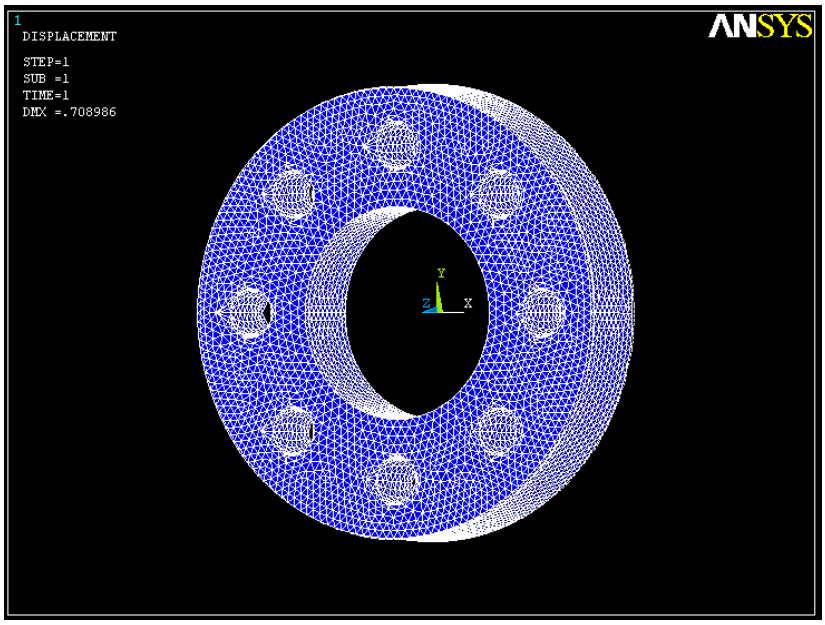

Fig. 4.95 - Flange FEM mesh

The Von Mises sigma trend is plotted in Fig. 4.96 and Fig. 4.97:

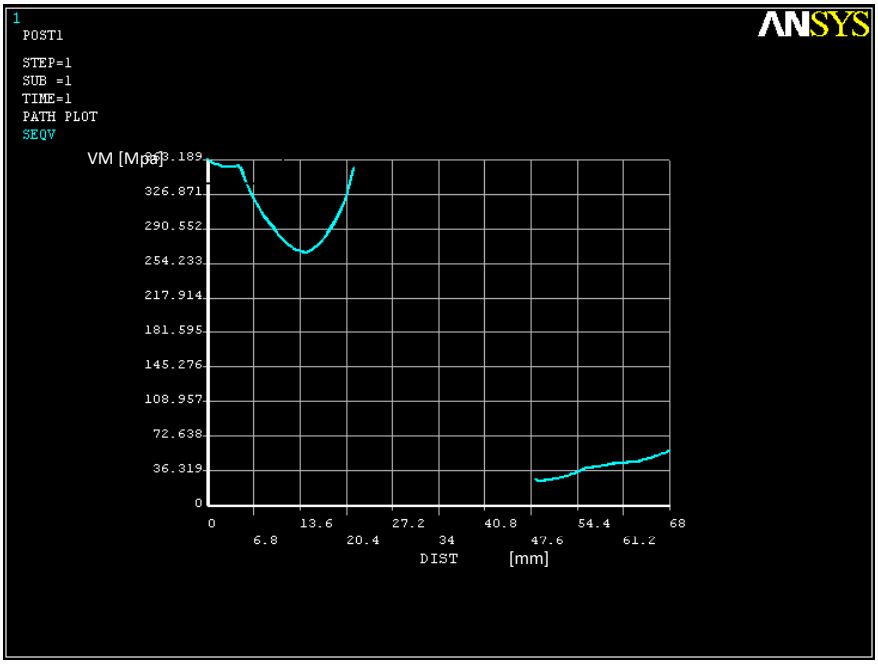

Fig. 4.96 - Von Mises sigma trend along the radius

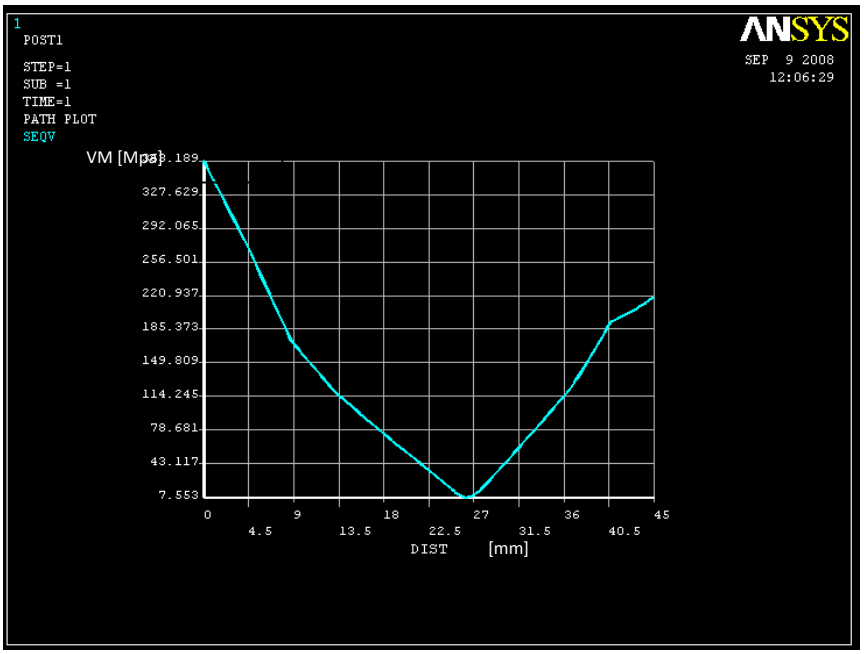

Fig. 4.97 - Von Mises sigma trend along the thickness

From the previous graphs is visible that the highest sigma value are only along the first 4 mm of the diameter, the whole structure can withstand the maximum expected loads, during the pressure peak of 6000 bar.
It is used a C50 steel with a safety factor of 1.4.

5. FE models of the terminal zone of the pump tube

The development of an analytical and FE model of the pump tube shows that the terminal zone of the pump tube can't resist to the limit conditions caused by the peak pressure during the shot phase (Fig. 4.98).

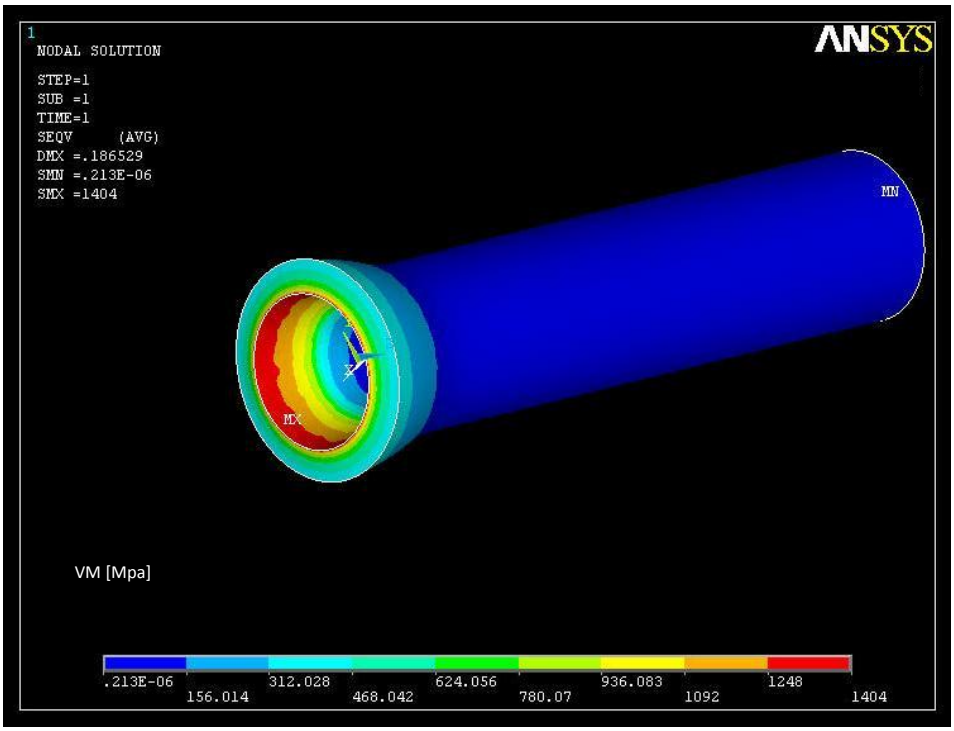

Fig. 4.98 - Von Mises sigma trend in the pump tube

To avoid this problem a double half-shell has been designed with an analytical and FE model (Fig. 4.99 and Fig. 4.100) jacketed to the terminal zone (Fig. 4.103).

This building technique allows the structure to resist to the loads in the terminal zone, where the piston stops his motion, compressing the gas that acts the shutter.

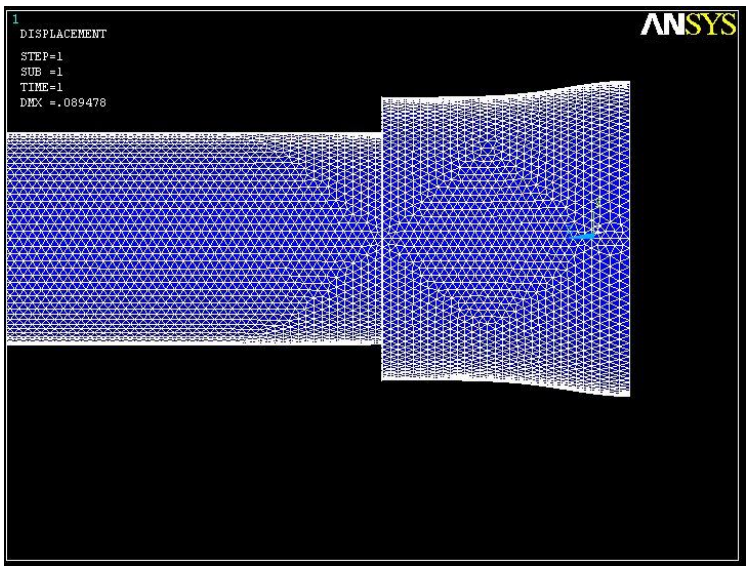

Fig. 4.99 - FEM's mesh of the system made by the pump tube and the shell, deformed after the action of the load

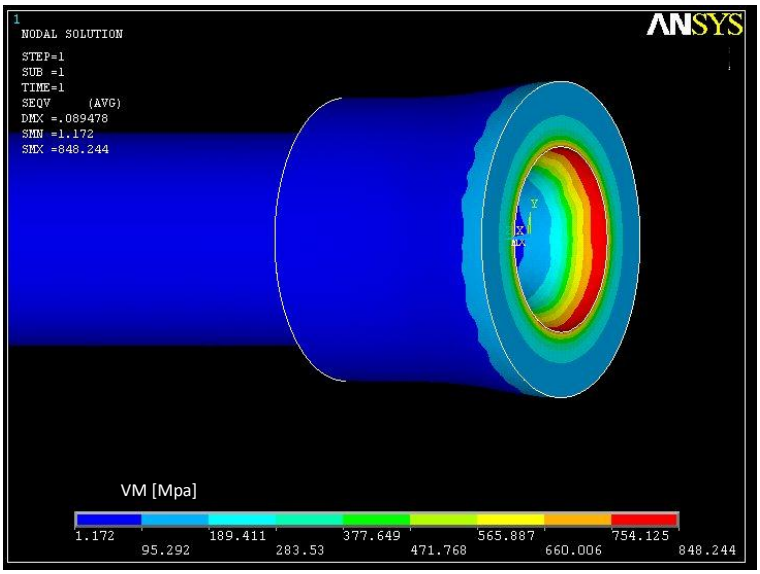

Fig. 4.100 - Von Mises sigma along the terminal zone of the jacketed pump tube

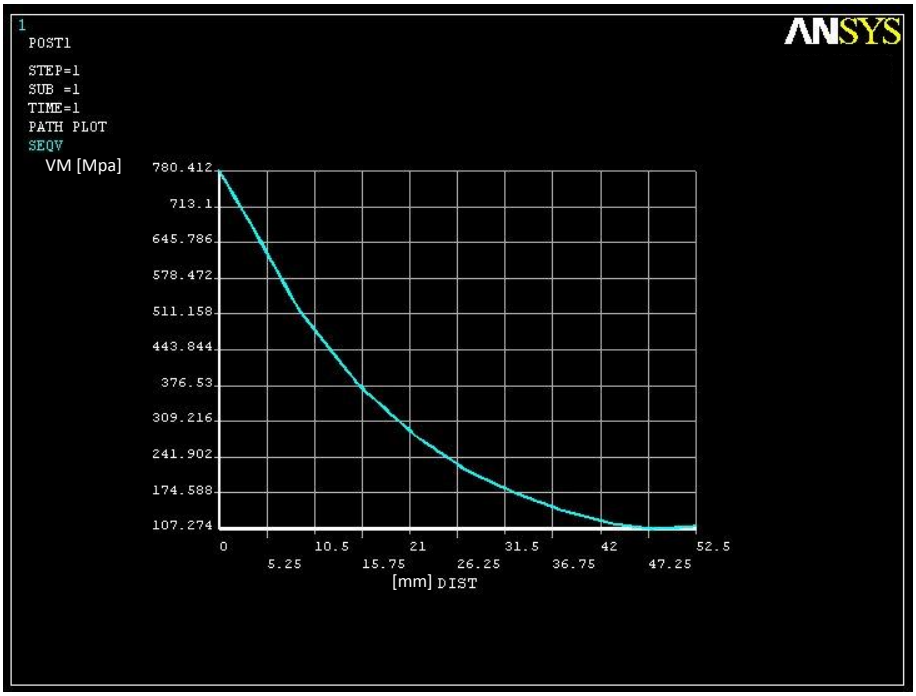

Fig. 4.101 - Von Mises sigma trend along the radius of the terminal zone of the jacketed pump tube

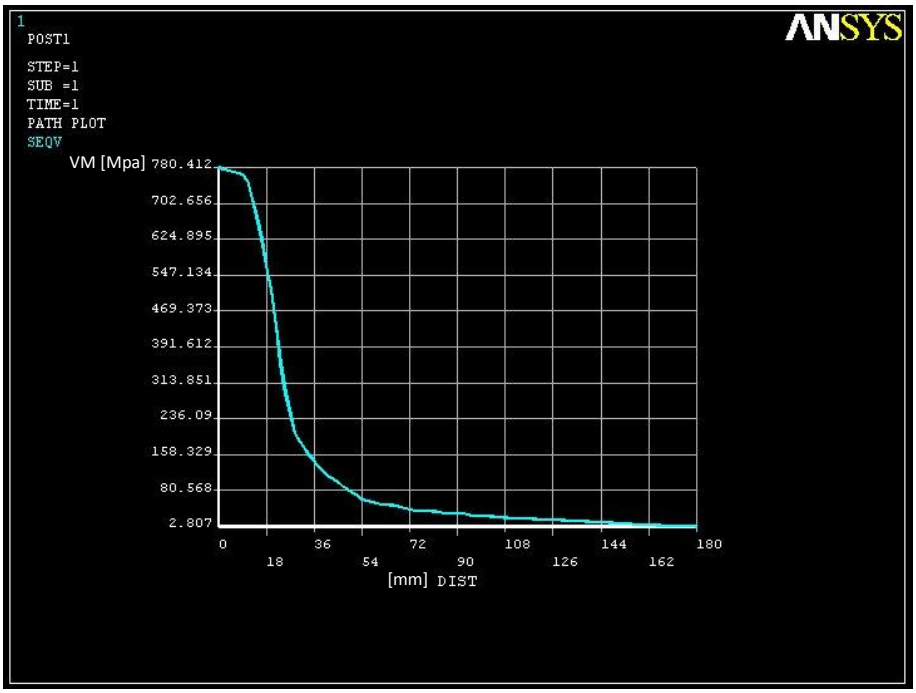

Fig. 4.102 - Von Mises sigma trend along the thickness of the terminal zone of the jacketed pump tube

Previous graphs (Fig. 4.101 and Fig. 4.102) show that there is a critic situation for the first 5 mm of the radius of the pump tube and along the first 15 mm of the length. This solution allows to withstand the maximum expected load.

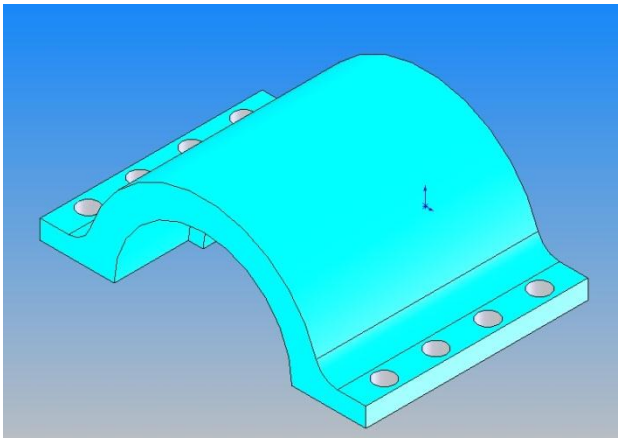

Fig. 4.103 - Shell to jacketed the pump tube

4.2.3.3 Support structure analysis

A 3-D model of the structure is realized with Femap software (Fig. 4.104), then a FEM analysis is done with MSC Nastran 2004 software.

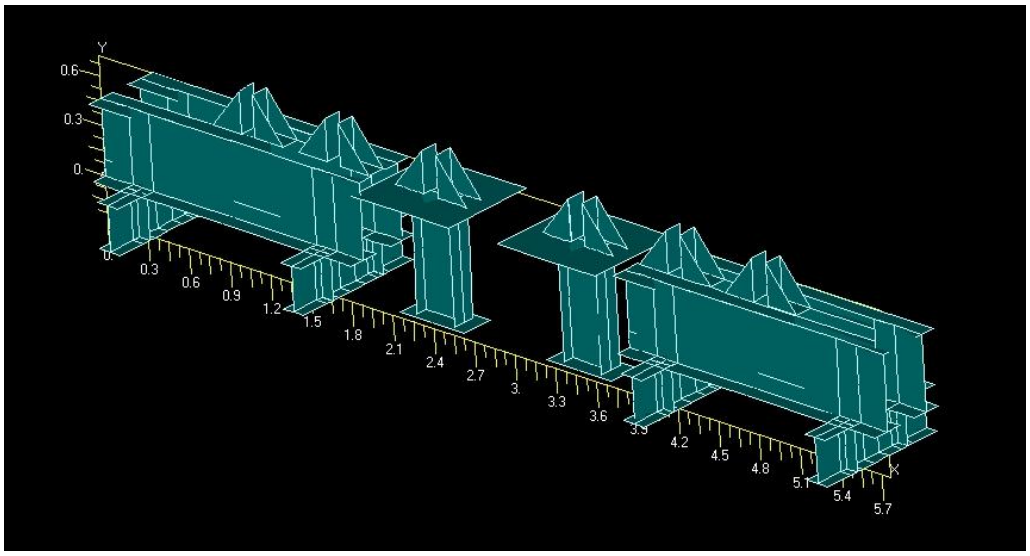

Fig. 4.104 - Support structural 3-D model

The different parts of the structure are simulate with the following type of elements (Fig. 4.105 - Element type, constraints and load of the structure supports FEM model):

- Plates: Plate (50 mm)
- Pump tube: Beam
- Reservoir and second stage valve: Mass

The reservoir is linked with the plates with element of rigid type. The structure is bounded to the ground with screws that are simulated with constraints of fixed type.

To do a static analysis a force of 1425497 N (equal to the one created by the pressure peak) is apply to the node corresponding to the second stage valve.

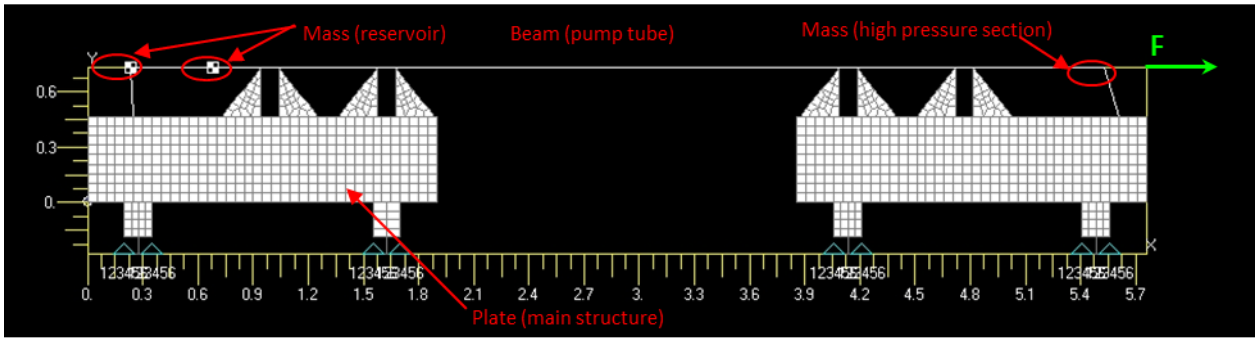

Fig. 4.105 - Element type, constraints and load of the structure supports FEM model

The simulations show (Fig. 4.106 and Fig. 4.107) that the maximum value of the Von Mises sigma is at the base of the structure.

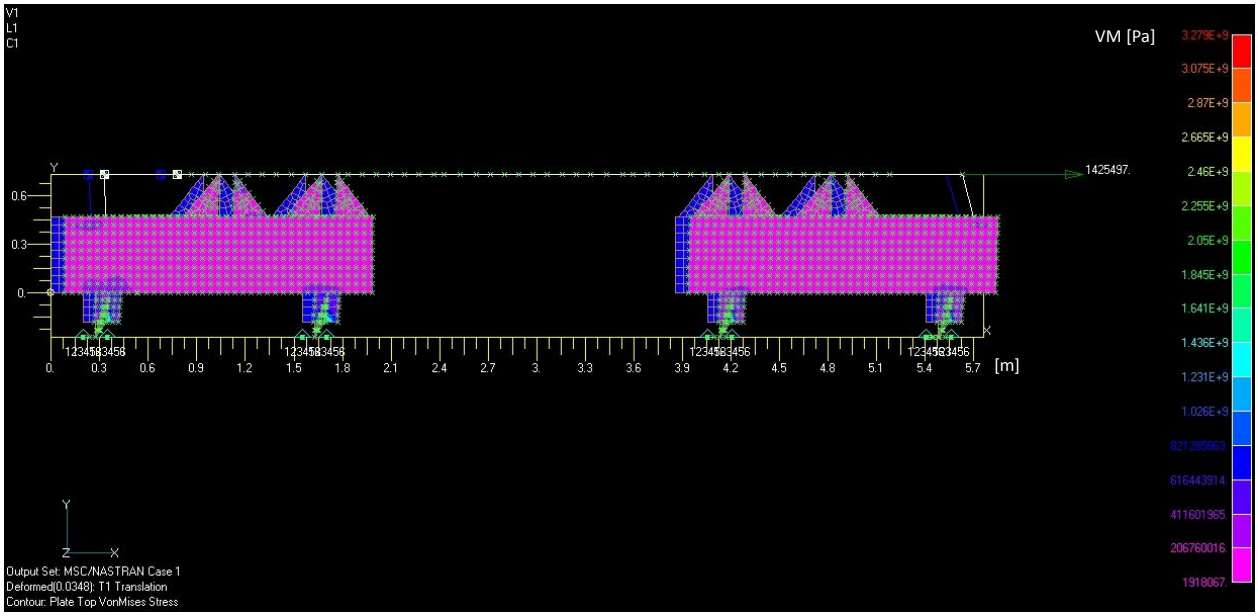

Fig. 4.106 - Von Mises sigma plot on the structure support

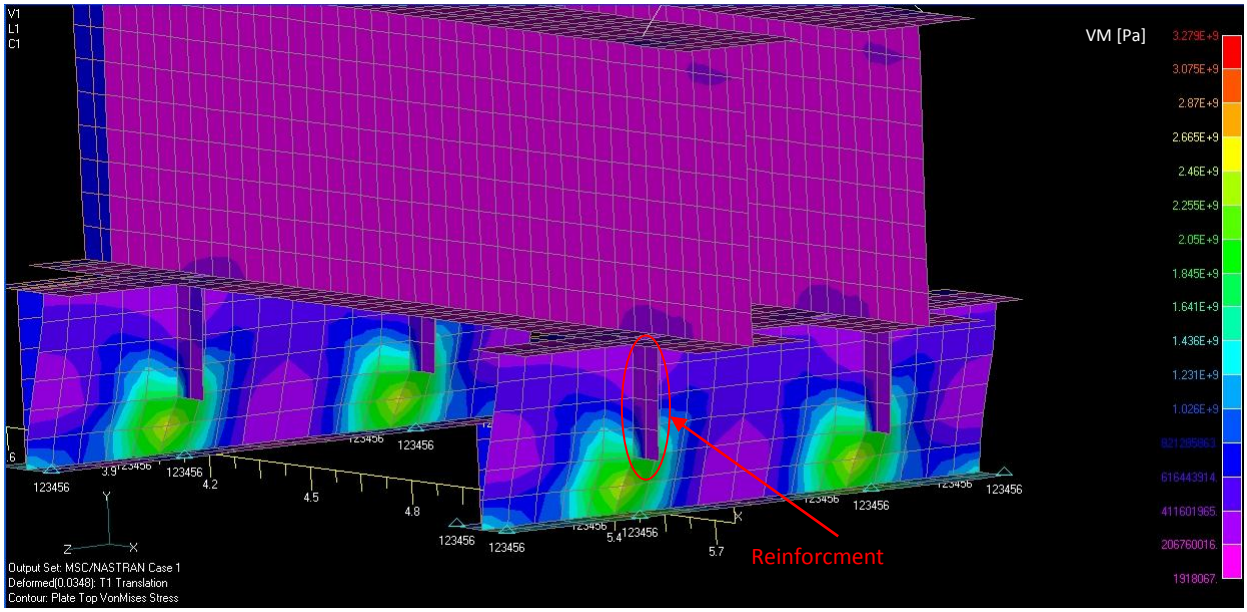

Fig. 4.107 - Detail of the Von Mises sigma plot on the structure support

Fig. 4.108 shows a photo of the supporting structure in the laboratory and of the new two stages LGG in the assembly phase.

Fig. 4.108 – LGG's supporting structure (left) and the new two stages LGG in the assembly phase (right).

4.3 Laboratory instrumentation for ejecta's effects and momentum measurement

This paragraph describes laboratory instrumentation and a method for evaluating the average properties of ejecta clouds produced by hypervelocity impacts on spacecraft external surfaces. In particular, the design, realization and preliminary testing of an instrument for assessing the speed, size and distribution of fragments is presented together with a numerical procedure to derive the requested information from experimental data. ([26])

The instrument is made by a supporting structure where there are targets representing spacecraft materials and an ejecta-evaluation assembly made by a copper witness plate coupled with appropriate sensors that estimate the momentum transmitted to the plate itself.
The procedure for deriving ejecta properties uses the information provided by the instrument and empirical equations available in the technical literature relating the ejecta total mass and the craters size to the impact conditions. A simplified Montecarlo procedure was also implemented to estimate the overall method uncertainty, which is mainly related to the accuracy of the empirical equations.
Results for a sample experiment on an aluminium bumper are reported in terms of total ejecta mass, average size and speed of the ejecta particles and total number of fragments. Moreover it is confirmed that the instrument and outlined procedure are able to successfully assess the fragments average speed and size, down to particles of 0.1 mm in diameter with reasonable accuracy.

These first results are the starting point for further evolution of the instrument that is described in the following paragraphs.

4.3.1 Ejecta instrument prototype

To set the instrument requirements, a reference model of the ejecta process was considered, following the one proposed by Seguier and Mandeville. The total mass of back-scattered fragments is divided into three contributions: cone, spall and jetting.
Only normal impacts were considered, jetting is negligible in most situations.

In this technological application the primary requirement for the instrumentation is to assess the total amount of ejecta and possibly the average size and speed of the fragments, while the mass distribution among the three classes (cone, spall and jetting) is of secondary importance.
The second requirement for the instrumentation is the ease of integration and operation and a low level of complexity for mechanical and electrical interfaces. This was due to the need to perform the tests as add-on to other experiments.

Two passive solutions were analysed: the first one consists on a collector (catcher) in which ejecta particles are trapped and could then be retrieved. The second option is a metallic witness plate on which a crater pattern is produced by impact of ejecta fragments. Both the catcher and the witness plate should be placed at close distance in front of the target and may be split in sectors to assess the ejecta amount as a function of the angular distance from the projectile's flight path.

In addition to these solutions, which provide off-line information, the option of using a more detailed characterization of the particle distribution in terms of size, velocity and direction of flight was kept open.

An instrument able to provide two different types of data was designed:

1. Off-line information come from direct recovery of fragments from a soft catcher or from inspection of the witness plates;
2. On-line information result from suitable sensors that measure the load transmitted by the fragments cloud to the passive catcher or witness plate. It was also considered the option of evaluating the ejecta cloud average speed using the same photo-detectors employed for measuring the velocity of the LGG projectiles.

4.3.1.1 Off-line measurements

As stated before the starting points for the instrument design were a simple passive particle collector and a metallic witness plate. The supporting structure was designed to locate both components ahead the target and to protect them from gas load and unlikely sabot failures (Fig. 4.109).

The main difference between the two solutions is that catchers made by soft material (*e.g.* low density foams) in principle allow the recovery of almost intact fragments, while witness plates give only indirect information on ejecta properties based upon the characteristics of the resulting impact craters (Fig. 4.110). On the other hand, catchers require long manual operations to retrieve particles, witness plates instead can be analysed automatically with suitable imaging systems.

To discriminate between the two choices, few impact experiments were conducted to evaluate the behaviour of different catchers made of low density foams for industrial application such as thermal and acoustic insulation. Aerogel was not considered because of the high cost and other issues related to its safe handling. Because of the extremely brittle nature of the foams, results were not satisfactory: ejecta fragments contributed to the global collapse of the catcher structure at every impact condition and recovery of fragments was not possible.

It was decided to employ metallic (copper) witness plates for the experimental activity. Useful information was retrieved by automatic analysis of the witness plate crater patterns performed with a dedicated image analysis procedure. Such software was developed in the past within the CISAS Hypervelocity Impact Laboratory and allows the evaluation of the total crater area together with the extent of the largest craters on the plate.

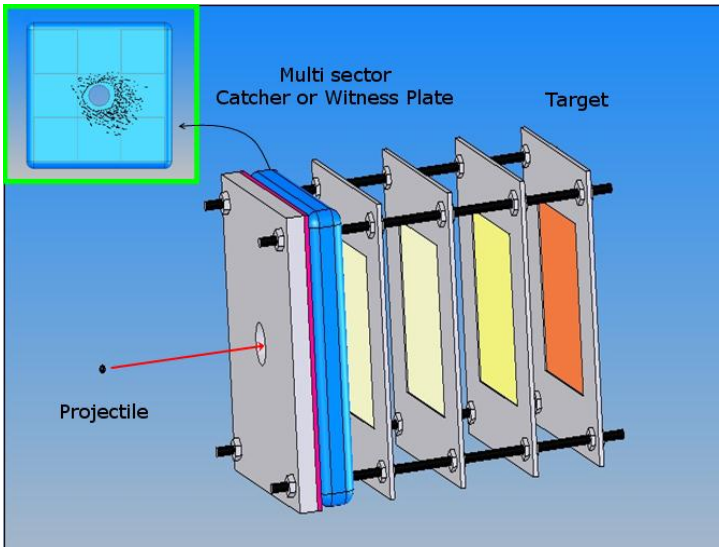

Fig. 4.109 - Ejecta collector schematic.

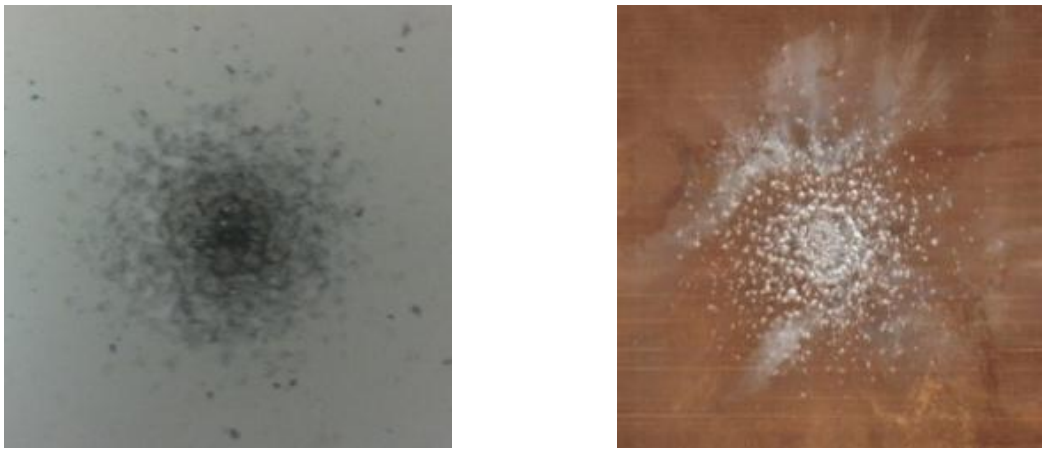

Fig. 4.110 - (a) Ejecta catcher: low density foam; (b) Witness plate

4.3.1.2 On-line measurements

To measure the load transmitted by the ejecta cloud to the structure, it was considered the option of coupling a thin PVDF (polyvinylidene fluoride) film to the witness plate rear surface, the one not hit by ejecta, as shown in Fig. 4.111. PVDF is a permanently polarized piezoelectric polymer able to provide charge signals related to the component deformation. It is available at relatively low cost and large area thin films can be easily cut in different sizes and shapes. Past experiments show that the magnitude of the electric signal produced by the impact of a single particle on PVDF depends upon the kinetic energy and the area affected by the shock. In particular, sensor charge is proportional to $m^a v^b$ where m and v are particle mass and velocity, while a and b are coefficients that derive from calibration. In this application several particles within the ejecta cloud continuously hit the sensor over a finite period of time and hence average information on ejecta fragments is contained in the time integral of PVDF signal rather than in its peak value. In fact, PVDF signal is dependent from the load transferred by the cloud to the witness plate and the signal integral is then related to the overall ejecta momentum, *i.e.* total mass and average speed.

Moreover, the assessment of the ejecta cloud tip speed was made possible by using photo-detectors already available into the LGG impact chamber (Fig. 4.112). The photo-detectors can resolve the time interval from the primary impact of the projectile on the target to the secondary strike of the fastest ejecta fragment on the witness plate.

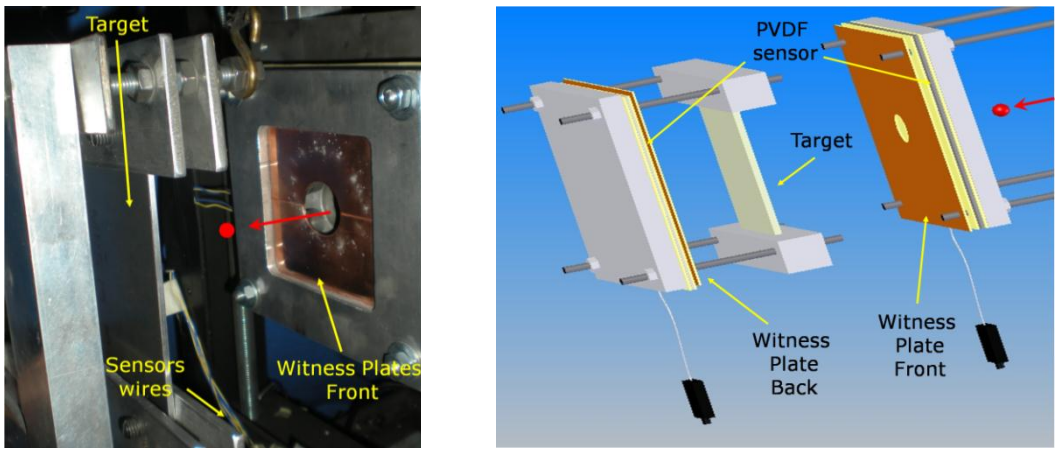

Fig. 4.111 - PVDF sensor coupled to the witness place rear surface. (a) Instrument assembly (a witness plate-PVDF assembly was used behind the target to collect information on down-range ejecta); (b) exploded view.

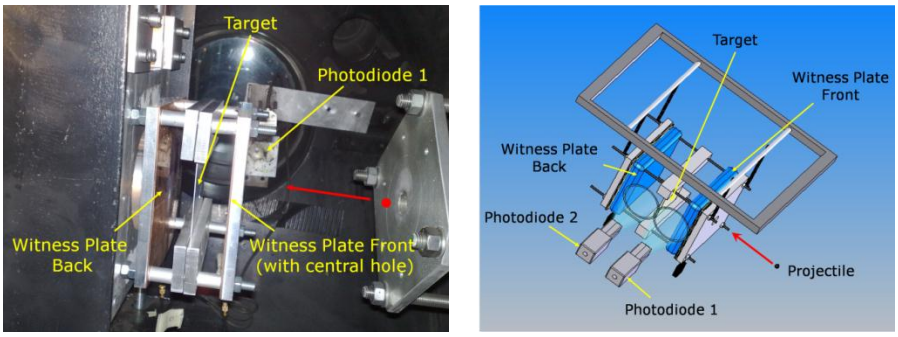

Fig. 4.112 - Target assembly on the left, the photo-detectors field of view is highlighted in the picture on the right.

4.3.1.3 Data utilization

The instrument assembly described above provides three independent sources of information deriving from:

1. Sensors: the output signal is dependent from the overall load transmitted by the ejecta cloud to the plate and is therefore related to the ejecta total momentum;
2. Photo-detectors: they are used to measure the time of flight of the ejecta cloud from the target to the witness plate, thus making it possible to evaluate the speed of the cloud tip;
3. Examination of the witness plates craters: their geometry and extent are related to the size and speed of the ejecta fragments. In particular, craters can be analysed by an imaging system which automatically provides the total crater area, the average area of the five largest craters and the average area of all crates detected on the plate.

In addition to the above information, the procedure for evaluating the average fragment mass and velocity employs well known empirical equations describing crater morphology and size as a function of impact conditions ([26]). Such relations are needed for deriving ejecta parameters from the analysis of the witness plate damage pattern. Specific assessment of the suitability of different crater equations was not performed, because the focus was the methodology's development: once a suitable analysis procedure is outlined, other equations could be used in the same way, affecting only the overall method uncertainty.

$$p = k_{\infty} \rho_p^{1/6} m^{0.352} v_n^{2/3} \qquad \text{Eq.4-2}$$

$$p / d_c = 9.60 \cdot \left(\frac{v_n}{c_T} \right)^{1.18} \qquad \text{Eq.4-3}$$

In the previous equations, p and dc are the crater depth and diameter expressed in cm; ρ_p, m and vn are the impactor density, mass and normal speed expressed in gcm^{-3}, g and km/s; c_T is the speed of propagation of longitudinal waves in the target expressed in km/s and k_∞ is a constant depending from the target material's hardness (*e.g.* k_∞=0.42 for Al alloys and $k\infty$=0.25 for steels). Moreover, a useful empirical equation is reported in Eq.4-4 which correlates the total mass of the ejecta with the kinetic energy of the primary projectile:

$$M = K \cdot 7.410 \cdot 10^{-6} (\rho_p / \rho_t)^{1/2} \cdot E_n^{1.133} \qquad \text{Eq.4-4}$$

In the above equation, *M* is the total ejecta mass, *K* is a constant depending on the target material, ρ_p and ρ_t are the impactor and target density and E_n is the impactor's kinetic energy in the normal direction. Values of all parameters in Eq.4-4 are expressed in SI units.

The procedure to assess the average fragment size and speed can be outlined as follows. The main assumption is that ejecta fragments have spherical shape, so that witness plate craters are hemispherical and Eq.4-2 and Eq.4-3 are valid.

1. From the analysis of the witness plate crater pattern, the total crater area $A_{c,tot}$ and the average area $A_{c5,avg}$ of the five largest craters are evaluated;

2. The average crater area and diameter are therefore:

$$A_{c,avg} = k_1 \cdot A_{c5,avg}; \qquad k_1 < 1 \qquad \text{Eq.4-5}$$

$$d_{c,avg} = 2 \cdot \left(\frac{A_{c,avg}}{\pi} \right)^{0.5} \qquad \text{Eq.4-6}$$

3. The speed v_{tip} of the fastest fragment in the ejecta cloud is calculated dividing the normal distance between the target and the witness plate by the ejecta tip time of flight deduced from the photo-detector signal. This means that v_{tip} is the ejecta tip speed projected onto a direction perpendicular to the witness plate.

4. The average normal fragment speed is:

$$v_{avg} = k_2 \cdot v_{tip}; \qquad k_2 \leq 1 \qquad \text{Eq.4-7}$$

The speed of ejecta depends on the fragmentation mechanism: cone particles are the faster ones and may travel up to the primary impactor velocity. On the other hand, spall fragments are much slower.

5. At this point, $d_{c,avg}$ and v_{avg} from Eq.4-6 and Eq.4-7 are inserted into Eq.4-2 and (2), which are then combined together to obtain the average ejecta fragment mass:

$$m_{avg} = f_1(A_{c5,avg}, v_{tip}, k_1, k_2) \qquad \text{Eq.4-8}$$

$$\Rightarrow \qquad m_{avg} = \frac{1.254}{c_T^{3.352} k_\infty^{2.841} \rho_p^{0.473}} \left(k_1 A_{C5,avg}\right)^{1.420} \left(k_2 v_{tip}\right)^{1.457}$$

Two parameters in Eq.4-8 come from measurements ($A_{c5,avg}$ and v_{tip}); m_{avg}, ρ_p and $A_{C5,\text{avg}}$ are expressed in g, gcm^{-3} and mm^2, c_T and v_{tip} are expressed in km/s.

6. The total mass M of the ejecta coming from Eq.4-4 may be related to m_{avg} in the following way (n_c is the number of "average" craters):

$$M = m_{avg} \cdot n_c = m_{avg} \frac{A_{c,tot}}{A_{c,avg}} = m_{avg} \frac{A_{c,tot}}{A_{c5,avg} \cdot k_1} \qquad \text{Eq.4-9}$$

Eq.4-9 can be solved for ($A_{c5,avg}$·k1). Such term is inserted into Eq.4-8 and then cancels out. Finally, Eq.4-6 is used to give an explicit expression for M. The final result is therefore:

$$\Rightarrow \qquad m_{avg} = \frac{3.669 \cdot 10^{-8} c_T^{7.981} k_\infty^{6.764} K^{3.381} \rho_p^{2.817} E_n^{3.831}}{A_{C,tot}^{3.381} \rho_T^{1.690} \left(k_2 v_{tip}\right)^{3.469}} \qquad \text{Eq.4-10}$$

In the above equation, m_{avg}, and $A_{C,tot}$ are expressed in g and mm^2; ρ_p and ρ_T are expressed in gcm^{-3}; c_T and v_{tip} are expressed in km/s and E_n is expressed in J.

Looking at Eq.4-10, it appears that neither k_1 nor $A_{c5,avg}$ are needed to assess m_{avg}. However, an additional piece of information is requested to evaluate the average fragment mass, since the degree of freedom related to the knowledge of $v_{avg}=k_2 v_{tip}$ has not been fixed yet. A first option for determining k_2 is to use PVDF signals, that can be experimentally related to m_{avg} and v_{avg}:

$$PVDF = f_2(M, v_{avg}) = c_1 M^{c_2} \left(k_2 v_{tip}\right)^{c_3} \qquad \text{Eq.4-11}$$

c_1, c_2 and c_3 are constants obtainable from PVDF calibration.
However, results reported in section 3 were not obtained by using Eq.4-11; rather, k2 was assumed to vary within the range 0.8-1.

As a concluding remark, the following two observations are considered:

- The described method allows to assess only average cloud properties without providing information about the volume distribution of fragments inside the 3-dimensional ejecta cloud structure. This is due to the specific architecture of the ejecta evaluation assembly but it is not a limit of the method's capabilities: getting information on the 3-dimensional spatial dependence of fragments properties becomes possible by simply splitting the witness plate in multiple sectors having size dependent from the spatial resolution requested. Even the sensor system could be split in multiple channels each of them refers to the individual witness plate sector under consideration. In summary, the spatial resolution of the method depends on the number of sectors in which witness plates are divided. Information on fragment size and speed is averaged over the sector.

- The employment of the procedure just outlined is affected by many sources of uncertainty. Most of them are related to the empirical nature of Eq.4-4 to

Eq.4-7, Eq.4-9 and Eq.4-10, that contain many parameters coming from a best fit of experimental data. In this framework, it was decided to cope with the need of assessing the uncertainty on the final results (m_{avg} and v_{avg}) through the application of a simplified Montecarlo procedure that varies all the relevant empirical parameters within reasonable ranges (*i.e.* based upon proved results presented in the technical literature and on experience). Such a procedure was employed to specify the uncertainty bound for the results of the test-case described in the following section. The Montecarlo analysis demonstrated that the most relevant source of uncertainty for m_{avg} is the value of K (Eq.4-6); after that, the knowledge of both $A_{C,tot}$, k_∞ (Eq.4-4) and k_2 (Eq.4-9) contributes significantly to the overall estimation accuracy.

4.3.1.4 Experimental results

This section reports the application of the procedure described in par. 4.3.1.3 to the test case of a 1.5 mm pure (99.5%) aluminium projectile hitting a 0.8 mm thick Al2024 bumper at 4.16 km/s.

Even though PVDF sensors were mounted as part of the instruments as reported in Fig. 4.111, in this specific case their signals were not used, due to some experimental difficulties that have not been solved to date: they are mainly related to a limited repeatability of the sensors output, which was often characterized by a poor signal to noise ratio and by a very high sensitivity to background interferences. After many attempts, it was recognized that the principal source of disturbance are the electrical connections between the film and the BNC cables used to collect the charge signal. Moreover, the available PVDF films (that were obtained as waste samples belonging to another program) resulted to be excessively sensitive for typical ejecta cloud inputs (they often caused sensors' saturation).

The unavailability of the PVDF data imposed a slight modification of the procedure outlined: the value of k_2 (which represents the ratio between v_{avg} and v_{tip}) was forced to vary in the interval 0.8 – 1. In this specific case, such high values of k_2 are justified by the fact that in ductile materials slow spall fragments are almost missing (this is confirmed by careful inspection of the target around the impact crater) while fast cone ejecta are prevalent. The choice of assuming that range of values for k_2 affects the overall uncertainty only slightly, since Montecarlo runs demonstrated that the current uncertainty on *K* (Eq.4-6) has a dominant effect on the estimation accuracy. So, the additional piece of information given by the use of PVDF sensors could provide only marginal improvement to the assessment of m_{avg}, as soon as more reliable values for K would become available.

Fig. 4.113 reports a raw (left) and post-processed (right) image of the front witness plate, on which an annular crater path is evident. Such damage feature results from the intersection of the witness plate surface and the ejecta cone.

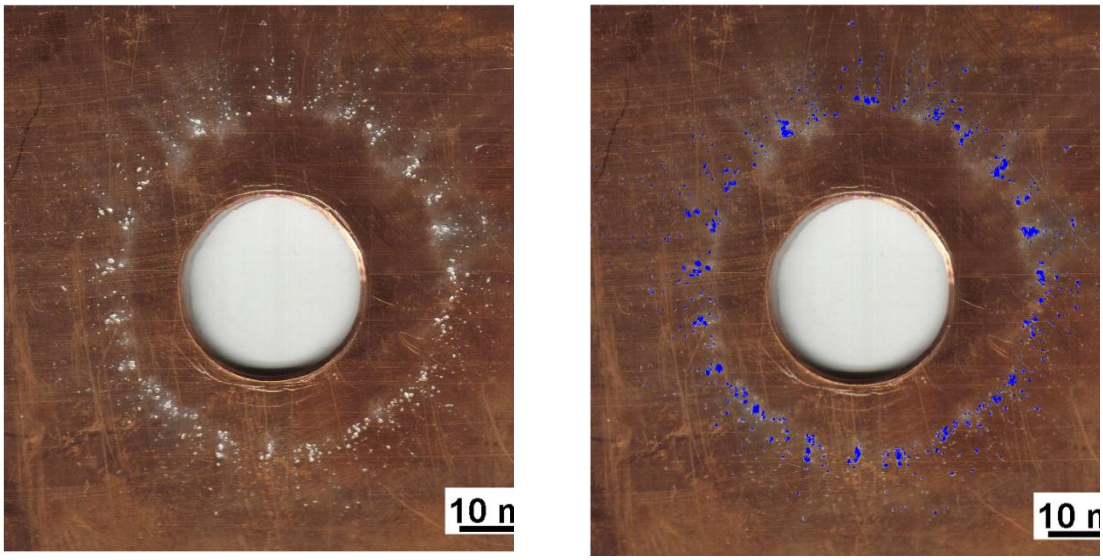

Fig. 4.113 - Witness plate with front ejecta. (a) raw and (b) post-processed image.

Main results of the analysis are given in Tab. 4-9. As stated before the uncertainties were estimated by means of a simplified Montecarlo procedure which varied the most important parameters of the equations within reasonable ranges. Such ranges are specified in Tab. 4-9. In particular, the choice of K (Eq.4-6) was made starting from the results reported by Gault, who performed a large number of impact tests on brittle rocky targets over a wide range of impact conditions. In that case, experimental data fit well for K=1. However, it was expected that the amount of ejected matter from ductile targets is lower than that coming from brittle targets at the same impact conditions and hence a value of K<1 was preferred. In fact, few spall fragments are ejected from ductile materials and plastic deformation prevents target disruption and formation of a large number of cone fragments. The range for K given in Tab. 4-9 was chosen looking at the results of Montecarlo simulations on which K was varied from 0.001 to 1: only within the interval K=0.2-0.4 the average crater number computed using Eq.4-11 became compatible to that obtained by automatic witness plate analysis.

Description	*Symbol*	*Unit*	*Value / range*	*Source*
Projectile density	ρ_p	gcm^{-3}	2.70 – 2.78	Material properties
Target density	ρ_T	gcm^{-3}	2.70 – 2.78	Material properties
Speed of propagation of longitudinal waves	c_T	km/s	3.95 – 4.15	Material properties
k_∞ coefficient in Eq.4-4	k_∞		0.40 – 0.45	[38]
K coefficient in Eq.4-6	K		0.20 – 0.40	Assumption
k_2 coefficient in Eq.4-9	k_2	-	0.8 - 1	Assumption
Speed of the ejecta cloud tip	v_{tip}	km/s	1.50±0.02	Photo-detectors
Ejecta cone angle	α	°	33±5	Witness plate analysis
Witness plate total crater area	$A_{c,tot}$	mm^2	19.72±4.93	Witness plate analysis
Total mass of up-range ejecta	M	mg	153.15±35.13	Eq.4-6
Mass of the average ejecta fragment	m_{avg}	mg	$(1.89\pm1.14)\cdot10^{-2}$	Eq.4-10
Diameter of the average ejecta fragment	d_{avg}	mm	$(2.3\pm2.0)\cdot10^{-1}$	m_{avg}
Speed of the average ejecta fragment	v_{avg}	km/s	1.35±0.15	Eq.4-9

Tab. 4-9 - Ejecta characterization for Shot No.8434. Main results.

The repeatability of the piezoelectric sensor output and the large uncertainty on the empirical equations used are the most critical issues that require consideration for the next optimization of the ejecta evaluation method.
For this reason, sensors other than PVDF (*e.g.* strain gauges) are evaluated, as described in the next paragraphs, to provide reliable information without adding complexity to the instrumentation package; moreover, accurate weighing of all components involved in a single test is being considered to avoid the use of empirical relationships describing the total mass of ejecta produced after HVI.

For this further development the ISO directive about the test procedures to evaluate spacecraft material ejecta upon hypervelocity impact are followed.

4.3.2 Ejecta instrument evolution

4.3.2.1 PVDF paint

This first solution has the same working principle of the PVDF film sensor used for the ejecta instrument prototype and uses the same polarized polymer.
The difference is that the polymer is applied as a paint on the back surface of the witness plate.
The sensor has 3 layers (Fig. 4.114):

- Layer “A”: Made of an Al alloy on which the secondary debris impact.
- Layer “B”: On which there is the PVDF paint
- Layer “C”: This is the electrode that collects the generated charge of the interaction between layer “A” and “B”

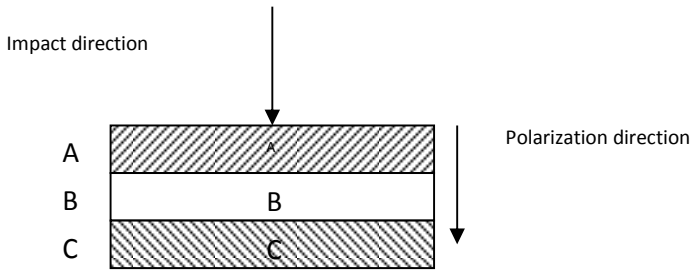

Fig. 4.114 - Sensor’s scheme

The BASF company gave free samples to do preliminary tests (Fig. 4.115).

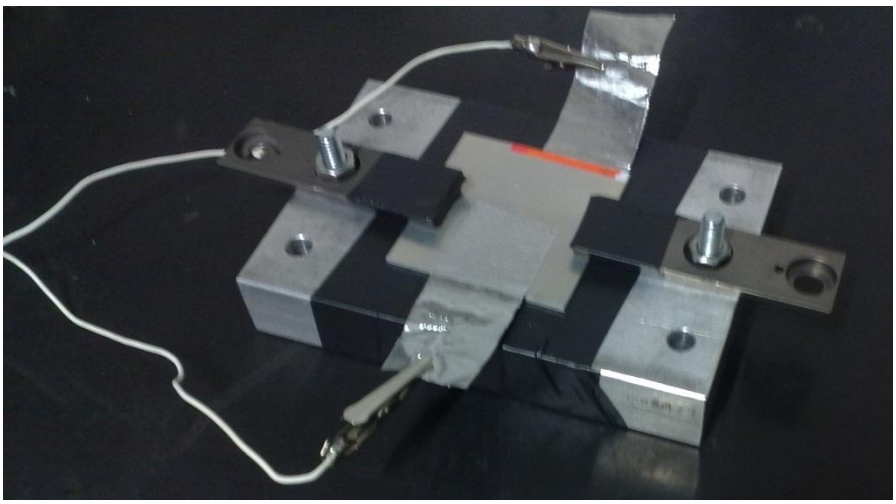

Fig. 4.115 - Aluminium sample plate with PVDF paint

The Al plate with the PVDF paint has been polarized with a tension of 700 V for 45 minutes.
The first drop tests (*i.e.* tests with steel spheres falling down from known height) show a repeatable output signal for the first hour after the polarization, with a high signal/noise ratio (Fig. 4.116).

This solution has no further study because of the problems linked to the duration of the polarization and to the conditioning of the signal in the LGG vacuum chamber.

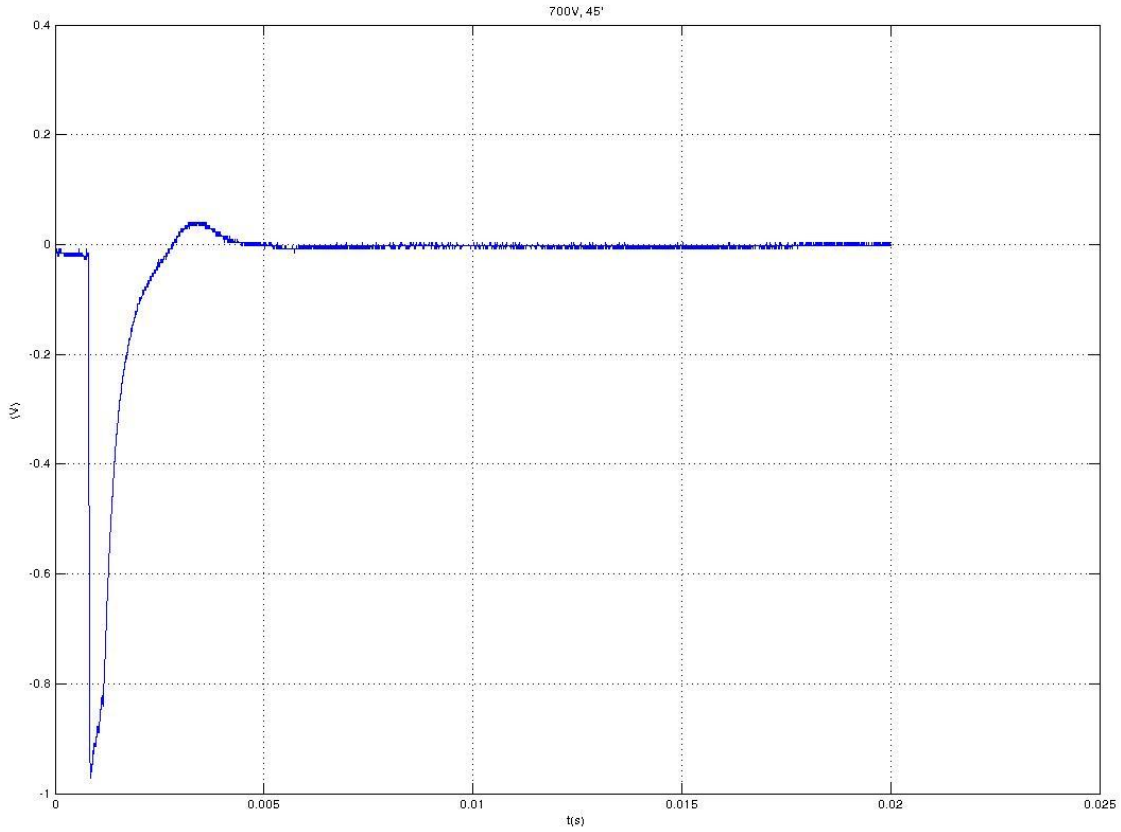

Fig. 4.116 – Example of a PVDF paint signal

4.3.2.2 Strain gauges preliminary tests

From a conceptual point of view the approach is the same of the previous one, even if in this case the mechanical deformation is linked to a resistance variation (piezoresistive sensor).
Usually a piezoresistive sensor is easier to manage as regard the signal conditioning if compared to a piezoelectric sensor.
For this reason this solution is evaluated also considering the transfer function and the bandwidth.

Preliminary tests were done with 2 ordinary linear strain gauges put in a mutual orthogonal position (the first one in radial direction from the witness plate centre, the second one in tangential direction), connected at opposite side of a Wheatstone bridge. This configuration allows to increase the system sensibility, using the addition of a radial and circumferential deformation (they are related by the Poisson coefficient of the witness plate's material).

Two configurations were implemented to apply the strain gauges to the witness plate (Fig. 4.117): in the first one the strain gauges are directly bounded to the witness plate, in the second one they are bounded on a thin steel plate (0.2 mm), this one is linked to the copper plate. The advantage of the second solution is that the strain gauges are available for different tests, the disadvantage consists in the difficulty of realize a good matching between the two parts.

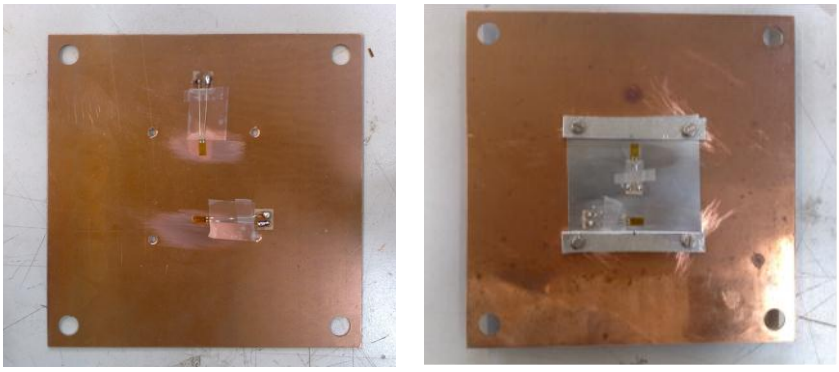

Fig. 4.117 - Solution with strain gauges bounded on the fitness plate and solution with strain gauges glued on the steel plate.

The 2 configurations were compared, with a hammer test. A comparison of the signal is plotted in Fig. 4.118.

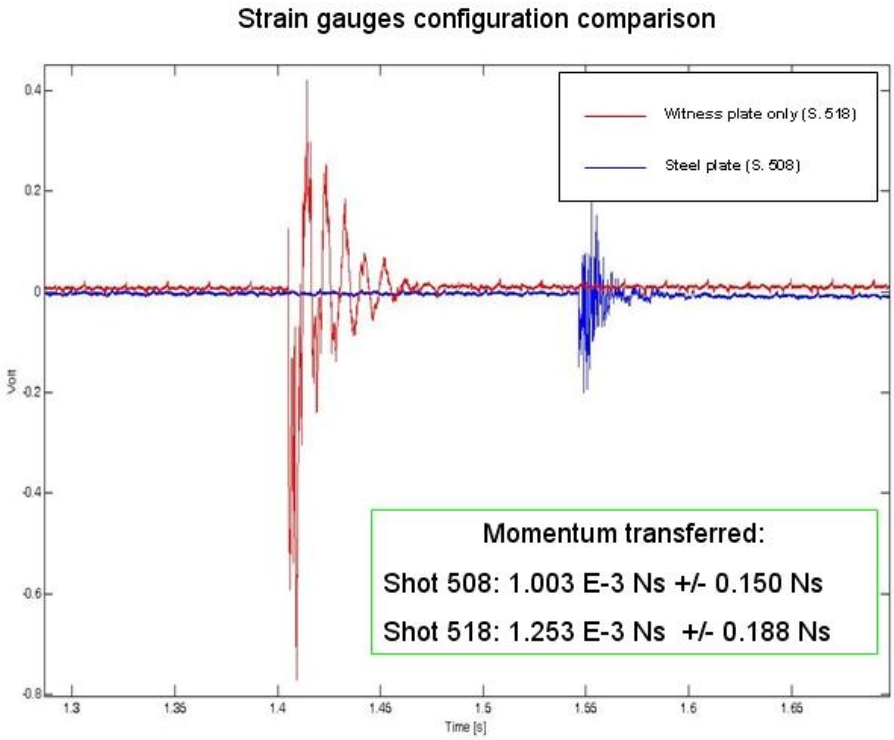

Fig. 4.118 – Comparison of the 2 configuration signals.

It is visible the filter effect of the steel plate used for the second solution. Moreover, the FFT signal analysis (Fig. 4.119) show the presence of a higher presence of harmonics in the second solution, maybe due to problem in the matching between the witness and the steel plate.

A band-pass filter was done to reduce the problems linked to the background noise and to the strains of the support structure during the tests.

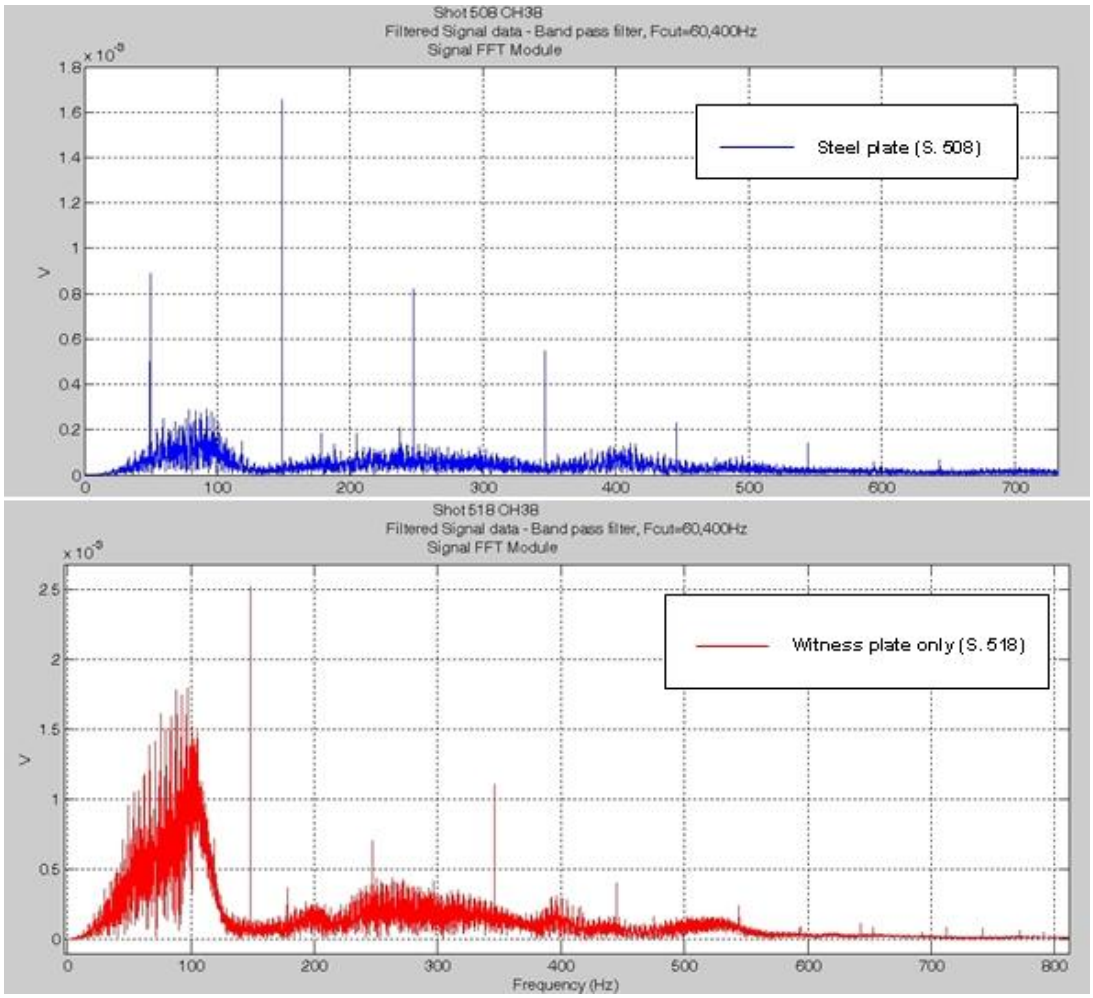

Fig. 4.119 – FFT comparison between the two solutions.

4.3.2.3 Flexi sensors

In the development of this solution the ISO proposal for the standardization of the ejecta characterization experiment (see 4.1.1) is taking in account.

This led to the realization of an integrated system (Fig. 4.121 and Fig. 4.122) for the experiment assembly in the vacuum chamber (Fig. 4.123), with the instrumentation for the measure of the mean velocity of the debris cloud's fragments.
The fragments collected are analysed by an automatic system for the post-impact witness plate analysis, using a high definition scanner and a software package for the image analysis (crater counting and measuring).

This instrumentation consists in piezoresistive load cell mounted of support pins of the WP. The ejecta cloud generate a mechanical load and these cells give a signal that can be correlated, after calibration, to the transferred momentum (Fig. 4.120).

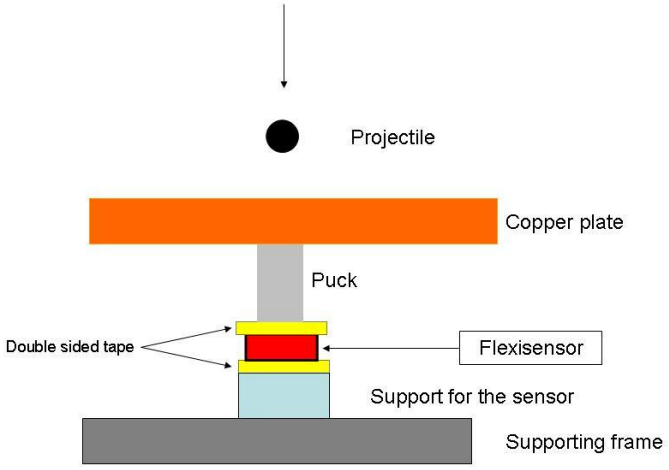

Fig. 4.120 – Instrumentation's scheme

Moreover, using the photodiode the record the flash caused by the impact it is possible to have an information about the mean Time of Flight of the ejecta cloud. This information can be used to derive, with the craters' analysis, the mass and velocity distribution of the fragments.

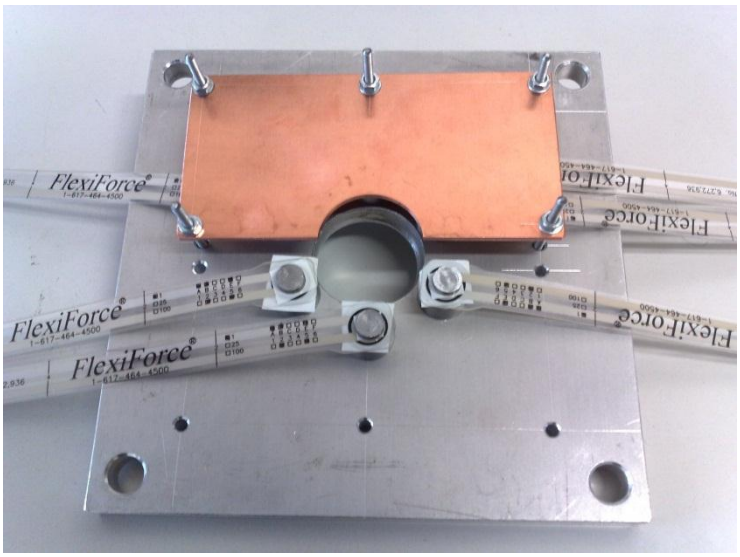

Fig. 4.121 – Instrumentation assembly

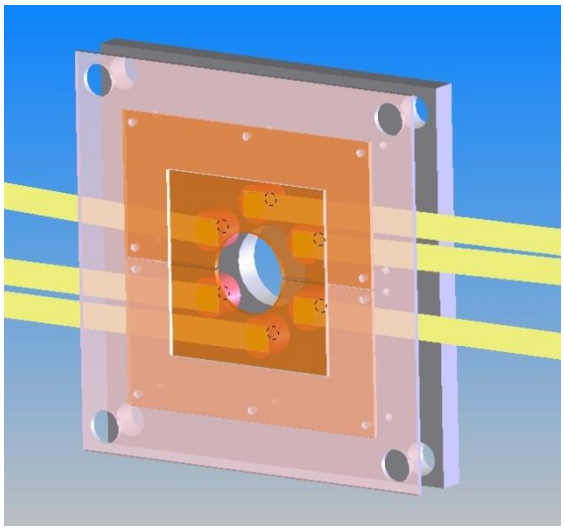

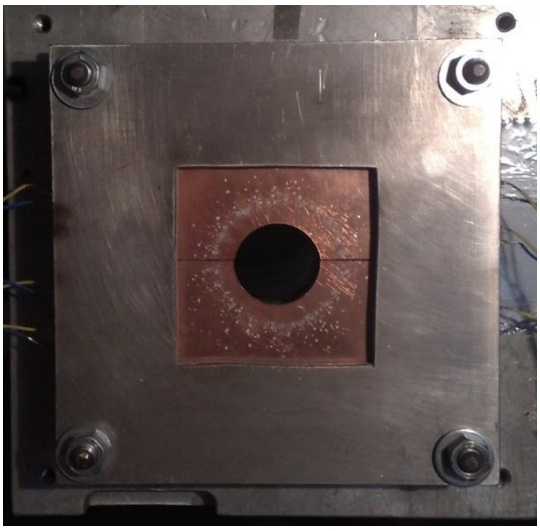

Fig. 4.122 - Support for the witness plate mounting

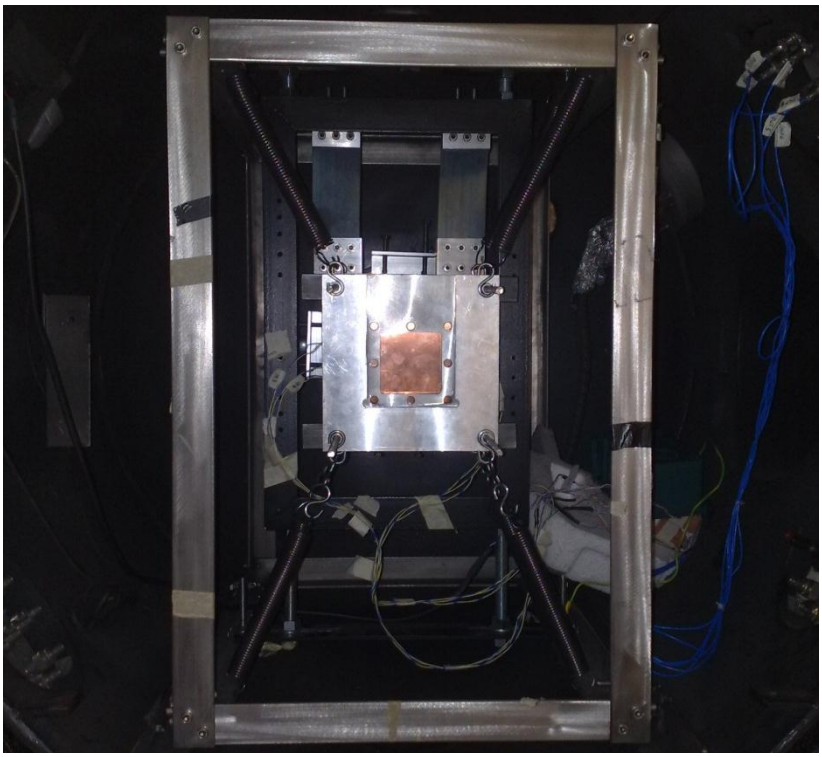

Fig. 4.123 – Experimental set up in the vacuum chamber

20 tests were done with the post-impact witness plate analysis, *i.e.* crater measurement and counting.

This information is available for 3 types of target (Aluminium alloy, Aluminium alloy covered by MLI and solar cells), with 2 impact velocity (4 and 5 km/s) and 3 different debris (*i.e.* projectile) dimensions (1, 1.5 e 2.3 mm).

In the following figures there are some examples for the 3 types of target.

From a first visual inspection of the WP, confirmed by the analysis results reported in Tab. 4-10 and in the following Fig. 4.124, Fig. 4.125 and Fig. 4.126, it is visible that, with the same impact conditions, metallic targets generate more ejecta than the same samples covered by MLI.

Moreover, the total fragments quantity generated by fragile targets (*i.e.* solar cells) is definitely greater than the quantity of the other 2 categories, with the creation of smaller fragments. ([27])

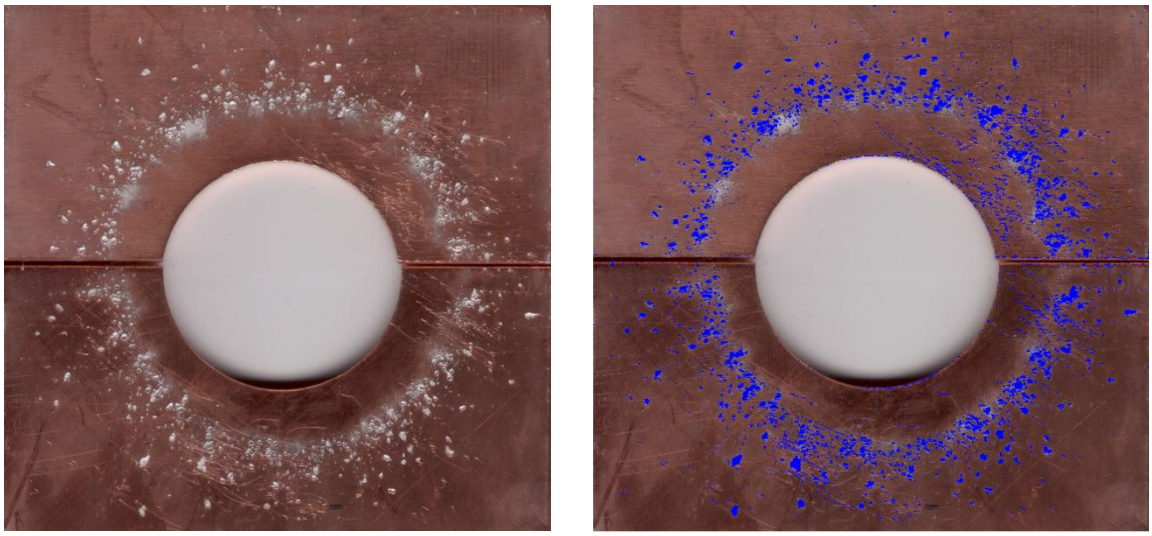

Fig. 4.124 - Shot n.8622 (Al target of 3 mm thick impacted by a 2.3 mm at 5.28 km/s projectile): Uprange Witness Plate - “Raw” (left) and analysed image (right)

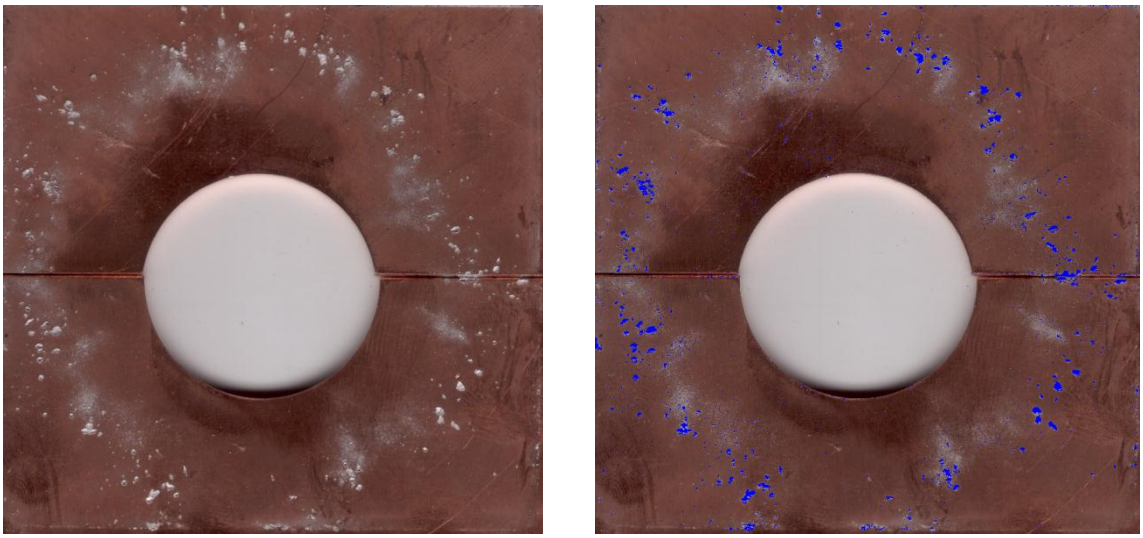

Fig. 4.125 - Shot n.8622 (Al target of 3 mm thick covered by MLI impacted by a 2.3 mm at 5.28 km/s projectile): Uprange Witness Plate - “Raw” (left) and analyzed image (right)

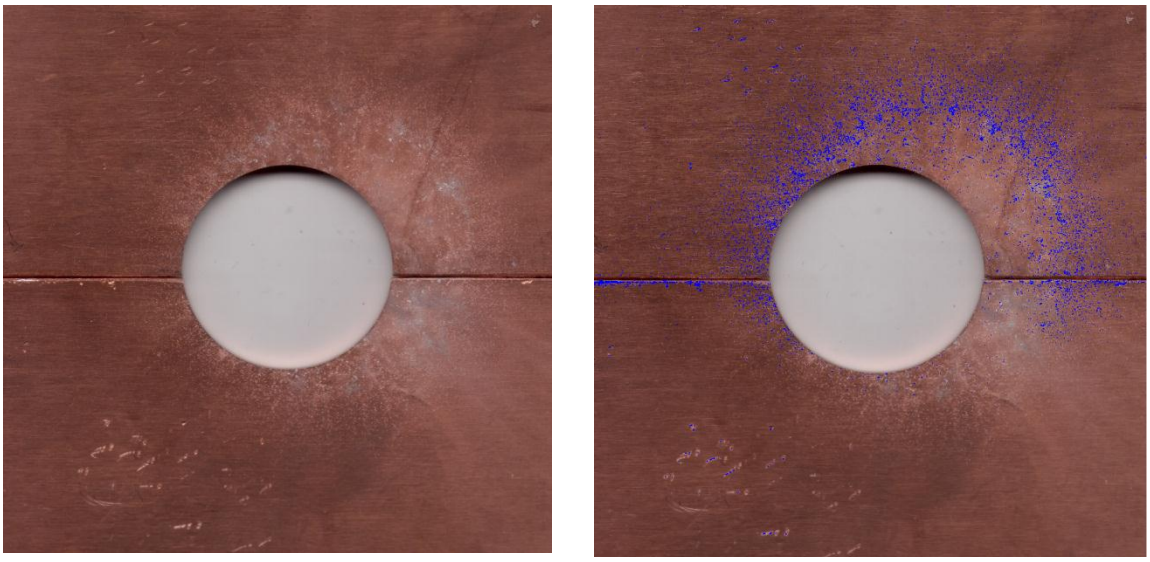

Fig. 4.126 - Shot n.8627 (Silicon Solar Cell impacted by a 2.3 mm at 5.16 km/s projectile): Uprange Witness Plate - “Raw” (left) and analysed image (right)

The preliminary analysis results are reported in Tab. 4-10.

Fig. 4.127, Fig. 4.128 and Fig. 4.129 resume the behaviour of different target for the analysed impact conditions.

Shot	Target	WP		Size distribution of crater diameter [mm]				Tot. craters
				0.025 - 0.05	0.05 - 0.1	0.1 - 1.0	>1.0	
8621	Al t=3mm	U	No.	1848	911	377	0	3136
		D	No.	-	-	-	-	-
8622	Al t=3mm	U	No.	3312	2048	1189	1	6550
		D	No.	1999	1054	674	28	6116
8623	Al t=3mm + MLI	U	No.	1053	514	324	0	1891
		D	No.	2400	1286	665	18	4369
8625	Al t=3mm + MLI	U	No.	930	377	152	0	1459
		D	No.	-	-	-	-	-
8626	Si Solar Cell	U	No.	4853	1137	90	0	6080
		D	No.	-	-	-	-	-
8627	Si Solar Cell	U	No.	5120	1068	86	0	6274
		D	No.	1705	288	34	1	2028
8629	Al t=3 mm	U	No.	2130	1080	598	0	3808
		D	No.	6144	1206	187	1	7538
8630	Al t=3 mm	U	No.	1428	728	385	0	2541
		D	No.	4157	715	134	0	5006
8631	Al t=3 mm	U	No.	3855	1215	430	0	5500
		D	No.	-	-	-	-	-
8632	Al t=3 mm	U	No.	1837	1469	982	0	4288
		D	No.	2395	738	324	16	3473
8634	Al t=3 mm + MLI	U	No.	1156	355	151	0	1662
		D	No.	9677	3121	494	3	13295
8635	Al t=3 mm + MLI	U	No.	733	356	170	0	1259
		D	No.	1265	250	45	0	1560
8637	Al t=3 mm + MLI	U	No.	511	190	65	0	766
		D	No.	-	-	-	-	-
8638	Al t=3 mm + MLI	U	No.	1245	498	236	0	1979
		D	No.	2229	811	413	7	3460
8640	Si Solar Cell	U	No.	8144	1965	156	1	10266
		D	No.	-	-	-	-	-
8641	Si Solar Cell	U	No.	15568	4188	372	1	20129
		D	No.	-	-	-	-	-

Tab. 4-10 - WP: witness plate, (U): “uprange WP”, (D): “downrange WP”. Craters number divided by dimensional classes.

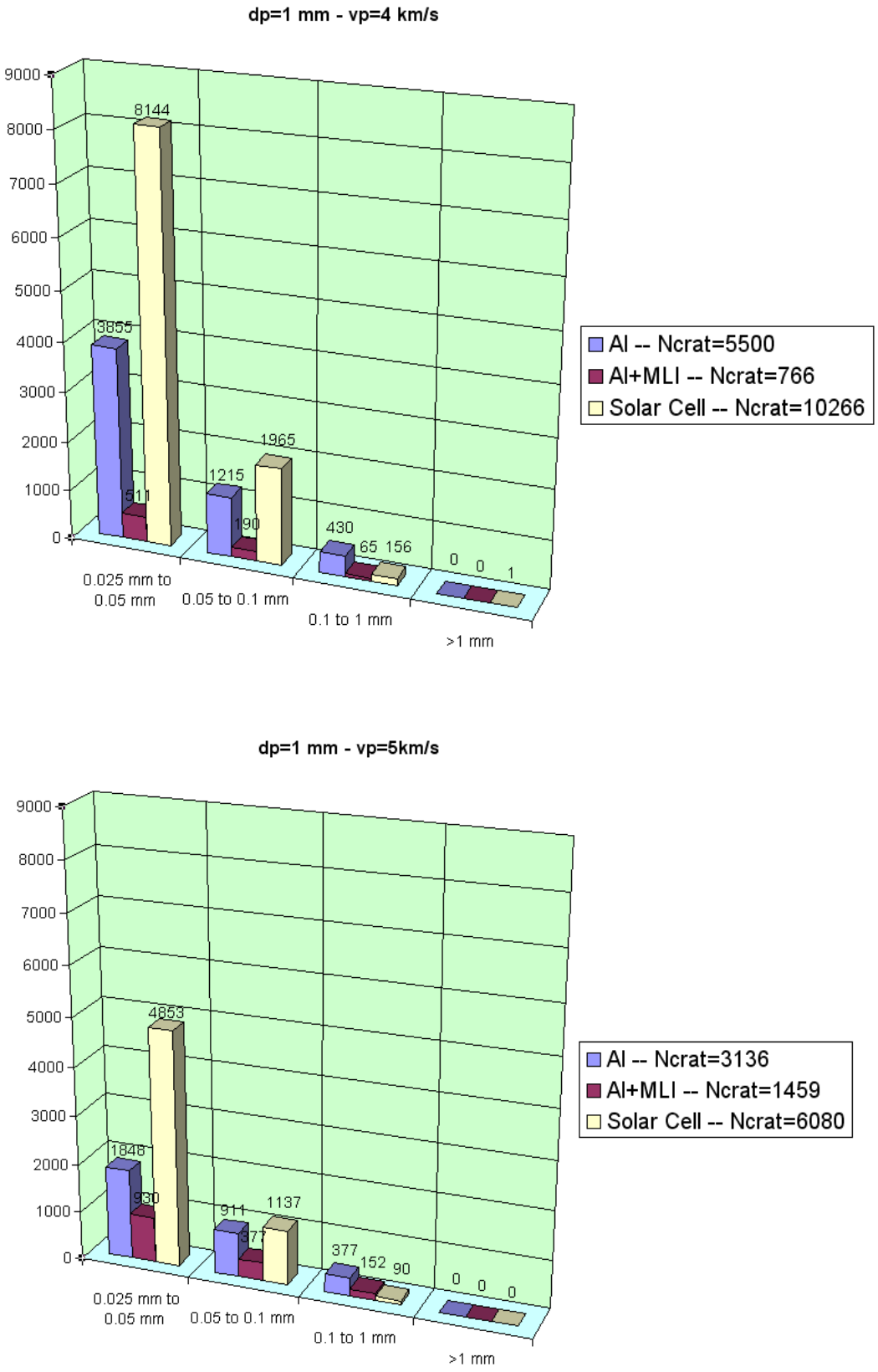

Fig. 4.127 - Number of craters generated by impacts at 4 km/s and 5 km/s with 1 mm projectile, catalogued by dimensional classes: comparison between different targets

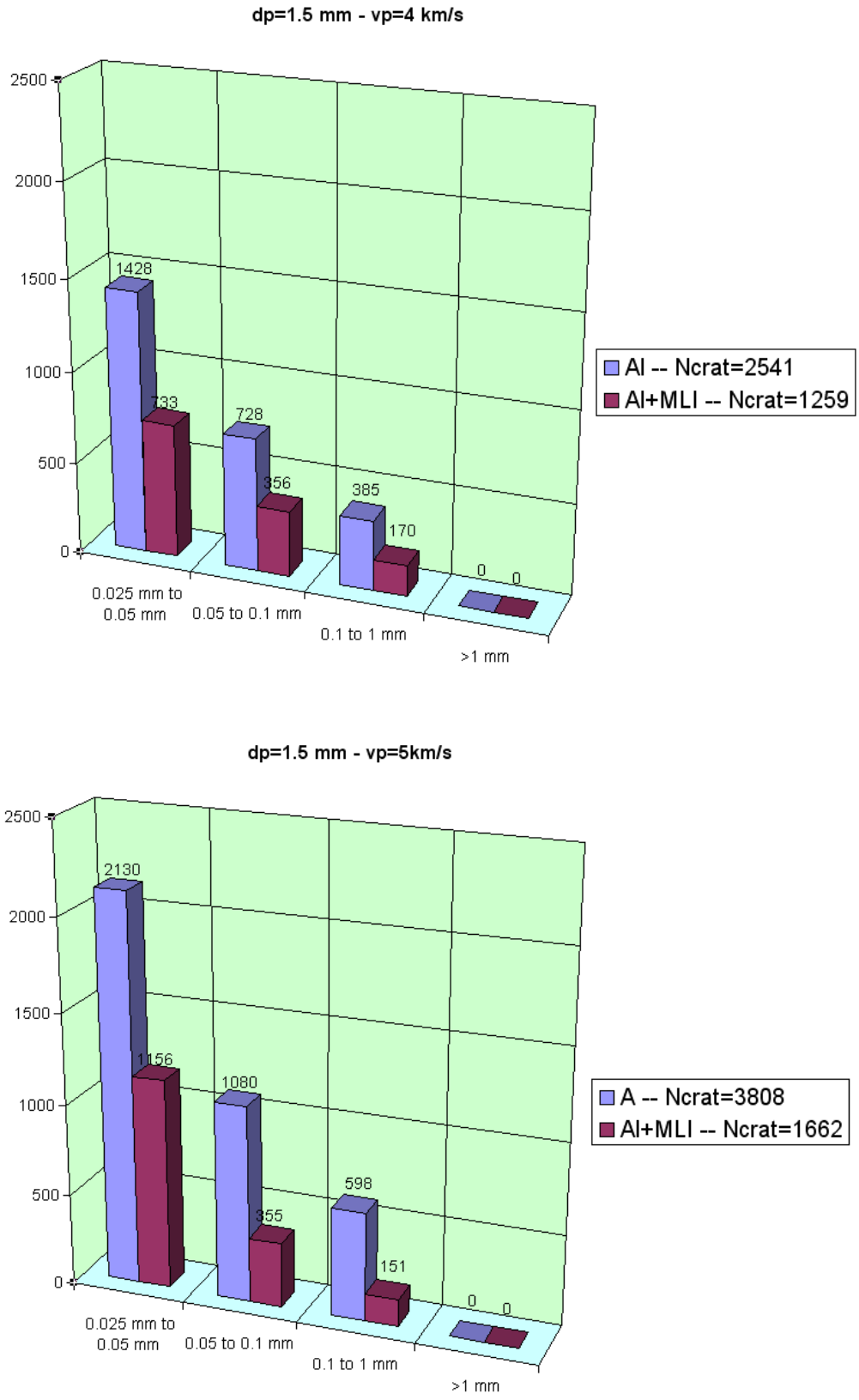

Fig. 4.128 - Number of craters generated by impacts at 4 km/s and 5 km/s with 1.5 mm projectile, catalogued by dimensional classes: comparison between different targets

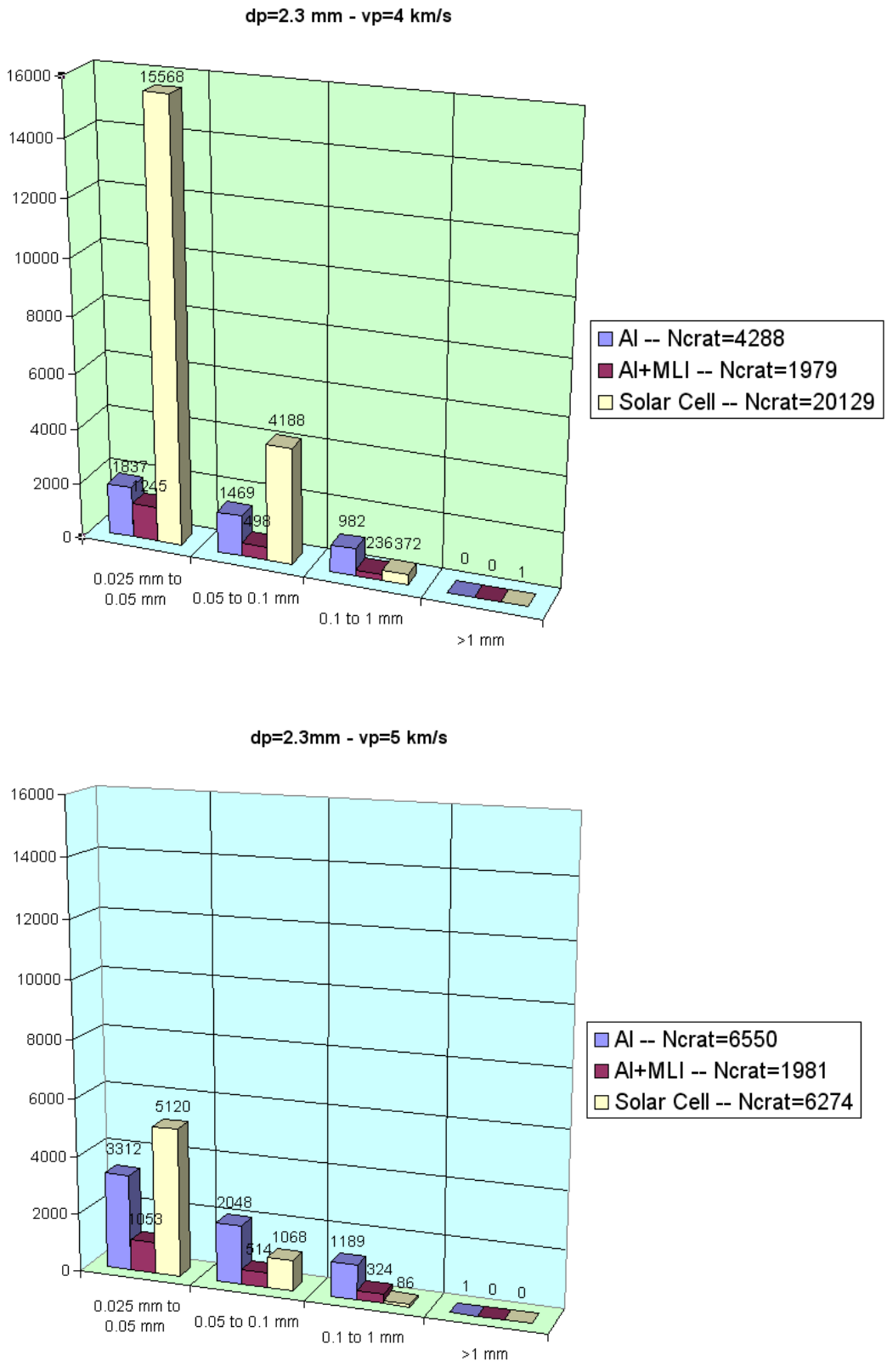

Fig. 4.129 - Number of craters generated by impacts at 4 km/s and 5 km/s with 2.3 mm projectile, catalogued by dimensional classes: comparison between different targets

Highlights:

- The HVI of a single object of the external surface of a spacecraft generates thousands of new debris for a total mass 1-2 orders of magnitude greater than the initial debris mass, this increase the total amount in the space environment.

- The number and the mass of the new fragments depend from the impact condition and from the configurations (material and geometry) of the impacted surface: as a rough indication, material covered by MLI generates less fragments than the metallic material directly exposed to the space. Moreover, fragile materials (*e.g.* solar cells) generate more fragments than ductile materials, nevertheless the dimensional distribution of these particles is unbalanced towards dimensions smaller than 50 μm and the total mass is consequently reduced.

- The actual procedure under estimate the quantity of the less energetic ejecta that can't leave well-defined traces of the copper witness plate. This particles include spall fragments (usually of great dimensions, so they are important for the space pollution) and fragments of MLI (they are light and of great dimensions => high area/mass ratio)

4.3.3 Evaluation of primary impact instrument for in-situ measurements

4.3.3.1 Primary impact instrument evaluation

The considered options for a primary impact instrument to assembly with the ejecta characterization instrument are:

1. Piezoelectric PVDF film
2. Strain gauges
3. Temperature sensors (thermoresistence and/or thermocouple)

These alternatives are evaluated with the following requirements:

- Bandwidth > 10 kHz (this value is due to the high range of frequencies generated by HVI);
- Capacity to detect sub-millimetre particles, *i.e.* the order of the dimensions of fragments generated by the impacts;
- Ease of signal processing;
- Low cost.

For sensors 1 and 2 the concept is to measure the global deformation of the witness plate, due to the impact of the fragments (Fig. 4.130). This kind of signal is related with the properties of the ejecta cloud and so with the characteristics of the "average ejecta fragment", this means that is not possible to analyse a single ejecta fragments but that is possible to retrieve the 'average' properties, like mass and velocity, of an 'ideal' fragment that mediates the characteristics of all the fragments hitting the witness plate. In each case the impact sensor will be protected by the copper plate. These alternatives were discussed previously for the ejecta instrumentation.

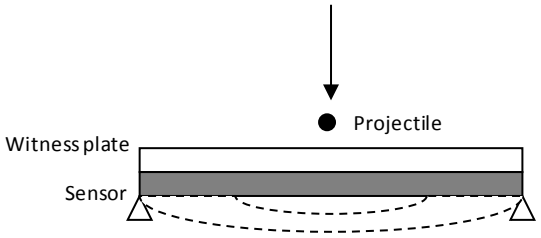

Fig. 4.130 - Working principle scheme

For the sensor number 3 the idea is to build a calorimetric system to assess the quantity of heat generated by the impact of the debris cloud, which is correlated with the properties of the fragments.

Calorimetric impact detection (Fig. 4.131) is based on the fact that a substantial part of the particle's kinetic energy E_{kin} is converted into heat when impacting the target. Consequently, the temperature of the target, in the following called "energy absorber", increases by ΔT which is measured by a contacted temperature sensor. This principle of calorimetric energy measurement is visualized in the next figure.

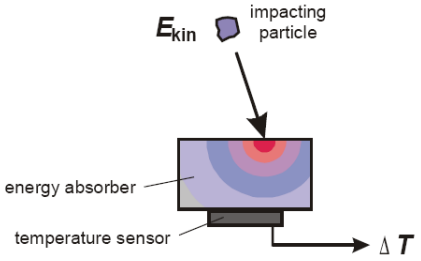

Fig. 4.131 - Calorimetric sensors working principle

The ratio between measurable calorimetric heat and kinetic energy of the impacting particle is called the heat conversion efficiency

$$\eta_{\mathrm{conv}} = \frac{E_{\mathrm{cal}}}{E_{\mathrm{kin}}}$$

After the determination of the heat conversion efficiency with the calibration in different experimental conditions it is possible to calculate the total kinetic energy of the ejecta cloud with the measure of the variation of temperature of the system.
The element "energy absorber" must be designed to work as a filter to contrast the high temperature gradient in the proximity of the craters. This means that after an impact the energy is located in a very small zone, with a temperature increase that as a peak very high (thousands of Kelvin degrees) but very short in its time interval (microseconds), this element allows to redistribute the energy of the impact in a larger zone. In this way it is possible to use ordinary sensors of temperature to monitor the phenomenon.

4.3.3.2 Primary impact instrument realization

In this paragraph, the realization of the experimental setup will be described (Fig. 4.132 and Fig. 4.133), show getting information from all the sensors at the same time. This allows to do a cross-calibration of the systems to do a comparative evaluation of their suitability for the application.

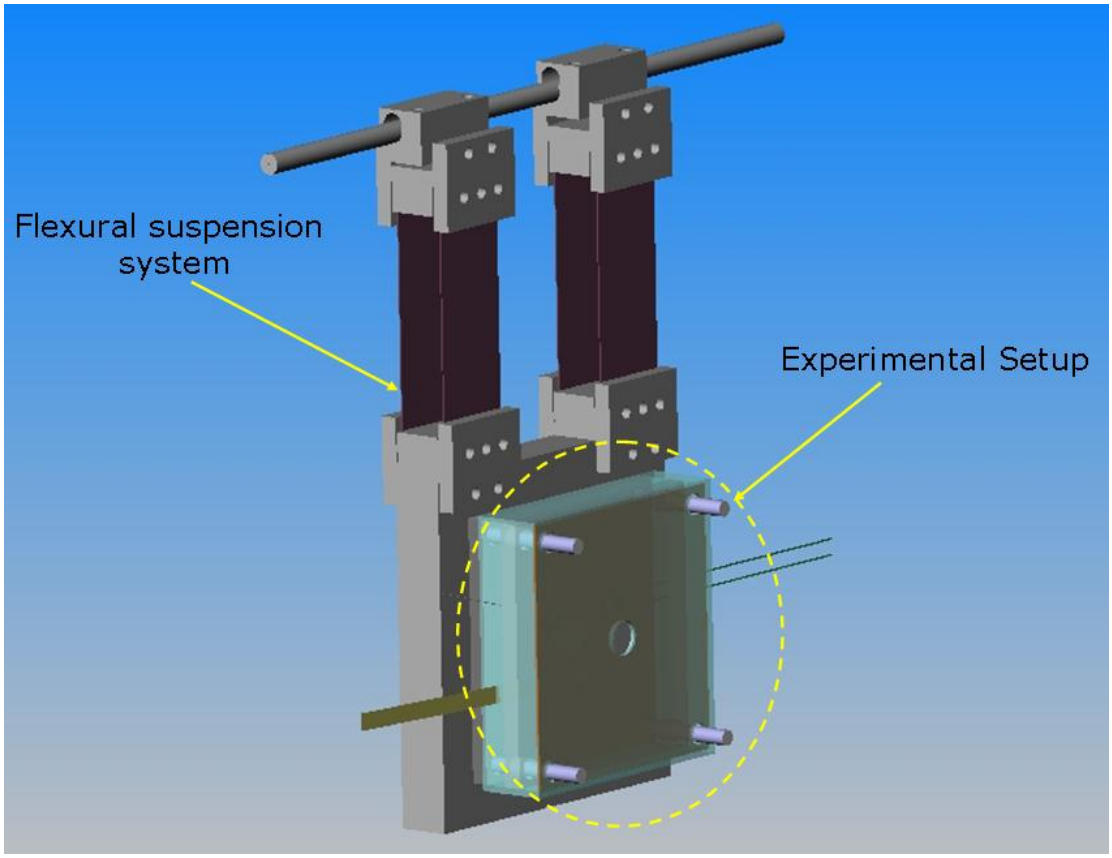

Fig. 4.132 - Assembly of the experimental setup for the comparative evaluation and the calibration of the impact sensors

The experiment is hanging on an elastic system that can work as a ballistic pendulum.
Fig. 4.133 shows an exploded view of the instrument, the main components and the support pins are visible, they are arranged at 120° from the shot axis.

The 3 used sensors are:

- Piezoelectric load cell (PVDF)
- Piezoresistive load cell
- PT100 sensor for calorimetric measurements

The solutions based on PVDF paints and strain gauges are discarded because of the prelimary evaluation presented before, that shows operational problems (for example PVDF paints require long time and instrumentation for the polarization).

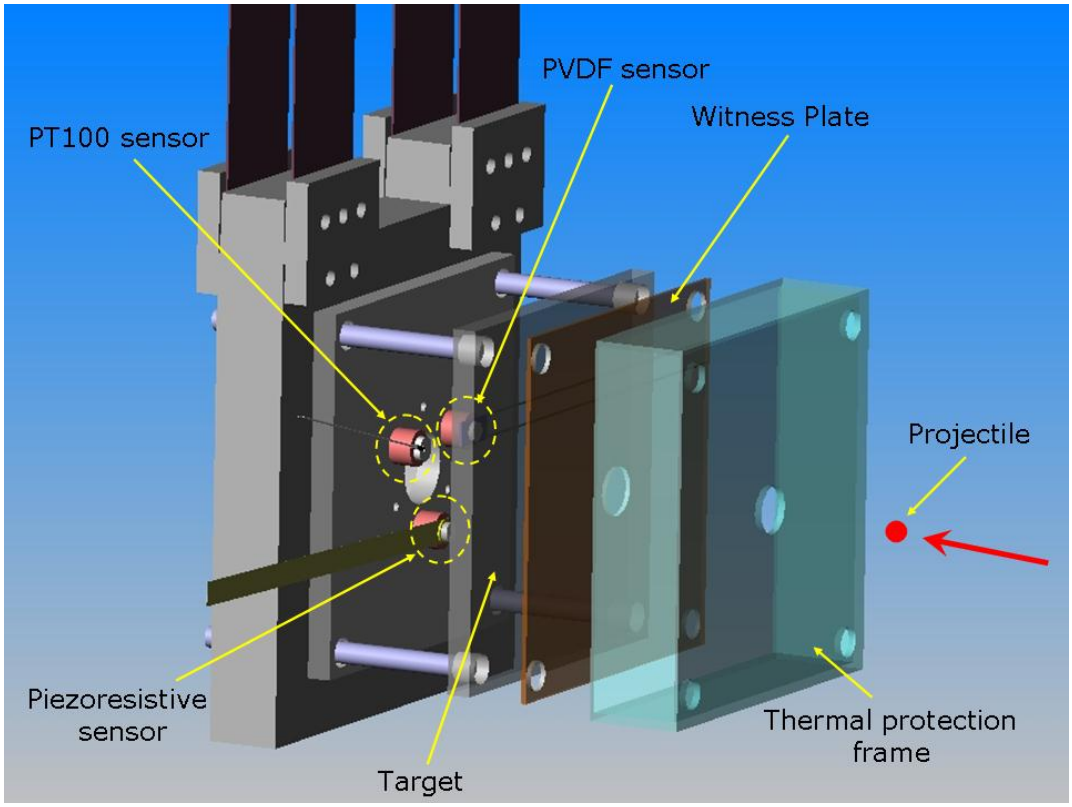

Fig. 4.133 - Assembly of the experimental setup for the comparative evaluation and the calibration of the impact sensors: exploded view

The experimental results show that the measurement system with the best efficiency is the one with PVDF piezoelectric load cells.
The calorimetric system with the PT100 didn't give a signal of good quality, due to the not optimal thermal control of the target and of the sensor. The signal of the PT100 is filtered by the high thermal inertia of the system, this doesn't allow to get information about the temperature's variation of a fast event like the impact.

For these reasons the paragraph 4.3.4 will show the results of the piezoelectric load cell (PVDF) and of the piezoresistive sensor (Flexiforce).

4.3.3.3 Oblique impacts

Starting from the previous concept the instrument is splitted in 2 parts, one with the primary impact system detection and one with the witness plate, to allow oblique tests (Fig. 4.134).

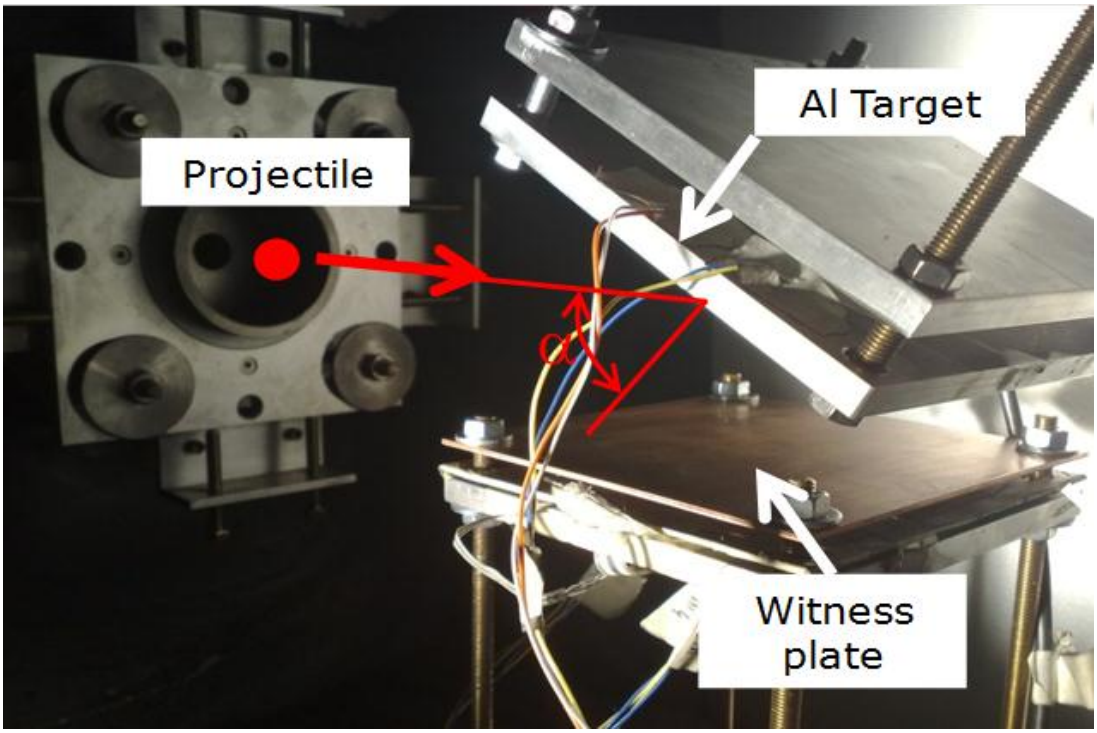

Fig. 4.134 - Assembly of the experimental setup for oblique tests

The tests' results are analysed also in this configuration with an automatic procedure to detect and count craters on the witness plate.
The collect data are combined with the previous results to get a better characterization of the phenomenon.

A comparison in the craters' distribution between a normal impact (Fig. 4.135) and an oblique impact (Fig. 4.136) is now shown.

These figures shows the damage patterns (highlighted in red), starting from the acquired image of the witness plate after the shot, with an intermediate analysis' phase where the automatic procedure identifies the scratches

already recognized on the copper before the test.

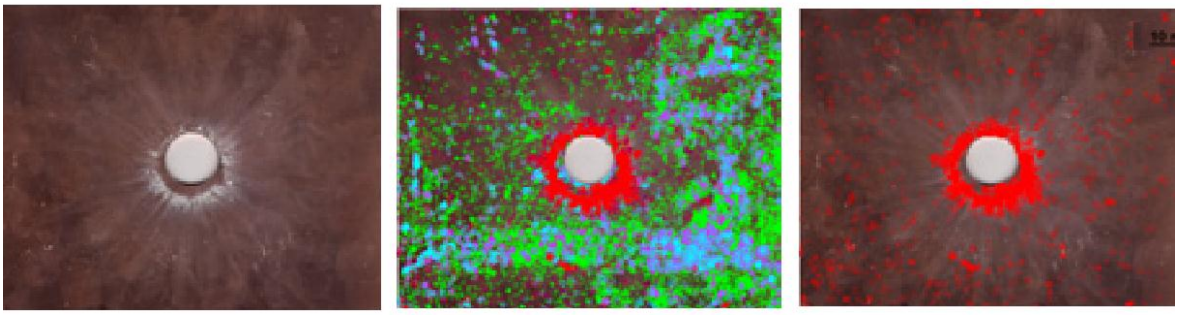

Fig. 4.135 - Example of witness plate analysis for test n. 8646 (dp=1.5 mm, vp=5.20 km/s, normal impact): starting image (left), recognized damages (center), real damage pattern (right)

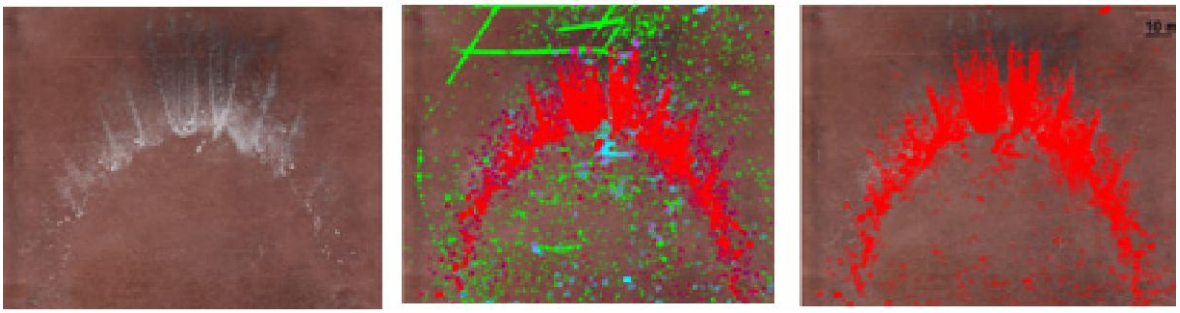

Fig. 4.136 - Example of witness plate analysis for test n. 8656 (dp=2.3 mm, vp=5.34 km/s, oblique impact at 45°): starting image (left), recognized damages (center), real damage pattern (right)

An example of results is reported in Fig. 4.137, where there is the craters' counting and the subdivision in classes of equivalent diameters (0.025–0.05 mm; 0.05-0.1 mm, 0.1-1 mm, >1 mm), according to IADC and ISO standards. ([27])

In the figure on the left there is a comparison between the behaviour of different materials with target's configurations at normal impact condition, the figure on the left shows the behaviour of one kind of target (Al 6082-T6 plate with a thickness of 10 mm) at different impact angles.

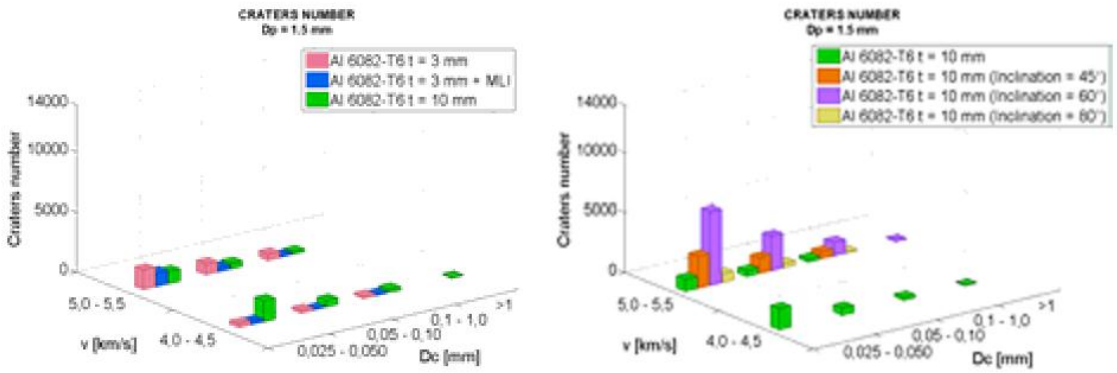

Fig. 4.137 - Crater counting, dp=1.5 mm

Taking in account the data scattering linked with the experimental uncertainties it is possible to do some considerations:

- A hypervelocity impact on any satellite's surface creates a great number of new debris in a wild range of dimensions.
- The number of ejecta increases with the dimensions of the impacting debris and with the impact velocity.
- The number of ejecta created of fragile materials (like solar cells' coverglass) is greater than the one of ductile materials (like Al), even though for metallic surface the linked risk is bigger, because in this case there is a high quantity of fragments with big dimensions.
- The MLI cover on metals reduces the number of the generated fragments.
- The effect of the impact angle needs a deeper investigation.

4.3.4 Transferred momentum evaluation

In this paragraph will be presented the results, regarding the transferred momentum evaluation, of the instrument for primary impact detection described in the paragraph 4.3.3.1.

Due to experimental constraints it was not possible to use sensors like laser Doppler transducers to measure directly the displacement of the ballistic pendulum supporting the instrument, so the evaluation of the transferred momentum is assessed with an indirect method that now will be described.

Because of the position of the PVDF and Flexiforce sensors, the signal represents the dynamic behaviour of the target-structure system, due to the external force caused by the impact (Fig. 4.138).

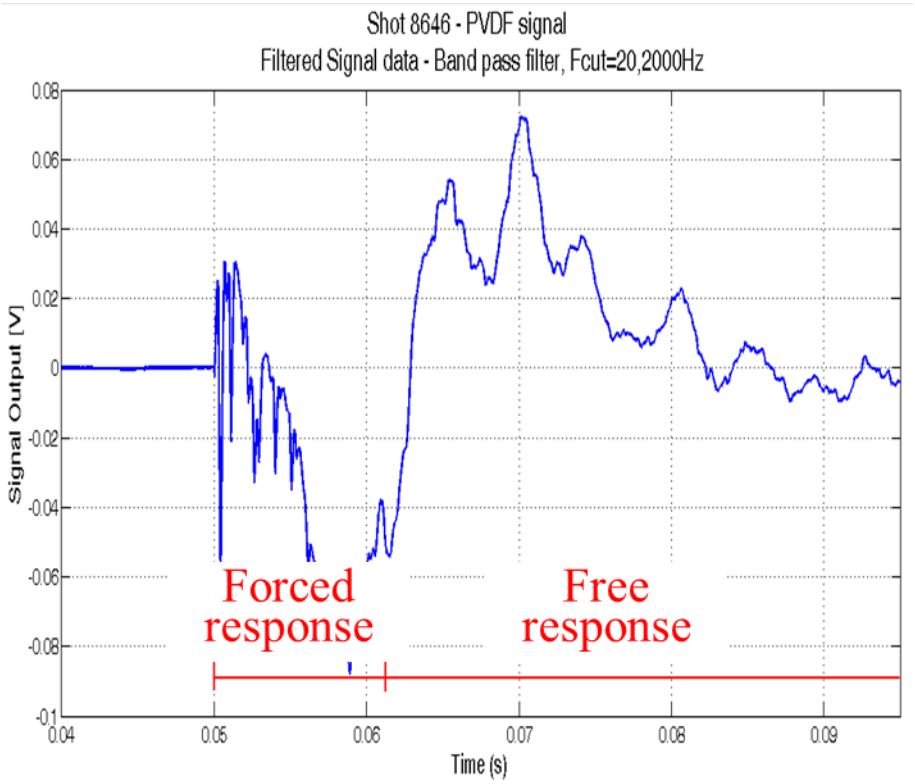

Fig. 4.138 - PVDF signal: forced and free response.

The signals are made by a combination of a forced response (with a duration similar to the time of application of the impulse, it has a quick damping), followed by a free response, linked with the vibrational modes of the system.

It is possible to model the external force caused by the projectile's impact on the target with an impulse shaped input. This means that it can excite a wild range of frequencies, from zero to a maximum linked with the maximum duration of the impulse. It is expected to find peaks in the excited vibrational modes analysing the Fourier transform's module of the sensors' signals

This is why the sensors are evaluated using the comparison between the modules of the Fourier transforms' signals.

Fig. 4.139 shows the Fourier transforms of the different inputs, using a simplified model. There is the assumption that every projectile gives to the target an input

with a force with a duration of DT=dp/vp (*i.e.* the time required by an undeformable sphere with a dp diameter and a vp velocity to enter into the target) and with an impulse equal to Q=Fmax*DT (*i.e.* the projectile's transferred momentum).

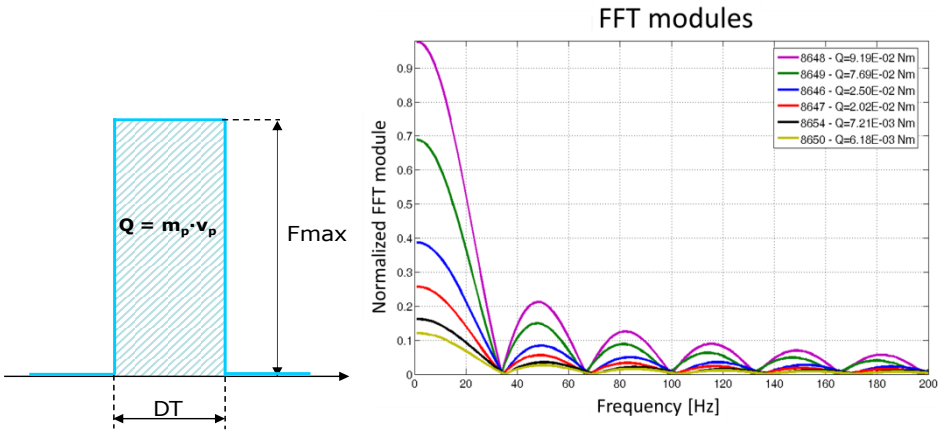

Fig. 4.139 - Simplified model of the impulse generated by the impact (left); Fourier transforms' modules of the tests

The frequency response of the sensors is related with characteristics of the impacting particle.

According to this method, for every test the sensors' signals are analysed in the following way:

- Band pass (20 Hz – 2 kHz) filtering, to remove the zero-shift and the static response of the system.
- Calculation of the Fourier transform using the FFT algorithm.
- Subdivision of the frequencies' range in bands (20-120 Hz, 120-500 Hz, 500-2000 Hz) and calculation for every band of the FFT module's integer.
- Correlation between the values of the calculated integers and the transferred momentum of the projectiles.

An example of the analysis's results is presented in Fig. 4.140 and Fig. 4.141.

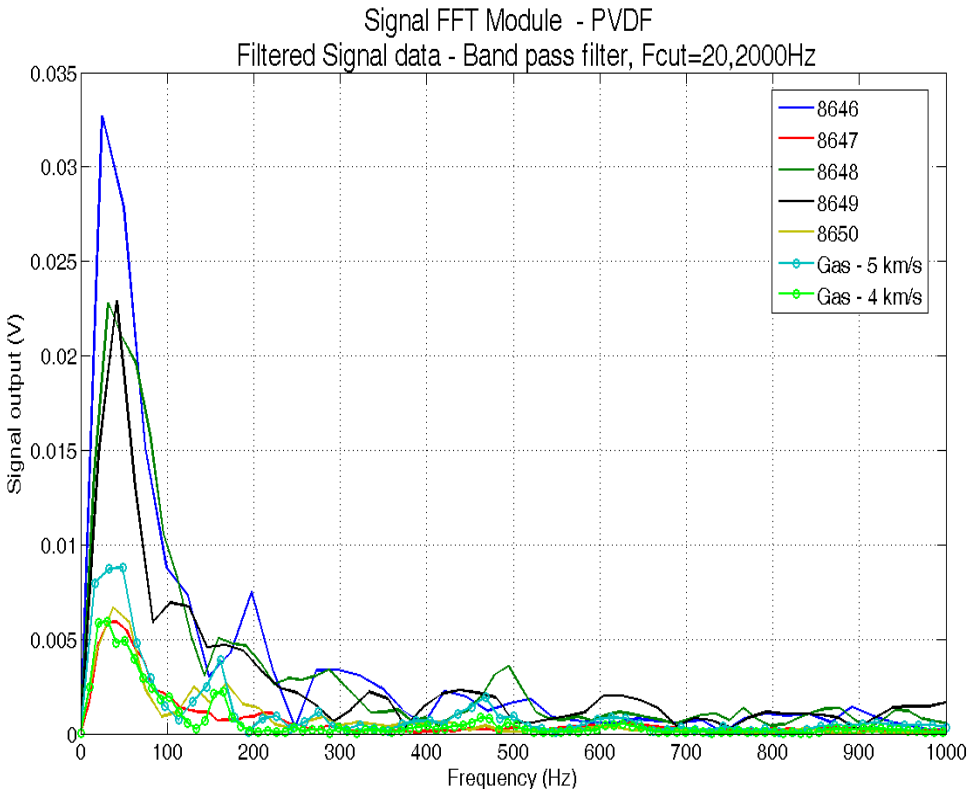

Fig. 4.140 - FFT modules of PVDF sensors' signals.

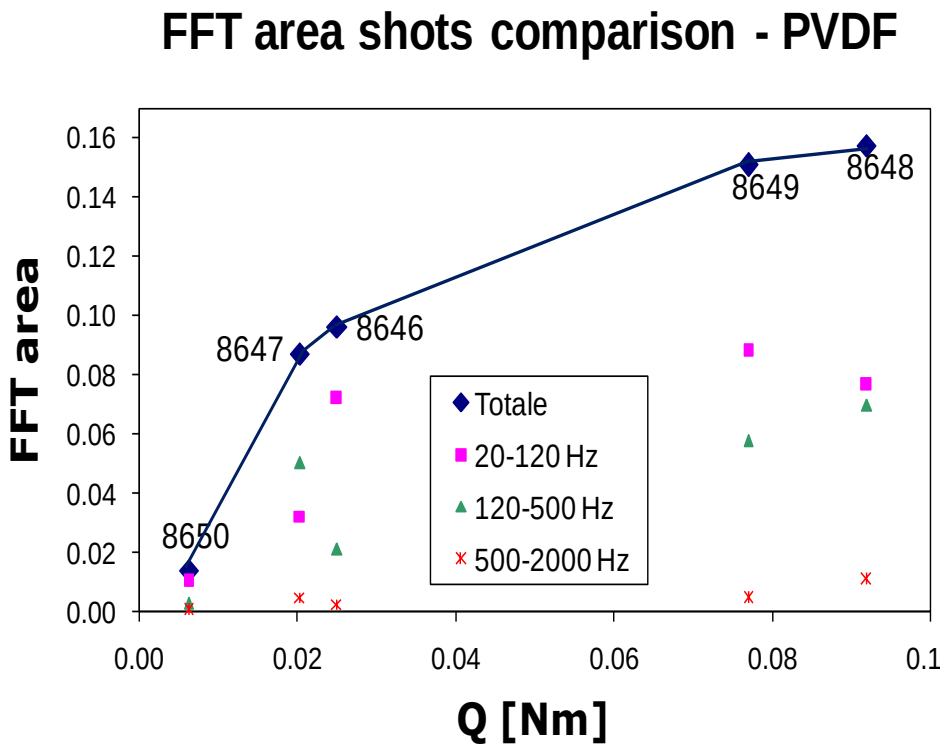

Fig. 4.141 - PVDF sensor. FFT's integer linked with the momentum of the projectiles: total values and values subdivided by bands.

The two figures show the FFT modules of PVDF sensors' signals and the FFT's integer linked with the momentum of the projectiles (total values and values subdivided by bands).
It is shown also the medium value of the facility background noise, evaluated firing sabot without projectiles. These values have the same order of magnitude of the effect due to the smallest and slowest projectile, *i.e.* the ones this the smallest quantity of transferred momentum.

These results show that it is possible to realize an efficient instrument to characterize the impact using PVDF sensors mounted of a supporting structure properly design to vibrate at pre-selected frequencies excited by the impact.
With a suitable calibration it will be possible to derive the characteristics of the impacting debris, starting from the FFT transforms' values.

4.4 Space instrumentation

The previous studies regarding laboratory instrumentation for the studies of ejecta and of the primary impacts open many possible scenario for space applications.

One of these could be about flexible multilayer meteoroid and debris protection shield embedded with biomarker and impact detectors ([36]).

In recent years, the development of flexible, inflatable structures for human space flight has drawn increased attention from research institutes and space industries. Potential applications of inflatable systems include the development of new manned modules for the space exploration, the design of novel manned vehicles for Earth, Lunar and interplanetary orbits and the construction of future surface habitats on the Moon, Mars and Earth-like planets. Inflatable systems are particularly attractive for their high packaging efficiency, which gives the opportunity of achieving large on-orbit volume after inflation, in spite of the limited launch mass, volume and cost.
In the above framework, it is possible to do a preliminary study for a concept based on a mother ship spacecraft with scouting mini-orbiting modules that can detect and quantify the amount of resources, dangers and presence of life on the targeted planet.

These mini-orbiting modules would be deployed by use of inflatable structures capable of withstanding entry into the targeted planet's atmosphere as well as impact detection (with piezoresistive or PVDF film/paint based sensors) and self-healing in order to fix any damage occurred during the orbiting, atmospheric entry and landing phases of the mission.
Self-healing composite materials have been designed which used a microencapsulated epoxy embedded into a structural composite matrix containing a catalyst capable of polymerizing the healing agent upon contact resulting in polymerization in the damaged region.
With continued miniaturization of devices and the evolution of new mission requirements that rely on advanced sensor technology, future spacecraft will have an increasing density of devices and sensors located throughout the structure and on external skins.
Multifunctional materials would be used to embed detectors that can quantify the amount of water, breathable air, raw materials and life.

5 Testing and engineering models for BLEs derivation

The content of this chapter is summarized in the following flow chart (Fig. 5.1).

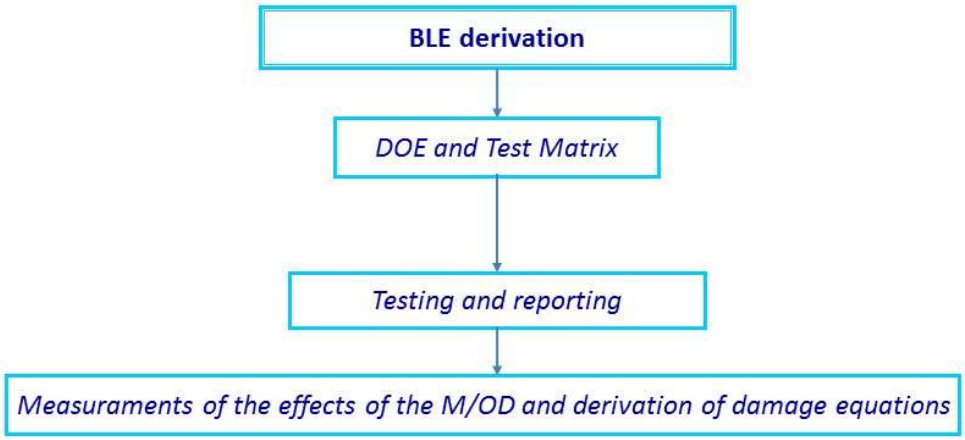

Fig. 5.1- Chap. 5 overview

The methodology to derive the Ballistic Limit Equations (BLE) will be described, starting from the Design of the Experiments (DOE) and the related Test Matrix, the testing and reporting phase and presenting the procedure to derive the equations in the end.

5.1 Design Of Experiments and Test Matrix

5.1.1 Cosmo-Skymed

In this paragraph the different types of targets, tested to study the Cosmo-Skymed satellites, will be described.

The targets' classes are:

1. Whipple Shield: the aim is to tune and validate the procedure to derive the damage equations for the following classes.

2. Aluminium Sandwich Panels (face +x, flight direction): the aim it to derive damage equations to support the Risk Assessment activity.

3. Aluminium Sandwich Panels covered by MLI (face +x, flight direction): the aim it to derive damage equations to support the Risk Assessment activity.

The Test Matrix is presented in Tab. 5-1 and Tab. 5-2. ([27])

The meaning of the symbols and the geometric configuration is described in Fig. 5.2.
The impact angle is measured between the projectile's velocity direction and the normal direction of the target.

Fig. 5.2 - Whipple Shield (left); Honeycomb sandwich panel (right)

Target		Experimental parameters				
material	Standoff	dp	alfa	vp nominal	vp measured	damage
	mm	mm	°	km/s	km/s	
Al bumper 0.8mm, Al wall 2mm	100	2.3	0	3.0	3.01	>BL
Al bumper 0.8mm, Al wall 2mm	100	1.5	0	3.0	3.01	<BL(NP)
Al bumper 0.8mm, Al wall 2mm	100	1.5	30	3.5	3.65	<BL(NP)
Al bumper 0.8mm, Al wall 2mm	100	2.3	30	4.0	4.03	>BL
Al bumper 0.8mm, Al wall 2mm	100	2.3	30	3.5	3.57	>BL
Al bumper 0.8mm, Al wall 2mm	100	3.2	30	4.0	3.86	>BL
Al bumper 0.8mm, Al wall 2mm	100	2.3	45	3.5	3.42	<BL(IS)
Al bumper 0.8mm, Al wall 2mm	100	3.2	45	4.0	3.80	BL(DS)
Al bumper 0.8mm, Al wall 2mm	100	2.3	45	3.0	3.06	<BL(NP)
Al bumper 0.8mm, Al wall 2 mm	100	3.2	45	3.5	3.37	>BL
Al bumper 0.8mm, Al wall 2mm	100	2.3	30	3.5	3.60	BL(DS)

Tab. 5-1. Experiments with Whipple Shields

Target		Experimental parameters			
material	standoff	dp	vp nominal	vp measured	damage
	mm	mm	km/s	km/s	
0.6-0.8_Al5052_HC_1”	74.6	1.5	>4.0	4.11	>BL
0.6-0.8_Al5052_HC_1”	74.6	1.5	>5.0	5.15	>BL
0.6-0.8_Al5052_HC_1”	74.6	1.9	>5.0	5.15	>BL
0.6-0.8_Al5052_HC_1”	74.6	1.9	>4.0	4.43	>BL
0.6-0.8_Al5052_HC_1”	74.6	2.3	>4.0	4.06	>BL
0.6-0.8_Al5052_HC_1”	74.6	2.3	>5.0	5.10	>BL
MLI+0.6-0.8_Al5052_HC_1”	74.6	1.5	>5.0	5.08	>BL
MLI+0.6-0.8_Al5052_HC_1”	74.6	1.5	>4.0	4.51	>BL
MLI+0.6-0.8_Al5052_HC_1”	74.6	1.9	>4.0	4.08	>BL
MLI+0.6-0.8_Al5052_HC_1”	74.6	1.9	>5.0	5.10	>BL
MLI+0.6-0.8_Al5052_HC_1”	74.6	2.3	>4.0	3.78	>BL
MLI+0.6-0.8_Al5052_HC_1”	74.6	2.3	>5.0	5.05	>BL

Tab. 5-2. Experiments with honeycomb sandwich panels

5.1.2 Manned modules shields

5.1.2.1 Introduction

In recent years, the attention of research institutes and factories operating in the space field has been driven to the development of flexible inflatable structures for human space flight. ([24])

In this framework, novel flexible concepts are required to provide adequate protection against to the threat posed by hypervelocity impacts (HVI) with micrometeoroids and orbital debris (MMOD), and new lightweight shields have to be developed to ensure full integration with inflatable structures.

Such shields are composed by a multi-layer shell with three main functional parts: a thermal protection, a MMOD shield and a pressure/air containment. In particular, the MMOD protection system is composed by several layers of flexible materials such as Kevlar and Nextel placed at adequate spacing from each other. The impact range includes projectiles from 1.9 to 3.2 mm, impact speed from 3 to 5.5 km/s and impact angle from 0° to 60°.

The most original part of the study is the application of a novel approach for BLE derivation, based upon the assessment of the impact damage produced on subsequent shield layers in different impact conditions. In contrast to common methods, it is proposed a possible procedure to statistically derive BLEs, starting from experiments in which the evolution of a damage parameter related to the failure is investigated. Such parameter has been obtained by properly combining injury levels measured by automatic inspection on different shield layers. In particular, for the purpose of evaluating the damage area on each sheet, an image analysis procedure implemented in Matlab environment has been employed. According to this method BLE have been deduced and presented together with statistically-based uncertainty bounds.

5.1.2.2 Background

Inflatable structures are structures made of a flexible outer membrane or fabric that is filled with gas, such as air or helium. The gas gives shape and strength to the structure. Uses include roofs and covers, sails, airships, furniture, aerospace structures, boats and air bags. One of several advantages of an inflatable is that it can be stored in a small space when not inflated, since inflatables depend on the presence of a gas to maintain their size and shape. Function fulfilment per mass used compared with non-inflatable strategies is a key advantage.

The last years' interests and developments in inflatable modules for human spaceflight stems from three main fields of application:

- Manned Elements attached to the International Space Station (ISS), to increase the current space station habitable volume or for future -gradual replacement of metallic modules at their end-of-life;

- Free Flyer Modules (in Low Earth or Low Lunar Orbits, or in the Lagrangian point L1) or Interplanetary Transfer Modules;

- Surface Habitats (Moon, Mars outposts).

In particular for medium and long term missions (ranging from 200 to 1000 days) it is currently envisaged a number of crew members up to 5 or 6 people. Estimations conducted by NASA have shown that an individual habitable volume around 100 m^3 will be required for these missions to maintain acceptable standards of life on-board.
To reach this goal, it will be necessary to achieve on orbit volumes up to 600 m3 and assure at the same time the compatibility with the current and the next generation of launch systems. It is envisaged that the increment in mass and volume capability will most probably not allow launching of rigid metallic modules, while the use of high packaging efficiency inflatable structures could provide large on orbit volumes after inflation, in spite of a limited volume/mass at launch.

The primary structure of a typical inflatable manned module is composed of a multi-layered shell. Every group of the composing layers has a specific main function assigned, although synergistic effects between the various groups are envisaged (for instance, the protection from the external environment). ([37])
However, knowledge of the behaviour of inflatable materials subjected to the harsh space environment is rather limited and future potential application of such systems demands for their thorough characterization under simulated orbital conditions. In particular, novel flexible concepts should guarantee sufficient protection against MMOD impacts and new lightweight shields have to be developed to ensure full integration with inflatable structures. Such systems are composed by a multi-layer shell with three main functional parts: a thermal protection, a MMOD shield and a pressure/air containment.

In particular, the MMOD protection system is composed by several layers of flexible materials such as Kevlar and Nextel placed at adequate spacing from each other.
As described in par. 3.2.2.2, Ballistic limit equations (BLEs) are developed to define impact conditions that results in threshold failure of specific spacecraft components or subsystems.
This State of the Art in the approach to space debris protection is based on a fail/no fail criteria and it take in account only one type of mechanical damage.
The actual Ballistic Limit Equations are not statistically based and don't consider the other types of damage and the correlated uncertainty.

5.1.2.1 Impact test campaign

- **Targets description**

The overall target's scheme is showed in the following Fig. 5.3. This scheme has not a high detail level because of disclosure problems linked to the data.
The target is subdivided in 3 stages (the first one is protected by a MLI cover). They are composed by cascades of Nextel and Kevlar layers, moreover the last stage has also 3 redundant air containment sheets.

The scheme is:

- I stage: 2 layers
- II stage: 4 layers
- III stage: 6 + 8 layers

The main concept behind this type of shield design is a hybrid between the Whipple shields and multishock shield one, *i.e.* the I stage allows the fragmentation of the debris and it is an absorber, the same for stage two, the third stage absorbs the residual energy of the impact.

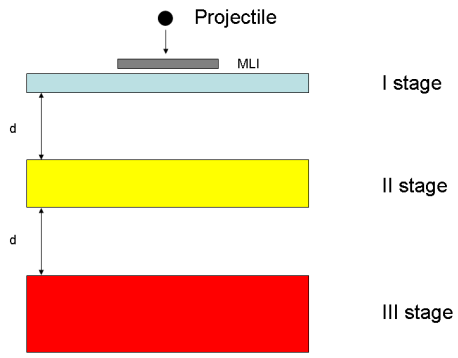

Fig. 5.3 - Schematic target overview

The failure mode considered here is represented by the penetration of the first bladder of the air containment, which is in the third stage.
The ballistic limit is defined as the smallest projectile that just perforates the first redundant bladder air containment system.

5.2 Testing and reporting

5.2.1 Cosmo-Skymed

5.2.1.1 Experiments with Whipple Shields targets

These tests are important to derive a new type of ballistic limit curve, also with oblique impacts, and to define and tune the procedure to obtain damage equations for Cosmo-Skymed's shields.

In Fig. 5.4 there is an example of this type of targets.

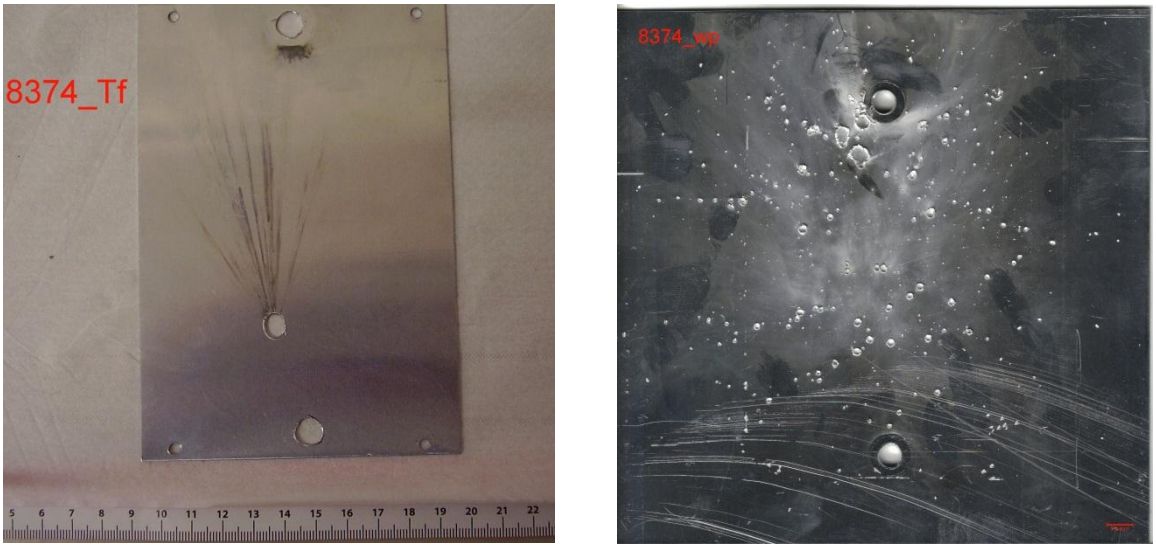

Fig. 5.4 - Whipple Shield (shot n.8374): bumper (left) e back wall (right)

5.2.1.1 Experiments with honeycomb sandwich panels and honeycomb sandwich panels covered by MLI

These types of targets are representative of the external structure of the Cosmo-Skymed satellites, regarding the flight direction (+x), that is the most critical in terms of impact's risks with space debris.

Official data about the structural configuration of the satellite were not available, so 2 sandwich panels of an overall surface of 1.2 x 1.8 m^2 were produced taking in account the info found with a literature review.

These panels have the following characteristics (Tab. 5-3) :

Overall thickness	[”]	1
Skin material	-	Al2024 T3
Front skin thickness	[mm]	0.6
Back skin thickness	[mm]	0.8
Honeycomb material	-	Al5052
Honeycomb type	-	3/16-001P
Adhesive	-	Epoxy Redux 609

Tab. 5-3 - Sandwich panels for Cosmo-Skymed satellites characteristics

12 tests were performed, all over the ballistic limit, to evaluate the damage created on the components inside the satellite, after the perforation of the main structure.
To study the effect of the MLI, 6 tests were made on the basic structure and 6 tests, with the same nominal conditions, were performed on the structure protected by the MLI.

In Fig. 5.5 and Fig. 5.6there is an example of this type of targets.

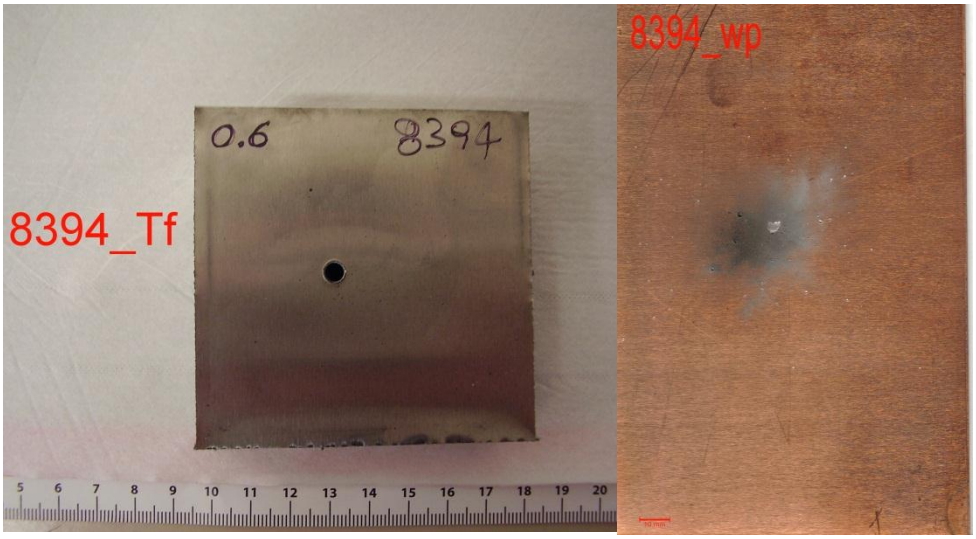

Fig. 5.5 - Sandwich panels for Cosmo-Skymed satellites: front skin (left) and witness plate (right)

Fig. 5.6 - Sandwich panels for Cosmo-Skymed satellites: front skin covered by MLI (left) and witness plate (right)

5.2.2 Manned modules protecting test summary

The impact range includes projectiles from 1.9 to 3.2 mm, impact speed from 3 to 5.5 km/s and impact angle from 0° to 60°.
The overall test campaign data can't be reported, due to disclosure problems.

In the tests that were done there are a little variation of the projectile's diameters used, the great part were done with a 0.29 cm diameter. Moreover there is only one shot with an inclination of 60°. The original test matrix of this campaign had different main drivers in comparison with the ones that needs this BLE derivation method.
This can lead to a great uncertainty in the results, in fact, to apply the procedure that will be described below there is a need for a minimum level of statistic; *i.e.* at least 3 different values of the projectile's diameter to monitor the analysed phenomena dependence from the diameter.

- **Target inspection and damage derivation**

The procedure used for data derivation is described hereinafter:

- The target is unmounted after the shot, this means that every single layer can be taken apart for further analysis;

- For every single layer of the set up a high resolution image is acquired;

- Information about the damage patterns are retrieved by automatic analysis of every single image performed with a dedicated analysis procedure, developed in Matlab® environment. This software detects colour's thresholds (different for every kind of layer) and then overlaps suitable colour maps to highlight the damage areas. In this way it is possible to identify holes and "dark areas" (*i.e.* the non-penetrated damage areas) on the target, as shown in Fig. 5.7 and Fig. 5.8.

- The data that the software gives as output, *i.e.* the areas, are used in the method to identify the ballistic limit curve.

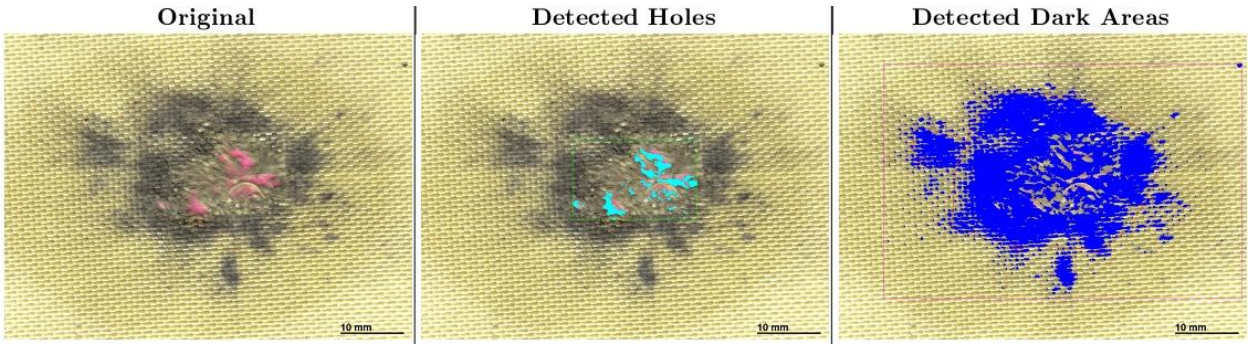

Fig. 5.7 - Damage on a Kevlar layer: raw picture (left), detected hole (center) and detected dark area (right)

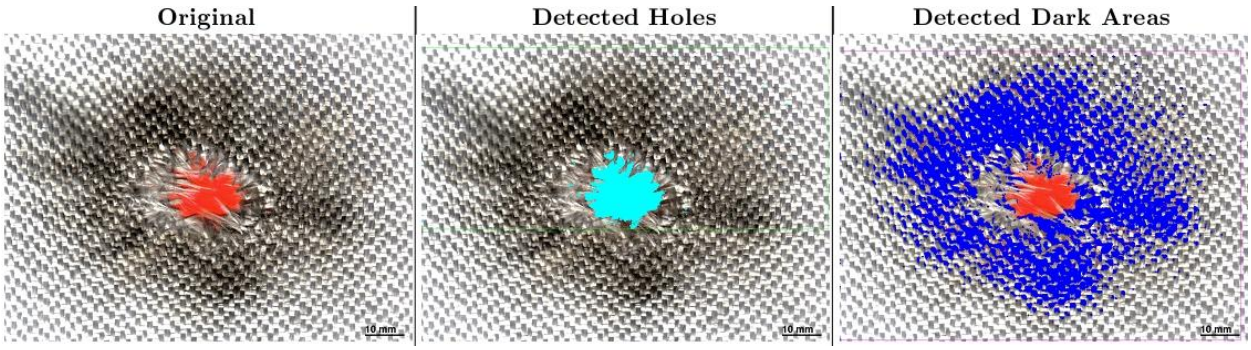

Fig. 5.8 - Damage on a Nextel layer: raw picture (left), detected hole (center) and detected dark area (right)

5.3 Measurements of the effects of the M/OD and derivation of damage equations

5.3.1 Introduction

This chapter will introduce a study about the derivation of damage equations measuring the effects of the M/OD on spacecraft's structures, for manned and unmanned missions.
The procedure to obtain the Cosmo-Skymed damage equations will be described first, focusing on honeycomb's shields. Then the damage equations will be introduced.

5.3.2 Cosmo-Skymed damage equations

The following cases will be described:

- BLE for Whipple Shields
- Damage(crater) equations for the internal damage evaluation for Cosmo-Skymed satellite

For both the situations, the determination of the equation following the procedure described in 3.3.2, that defines a 'damage parameter' Π linked to the failure mechanism.
For every protection system, the value of the damage parameter is measured and related to the impact conditions (*i.e. dp, vp,* α, etc.), to derive an empirical relation *f* (Damage Predictor Equation) that describes the Π variation:

$$\Pi = f\,(dp, vp, \alpha, \ldots)$$

The damage parameter for this situation is the total crater area (CA) on the Witness Plate (Fig. 5.9). The WP function is to give information about the debris cloud, using the craters that the impacts generate. It is reasonable to asses that the increase of the crater area means a higher damage of the target. This choice it is not the optimum for the correlation with the failure phenomena (in fact the experimental scattering is high), but it is very easy to implement and speed up the procedure for the measurement of the damage

parameter.

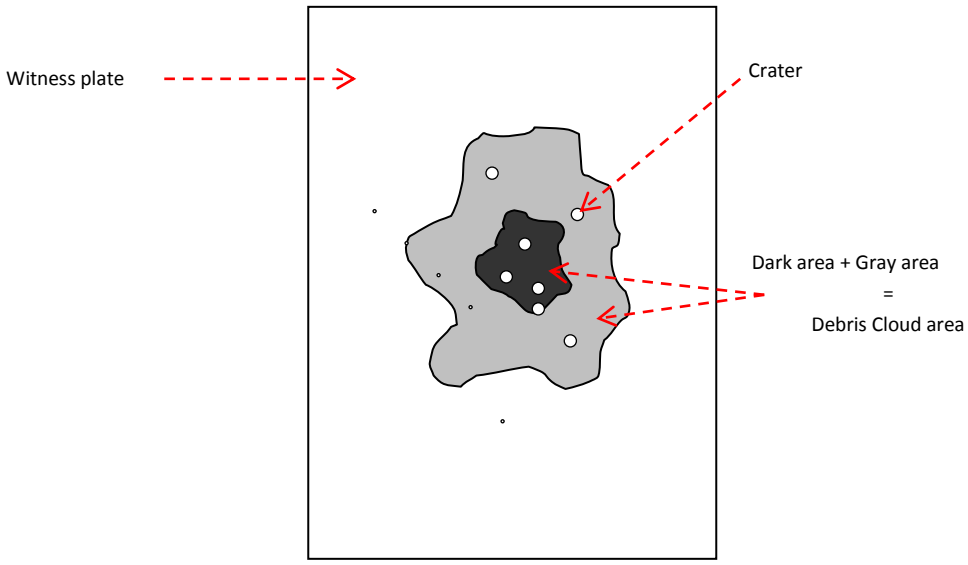

Fig. 5.9- WP scheme and definition of the damage parameter

To derive the damage equations the procedure is:

- High resolution scanning of the WP;
- Matlab analysis of the images, to evaluate the crater area;
- Experimental data fitting, to co-relate the crater area with the damage parameter
- Damage equations derivation

5.3.2.1 BLE for Whipple Shields

Regarding the Whipple shields an empirical damage equations was obtained and then it was expressed as function of the projectile diameter *dp*.

$$dp_{FIT} = f_1(CA, v_p) \pm \delta_{dp} = (4.977 \cdot 10^{-6} \cdot CA^{1.814} \cdot v_p{}^{0.412} + 1.484) \pm 0.401 \quad [\text{mm}] \qquad \text{Eq. 5-1}$$

$$\delta = \sqrt{\frac{\sum \left[f(CA, v_p)_{\text{Experimental}} - f(CA, v_p)_{\text{Fit}} \right]^2}{(n-1)}} \qquad \text{Eq. 5-2}$$

The calculated uncertainty related to the data fitting of the projectile diameter is:

$$\delta_{\text{mean value}} = 19{,}5\%$$

Where vp is the projectile velocity and CA is the Crater Area.
The uncertainty bound was calculated using the following relation:

$$i_{tot} = \sqrt{\left(\frac{\partial f(\mathrm{CA}, \mathrm{v_p})}{\partial \mathrm{CA}}\right)^2 \cdot i_{CA}^2 + \left(\frac{\partial f(\mathrm{CA}, \mathrm{v_p})}{\partial \mathrm{v_p}}\right)^2 \cdot i_{vp}^2 + \delta^2} \qquad \text{Eq. 5-3}$$

In this case i_{tot} is the overall uncertainty that combines the main sources of uncertainty due to δ, CA and v_p.
The following values were used:

- i_{CA} = 94 mm^2
- i_{vp} = 0.25 km/s (this value derived from the uncertainty related with the laser blades that measure the projectile velocity)

The identified critic value for the Crater Area is: CA = 457 mm^2 .

The following equation (Eq. 5-4) is derived using all the experimental data for Whipple Shields.

BLE Whipple Shield

$$dp_{BL} = 0.444 \cdot v_p^{\,0.412} + 1.484 \quad [\mathrm{mm}] \qquad \text{Eq. 5-5}$$

Mean error: 25%

This BLE is valid for the 3-7 km/s range and is referred to the Al6082-T6 target.
In the following Fig. 5.10 there is the correlation between the impact parameters (dp, vp) and the damage parameter (Crater Area, CA).
In Fig. 5.11 there is a comparison between Eq. 5-5, the classic Christiansen equation in the intermediate range and the experimental data.

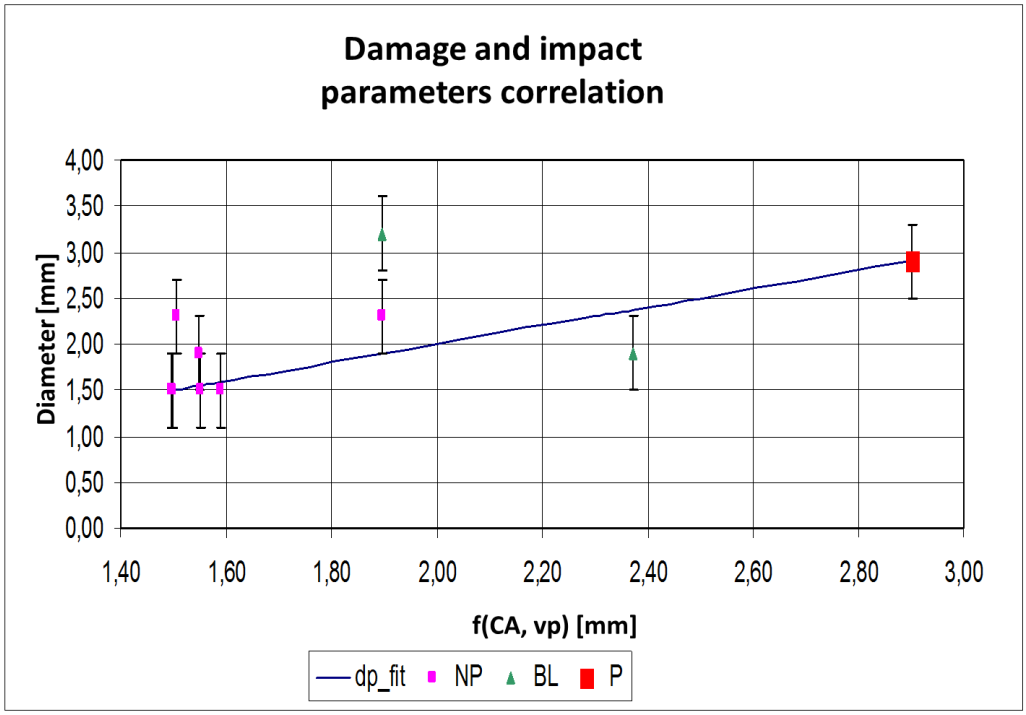

Fig. 5.10 - Damage parameter fit

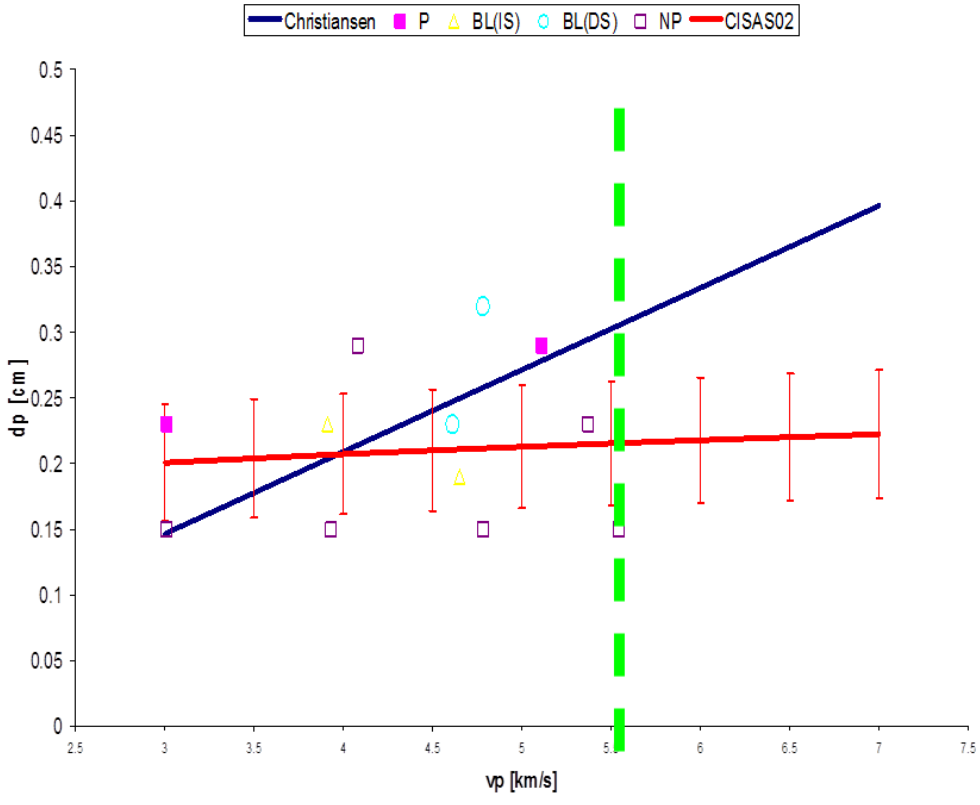

Fig. 5.11 - BLE for Whipple Shields

It is visible the compatibility between the 2 equations, within the experimental range. Outside this range (*i.e.* between 5.2 and 7 km/s), there are differences.
The most important novelty that this equation introduce is the possibility to specify an uncertainty bandwidth, needed for a statistical use of the data, this allow to give a confidence interval to the Risk Assessment valuations.
The obtained bandwidth is around 25% (mean), this is a very good preliminary result that shows how this approach needs further studies.

5.3.2.2 Damage equations for the internal damage evaluation for Cosmo-Skymed satellite

To obtain Damage Equations to study the internal damage for Cosmo-Skymed satellite 3 types of damage parameters were identified, all linked with the damaged area on the copper witness plate after the impact test.
For the given configurations the parameters are measured in different experimental conditions. These measures are used to develop an empirical model (Damage Predictor Equation) to describe the variation of the damage parameter, also across failure conditions.
The comparison of the DPE with the critical value of the parameter above determined could allow the evaluation of the BLE together with its confidence bounds.

Starting from the experimental data available, a single BL curve that is applicable to the target was determined. The ballistic limit curve is given with its band of uncertainty, which comes up from the combination of all the most relevant uncertainty sources, *i.e.* the data scattering around the ballistic limit and the confidence in the fit of data with the proposed Damage Predictor equation.
The procedure here used to derive the DP equation is based upon the definition of a damage parameter that is physically related to the perforation phenomenon. Such parameter must vary monotonically across the failure threshold, assuming a particular critical value (that can be individuated from the experiments) around the ballistic limit. All the available data, even well away from the BL, can be used to statistically follow the critical parameter evolution. In this way, it is possible to provide an estimation of the test conditions at the ballistic limit, even inside the bounds defined by the two closest NP and P experiments.

12 experiments were done, varying the debris diameter (1.5, 1.9, 2.3 mm) and the impact velocity (~4 e ~5 km/s). Sandwich panels with and without MLI were tested.

Equations for the 2 types of tests are reported, they are related to:

- Crater Area (CA)
- Dark Area (DA)
- Debris Cloud Area (DC)

The equations are derived with common statistical methods of experimental data interpolation and best fitting.
For both the classes (with and without MLI) there are also reported images of the damaged WP and of image analysis.

1. Sandwich panel without MLI

   As an example the WP of the test n. 8394 is shown in Fig. 5.12. The scanned image, with a resolution of 300 dpi, is then analysed to evaluate the damage parameters, *i.e.* Crater Area CA, Dark Area DA and Debris Cloud Area DC (Fig. 5.13 and Fig. 5.14)

Fig. 5.12 - Test n.8394: Witness Plate of a sandwich panel without MLI; dp=1.9 mm, vp=5.15 km/s

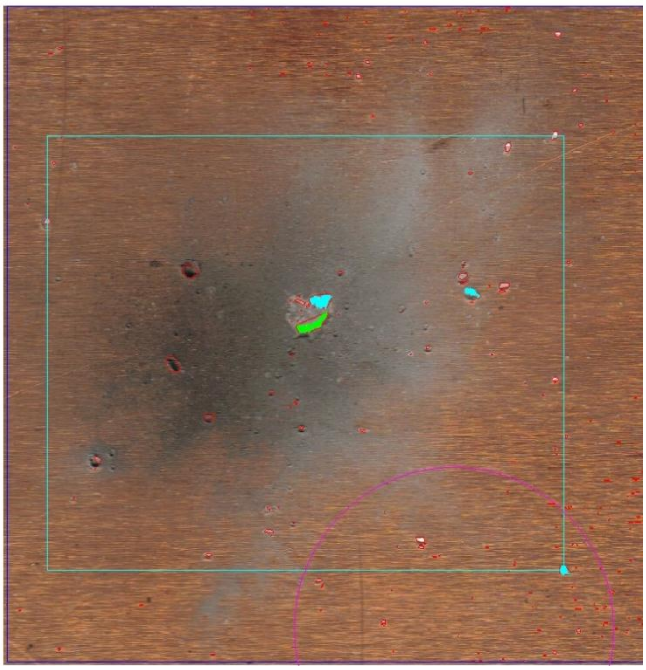

Fig. 5.13 - Test n.8394: Crater Area

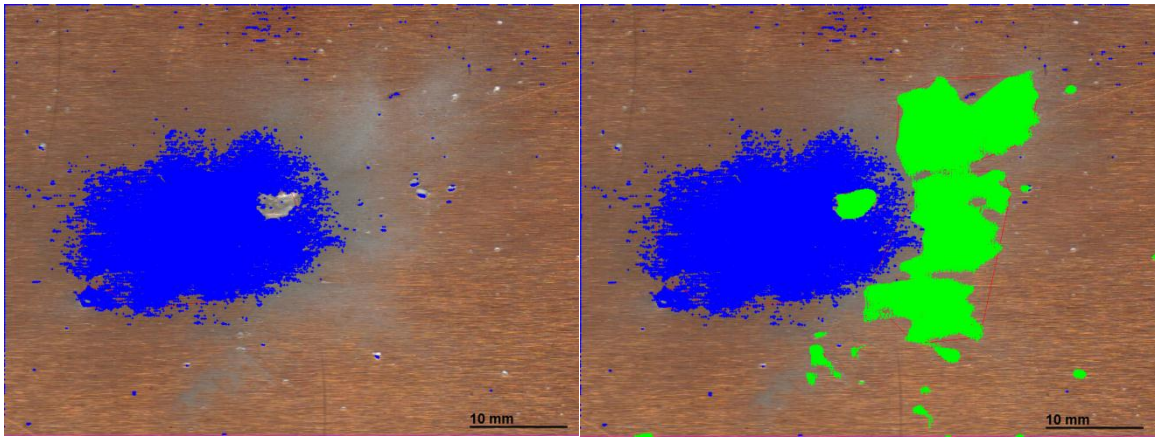

Fig. 5.14 - Test n.8394: Dark Area (left) and Debris Cloud Area (right)

The related equations are:

Crater Area

$$CA = f_1(d_p, v_p) \pm \delta_{CA} = (41.616 \cdot d_p^{1.6052} \cdot v_p^{-1.3395} - 1.7534) \pm 2.04$$

Mean error: 15%

Eq. 5-6

Dark Area

$$DA = f_2(d_p, v_p) \pm \delta_{DA} = (11.532 \cdot d_p^{1.4874} \cdot v_p^{1.2631} - 61.9) \pm 99.61$$

Mean error: 67%

Eq. 5-7

Debris Cloud Area

$$DC = f_3(d_p, v_p) \pm \delta_{DcA} = (33.902 \cdot d_p^{0.97635} \cdot v_p^{0.99726} + 41.328) \pm 156.17$$

Mean error: 47%

Eq. 5-8

Fig. 5.15, Fig. 5.16 and Fig. 5.17show graphs with the fit.

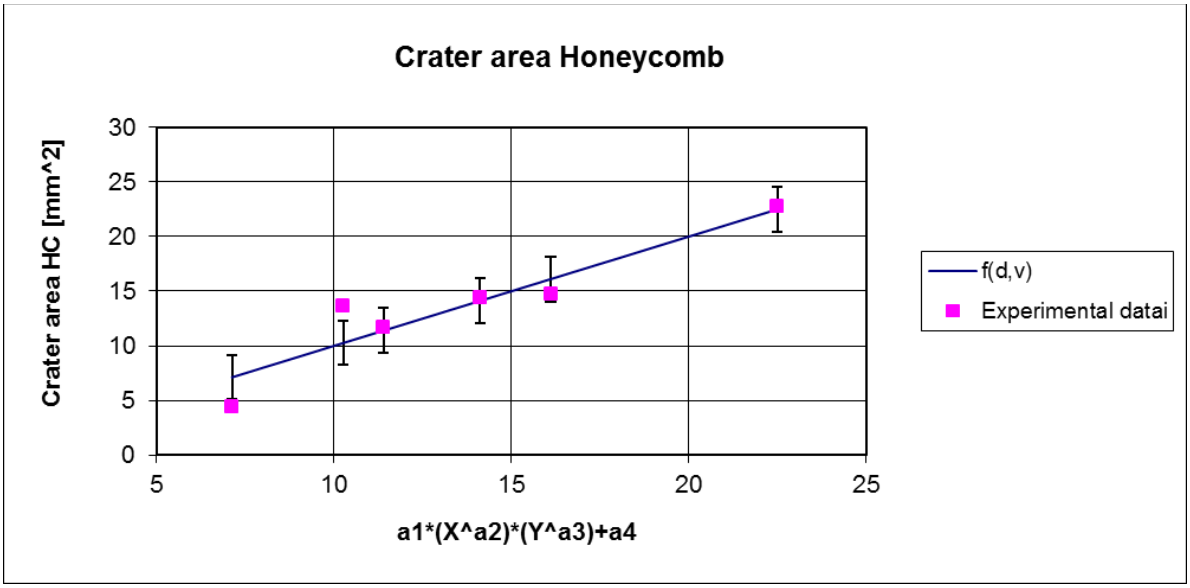

Fig. 5.15 - Crater Area (fit and experimental data)

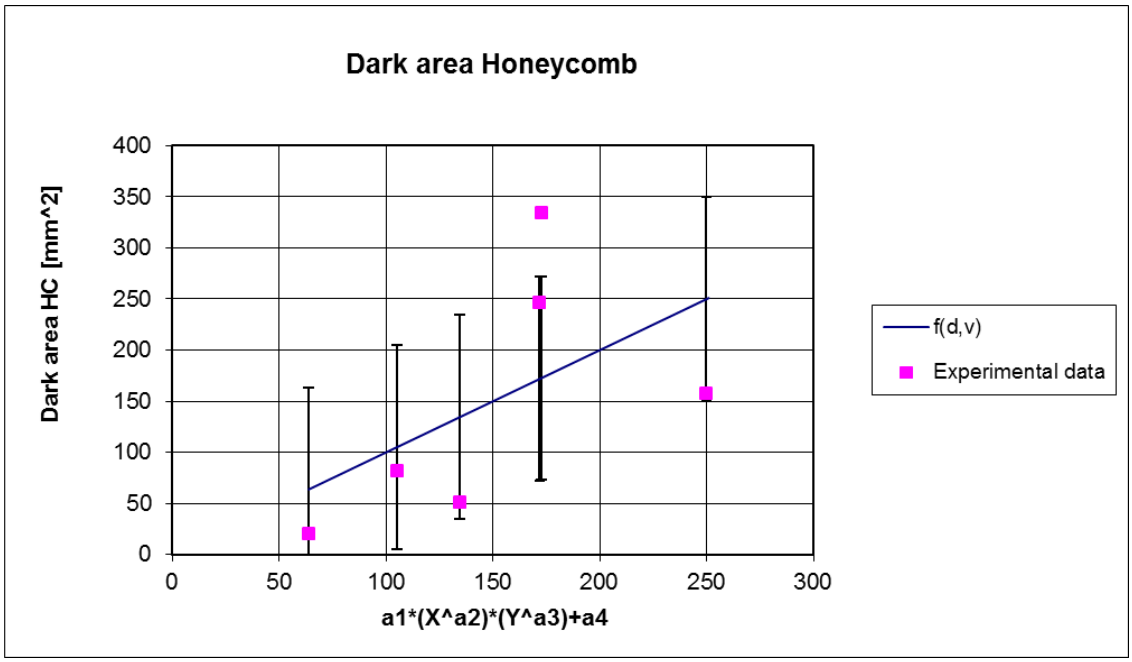

Fig. 5.16 - Dark Area (fit and experimental data)

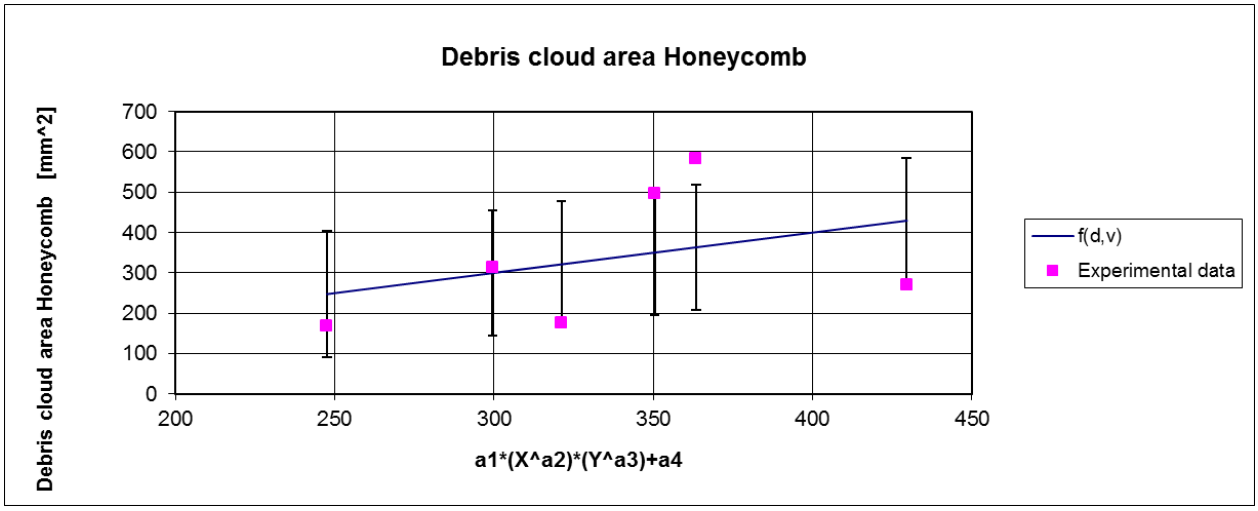

Fig. 5.17- Debris Cloud Area (fit and experimental data)

The best results for this kind of shield are obtained measuring the crater area, where the fitting with the equation shows a mean error around 15%.

2. Sandwich panel with MLI

As an example the WP of the test n. 8425 is shown in Fig. 5.18. The scanned image, with a resolution of 300 dpi, is then analysed to evaluate the damage parameters, *i.e.* Crater Area CA, Dark Area DA and Debris Cloud Area DC (Fig. 5.19 and Fig. 5.20).

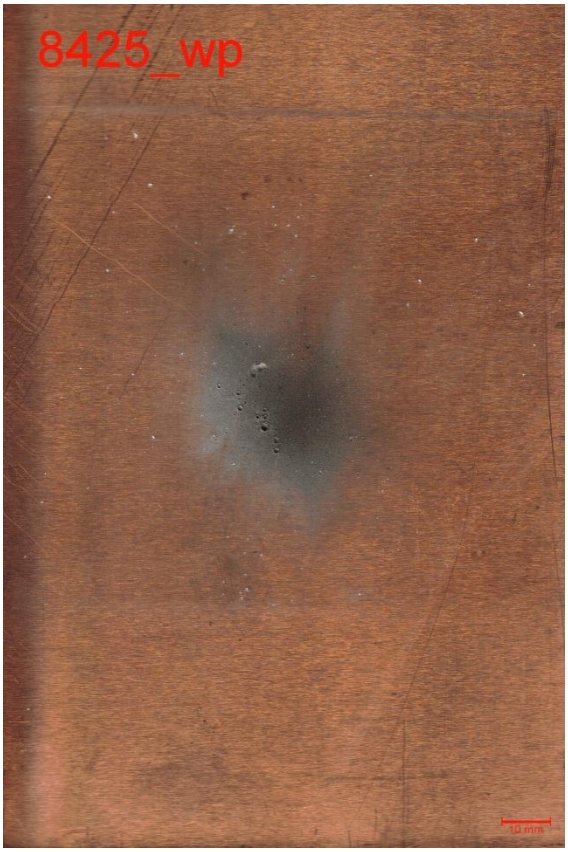

Fig. 5.18- Test n.8425: Witness Plate of a sandwich panel without MLI; dp=2.3 mm, vp=5.05 km/s

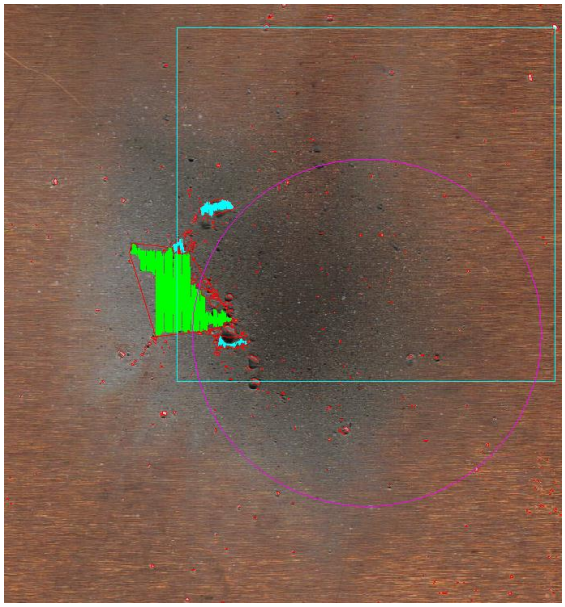

Fig. 5.19 - Test n.8425: Crater Area

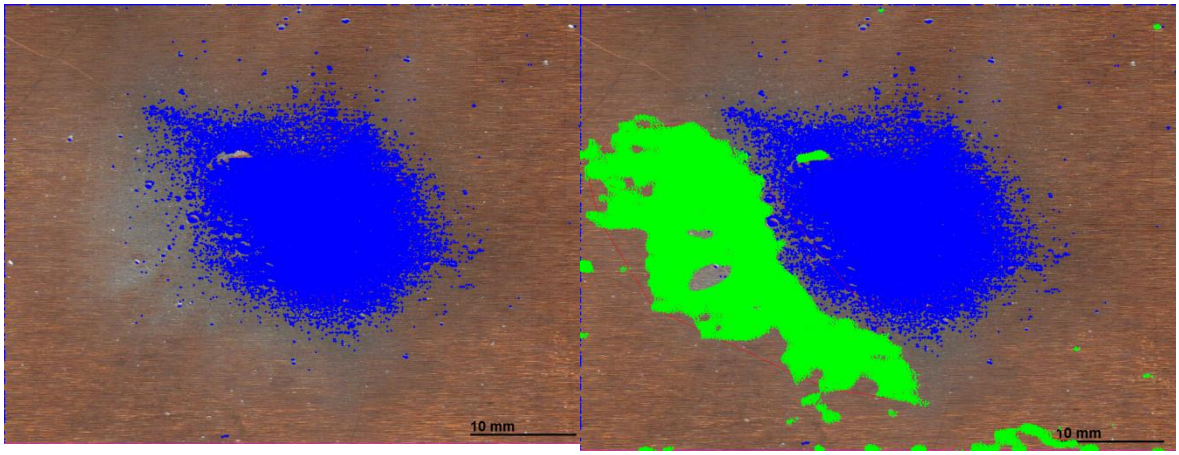

Fig. 5.20 - Test n.8425: Dark Area (left) and Debris Cloud Area (right)

The related equations are:

Crater Area

$$CA = f_1(d_p, v_p) \pm \delta_{CA} = (3.343 \cdot 10^{-6} \cdot d_p^{\,9.8935} \cdot v_p^{\,4.9603} - 1.6893) \pm 3.13$$

Mean error: 32%

Eq. 5-9

Dark Area

$$DA = f_2(d_p, v_p) = (2.495 \cdot 10^{-3} \cdot d_p^{\,6.5699} \cdot v_p^{\,3.9107} - 15.243) \pm 15.52$$

Mean error: 15%

Eq. 5-10

Debris Cloud Area

$$DcA = f_3(d_p, v_p) \pm \delta_{DcA} = (0.24426 \cdot d_p^{\,5.6367} \cdot v_p^{\,1.9375} - 5.6337) \pm 37.82$$

Mean error: 15%

Eq. 5-11

Fig. 5.21, Fig. 5.22 and Fig. 5.23show graphs with the fit.

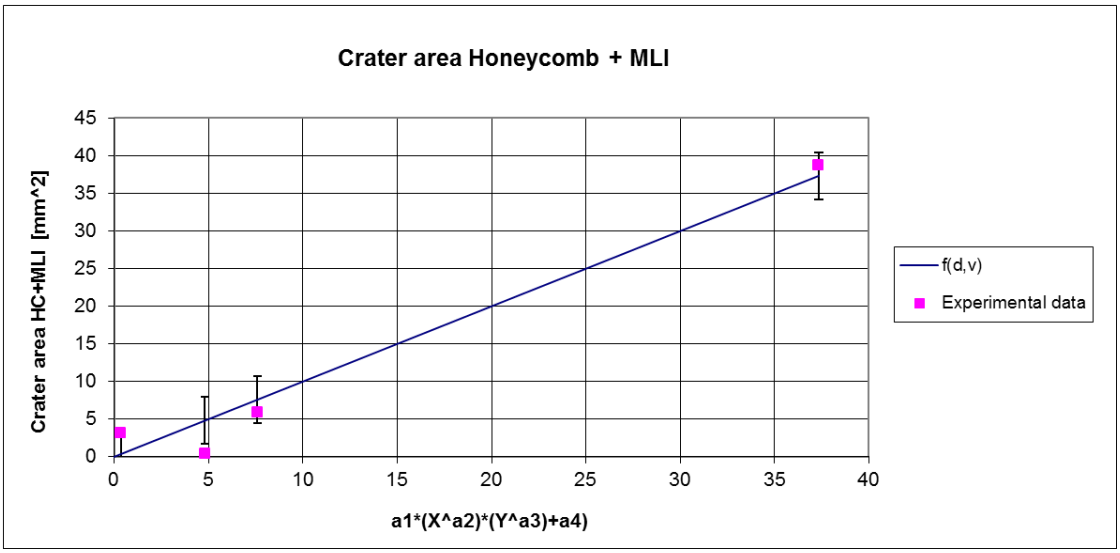

Fig. 5.21 - Crater Area (fit and experimental data)

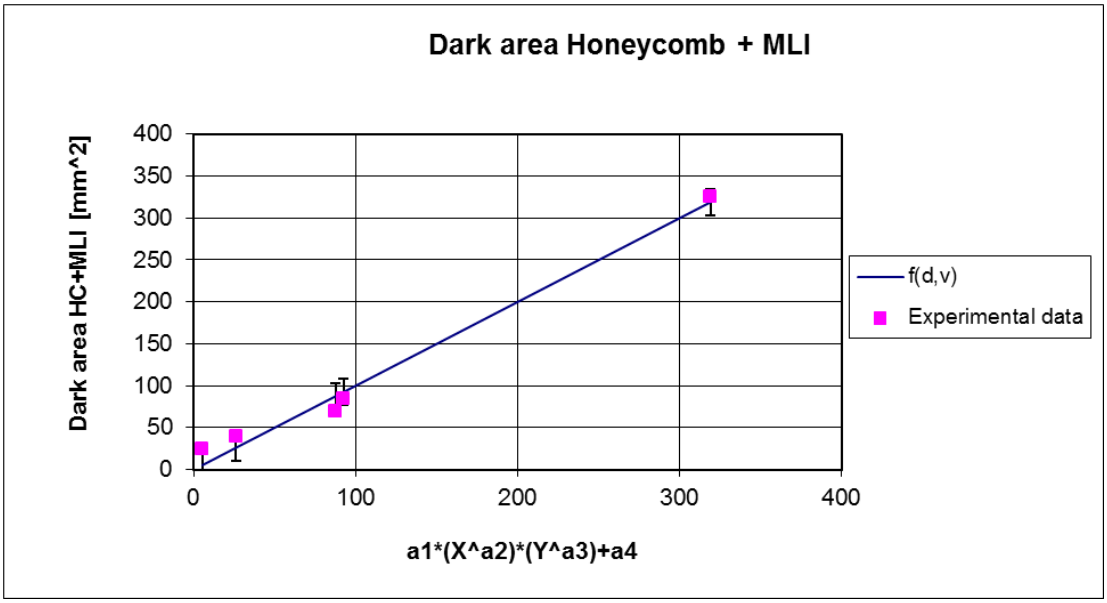

Fig. 5.22 - Dark Area (fit and experimental data)

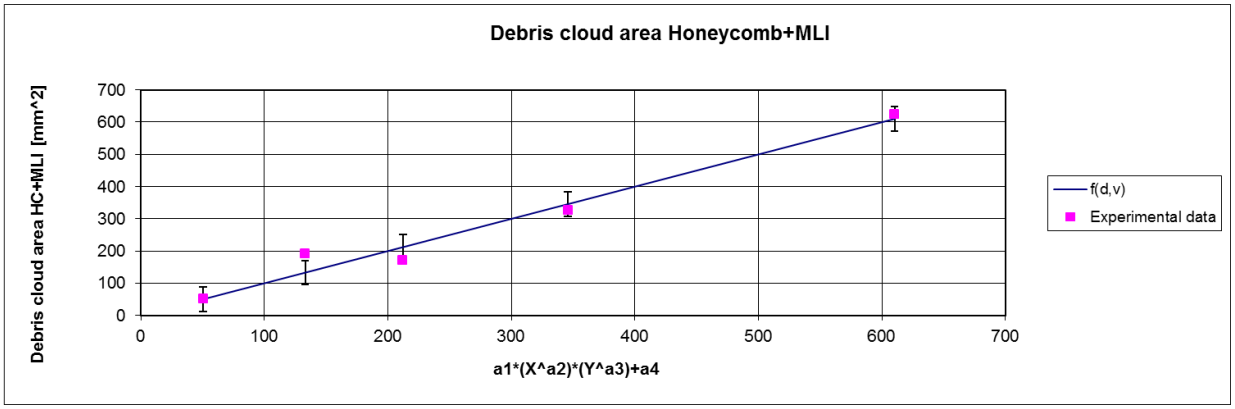

Fig. 5.23 - Debris Cloud Area (fit and experimental data)

Due to the use of the MLI the behaviour of this shield is different in comparison with the previous one, the best results are obtained measuring the dark and debris cloud area, where the fitting with the equation shows a mean error around 15%.

The difference could be explained with the fact that the MLI cover creates a greater amount of small fragments that allows a better definition of the debris clouds area on the damaged pattern on the witness plate.

5.3.3 Inflatable structures damage equations

A flow chart of the procedure for data analysis about the derivation of the ballistic limit equations is presented in Fig. 5.24.

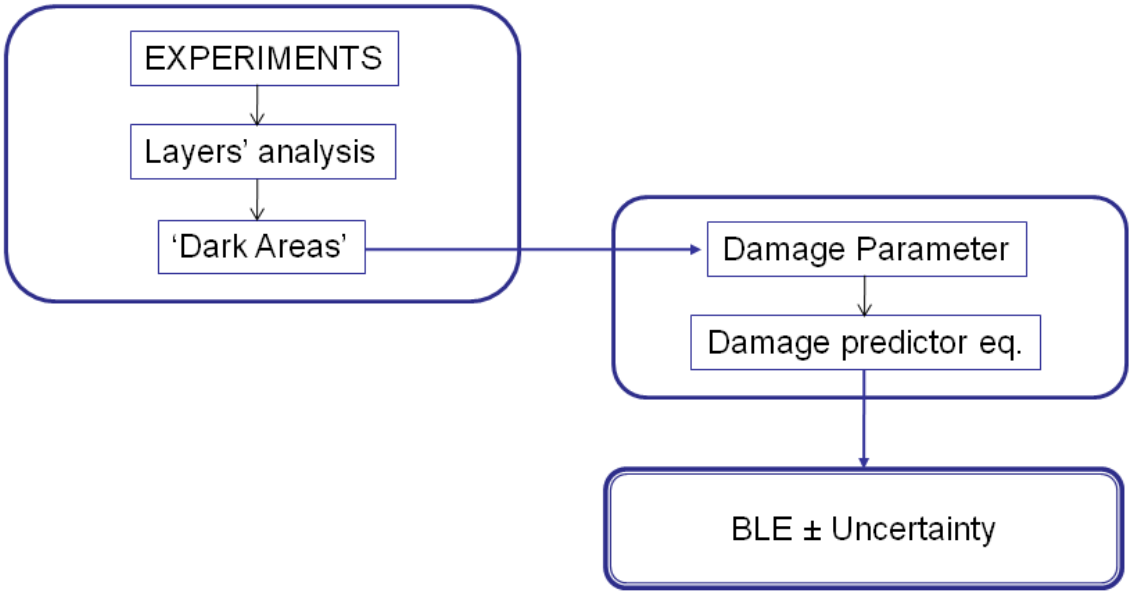

Fig. 5.24 - Data analysis procedure

In contrast to the common method described before, the flow chart in Fig.4 shows a possible procedure to statistically derive BLEs. starting from experiments in which the evolution of a damage parameter related to the failure is investigated. For a given configuration, such a parameter is measured in different experimental conditions and the critical value that it assumes when failure just occurs is known together with its measurement uncertainty. On the other hand, the same measures are used to develop an empirical model (Damage Predictor Equation, DPE) to describe the variation of the damage parameter, even across failure conditions. The comparison of the DPE with the critical value of the parameter above determined finally allows the evaluation of the BLE together with its confidence bounds.

In particular, for the purpose of evaluating the holes area and the damage area on each shield layer, it has been employed an automatic image analysis procedure implemented in Matlab environment.
The defined damage indicators have been compared based upon their sensitivity to ballistic limit detection and BLE have been derived accordingly, including the specification of statistically-based uncertainty bounds.
Although the damage evaluation has been here used to derive BLE of an already fixed shield configuration, future perspectives are finally given to adapt the described procedure for design and optimization of inflatable meteoroid and debris protection systems.

- **Statistic approach and Damage Parameter**

The previous scheme now will be described in detail.
Starting from the experimental data available, a single BL curve that is applicable to the target was determined. The ballistic limit curve is given with its band of uncertainty, which comes up from the combination of all the most relevant uncertainty sources, *i.e.* the data scattering around the ballistic limit and the confidence in the fit of data with the proposed Damage Predictor equation.
The procedure here used to derive the DP equation is based upon the definition of a damage parameter that is physically related to the perforation phenomenon. Such parameter must vary monotonically across the failure threshold, assuming a particular critical value (that can be individuated from the experiments) close to the ballistic limit. All the available data, even well away from the BL, can be used to statistically follow the critical parameter evolution. In this way, it is possible to provide an estimation of the test conditions at the ballistic limit, even inside the bounds defined by the two closest NP and P experiments. The new procedure is detailed in the following.

As a first step, a Damage Parameter is selected: it is related to the response of the shield and can therefore identify the perforation threshold. In our case, the DP is defined as follows:

$$\Pi = \left(\frac{Lts}{DA_{tot(fs-ss)}} \right) \cdot \overline{DA}_{avg(ss\text{-}ts)} \quad [\mathrm{mm}^2] \qquad \text{Eq. 5-12}$$

Where Π is the Damage Parameter, Lts is the damage area on the first layer of the third shield stage, DAtot(fs-ss) is the sum of the “dark areas” in the first layers (made by the layers of first and second stage plus the first layer of the third stage) and DAavg(ss-ts) is the mean value of dark areas in the layers of third stage, *i.e.* all the layers before the first air containment.
The first part of the parameter, $\left(\frac{Lts}{DA_{tot(fs-ss)}} \right)$, gives an assessment of the damage on the the first layer of the third stage, weighted by the overall dark areas of the previous layers. This allow to take into account the effects of the impact conditions of the different tests, *i.e.* the first part of the parameter defines the efficiency of stage one and stage two, giving a value that describes how much the third stage absorbed in comparison with the energy absorbed by the first two stages.
The second part, *i.e.* $\overline{DA}_{avg(ss\text{-}ts)}$, takes in account the effect of the damage in the last stage, that is the most critical one. It describes the evolution of the damage.
Π defines an ‘equivalent damage’, with increasing value of this parameter the shield pass from

non-penetrating (NP) to penetrating (P) condition, this means that the overall behaviour of the MMOD protection is monotone function of a measurable parameter that can be correlated to the experimental conditions.

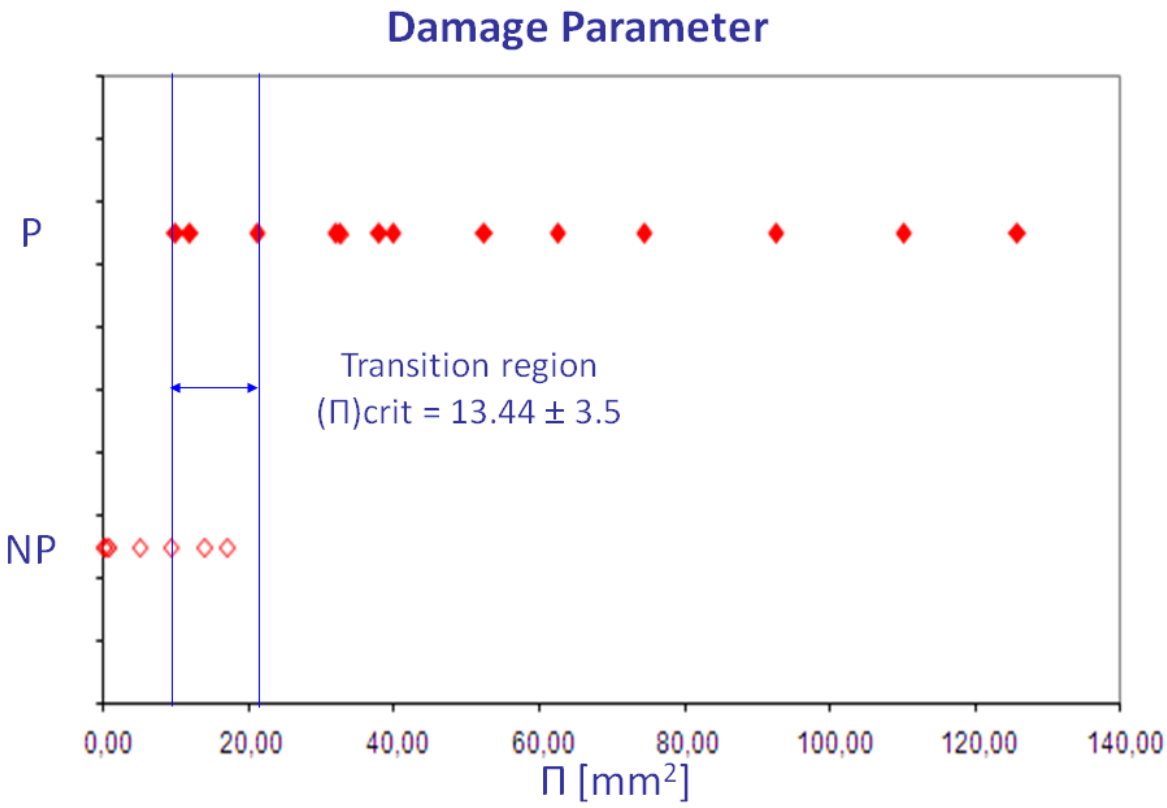

Fig. 5.25 - Summary of experimental data. NP: No Perforation. P: Perforation.

As Π increases, a transition region which defines experimentally the BL threshold is highlighted from non-perforating to perforating impacts. Such region is comprised between the minimum value of Π that produces penetration and the maximum value of Π that does not produce penetration. From the plot, the critical value of Π is determined as:

$$(\Pi)\text{crit} = 13.44 \pm 3.5 \quad \text{mm}^2$$

Fig. 5.25 shows that the definition of parameter Π describes the trend of the damage with an uncertainty of about 25%.

The uncertainty value is due to:

- Accuracy of image analysis;
- Data scattering link to the mounting repeatability of the target.

- **Damage predictor equations**

The Damage Parameter allows to correlate the data of the image analysis procedure with the impact conditions of every shot.
At this point a Damage Predictor correlation is developed from regression analysis (Fig. 5.26) to relate the parameter Π with projectile and impact parameters (diameter and velocity).

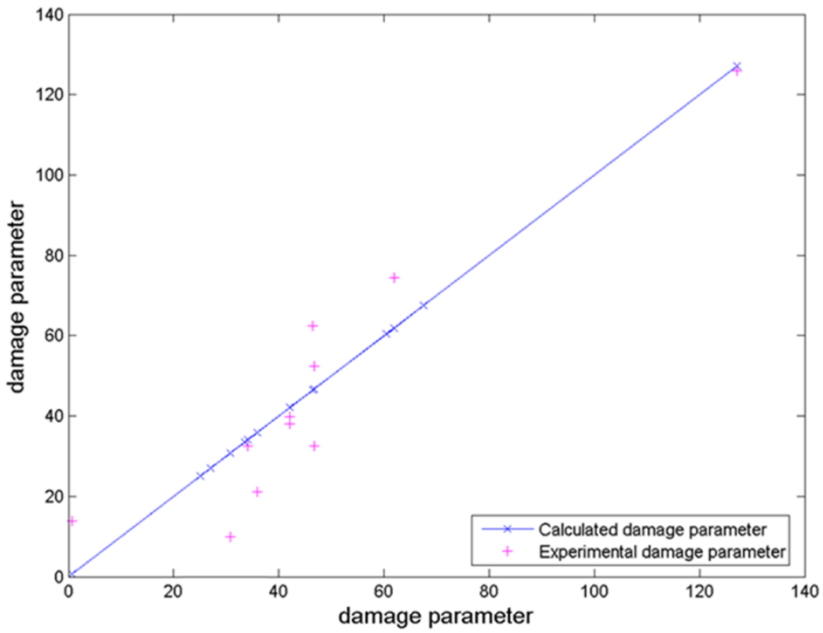

Fig. 5.26 - Damage parameter, fit of experimental data

For the materials and targets considered in this study,

$$\Pi = \left(\frac{A + d_p}{B + C \cdot v_n^{\,2}} \right) + D \cdot v_n \quad ; \quad r2 = 0.74 \qquad \text{Eq. 5-13}$$

Where dp is the projectile diameter (mm) and vn is the projectile velocity (km/s) and the coefficients are:

A= -1.500E0;
B= 1.050E-2;
C=-3.124E-4
D= 6.293E1;

The correlation coefficient r2 provides a measure of the goodness of the fit (r2 =1 is a perfect fit).

- **Ballistic Limit Equations**

The ballistic limit equation is finally developed:

$$d_p = [(\Pi_{crit} - D \cdot v_n) \cdot (B + C \cdot v_n^2) - A] \pm U_{crit} \qquad \text{Eq. 5-14}$$

The ballistic limit curve is given with its band of uncertainty ± Udcrit, that was calculated by propagating to the final result the uncertainty on Π and the uncertainty on the empirical correlation developed, according to ISO standards.
To assess the combined uncertainty the following relations were used:

$$\delta = \sqrt{\frac{\sum \left[f(\Pi, v_n)_{Experimental} - f(\Pi, v_n)_{Fit} \right]^2}{(n-1)}} \; ; \qquad \text{Eq. 5-15}$$

$$i_{tot} = \sqrt{\left(\frac{\partial f(\Pi, v_n)}{\partial \Pi} \right)^2 \cdot i_\Pi^2 + \left(\frac{\partial f(\Pi, v_n)}{\partial v_n} \right)^2 \cdot i_{vn}^2 + \delta^2} \; ; \qquad \text{Eq. 5-16}$$

Where δ is calculated comparing experimental data with the results of the fitting, and i_{tot} is the overall uncertainty that combines the main sources of uncertainty due to δ (25%), Π (70%) and v_n (5%).

For the damage parameter and for the normal velocity of the projectile the following values were used:

- i_{vn} = 0.25 km/s (this value derived from the uncertainty related with the laser blades that measure the projectile velocity)
- i_{Π} = 3.5 mm^2

As mentioned before there is a very little variation of the projectile's diameters used for the tests, the great part were done with a 0.29 cm diameter. Moreover there is only one shot with an inclination of 60°.
So the analysed velocity range arrives till 4.25 km/s , over this velocity there is no direct dependence from projectile's diameter and it is impossible to derive the curve in a statistic way.

In particular, it was found that the most critical source of uncertainty is related to the fit of (Π) data with equation $\Pi = \left(\frac{Lts}{DA_{tot(fs-ss)}} \right) \cdot \overline{DA}_{avg(ss-ts)} \quad [\mathrm{mm}^2]$ Eq. 5-12, which gives a constant contribution to Udcrit.
This was mainly due to:

- Fragmentation phenomenon and damaging process between layers of the same stage and between different stages;
- The damaging process is also linked to the repeatability in the montage of the stages;
- Uncertainty linked with the image analysis procedure.

The following Fig. 5.27, plot the ballistic limit bands, with a mean value of uncertainty of 30%, together with experimental points, for the MMOD shields. dp is the projectile diameter, vn is the normal projectile velocity. The plots confirm that the predictions of the BL equation are consistent with the experimental results.

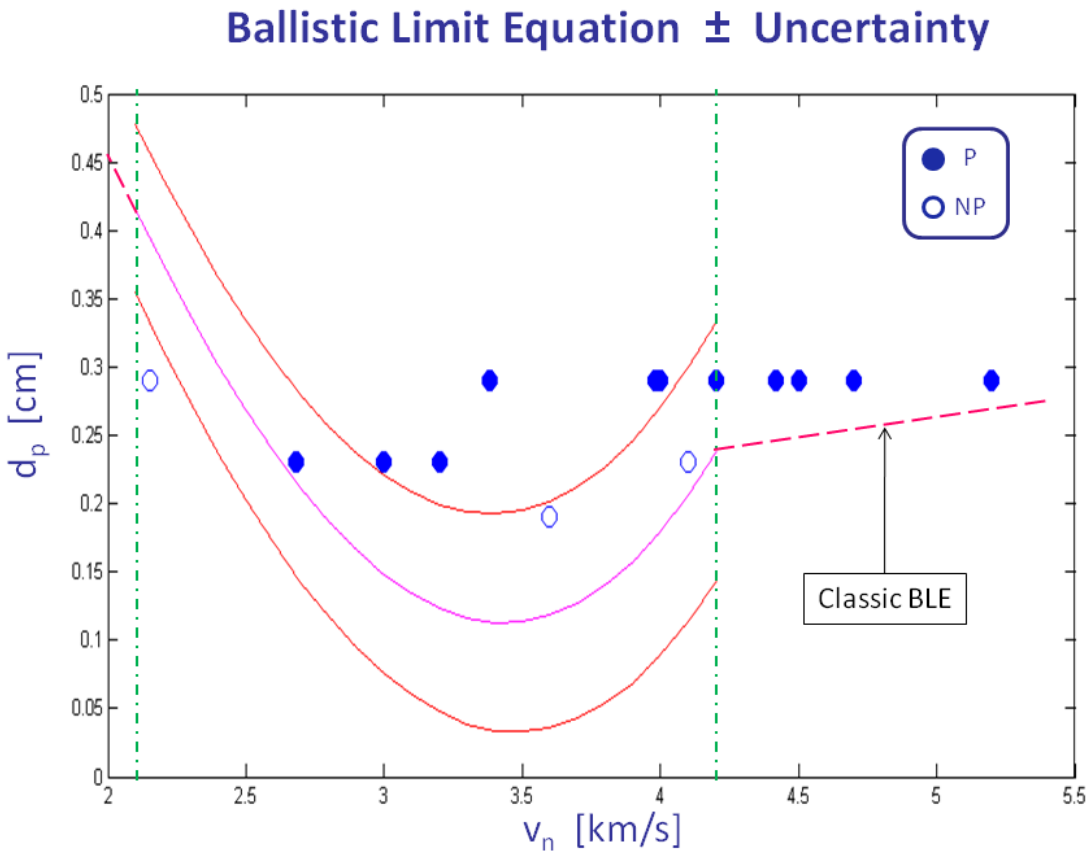

Fig. 5.27 - Experimental data (NP: No Perforation; P: Perforation) and Ballistic Limit (BL) band for inflatable structures

6 Conclusions

The aim of the research documented in this thesis was the study of measurement techniques for assessing and reducing the risk posed by micrometeoroid and orbital debris to space vehicles. Moreover the introduction of the scientific-technical background and the selection of 2 case studies were presented.

Within this aim, the following objectives had to be achieved:

- Improvement and development of acceleration techniques to simulate hypervelocity impacts due to space debris in orbit around the Earth;
- Design of instrumentation able to study primary and secondary impacts' effects;
- Implementation of a procedure to define damage and ballistic limit equations.

In order to achieve the objectives described above, the following work was pursued:

- Development of an upscaled version of the existing CISAS two stage LGG, with the design of the supporting structure and of the high pressure section, able to withstand pressure and temperature peak values up to 6000 bar and 3000 K.
- Studies about 2 single stage LGGs:
    - CISAS HVI facility: Gasdynamical analysis and sabot stopping system design for a single stage gun able to fire up to 0.12 kg at 1000 m/s;
    - Cranfield University facility: Sabot stopping system and impact chamber design for a maximum launch package of 40 g at 300 m/s;

- Design and development of an instrument for ejecta characterization, starting from a prototype using PVDF film sensors, doing studies about strain gauges sensors and realizing an evolution of the instrument using piezoresistive sensors. This instrument allows to detect submillimetric particles and to classify them following proposed ISO standards.
- Design and development of an instrument for primary impact detection, using 3 types of sensors, *i.e.* piezoelectric load cell (PVDF), piezoresistive load cell and PT100 sensor for

calorimetric measurements, at the same time to do a comparative evaluation of their suitability for the application. Results from the PVDF sensor signal allow to link the FFT module's integer with the momentum of the projectiles.

- The work described above led to a procedure to define damage predictor equations for Cosmo-Skymed satellites and Ballistic Limit Equations for inflatable structures, like the ones that will be used for future manned modules. These equations are statistically based and have an associated uncertainty bound. This aspect may give a new scenario for the MMOD shields' design in the future, in terms of weight and efficiency.

Therefore, all objectives of the research were met and future studies are now proposed:

- Further development of the CISAS single stage LGG;
- Evolution of the instrument for the ejecta characterization, testing sensors with higher performances and doing proper impact test campaign designed specifically for this kind of study, to obtain an extended statistic database;
- This will allow to refine the procedure to define BLEs and to reduce the associated uncertainty bound.

References

[1] *Space Debris Environment Remediation Concepts*, H. Klinkrad and N.L. Johnson, Fifth European Conference on Space Debris, 2009

[2] *Space Debris*, M. Griffiths, Postnote, n. 355 (2010)

[3] *Uncertainty considerations for ballistic limit equations,* W.P. Schonberg et al, , Int. J. of Impact Eng., 26, 713-724 (2001)

[4] *Effects of uncertainty in hypervelocity impact performance equations and other parameters on variance in spacecraft vulnerability predictions*, H. J. Evans and J. Williamsen, International Journal of Impact Engineering 23 (1999) 225-236

[5] *The terrestrial particulate environment and its future evolution*, R. Jehn, H. Klinkrad and H. Sdunnus, Int. J. Impact Engng, Vol. 20, pp.443-454, 1997

[6] *The ESA space debris mitigation handbook*, D. Rex et al, Adv. Space Res. Vol. 23, No. 1, pp. 215-225,1999

[7] *Characterizing secondary debris impact ejecta*, W. Schonberg, International Journal of Impact Engineering 26 (2001) 713-724

[8] *Secondary debris impact damage and environment study*, G.Y. Shepard et al, Int. J. Impact Eng Vo1.14, pp.671-682, 1993

[9] *Impact effects from small size meteoroids and space debris*, G. Drolshagen, Advances in Space Research 41 (2008) 1123–1131

[10] *Adverse effects of space debris on astronomy*, D. McNally, Adv. Space Res. Vol. 19, No. 2, p. 399-432.1997

[11] *Study on Space Debris and Impact Effect on Spacecraft*, H. Hai et al, Nuclear Physics B (Proc. Suppl.) 166 (2007) 282–285

[12] *Electromagnetic properties of impact-generated plasma, vapor and debris*, D.A. Crawford et al, International Journal of Impact Engineering 23 (1999) 169-180

[13] *Experimental measurements of hypervelocity impact plasma yield and energetics*, P. R. Ratcliff, Int. J. Impact Engng, Vol. 20, pp. 663-674, 1997

[14] *Analysis of transient vibrations on complex targets representing elementary configurations of GOCE satellite*, D. Pavarin, A. Francesconi et al., International Journal of Impact Engineering 35 (2008) 1709–1715

[15] *Generation of transient vibrations on aluminum honeycomb sandwich panels*

subjected to hypervelocity impacts, A. Francesconi, D. Pavarin et al, International Journal of Impact Engineering 35 (2008) 1503–1509

[16] *Characterizing the transient response of CFRP Al HC spacecraft structures induced by space debris impact at hypervelocity*, S. Ryan et al, International Journal of Impact Engineering 35 (2008) 1756–1763

[17] *Private document to define a proposal for deriving new ballistic equations defining and using a damage parameter,* A. Francesconi

[18] *Ballistic limit equations for spacecraft shielding*, E. L. Christiansen and J. H. Kerr, International Journal of Impact Engineering 26 (2001) 93-104

[19] *Secondary impact hazard assessment*, W.R. Stump, E.L. Christiansen, Report No. 86-128, Eagle Engineering Inc., Houston, Texas, 1986

[20] *Protection Manual (ver.4)*, IADC WG3 members

[21] Space debris: Assessing risk and responsibility, A. M. Bradley et al., Advances in Space Research 43 (2009) 1372–1390

[22] *Hypervelocity impacts and damage laws,* M. Lambert, Adv. Space Res. 1997; 19(2): 369-378

[23] *COSMO-SkyMed an existing opportunity for observing the Earth*, F. Covello et al, Journal of Geodynamics 49 (2010) 171–180

[24] *Impact damage and ballistic limit equations for flexible multilayer meteoroid and debris protection shields*; L. Barilaro, A. Francesconi, C. Giacomuzzo, R. Destefanis (2010); ARA 2010 Congress. Thun (Switzerland), 12-17 September, 2010

[25] *Engineering Design of Instrumentation for Life Detection Planetary Exploration Missions*, Juanes-Vallejo C. M. (2011), PhD Thesis, Cranfield Health, Cranfield University, UK

[26] *A method to assess the average properties of spacecraft ejecta from hypervelocity impact*; A. Francesconi, C. Giacomuzzo, L. Barilaro; HVIS 2010 Congress, Freiburg (Switzerland) 4-12 April, 2010

[27] *ASI SD2 RA4 issue2.0*; A. Francesconi, C. Giacomuzzo, L. Barilaro et al., 2011

[28] *NASA Handbook for limiting orbital debris*; 8719.14 (approved: 2008-07-30)

[29] *Space Debris*, H. Klinkrad (2010), Encyclopedia of Aerospace Engineering

[30] *International Space Station*, NASA website accessible at www.nasa.gov/mission_pages/station/main/index.html

[31] *Orbital Debris Quarterly News*, Volume 12, Issue 4, October 2008

[32] *Orbital Debris Quarterly News*, Volume 12, Issue 4, October 2008

[33] *Private document to define a proposal for ejecta characterization following ISO standards*

[34] *ESA MASTER*, accessible at www.master-model.de

[35] *The New NASA Orbital Debris Engineering Model ORDEM 2000*, J-C Liou et al., NASA/TP—2002-210780

[36] *Flexible multilayer meteoroid and debris protection shields embedded with biomarker and impact detectors*; L. Barilaro, C.M. Juanes-Vallejo, A. Francesconi; abstract for 100 Year Starship Study Public Symposium, Orlando (USA), 30 Septmber-3 October 2011

[37] *Selectig materials to protect inflatable structures from the space environment*, R. Destefanis

[38] *Hypervelocity impacts and damage laws*, Lambert M., Adv. Space Res. 1997; 19(2)

Abbrevations and acronyms

ASI	Agenzia Spaziale Italiana
BL/BLE	Ballistic Limit / Ballistic Limit Equation
CFD	Computational GasDynamics
CFRP	Carbon Fiber Reinforced Plastic
CISAS	Centro Interdipartimentale Studi ed Attività Spaziali “G. Colombo”
COTS	Commercial, Off-The-Shelf
GEO	Geosynchronous Earth Orbit
GTO	Geosynchronous Transfer Orbit
HEO	High Eccentricity Orbit
HVI	Hypervelocity Impact
IAC	International Astronautical Congress
IADC	Inter-Agency space Debris Coordination committee
ISO	International Organization for Standardization
ISS	International Space Station
LEO	Low Earth Orbit
LGG	Light Gas Gun
MEO	Medium Earth Orbit

List of figures

Acknowledgments

To thank everyone in detail will require many other pages, so I will just write a quick random list:

- My Svpreme Master AF
- Eng. Cianphreska
- Eng. Cocola
- Dr. CMJV of Demonios Team
- SCRAT! (Asiago_m, TL, Ciocci, Roger, Duzzino, Curling…, Mitch, Hispanico)
- Eng. Pietro
- Eng. Umberto B.
- Prof. Cesare
- Tasinato
- Masiero
- Cinzia G.
- Amalfi
- Eng. Martosaura
- Eng. Frociolass
- Eng. Moretto
- Eng. Selmo
- Yuval
- Eng. Alberto Bettella
- Eng. Manente
- Eng. Tomaello
- Prof. Rade, Dr. Kevin Hughes and Mrs. Marion
- Pepe
- The ASD board
- The Shu crew
- Ambrofora
- Ilaria and Easyjet
- Olle, Helen & the REXUS-BEXUS people
- Ticià
- Eng. Giulia G.
- Eng. Dorry
- Anna Utopia
- PinS
- Mirra
- The funny Serena&Elettra scientific duo